Assessing the Barriers to Lower Complexity Amplifiers for 1064 nm Picosecond Lasers

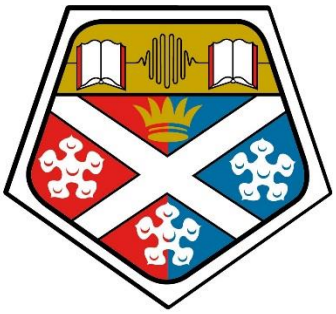

University of Strathclyde Glasgow

Thomas Ewan Bennett

A thesis presented in fulfilment of the requirements for the degree of Doctor of Philosophy to the University of Strathclyde, Department of Physics

2021

Declaration of Authenticity and Author's Rights

This thesis is the result of the author's original research. It has been composed by the author and has not been previously submitted for examination which has led to the award of a degree.

Acknowledgments

There are many people to thank for all the help and assistance I have received throughout my PhD, not least of all Professor Alan Kemp. I would like to thank Alan for his seemingly unending patience and excellent knowledge and advice, which has always been shared freely. I don't believe it is an exaggeration to say that without his help and understanding, I would not have completed this thesis. I am forever grateful.

On the theme of patience, I would also like to thank John Mark Hopkins for his constant support and forbearance. As well as learning a great deal from John Mark, I was also delighted to have many excellent conversations about 80's pop culture, obscure bands and many other eclectic subjects over a tub of Chicken Cottage's finest. My thanks also go to David Burns who taught me a great deal, not only regarding photonics and but also about fine dining. I enjoyed the many lunches out in Glasgow and the episode on the swinging chairs will live long in the memory. To David Stothard, not only a great scientist and renaissance man but a wordsmith as well. I still remember your many eloquent and witty turns of phrase as well as all your great help, thank you.

I always felt that I didn't have my own post doc until Gerald Bonner came to my rescue. I would like to thank him for his considerable help at a crucial time and for always having the time to discuss ideas and to work on things in the lab with me. I enjoyed working with you tremendously and always enjoyed our discussions on theology and all manner of other things. A thank you also to Loyd McKnight, I will forever be disappointed that we didn't get to build a gin and tonic fountain laser or that we never quite got to the bottom of the world's economic woes. We did, however, win the pub quiz twice and I am thankful for your friendship and advice.

To all the other researchers at the IOP and Fraunhofer: Peter, Rolf, Jonathan, Benoit, Johannes, Niall, Christopher, John, Simon and those I have forgotten here, thank you for your help, advice and for always being friendly and nice.

My time at the IOP and Fraunhofer was made all richer by the fact I got to share it with Sean and Daniel. Thank you for the slaggings and terrible patter, the games of 5s and the trips to Chunky Chicken. Danny, thanks for all the dubious facts and general knowledge as well, I still can't believe that you didn't make it onto University Challenge. I would also like to thank all the other students for the trips to the pub and a general sense of camaraderie: Bryn, Caroline, Anne-Marie, Antonio, Abigail, Joao, Elisabeth, Lea and everyone else that I've failed to mention.

I could not have gotten through this PhD without the considerable help from so many people at both the IOP and Fraunhofer. I loved my time at both places and would like to thank Tim Holt and Lynda for being so lovely and welcoming. Thank you to Simon Andrews for the ferocious cuddles and for being frank and candid when I needed it and to Iona. Thank you to Lisa, Sharon, Joanna and Ewan for all their help throughout the years (although Ewan's jokes were always terrible) and many thanks go to Paul Hynd for all the many great things he made for me.

Lastly, I would like to thank my family. Thank you to Lorraine, John, Abi, Louise and Steven for your support over the years. A big thanks to Louise especially for finishing your PhD before me and for never letting me forget it. However, your performances at the many pub quizzes we attended left a lot to be desired so thankfully we had Steven to make up for it. Thank you to you both for the encouragement and de-stressing. Most of all, thank you to my parents, May and Ewan, and my wife, Claire, for their constant support and patience with me. Thank you to Mum and Dad for instilling a value for learning and for always encouraging me to push myself and for giving me the confidence to do it. To Claire, when we started going out I had not long started my PhD and now, here we are, married for five years and I'm just finishing. Thank you for putting up with everything.

Abstract

Ultrafast pulsed lasers are a key industrial tool for precision machining and there is a requirement to reach higher average powers of 100 W and beyond. This thesis explores the design considerations of low complexity, picosecond, thin-disk, Nd:YVO_4 amplifiers at a seed wavelength of 1064 nm to reach this goal of 100 W with excellent beam quality.

Through modelling and experiment, the barriers and challenges of this amplifier architecture were explored and developed. The critical role of temperature and its deleterious effects on amplifier performance were examined in great detail and modelled, as were the effects of energy transfer up-conversion. These effects were incorporated into the amplifier model and allowed an estimation of the number of passes of the seed beam required to reach an output of 100 W for various amplifier parameters.

The role of Nd:YVO_4 as a gain material for amplifying picosecond pulses generated by a microchip Q-switched laser was also explored. The performance of three amplifier stages were examined and modelled, showing that doping concentration is a key choice when designing amplifiers in this power regime.

Contents

Chapter One

Introduction

1.1 Lasers in manufacturing

In industry today, there is a need for more advanced tools and processes for material machining. Whether that is to increase the accuracy and intricacy of machining or working with traditionally difficult to machine materials, advanced processes in machining have been developed to overcome the limitations of traditional, mechanical methods. There are many different types of advanced machining processes such as: electro-discharge machining; electrochemical machining; chemical processes, such as blanking and photochemical machining; ultrasonic machining; jet machining processes such as abrasive jet and water jet machining; and beam machining processes. With beam machining there are various subtypes: electron beam machining; ion and plasma beam machining; and laser beam machining [1]. Laser beam machining is an incredibly versatile and powerful tool for material processing and the technology, specifically the laser amplifiers, used in laser machining systems, will be the focus of this thesis.

The concept of the optical maser, or laser, was first proposed by Shawlow and Townes in 1958 [2] and two years later Maiman demonstrated the first laser using ruby as a gain medium [3]. In 1965, Western Electric, an electrical engineering and manufacturing company, used lasers in an industrial application for the first time. They used a ruby laser for machining, drilling holes in diamond dies for wire extrusion [4]. In 2017, the laser industry reported revenues of almost $12.5 billion, with applications in sectors such as communications, the military, medicine, lithography, instrumentation and materials processing. Material processing is one of the biggest sectors by revenue [5].

This chapter will first give an overview of how lasers are used in a host of different material processing applications as well as machining, which incorporates drilling and cutting. Lasers are also used for marking, surface treatment and welding. These various processes will be discussed, looking at laser beam machining in more depth. Ultrashort laser pulse machining, where the laser pulse duration is on the order of femtoseconds to a few picoseconds, is of particular interest since this thesis is mainly concerned with the results of a project that sought to amplify a commercially available laser that is primarily used for ultrashort pulse, laser machining applications.

At the beginning of the project, the aim was to design and construct a laser amplifier with this commercially available, mode-locked laser as the seed source. The industrially driven target was to reach an average output power of 100 W, from a starting average power of 15 W, whilst maintaining the good beam quality of the seed source. As this project had a focus on the commercial viability of the laser amplifier, manufacturability of the amplifier was also a primary concern. A thin-disk architecture was chosen for the amplifier, using Nd:YVO_4 as the gain material. While thin-disk amplifiers typically involve many passes of both the pump and seed beams, which can be detrimental to manufacturability, this project had an emphasis on achieving 100 W of output power in a minimum number of passes of the seed beam, to enable a simpler construction. The reasons for choosing a thin-disk architecture and Nd:YVO_4 as the gain medium will be discussed in the latter part of this chapter.

Chapter 2 outlines the theory behind laser amplifiers and the creation of a simple, laser amplifier model. In the third chapter, the laser amplifier model is adapted and made more complex to better reflect the real laser amplifier that was constructed. The results obtained from the amplifier model were compared with empirical results from laser amplifier experiments which explored various Nd:YVO_4 doping concentrations, pump and seed beam radii and different numbers of passes of the seed beam. This chapter also explores the deleterious effects of increased temperature on the performance of Nd:YVO_4 as a laser gain material in an amplifier and its limitations for high power regimes. The amplifier models developed in Chapters 2 and 3, and the amplifier experiments that were conducted, allowed an

estimate to be made of how many passes of the seed beam would be required to achieve an output power of 100 W from the amplifier. Chapter 4 then explores Nd:YVO_4 as an amplifier gain material in a low power regime for amplifying picosecond pulses from a Q-switched microchip laser which also uses Nd:YVO_4 as a gain material. This setup of an amplified Q-switched microchip laser also has the potential to be used as a laser machining tool.

1.2 Material processing with lasers

Material processing involves processes that convert raw materials into finished goods, and today the laser is an important tool for many applications. Using lasers in material processing works on the principle that a laser beam of sufficient intensity incident on a material modifies that material. This enables various processes such as cutting, drilling, marking, welding, sintering and heat treatment of materials, but for all of these processes, there are three main mechanisms for altering the material: melting, ablation and chemical degradation [1]. When a laser beam is incident on the material, the light is absorbed and one of these three processes occurs to alter the material.

Material processing with lasers can be performed on many different types of materials and no mechanical contact with the workpiece is required. The laser interacts with the material through thermal processes so, while the material has to be able to absorb the laser light, other material properties are less important, such as brittleness or hardness, which offers opportunities to work with materials that are difficult to machine using mechanical methods.

Some of the techniques that use lasers to alter a material will be examined briefly, such as laser beam welding, surface treatment of materials using lasers and laser marking. Laser machining will then be discussed in more detail in the next section.

1.2.1 Laser beam welding

Laser beam welding can be used to join two surfaces together, in materials such as metals or plastics, due to the high intensities of a focussed laser beam. Laser beam welding has many advantages over other methods of welding such as electric resistance welding or gas tungsten arc welding. Laser beam welding is a high-speed process with low heat input and, therefore, a narrow heat affected zone. It can be used to weld heat sensitive materials, such as heart pacemakers [6]. Another method of welding with high intensity beams is electron beam welding, but this requires a vacuum and generates x-rays, whereas laser beam welding can be conducted in air and is also not sensitive to magnetic materials [4].

Laser beam welding occurs via two different mechanisms, conduction welding and keyhole welding. Conduction welding occurs when the intensity of the laser beam is large enough to melt the material but not to cause evaporation. The laser beam, incident on the surface of the material heats the surface, and the heat penetrates down into the material. This melts the material, allowing the two surfaces to be welded together. The longer the laser pulse, the deeper the weld, as the heat has more time to be conducted into the material. These welds are typically wider than they are deep.

Keyhole welding requires higher beam intensities to evaporate material, rather than just melting it. The laser beam first creates a pool of molten material which is then evaporated. This creates a keyhole which increases the absorptivity of the material significantly as the beam undergoes multiple reflections inside the keyhole. Due to the evaporation, vapour is created which induces a pressure that drives the molten material outwards. The laser beam is then translated, moving the keyhole along as the beam moves. The molten material closes in behind the keyhole, creating a seal between the two pieces of material being welded. This creates a deep but narrow weld. Both continuous wave lasers and pulsed lasers can be used for laser beam welding, depending on the application.

1.2.2 Surface treatment of materials using lasers

Laser surface treatment is used to increase the resistance of material surfaces to wear, corrosion, high temperatures and oxidisation [7], [8]. The surface of an engineering material is often more exposed to the environment compared to the bulk of a material and can be subject to various friction forces and wear if it is in contact with other materials that may be moving. There are many traditional engineering methods that can change the composition or microstructure of a material's surface in order to enhance its properties to make it more resistant. Some of these are: galvanisation; flame or induction hardening; carburising and diffusion coating [7].

Like laser welding, there are alternative high-intensity beam processes that can be used for laser surface treatment such as ion, electron and laser beam treatment. The same drawbacks apply to ion and electron beam techniques for surface treatment as they did for laser welding. Lasers are easier to implement in an industrial setting and still offer the same advantages over traditional treatments such as: greater precision; flexibility; chemical cleanliness; no mechanical contact with the work piece; and reduced thermal distortion. Initial set-up costs can still be high, however, and it is not always the most efficient technique for covering large surface areas [4], [7], [9].

Laser surface treatments can be broadly separated into two categories; the first, where changes in the surface properties are produced by changes in the material's microstructure, and the second, where both the microstructure and the composition of the material is changed. Techniques such as laser hardening and laser melting fall under the former whereas laser alloying and laser cladding would be categorised under the latter.

Laser hardening involves the rapid heating of a material's surface but below the melting temperature of the material. Laser surface melting is similar but the temperature is raised above the melting temperature. Both techniques use the rapid heating and cooling of the material to alter its microstructure, through the diffusion of atoms in the affected area, which can improve the surface properties like wear resistance [10].

As the laser beam is only absorbed in a shallow layer at the surface of the material, the bulk of the material is unheated and this leads to large temperature gradients between the surface and the bulk and, therefore, rapid cooling of the material. This is known as self-quenching. It is important to optimise the spot size and scanning speed of the laser beam, as a laser beam that is incident on a fixed area for too long can increase the temperature in deeper layers of the material and lead to shallower temperature gradients which can compromise the self-quenching process. It is also important to optimise the laser beam intensity so that it is low enough to avoid melting the material, if that is required, but as high as possible to increase process efficiency [11]. Compared to traditional techniques for surface hardening such as induction hardening or flame hardening, laser hardening offers certain advantages such as reduced thermal distortion of the material and very localised heating [4].

In certain applications, alloys can have advantageous properties like increased wear resistance or hardness, but it can be expensive to have a whole part made from that alloy. Laser surface alloying and laser surface cladding are both methods used for creating alloys only on the surface of a material, which is a cheaper alternative [12]. This creates a surface that is distinct from the bulk material by altering the microstructure and the chemical composition of the surface [4].

Laser surface alloying is very similar to laser surface melting, but here another material is added into the melt pool, creating a mixture of the two materials with desired properties such as increased wear, corrosion protection and oxidisation protection [8]. A layer of one material can be deposited on the surface of another substrate material: when they are melted together, there is a rapid mass transfer from one to the other in the melt pool though diffusion or convection. The subsequent, rapid cooling of the surface then leads to the re-solidification of the material [7]. Laser alloying creates fine microstructures in the material and provides very homogenised mixing of the two materials with the melt depth being between 1 µm and 2000µm [4]. Parameters such as the depth of the alloying, the chemical make-up of the alloy and its microstructure are dependent on many variables such as: the incident laser beam energy; the laser beam profile and diameter; the

interaction time between the laser beam and the workpiece; and the various intrinsic properties of the materials being used [7].

1.3 Laser machining

Traditional machining practices, where mechanical mechanisms are used to remove material, have been used for many years but have some disadvantages. Due to the cutting forces applied to a material being machined, material damage can occur as well as tool wear and machine vibration. It can be difficult to machine brittle materials. The removal rate of material is limited by various factors such as the maximum tool force that can be applied, build-up edge formation or tool chatter [1], [13], [14]. Advanced machining processes, such as laser beam machining, can be used to try and overcome some of the limitations experienced by mechanical machining.

Laser machining is advantageous when processing materials that have a high degree of toughness or brittleness as there are no cutting forces on the material. This means there is no mechanically induced damage, tool wear or machine vibration. If a material being machined by a laser has desired thermal properties like low thermal diffusivity and conductivity, this is an advantage [1].

1.3.1 Laser drilling

Laser drilling has many applications such as drilling cooling holes in turbine blades [15], [16], creating vias between layers in printed circuit boards [17], [18] and engineering holes in teats for baby bottles [19], [20]. Drilling involves a laser beam that is focussed onto the piece of material that is to be drilled as in Figure 1.1. The laser beam is absorbed by the material at the surface initially, heating the material which reaches the melting point, creating a melt zone. As more energy is absorbed, the material evaporates and creates a keyhole in the material with a melt layer at the bottom. The absorptivity of the material increases substantially due to multiple

reflections within the keyhole and this accelerates the process due to the extra heating from the enhanced absorptivity [4].

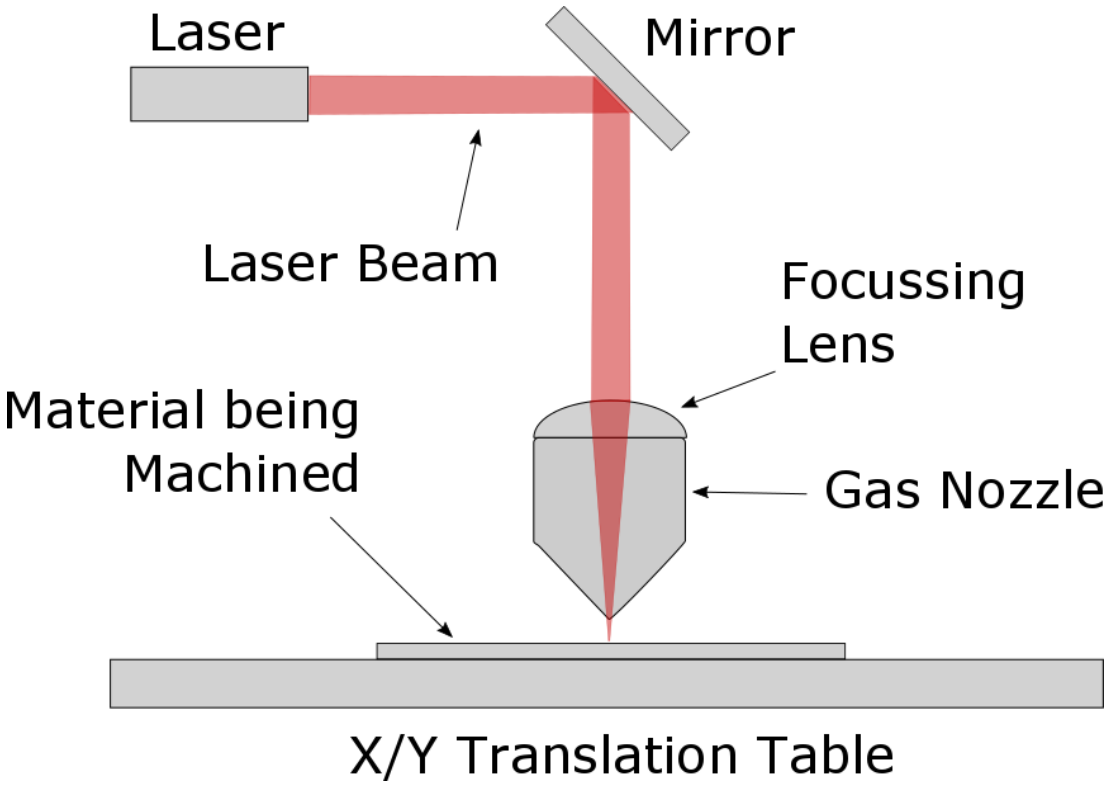

Figure 1.1 – A simplified schematic of a laser drilling station. The laser beam is focussed onto the material to be machined using a lens, or sometimes a curved mirror may be used. The material is normally secured to a translation table so it can be moved. A gas nozzle directs gas onto the area being machined to blow any melted material through the drilling hole, as discussed in section 1.3.5.

As the keyhole deepens, vapour is generated as the material evaporates and this vapour escapes upwards through the hole, exerting a downwards force on the melt surface at the bottom. This force, combined with a temperature gradient across the surface of the melt, which creates variations in surface tension, pushes the molten material to the edges of the hole. The combined forces from the high pressure at the bottom of the hole and the drag from the escaping vapour push the melt up the walls

of the hole and out the top. Material is removed from the hole in the form of both vapour and ejecta. When the laser is stopped, the melt that was ejected from the hole falls back around the edge of the hole as spatter. Melt still in the hole can re-solidify as a recast layer. Generally, the more melt there is in and around the hole, the worse the quality of the machining.

For some applications, spatter is unacceptable as it would leave the surface rough. This could affect applications like drilling cooling holes in turbine blades by affecting fluid flow or interfere with other surfaces in contact with the material. Although, the recast layer inside the hole is usually very thin, it may have varying properties from the bulk of the material and this could lead to stresses inside the material if cracks form.

The amount of material that is ejected as vapour, as opposed to melt, is determined by a number of factors, both in the material parameters and the laser beam parameters. The thermal diffusivity, α, and thermal conductivity of the material are important, as are the laser pulse energy, peak power and pulse duration, t_{pulse}. The amount of thermal penetration down into the material is proportional to $\sqrt{\alpha t_{pulse}}$ [4]. For shorter pulses, a higher proportion of material is evaporated, which gives a better quality hole with less spatter and a reduced recast layer but the penetration depth suffers. Another technique to reduce spatter on the material surface is to coat the surface in a layer of another material that can be removed later, taking the spatter with it [4].

1.3.2 Issues associated with laser drilling

There are some issues associated with laser drilling that can lead to a deterioration in the quality of the holes drilled or in the efficiency of drilling. If the laser intensity is large enough, the material being machined can be converted into a plasma. This can be detrimental to the machining process as the laser beam can be absorbed in the plasma instead of being absorbed in the material being machined, if the plasma frequency is close to the frequency of the laser beam. For metals, a laser beam

intensity of $3x10^6\ Wcm^{-2}$ can induce evaporation of the material and at intensities of $10^8\ Wcm^{-2}$ a plasma will form [4]. The beam can also be scattered as it passes through the exiting vapour.

Tapering is another issue with laser drilling where the hole can become conical or even egg-timer shaped due to various laser beam parameters such as: the focal position of the beam; pulse power; pulse duration; and the number of pulses. This can be a particular issue for single-shot drilling where the hole is made entirely with a single pulse. For multiple-shot drilling, the power and focus of the laser beam can be adjusted to minimise tapering. Trepanning is one technique that can be used to minimise tapering, where the laser beam is moved around to cut a hole larger than that made from a single, stationary beam. This will be discussed in more detail in the next section.

1.3.3 Methods of drilling

There are variations in the method used for laser beam drilling. Single shot drilling is where one laser pulse starts and completes a hole. Multiple shot drilling uses multiple pulses to drill a hole. These methods of drilling have the advantage of being quick but lack the precision of other methods where the laser beam parameters can be adjusted. They also have the disadvantage that if the hole that is required has a larger diameter than the laser beam, then the laser has to be defocussed which leads to a reduction in the beam intensity. This slows down the rate of penetration and can lead to larger heat-affected zones [4].

Trepanning is a slower process but offers better quality holes. This involves the beam initially piercing the material and then moving around the edge of what will be the hole to effectively cut it out. Smaller beam diameters can be used, since the beam moves around the feature to be drilled and so higher intensity beams can be achieved which leads to higher quality holes. Almost any shape can be cut out using this method but it requires a pulse repetition rate that is high enough to ensure that the material does not start to re-solidify between pulses. Pulses also have to overlap

spatially to ensure a smooth edge to the feature being drilled; the smaller the feature, the tighter the overlap due to the higher radius of curvature of smaller features. This leads to a requirement for higher repetition rates for smaller features [4].

Helical trepanning is a variation on trepanning which achieves higher precision holes but is a slower method. Here, single pulses do not penetrate all the way through the material but rather, the hole is created by spiralling around the feature moving deeper each time until penetration occurs.

1.3.4 Double pulse drilling

Double pulse drilling is another method of drilling that uses two pulses, incident on the material but separated only by a very small time, on the order of tens of nanoseconds. It has been shown that, for nanosecond pulses, double pulse drilling can improve material removal rates by three to ten times and minimise the heat-affected zone, compared to single pulse drilling [21]. Using picosecond pulses, Campbell et al [22] doubled drilling speed compared to single pulse drilling. The single pulse energy was the same as the combined energy of both pulses in the double pulse drilling. The effect was not observed if the pulse separation was too long or too short [4].

There are different theories as to why an improvement in drilling is seen with double pulses. One is that the second pulse interacts with a plasma generated by the first pulse [22]. Initially, the plasma has a high electron density which defocusses the laser pulse. After a short period, the electron density is decreased as the electrons repel each other and the plasma then focusses the laser beam. If the second pulse arrives during the period of time when the electron density is decreased then it will be focussed, providing an improvement in performance. An alternative theory is that there will be cooling ablation products from the first pulse that interact with the second pulse, inducing a second plasma wave that clears away debris more efficiently [21].

1.3.5 Laser cutting

Laser cutting incorporates the same principles as laser drilling in that a cut has to begin with a penetrative hole. Once a hole has been made, the dynamics change slightly as laser cutting applications can use a gas jet to blow away the melt through the hole made by the cutting process (the cut kerf). This process is referred to as 'melt and blow cutting'. This is advantageous as less powerful laser beams can be used as the material only has to reach the melting point and not the boiling point. Approximately half the power is used in this process in comparison to cutting by evaporation of the material. A problem associated with laser cutting in this manner is melt clinging to the bottom surface of the material because the melt is pushed down through the kerf [4].

Blind holes, where the hole only penetrates part way through a material, can also be made by introducing a side gas jet in addition to the gas jet that blows from above the cut [23]. The side jet combines with the downwards jet to create a vortex that pushes the melt back up through the cut kerf.

Another form of cutting is controlled fracture which can be used on brittle materials that are prone to thermal fractures. If a laser beam heats a part of the material, it will expand and cause stresses in the surface so that a crack will appear. The crack can then be guided by moving the laser beam. The disadvantage of this method is that at material edges, the stresses acting on the material become less predictable so this technique is better used for cutting shapes that are enclosed on the material surface [4]. Lasers can also be used to etch a groove in a material, or a line of holes, that weaken the structure of the material so that it can be mechanically snapped.

1.4 Ultrashort pulse machining

For many of the laser machining techniques described in the previous sections, the effect of the laser beam on the material can be understood in terms of classical thermodynamics. A continuous wave laser beam, or laser pulses on the order of nanoseconds or longer, acts as a heat source that raises the temperature of the

material as it absorbs the energy of the laser beam. If the energy absorbed is sufficient to increase the temperature of the material above the melting point, the material will melt and likewise for the vaporisation threshold, the material will evaporate. The material is in thermal equilibrium as the process occurs on relatively long timescales [24], [25] and this leads to thermal energy penetrating more widely into the material and larger heat affected zones [26].

For ultrashort pulsed laser machining, where pulses are in the picosecond and femtosecond regime, the thermal processes are no longer in equilibrium and the process of material removal occurs on a timescale faster than the time taken for heat to diffuse into the bulk of the material [26]. Ablation, with very little heating of the surrounding area, results in higher quality machining with greatly reduced heat affected zones, as shown in Figure 1.2. Although picosecond and femtosecond pulses offer better quality machining with higher precision, material removal rates are lower than with longer pulses, which means less efficient machining. This can be partly due to the lower average powers associated with ultrafast lasers but also because of the different ablation mechanisms that occur with ultrashort laser pulses [27], [28].

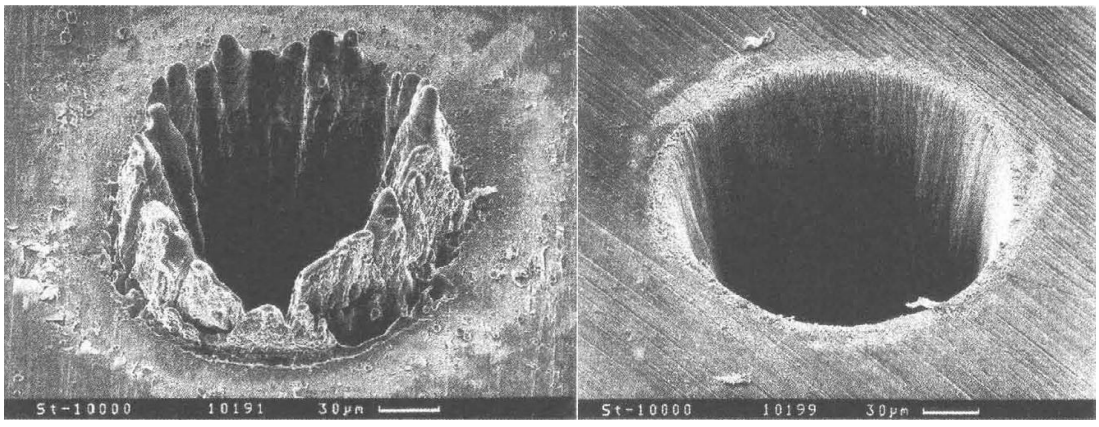

Figure 1.2 – An example of two laser machined holes in stainless steel. The picture on the left is a hole machined using a nanosecond laser pulse and the picture on the right is a hole machined using a femtosecond laser pulse [29].

1.4.1 Ultrashort pulse ablation mechanisms

The thermodynamics of a system which is absorbing ultrashort laser pulses cannot be considered in terms of classical thermodynamics, like with pulses on the order of microseconds or longer [28]. Light is absorbed in materials by electrons, where the laser energy is absorbed by free electrons in the conduction band of the material. These electrons transfer energy via electron-electron scattering on time-scales of the order of sub-femtoseconds to a few femtoseconds. The electrons then transfer energy to the lattice of the material, via electron-phonon scattering, on the order of picoseconds. This is called the electron-phonon relaxation time, and when the laser pulse duration is much longer than the electron-phonon relaxation time, the electron and lattice temperatures can be considered to be in equilibrium. However, when the pulse duration is less than, or on the order of the electron-phonon relaxation time, the temperatures of the electrons and the lattice have to be considered separately.

The longer time taken to transfer the energy from the electron subsystem to the lattice means that very high temperatures and pressures can be reached within the material. Electrons have a low heat capacity, compared to the material lattice, and can reach very high transient temperatures while the lattice is still cold. During this stage of the process, electrons can be emitted from the material via photoelectric and thermionic effects. The lattice is then heated as the electrons transfer energy to it. If the pulse energy is large enough, the material in the target is vaporised as the ions in the lattice break the bonds with the lattice structure and a transition straight from a solid to a vapour occurs. This leads to a rapid expansion before the material is expelled from the surface. The melt-free ablation is more dominant when the pulse width is shorter, so there is less heat affected zone for femtosecond pulses compared to picosecond pulses where more melting of the material may occur [25], [26], [28], [30]–[35].

1.5 Lasers for machining

Often, for applications requiring continuous wave emission or pulses down to hundreds of microseconds in length such as laser cutting, CO_2 lasers are used that operate at a wavelength of 10.6 µm, with powers ranging from tens of watts to tens of kilowatts [25], [36]–[38]. For nanosecond pulses, Q-switched, Nd:YAG lasers are widely used, emitting at a wavelength of 1064 nm. These can be useful for drilling applications. Good beam quality can also be important, depending on the application, to achieve small feature sizes and to reach high intensities.

For ultrashort pulse laser machining, ultrashort pulses, of femtosecond or picosecond duration, are required by definition. This normally entails a mode-locked laser source. Good beam quality is often required and higher average powers are advantageous as they provide higher material removal rates and deeper ablation depths which lead to more efficient machining. A master oscillator power amplifier (MOPA) configuration can be a useful system architecture to achieve both short and stable pulses along with good beam quality. A MOPA starts with a relatively low power oscillator that has been optimised for the parameters required, such as pulse duration or beam quality. This then acts as the seed source for the power amplifier stage where higher average powers are reached whilst maintaining the optimised parameters achieved with the oscillator.

The project that comprised the majority of the content of this thesis used a commercially available, picosecond, machining laser that utilises a MOPA configuration. The master oscillator was a mode-locked fibre laser that was amplified by a regenerative amplifier which delivered an average output power of 15 W at 1 MHz with a pulse duration of less than 15 picoseconds and an M^2 value that was less than 1.4. The main goal of the project was to design and build a subsequent amplifier stage, using the output of the regenerative amplifier as the input seed source, to take the average power to approximately 100 W with a route to power scaling to kilowatt levels. The next section will examine various types of laser

amplifiers that were considered to amplify this commercially available machining laser to 100 W with a route to scaling the power further.

1.6 Laser amplifiers

There are many different types of laser amplifier and this section will briefly look at rod amplifiers, fibre amplifiers, regenerative amplifiers and slab amplifiers before finally discussing the merits of thin-disk amplifiers, which is the architecture that was chosen to amplify the commercially available laser used in the project. There are many challenges associated with working at high powers, but heat may be the most limiting factor. Many of these different laser amplifier designs have been designed to deal specifically with heat, such as the thin-disk amplifier.

1.6.1 Rod amplifiers

Rod amplifiers are so-named due to the shape of the gain medium where the length of the crystal that runs parallel to the laser beam's direction of propagation is typically longer than the other two dimensions that run perpendicular to the direction of propagation, as shown in Figure 1.3 [39]. Whilst a rod shape would typically have a circular cross-section, square or rectangular cross-sections may also be described as rods.

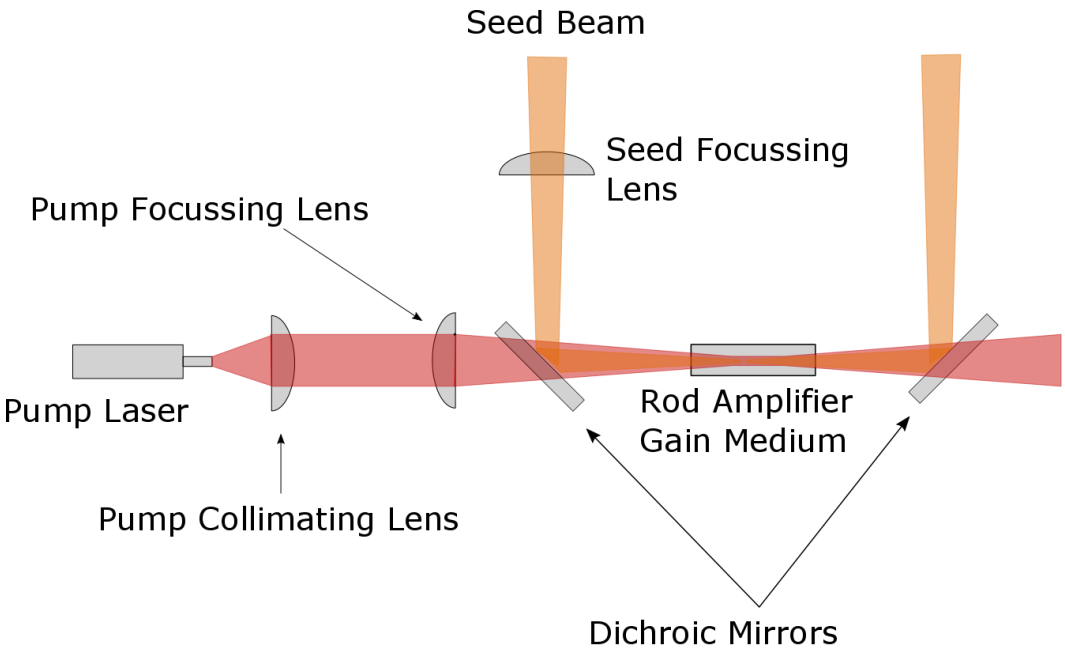

Figure 1.3 – A diagram of an end-pumped rod amplifier. The pump beam is transmitted through a dichroic mirror into the gain medium and the seed beam is reflected by the same dichroic mirror into the gain medium, collinear with the pump beam.

Rod amplifiers can be pumped with lamps that run parallel to the laser crystal, such as arc lamps, for continuous wave operation, or flash lamps for pulsed systems. They can also be pumped using diode lasers, as shown in Figure 1.3. One of the advantages of diode pumping a rod amplifier over something like a thin-disk amplifier, which will be discussed in a subsequent section, is the longer axis in the direction of propagation allows for more pump light to be absorbed without the need for multiple passes of the pump beam. However, it also means that the pump and seed beam radii may not be of a uniform diameter throughout the rod, and care has to be taken to ensure that the pump and seed beam adequately overlap to ensure good beam quality, if that is required.

The gain material in rod amplifiers is generally cooled along the long edges, as the seed beam, and sometimes the pump beam, enter and exit the crystal at the end facets. This can lead to problems with thermal lensing, where temperature gradients

within the gain medium can create an aberrated thermal lens. Since the heat generated within the gain material has to move to the outside of the rod, where the cooling surface interacts with the crystal, the temperature at the centre of the rod is greater than that at the outside. The refractive index of the material is temperature dependent and therefore there is a varying refractive index across the cross-section of the rod. This means the beam experiences different phase shifts across its transverse plane just like when a beam passes through a normal lens. The gain material also undergoes mechanical stresses from the temperature gradients within it, resulting in bulging of the end faces of the crystal; this can also lead to lensing effects. Improved cooling of the gain medium does not reduce the thermal lens as it is the temperature gradient, and not the absolute temperature, that creates the issue.

1.6.2 Fibre amplifiers

Fibre amplifiers, as shown in Figure 1.4, are capable of delivering very high powers with good efficiency and high beam quality [40]–[44]. Fibres are waveguides and if they are rare-earth doped then they can be used as a laser gain material for fibre lasers and fibre amplifiers. Fibre amplifiers can have large single-pass gain due to the very long interaction length of the seed beam with the gain material, which comprises the whole length of the fibre. By using a single-mode fibre, good beam quality can also be maintained for the seed beam, even for high output powers. Fibre amplifiers can deal with the high temperatures that are associated with high power systems due to their large surface to volume ratio, which improves heat extraction from the amplifier [43].

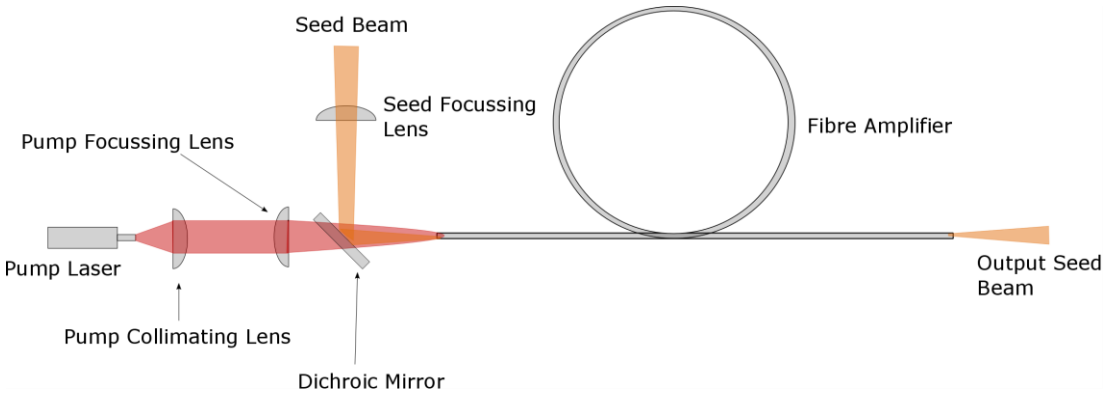

Figure 1.4 – A diagram of a fibre amplifier pumped with a laser. The pump laser passes through a dichroic mirror before it is launched into the fibre. The seed beam is reflected off the dichroic mirror before it is launched into the fibre.

High power fibre amplifiers normally utilise double-clad fibres [41], [43], where the pump beam propagates in an inner cladding and the seed beam propagates in a single-mode fibre core, as shown in Figure 1.5. If the fibre simply comprised the single-mode fibre core, then a single-mode laser pump source would be required to ensure the pump beam could be launched into the fibre. Since most of the highest power pump sources are multi-mode lasers, smaller pump powers would have to be used with only a single-mode fibre, which would restrict the output powers that could be achieved using a fibre amplifier. By utilising an inner cladding to launch the pump beam, multi-mode pump sources can be used, increasing the pump power available. The single-mode fibre core within the inner cladding ensures that good beam quality can be maintained for the seed beam.

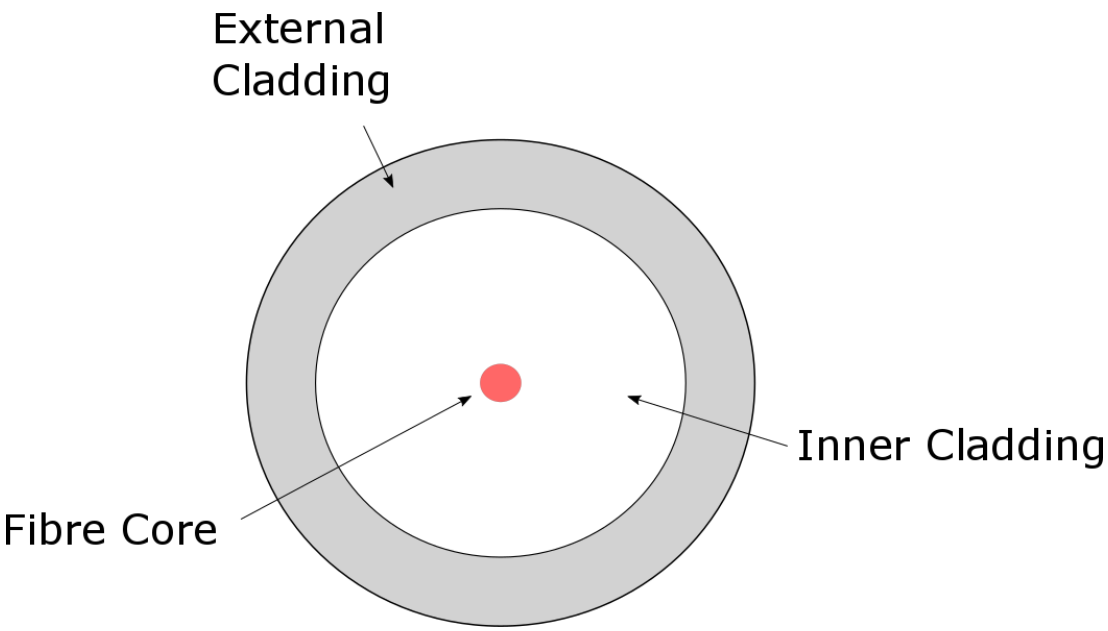

Figure 1.5 – A diagram of a double-clad fibre showing the fibre core at the centre, which guides the seed beam through the fibre. The fibre core is surrounded by the inner cladding that guides the pump beam and an external cladding comprises the outer most layer.

The main drawback to using fibre amplifiers is nonlinear effects, induced at high peak powers, which can be particularly troublesome for amplifying ultrashort laser pulses. Such nonlinear effects include stimulated Brillouin scattering [45]–[47], self-phase modulation [48]–[50], self-focussing [51], [52] and stimulated Raman scattering [41], [53]. These effects can be overcome somewhat by using technologies such as photonic crystal fibres [54]–[57] or chirped pulse fibre amplifiers [58]–[60]. Photonic crystal fibres allow the intensity of the laser pulse to be reduced by using larger core diameters. This would normally have the effect of deteriorating the beam quality but single-mode operation can be maintained using specific arrangements of holes around a solid area that comprises the fibre core. This provides fibres with low effective numerical apertures but with larger core diameters. Chirped pulse amplification, a technique that is used in many different amplifier architectures, reduces the peak power of the laser pulse by stretching it in the time domain. The

pulse duration is lengthened before the pulse enters the fibre amplifier and, once it has been amplified, the pulse is compressed, maintaining the ultrashort pulse length but without the high peak powers in the amplifier.

1.6.3 Slab amplifiers

Slab amplifiers are characterised by a gain medium that has one very thin dimension in comparison to its other two dimensions, hence the name 'slab'. This geometry allows for very good heat extraction which lends itself to high power operation. The thin dimension of the slab design allows for one dimensional heat flow through the faces of the slab with large surface areas [39], [61]. Beam quality and extraction efficiency can be poor in slab amplifiers in comparison to other amplifier architectures such as thin-disks and fibre amplifiers.

Slab amplifier pumping can be broadly described in two ways, either face pumped, as shown in Figure 1.6, or side pumped, as shown in Figure 1.7. Face pumped slab amplifiers are well suited to flash lamp pumping owing to the large surface area of the face sides which aids the absorption of the low brightness pump light. Diode pumping is also possible with a face pumped geometry [62]. This type of pumping often requires higher doping concentrations of the gain medium, or thicker slabs, due to the short interaction length of the pump with the gain material and the entire slab volume absorbs the pump light. Slab amplifiers benefit from having heat extracted from the face surfaces, due to the large surface areas, and if the amplifier is face pumped, then the faces of the slab must be transparent at the pump wavelength and, if any cooling material is applied, such as a cooling liquid or heat sink, this must also be transparent at the pump wavelength.

With higher brightness laser diodes, edge pumping can be achieved as the pump light can be focussed into the smaller edges. This allows heat extraction at the face surfaces to be decoupled from the pumping at the edge surfaces and, as the pump beam traverses a longer path within the gain medium, pump absorption is improved. An edge pumped slab amplifier can have multiple, different orientations of both the

pump and seed beams, each with their own advantages and disadvantages. The pump beam can either enter via the same surface as the seed beam or it can pass through the surface perpendicular to the seed beam, as shown in Figure 1.7. The advantage of separating the seed and pump beam entry surfaces is the avoidance of using dichroic optics; however, the overlap between the seed and pump beams is compromised as they travel along different paths, which is deleterious to the quality of the output beam. Another disadvantage of this orientation is that more surfaces have to be suitably coated to provide high or low reflectivity where applicable.

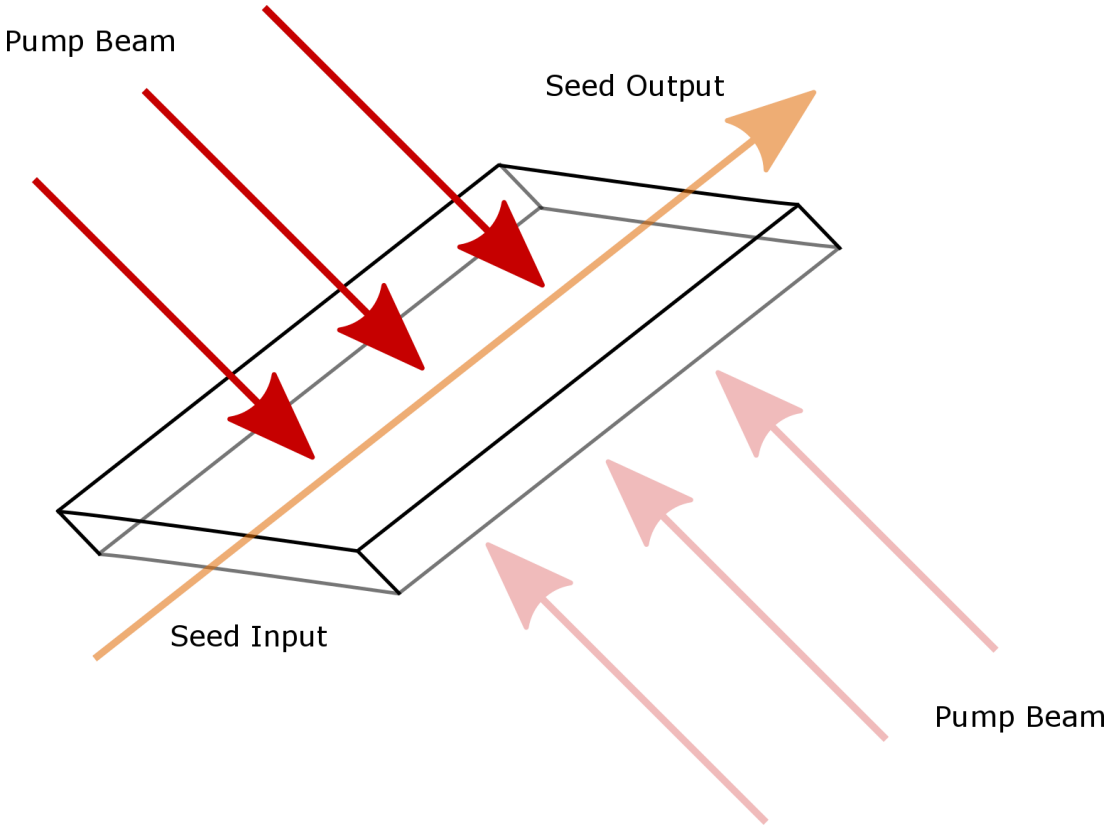

Figure 1.6 – A face pumped slab amplifier showing the gain medium being pumped on both large faces from the top and bottom. The seed beam enters through one side of the slab amplifier, exiting through the opposite side.

Dichroic optics can be utilised to allow the pump and seed beams to enter via the same surface reducing the number of surfaces that require optical coatings. It also

provides improved pump and seed overlap as they can follow the same beam path. Parasitic oscillations can be an issue due to the multiple, reflective surfaces in a slab amplifier, along with thermally induced distortions but these effects can be reduced using techniques such as coated edges on the slab, un-doped sections or zig-zag beam paths, as utilised in the Innoslab design [63].

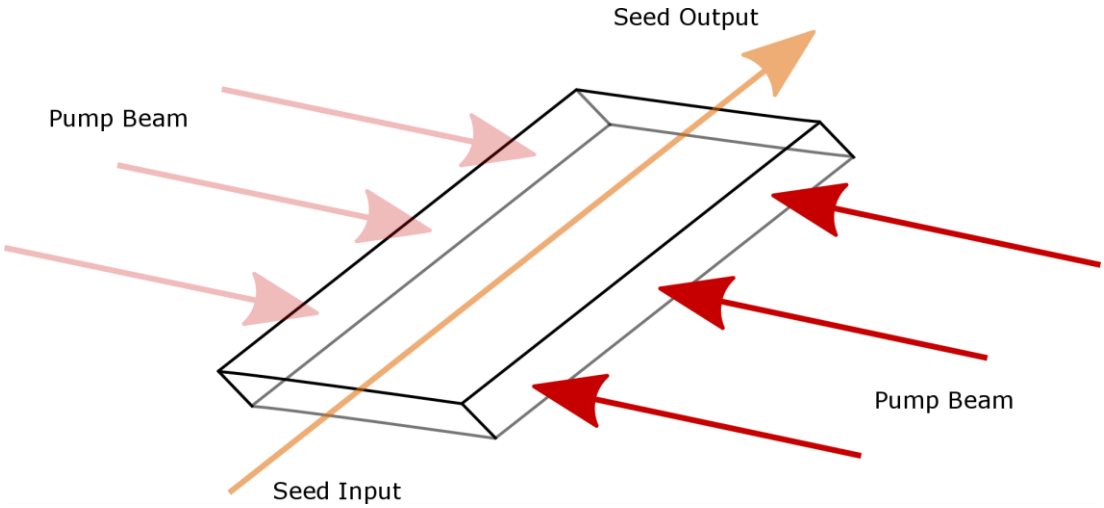

Figure 1.7 – A side pumped slab amplifier showing the gain medium being pumped on the side faces from both sides. The seed beam enters through the edge of the slab amplifier and exits through the opposite face. The pump could also be pumped on the faces the seed beam enters and exits and still be referred to as an edge pumped slab amplifier.

1.6.4 Regenerative amplifiers

A regenerative amplifier amplifies laser pulses by using an optical switch to confine a laser pulse within an amplifier cavity for a number of round trips before switching the pulse back out again. The amplifier cavity contains a pumped gain medium which provides gain to the laser pulse on each round trip. The switching of the laser pulse in and out of the cavity is actively controlled and so the number of round trips, and therefore the gain of the amplifier, can be modified [39], [64].

Figure 1.8 shows a schematic diagram of a regenerative amplifier. An optical switch, such as a Pockels cell, is used to inject an input seed pulse into the amplifier resonator

cavity by altering the polarisation state of the input seed pulse. The amplifier gain medium in the amplifier cavity is pumped so that it has stored energy which is extracted once the pulse enters the cavity. The pulse undergoes many roundtrips through the cavity until the optical switch is activated again and switches the pulse out of the cavity. Since each amplified pulse undergoes many roundtrips in the cavity it is important to ensure that losses in the cavity are minimised as they have a cumulative effect on the net gain of the amplifier.

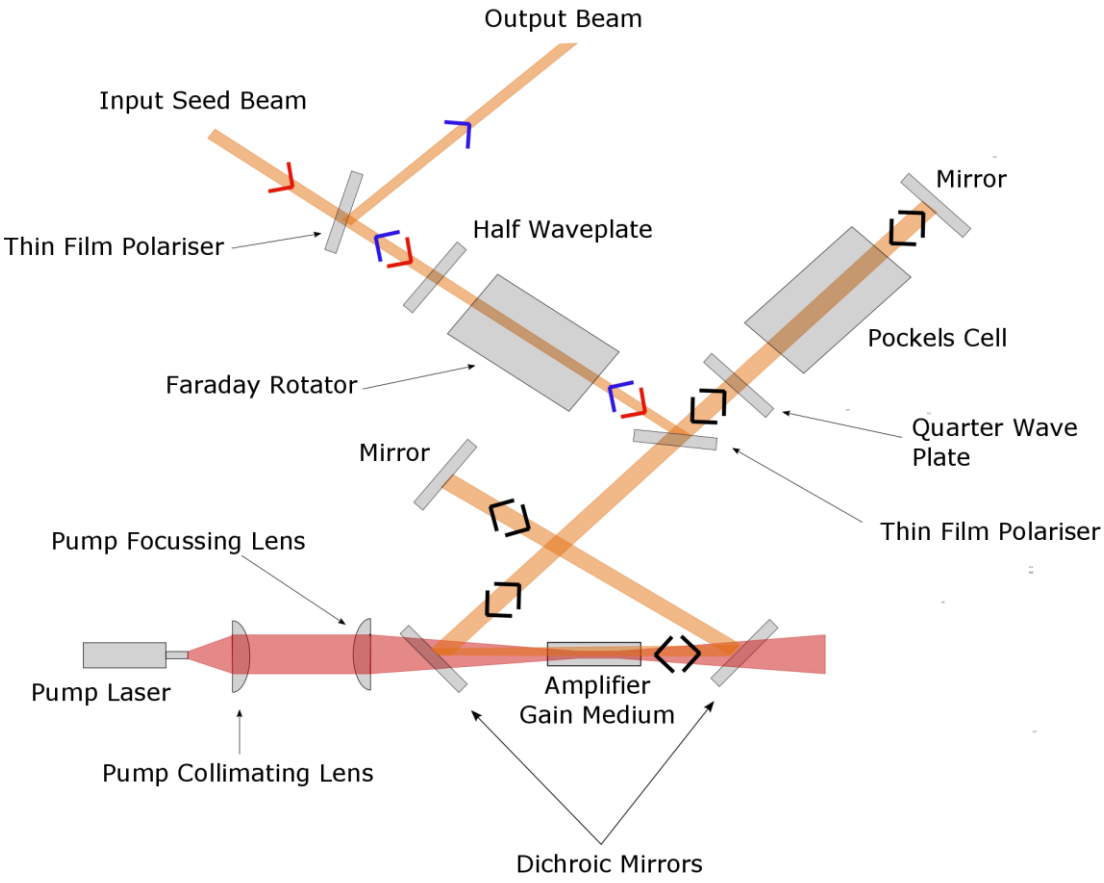

Figure 1.8 – A diagram of a regenerative amplifier. The input seed beam (red arrows) is coupled into the regenerative amplifier cavity using the Pockels cell. The beam within the resonant cavity is indicated by the black arrows. The amplifier gain medium is pumped by the pump laser and dichroic mirrors are used to transmit the pump wavelength and reflect the seed wavelength. The output beam (blue arrows) is then transmitted out of the amplifier.

The commercially available laser, discussed in Section 1.1 of this chapter, which is used as a seed source for the majority of the amplifier systems discussed in this thesis, already incorporates a regenerative amplifier. The master oscillator is a mode-locked fibre laser which seeds a regenerative amplifier, which also serves to reduce the pulse repetition rate of the whole system. The regenerative amplifier injects a pulse into the amplifier cavity and while it undergoes many roundtrips within the cavity, subsequent laser pulses from the master oscillator are rejected.

1.6.5 Thin-disk amplifiers

The concept of a thin-disk was first proposed by Giesen et al in 1993 [65] as a gain medium architecture that could facilitate high power operation. The principle behind the thin-disk is a laser gain material that is very thin and mounted to a heat sink and pumped with a top-hat pump beam profile in order to produce a homogenous and one-dimensional heat flow within the crystal as shown in Figure 1.9. Using a top-hat pump beam profile does have drawbacks, however. Top-hat pump beam profiles have an increased M^2 value which means that the propagation of a top-hat pump beam is non-gaussian in nature and so the intensity profile varies with respect to distance. High temperatures are usually the limiting factor in high power laser and amplifier operation but this design reduces thermal distortions. Thin-disks provide better beam quality for similar output powers compared to rods and are suitable for the amplification of ultrashort pulses [66].

Thin-disk amplifiers typically have highly reflective coatings at the pump and seed beam wavelengths on the back surface of the gain medium and corresponding anti-reflection coatings on the front surface. The back surface is bonded to a heat-sink that extracts the heat from the back of the thin-disk. This architecture limits the amount of transverse heat flow in the gain medium which reduces thermal distortions such as thermal lens effects. This means good beam quality can be maintained even if the crystal experiences high temperatures. Thin-disks are typically

on the order of hundreds of microns thick and the high surface-to-volume ratio provides efficient heat extraction.

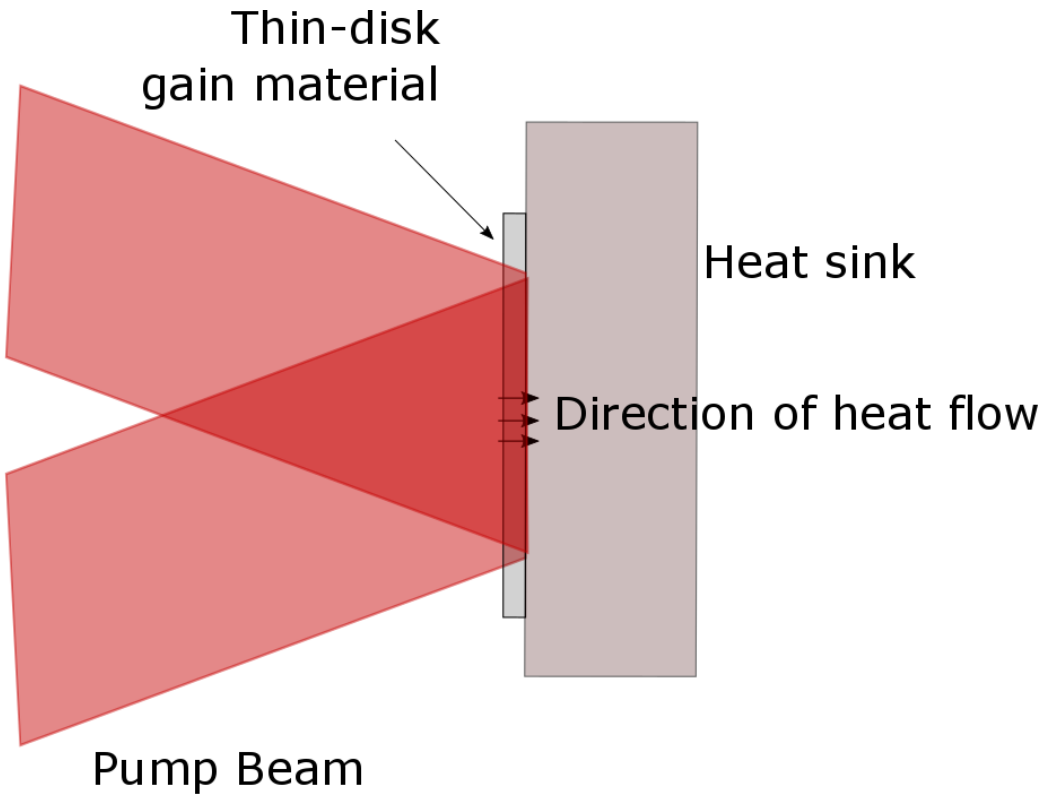

Figure 1.9 – A gain material with a thin-disk architecture is pumped by a pump laser. The back face of the gain material is usually coated to be highly reflective at the pump and seed wavelength for both lasers and amplifiers. The diagram shows the one-dimensional heat flow into the heat sink.

With such a thin crystal, one of the disadvantages of thin-disks is the difficulty absorbing adequate pump energy. The pump beam has a short interaction length as it passes through the gain material, and is reflected back out again with most of the pump energy unabsorbed. Multiple passes of the pump beam, where it is redirected and imaged back onto the thin-disk, are usually required to provide sufficient pump absorption, and for thin-disk amplifiers, a similar multi-pass arrangement of the seed beam is also required to extract adequate energy from the pumped gain medium.

This can lead to very complicated amplifier systems which don't particularly lend themselves to easy and robust manufacturing. One design that provides multiple passes of the pump beam is to use a parabolic mirror to focus a collimated pump beam onto the gain medium before re-collimating the reflected beam. The pump beam is then redirected onto another part of the parabolic mirror to be focused again, as shown in Figure 1.10. This provides a compact system that can deliver multiple passes of the pump beam through the thin-disk gain medium.

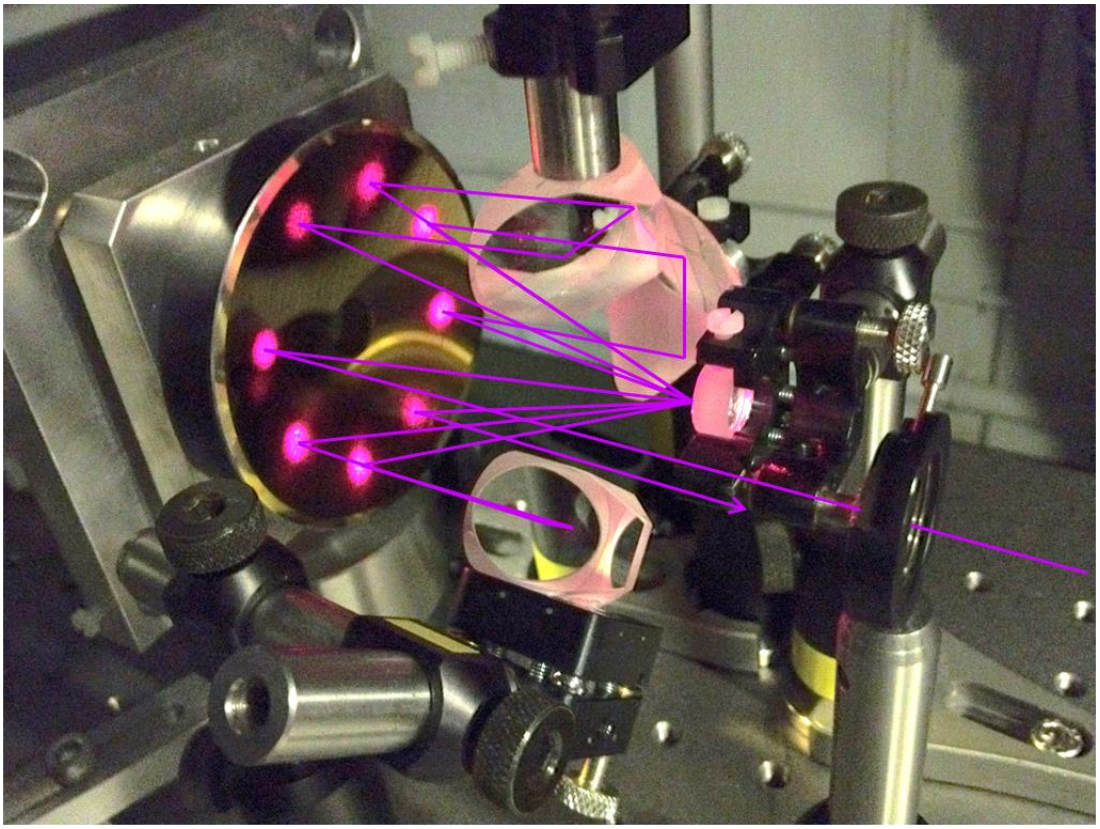

Figure 1.10 – A parabolic mirror focusing a collimated beam onto a central mirror, in the position the thin-disk would sit, before re-collimating the beam again. The porro prisms redirect the beam onto different parts of the parabola. There is a hole in the centre of the parabola to allow the seed beam to pass through and access the thin-disk.

A thin-disk was the amplifier design chosen to amplify the commercially available picosecond machining laser, which was the main goal of the project that comprises the majority of this thesis. With the industrial flavour of this project, simply achieving the highest brightness possible from the amplifier was not the only consideration. Other considerations were taken into account such as cost and ease of manufacture. Thin-disk amplifiers are not the simplest design to manufacture when the many passes of the pump and seed beams are taken into consideration so any effort to reduce the number of passes would be welcome from a laser manufacturer's perspective.

With these factors in mind, the idea of a thicker thin-disk was considered to try and balance the advantages of the thin-disk with its disadvantages. A thicker disk would require fewer passes of the pump beam to achieve the required pump absorption and fewer passes of the seed beam for the extraction of that energy, but would still maintain some of the advantages in thermal management, although not as effectively as a thinner disk. The objective of this project was to scope out routes towards the industrially-set target output power of 100 W and to assess the extent to which this could be achieved with fewer pump and seed beam passes in order to enable the future design of an amplifier that was easier to manufacture.

Figure 1.11 shows the effect of varying the gain medium thickness on the number of passes required for the pump beam. The graph displays the absorbed pump power as a function of the number of passes for different thicknesses of gain medium. The following equation was used to calculate the absorbed pump power,

$$P_a = P_i\big(1 - exp(-\alpha l)\big) \qquad \text{Equation 1.1}$$

Where P_a is the absorbed pump power, P_i is the incident pump power, α is the pump absorption coefficient and l is the length of the gain medium. For Figure 1.11, the length used in Equation 1.1 is the thickness of the gain medium multiplied by the number of passes. A value of 40 cm^{-1} was chosen for the pump absorption coefficient due to considerations outlined later in Section 1.7. An incident pump power of 200 W was used for all the data. Figure 1.11 shows that making the gain medium thicker can

have a large impact on the number of pump beam passes required to absorb an adequate amount of pump power, making the design of the laser amplifier easier to manufacture.

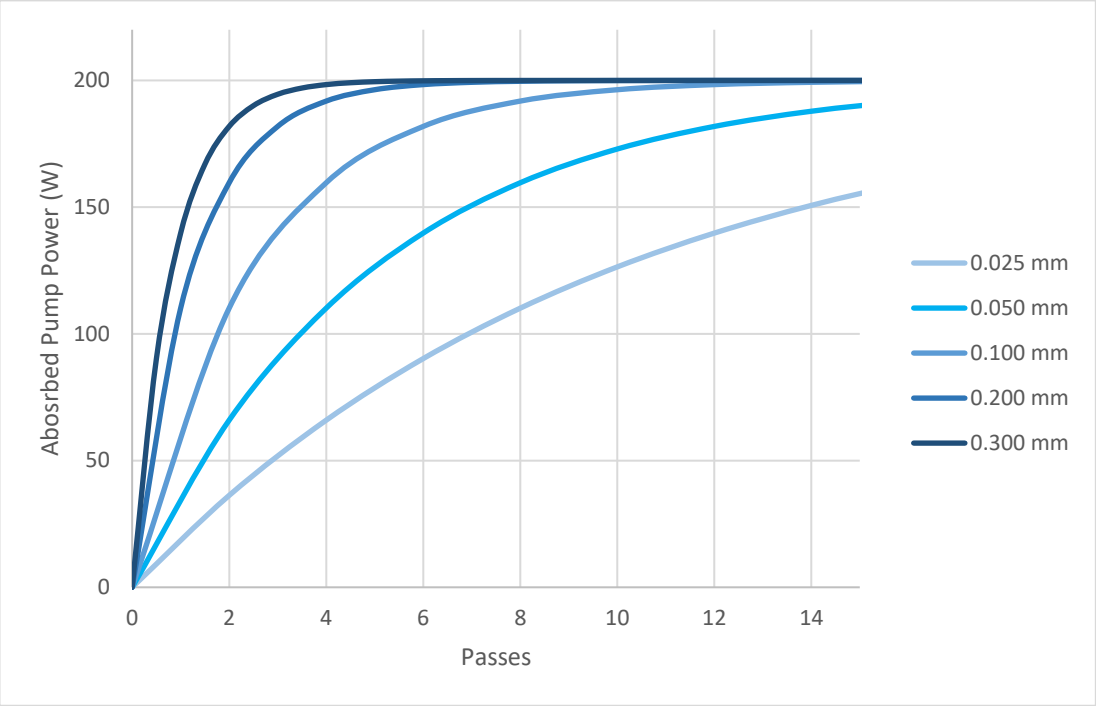

Figure 1.11 – The absorbed pump power as a function of the number of pump beam passes for varying gain medium thicknesses.

1.7 Gain Material

It is evident from the scientific literature that ytterbium (Yb) doped crystals are the gain material of choice for high power operation in both lasers and amplifiers. Ytterbium is used in all different laser and amplifier architectures: fibres [67]–[71]; slabs [72]–[75]; rods [76]–[80]; regenerative amplifiers [81]–[83]; and thin-disks [84]–[87]. Ytterbium doped gain media are particularly suited for high power operation due their quasi-three-level behaviour which leads to a small quantum defect. Yb:YAG is typically pumped at 940 nm with an emission wavelength of 1030 nm or 1050 nm. It also does not suffer from deleterious quenching processes or excited-state

absorption [88]–[90] which reduces thermal effects at high powers. Quenching processes and excited-state absorption are discussed in more detail in section 2.2.4.

However, the emission wavelength of the seed laser primarily used in this thesis was 1064 nm, so ytterbium doped gain media could not be used. Instead, neodymium (Nd) doped crystals were considered as they offer an emission wavelength around 1064 nm. Three gain materials were considered: Nd:YAG; Nd:YVO_4; and Nd:$GdVO_4$. Table 1.1 compares some relevant characteristics of the three materials when they are pumped at a wavelength of 808 nm and the emission wavelength is around 1064 nm. The numbers in Table 1.1 are for each material doped at a concentration of 1 atm %.

The theory of laser amplification will be discussed in much more detail in the next chapter, but here the stimulated-emission cross-section (σ_e) and fluorescent lifetime parameters (τ) broadly relate to the gain of the material and the larger these two parameters are, the better the amplifier should perform. The pump absorption coefficient provides an indication of how well the material will absorb the pump energy and the thermal conductivity alludes to the material's ability to operate at high powers, and consequently, high temperatures.

	Nd:YAG	Nd:YVO_4	Nd:$GdVO_4$
Stimulated Emission Cross-section (x10^{-19} cm^2)	2.7 [91]	14.4 [92]	8
Fluorescent Lifetime (µs)	236 [91]	96 [92]	90
Pump Absorption Coefficient (cm^{-1})	9.1	48.4 [92]	78
Thermal Conductivity (W/m.K)	14	5.1 [93]	11.7

Table 1.1 – A comparison of various characteristics between Nd:YAG, Nd:YVO_4 and Nd:$GdVO_4$ gain materials all doped at 1 atm %. Where relevant, the values for Nd:YVO_4 were for the π polarisation axis as the crystal is anisotropic.

The importance of gain can be seen in Figure 1.12, which shows the output power of a very simple laser amplifier model as a function of the number of passes of the seed beam. This is shown for various values of gain, where the gain is the output seed power divided by the input seed power for each pass of the seed beam. Increasing the gain leads to fewer passes of the seed beam to reach a given value of output power, which leads to a simpler laser amplifier design.

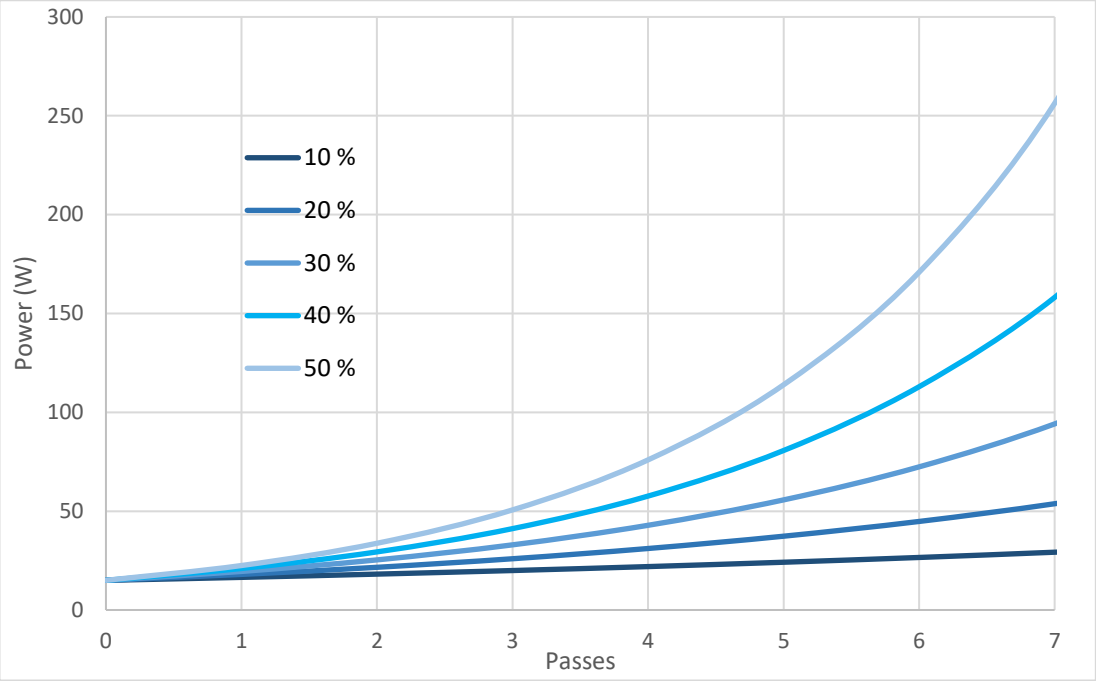

Figure 1.12 – The output power of a laser amplifier as a function of passes of the seed beam for varying values of gain.

With the importance of pump absorption and gain being shown in Figure 1.11 and Figure 1.12, Nd:YVO_4 was chosen as the most suitable gain material for a low-complexity, thin-disk amplifier based on the parameters set out in Table 1.1. The stimulated-emission cross-section of Nd:YVO_4 is superior to both Nd:YAG and Nd:$GdVO_4$, whilst Nd:YAG has a much higher fluorescence lifetime than both Nd:YVO_4 and Nd:$GdVO_4$, which both have similar values. Table 1.2 shows a figure of merit based on these two parameters multiplied together, where a larger value is better.

The figure of merit gives an idea of the overall gain of the material, and Nd:YVO_4 has the largest. The pump absorption coefficient (α) and the thermal conductivity (k) were also multiplied together for each material to reflect each crystal's ability to handle high pump powers in a thin-disk geometry. Again, a larger figure of merit is desirable. Here, Nd:$GdVO_4$ clearly has the largest figure of merit with much smaller values for both Nd:YAG and Nd:YVO_4. One other advantage that Nd:YVO_4 and Nd:YAG have over Nd:$GdVO_4$ is that they have wide spread commercial availability and industry acceptance. Overall, Nd:YVO_4 was considered the most suitable choice and with a bandwidth of 0.96 nm on the 1064 nm transition, pulse durations down to 1.8 ps can be amplified [94] which would support the pulse duration of the seed laser, which is approximately 15 ps.

	Nd:YAG	Nd:YVO_4	Nd:$GdVO_4$
$\sigma_e.\tau$ ($x10^{-23}cm^2.s$)	6.4	13.8	7.2
$\alpha.k$ ($W/[cm^2.K]$)	1.3	2.5	9.1

Table 1.2 – A comparison of two figures of merit for each of the gain materials under consideration, based on values taken from Table 1.1.

Figure 1.13 below, shows the main fluorescence transitions that are involved in Nd:YVO_4. Displayed is the main pump transition, at a wavelength of 808 nm, which involves a transition from the $^4I_{9/2}$ energy level up to the $^4F_{5/2}$ level. From there, a non-radiative transition occurs to the $^4F_{3/2}$ level, where the energy is lost as heat. From $^4F_{3/2}$ the ion decays to $^4I_{11/2}$ and this is the main laser transition which corresponds to a wavelenght of 1064 nm. There is a final decay, back to the $^4I_{9/2}$ level which is, again, a non-radiative decay where the energy is lost as heat [95]. The quantum defect is the percentage of energy that is lost to heating and, if all ions

transition through stimulated-emission, that value is 24 % for Nd:YVO_4. This is a simplified version of the energy levels involved in Nd:YVO_4, but it serves to give an overview of the main pump and laser transitions.

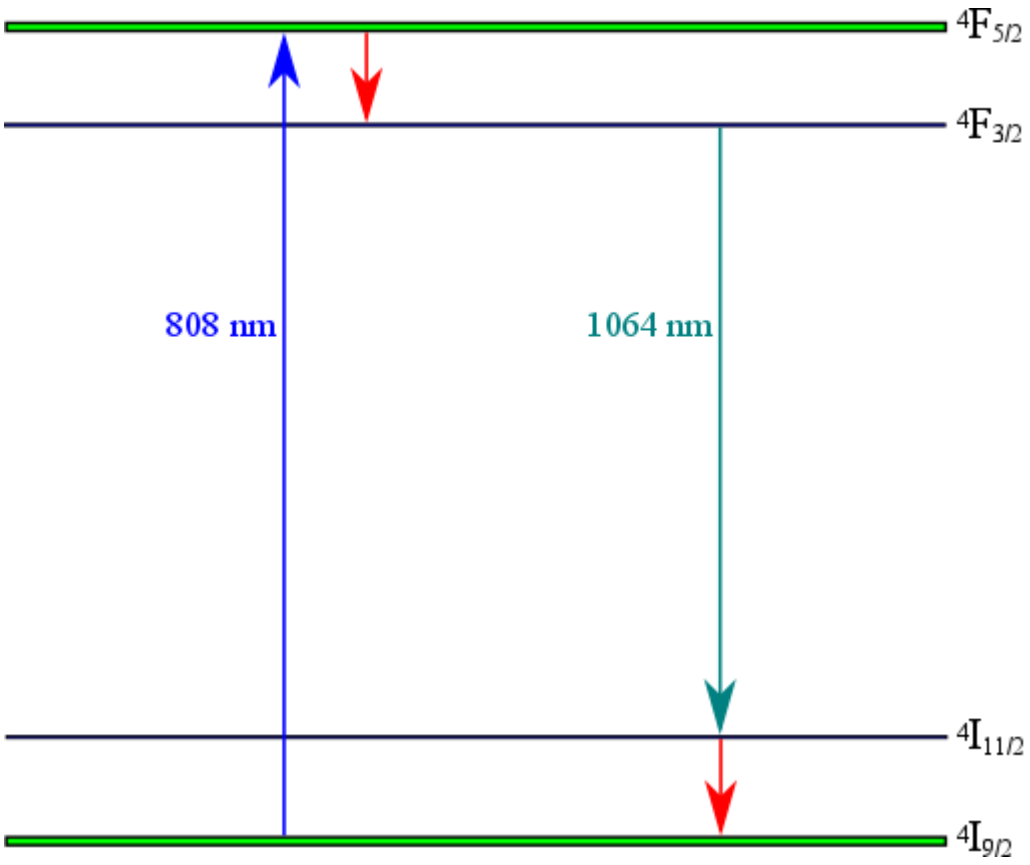

Figure 1.13 – An energy level diagram of Nd:YVO_4 showing the main pump transition (808 nm) in blue and the stimulated-emission transition (1064 nm) in dark green. The red arrows in the diagram indicate non-radiative transitions where the energy becomes heat.

1.8 Conclusions

Lasers have been used as an industrial tool for material processing almost since their inception and can be utilised in many different ways for various applications. Ultrafast pulsed lasers are particularly applicable to high precision and high quality drilling due to their very short pulse lengths, which interact with materials without depositing

significant amounts of heat. However, there is a requirement for these ultrafast lasers to reach higher average powers, of 100 W and beyond, to increase manufacturing throughput, but this is a cost, and hence, complexity sensitive market. Hence, the majority of this thesis discusses the results of a project that sought to assess whether it might, in the future, be possible to meet this demand, by amplifying a commercially available, ultrafast laser with a simplified thin-disk amplifier based on Nd:YVO_4.

There are many different amplifier architectures that have been designed to operate at high powers, where thermal management is a key requirement, and the design chosen here, a thin-disk amplifier, has proven to be adept at high powers. As the project in question was conducted with an industrial partner looking to manufacture any solution, there was a particular focus on manufacturability and cost. Unfortunately, a thin-disk amplifier can be quite complex in its design as many passes of the pump and seed beam are required due to the short length of the gain medium, which also gives the design its superior thermal qualities. To try and simplify the multi-passing arrangements of the amplifier, the idea of having a thicker disk was considered, where both the pump and seed beams would have a longer interaction length for each pass of the gain medium.

Nd:YVO_4 was chosen as the gain medium for the amplifier. A neodymium doped gain material was forced upon the design due to the emission wavelength of the commercial seed laser being 1064 nm. Nd:YVO_4 was chosen, in particular, primarily because of its high stimulated-emission cross-section. The next chapter will further explore the theory behind laser amplifiers and seek to model the performance of the Nd:YVO_4 laser amplifier.

1.9 References

[1] A. K. Dubey and V. Yadava, “Laser beam machining-A review,” *Int. J. Mach. Tools Manuf.*, vol. 48, no. 6, pp. 609–628, 2008.

[2] A. L. Schawlow and C. H. Townes, “Infrared and optical masers,” *Phys. Rev.*, vol. 112, no. 6, pp. 1940–1949, 1958.

[3] T. H. Maiman, “Simulated optical radiation in ruby,” *Nature*, vol. 187, pp. 493–494, Aug. 1960.

[4] W. M. Steen and J. Mazumder, *Laser Material Processing*. 2010.

[5] K. Kincade, A. Nogee, and G. Overton, “Lasers enabling lasers,” vol. 2018, no. January, 2018.

[6] T. Kramár and P. Kova, “The laser beam welding of titanium grade 2 alloy,” vol. 0638, pp. 77–79, 1805.

[7] J. Dutta Majumdar and I. Manna, “Laser processing of materials,” *Sadhana*, vol. 28, no. 3–4, pp. 495–562, 2003.

[8] J. Dutta Majumdar and I. Manna, *Laser surface engineering of titanium and its alloys for improved wear, corrosion and high-temperature oxidation resistance*. Elsevier Ltd., 2014.

[9] W. Bloehs, B. Grünenwald, F. Dausinger, and H. Hügel, “Recent progress in laser surface treatment: I . Implications of laser wavelength,” *J. Laser Appl.*, vol. 8, no. 1, pp. 15–23, 1996.

[10] A. Roy and I. Manna, “Laser surface engineering to improve wear resistance of austempered ductile iron,” *Mater. Sci. Eng. A*, vol. 297, no. 1–2, pp. 85–93, 2001.

[11] W. Bloehs, B. Grünenwald, F. Dausinger, and H. Hügel, “Recent progress in laser surface treatment: II. Adopted processing for high efficiency and quality,” *J. Laser Appl.*, vol. 8, no. 2, p. 65, 1996.

[12] M. Riabkina-Fishman and J. Zahavi, “Laser alloying and cladding for improving surface properties,” *Appl. Surf. Sci.*, vol. 106, pp. 263–267, 1996.

[13] H. Schulz and T. Moriwaki, “High-speed Machining,” *CIRP Ann. - Manuf. Technol.*, vol. 41, no. 2, pp. 637–643, 1992.

[14] M. Sekar, I. Kantharaj, and S. A. Siddhappa, “Machining Chatter Analysis for High Speed Milling Operations,” *IOP Conf. Ser. Mater. Sci. Eng.*, vol. 247, no. 1, 2017.

[15] Z. Y. Li, X. T. Wei, Y. B. Guo, and M. P. Sealy, “State-Of-Art, Challenges, and Outlook on Manufacturing of Cooling Holes for Turbine Blades,” *Mach. Sci. Technol.*, vol. 19, no. 3, pp. 361–399, 2015.

[16] Y. Z. Liu, “Coaxial waterjet-assisted laser drilling of film cooling holes in turbine blades,” *Int. J. Mach. Tools Manuf.*, vol. 150, no. September 2019, p. 103510, 2020.

[17] A. Kestenbaum, J. F. D’Amico, B. . Blumenstock, and M. A. DeAngelo, “Laser drilling of microvias in epoxy-glass printed circuit boards,” *IEEE Trans. Components, Hybrids, Manuf. Technol.*, vol. 13, no. 1055–1062, 1990.

[18] H. Zheng, E. Gan, and G. C. Lim, “Investigation of laser via formation technology for the manufacturing of high density substrates,” *Opt. Lasers Eng.*, vol. 36, pp. 355–371, 2001.

[19] B. F. Pados, J. Park, S. M. Thoyre, H. Estrem, and W. B. Nix, “Milk Flow Rates From Bottle Nipples Used for Feeding Infants Who Are Hospitalized,” *Am. J. Speech-Language Pathol.*, vol. 24, pp. 671–679, 2015.

[20] K. E. Mcgrattan, D. H. Mcfarland, J. C. Dean, and E. Hill, “Effect of Single-Use, Laser-Cut, Slow-Flow Nipples on Respiration and Milk Ingestion in Preterm Infants,” *Am. J. Speech-Language Pathol.*, vol. 26, pp. 832–839, 2017.

[21] A. C. Forsman, P. S. Banks, M. D. Perry, E. M. Campbell, A. L. Dodell, and M. S. Armas, “Double-pulse machining as a technique for the enhancement of material removal rates in laser machining of metals,” *J. Appl. Phys.*, vol. 98, no. 3, 2005.

[22] “Campbell, B. R., Lehecka, T. M., Semak, V. V., & Thomas, J. G. (2007). Effect of the double pulse format for picosecond pulse laser drilling in metals. In 26th International Congress on Applications of Lasers and Electro-Optics, ICALEO 2007 - Congress Pro.”

[23] W. O. Neill, M. Voglsanger, A. Elboughey, and W. M. Steen, “On the selective removal of steel by laser-assisted,” vol. 215, pp. 1051–1064.

[24] J. Reif, “Basic Physics of Femtosecond Laser Ablation,” pp. 19–41, 2010.

[25] Y. L. Yao, H. Chen, and W. Zhang, “Time scale effects in laser material removal: a review,” *Int. J. Adv. Manuf. Technol.*, vol. 26, no. 5–6, pp. 598–608, 2005.

[26] J. K. Chen, J. E. Beraun, L. E. Grimes, and D. Y. Tzou, “Modeling of femtosecond laser-induced non-equilibrium deformation in metal films,” *Int. J. Solids Struct.*, vol. 39, no. 12, pp. 3199–3216, 2002.

[27] S. S. Singh, P. K. Baruah, A. Khare, and S. N. Joshi, “Effect of laser beam conditioning on fabrication of clean micro-channel on stainless steel 316L using second harmonic of Q-switched Nd:YAG laser,” *Opt. Laser Technol.*, vol. 99, pp. 107–117, 2018.

[28] K. H. Leitz, B. Redlingshöer, Y. Reg, A. Otto, and M. Schmidt, “Metal ablation with short and ultrashort laser pulses,” *Phys. Procedia*, vol. 12, no. PART 2, pp. 230–238, 2011.

[29] H. K. Tonshoff, F. V. O. N. Alvensleben, A. Ostendorf, G. Kamlage, and S. N. O. L. Te, “Micromachining of Metals Using Ultrashort Laser Pulses,” no. 4, pp. 1–6, 1999.

[30] R. W. Schoenlein, W. Z. Lin, J. G. Fujimoto, and G. L. Eesley, “Femtosecond studies of nonequilibrium electronic processes in metals,” *Phys. Rev. Lett.*, vol. 58, no. 16, pp. 1680–1683, 1987.

[31] S. S. Mao, X. Mao, R. Greif, and R. E. Russo, “Initiation of an early-stage plasma during picosecond laser ablation of solids,” *Appl. Phys. Lett.*, vol. 77, no. 16, pp. 2464–2466, 2000.

[32] B. N. Chichkov, C. Momma, S. Nolte, F. Von Alvensleben, and A. Tünnermann, “Femtosecond, picosecond and nanosecond laser ablation of solids,” *Appl. Phys. A Mater. Sci. Process.*, vol. 63, no. 2, pp. 109–115, 1996.

[33] S. Nolte *et al.*, “Ablation of metals by ultrashort laser pulses,” *J. Opt. Soc. Am. B*, vol. 14, no. 10, p. 2716, 1997.

[34] J. Krüger and W. Kautek, “The Femtosecond Pulse Laser: a New Tool for Micromachining,” *Laser Phys.*, vol. 9, no. 1, pp. 30–40, 1999.

[35] J. König, S. Nolte, and A. Tünnermann, “Plasma evalution during metal ablation with ultrashort laser pulses,” *Opt. Express*, vol. 13, no. 26, pp. 10597–10607, 2005.

[36] M. K. Cidade, F. L. Palombini, L. da C. Duarte, and S. Paciornik, “Investigation of the thermal microstructural effects of CO2laser engraving on agate via X-ray microtomography,” *Opt. Laser Technol.*, vol. 104, pp. 56–64, 2018.

[37] C.-C. Ho, K.-Y. Shen, C.-S. Chen, Y.-J. Chang, J.-C. Hsu, and C.-L. Kuo, “Swirling gas jet-assisted laser trepanning for a galvanometer-scanned CO<inf>2</inf>laser,” *Appl. Sci.*, vol. 7, no. 5, 2017.

[38] J. Meško, R. Nigrovič, and A. Zrak, “The Influence of Different Assist Gases on Ductile Cast Iron Cutting by CO2Laser,” *Arch. Foundry Eng.*, vol. 17, no. 4, pp. 109–114, 2017.

[39] W. Koechner and M. Bass, *Solid-State Lasers*. 2003.

[40] R. Paschotta, “https://www.rp-photonics.com/fiber_amplifiers.html.” [Online]. Available: https://www.rp-photonics.com/fiber_amplifiers.html.

[41] R. Paschotta, "https://www.rp-photonics.com/high_power_fiber_lasers_and_amplifiers.html." [Online]. Available: https://www.rp-photonics.com/ high_power_fiber_lasers_and_amplifiers.html.

[42] J. Limpert, A. Liem, H. Zellmer, and A. Tunnerman, "500 W continuous-wave fibre laser with excellent beam quality," *Electron. Lett.*, vol. 39, no. 8, pp. 5–6, 2003.

[43] C. Jauregui, J. Limpert, and A. Tünnermann, "High-power fibre lasers," *Nat. Photonics*, vol. 7, no. 11, pp. 861–867, 2013.

[44] J. Limpert *et al.*, "High-power femtosecond Yb-doped fiber amplifier," *Opt. Express*, vol. 10, no. 14, pp. 628–638, 2002.

[45] A. Kobyakov, M. Sauer, and D. Chowdhury, "Stimulated Brillouin scattering in optical fibers," *Adv. Opt. Photonics*, vol. 2, no. 1, pp. 1–59, 2010.

[46] Y. Aoki, K. Tajima, and S. Murata, "Input Power Limits of Optical Fibers Due To Stimulated Brillouin Scattering in Fsk Coherent Optical Transmission Systems.," *J. Light. Technol.*, vol. 6, no. 5, pp. 710–719, 1987.

[47] Y. Jeong *et al.*, "Single-frequency, polarized ytterbium-doped fiber MOPA source with 264 W output power," in *CLEO, San Francisco, May, postdeadline paper CPDD1*, 2004, pp. 16–21.

[48] C. Lin and R. H. Stolen, "Self-phase-modulation in silica optical fibers," *Phys. Rev. A*, vol. 17, no. 4, pp. 1448–1454, 1978.

[49] C. Lin and H. Kogelnik, "Optical-pulse equalization of low-dispersion transmission in single-mode fibers in the 1.3-1.7-um spectral region," *Opt. Lett.*, vol. 5, no. 11, pp. 476–478, 1980.

[50] T. Kato, M. Hirano, T. Fujii, T. Yokokawa, Y. Yamamoto, and M. Onishi, "Design optimization of dispersion compensating fibers and their packaging techniques," *J. Opt. Fiber Commun. Reports*, vol. 4, no. 2, pp. 86–109, 2007.

[51] M.-Y. Cheng, Y.-C. Chang, A. Galvanauskas, P. Mamidipudi, R. Changkakoti, and P. Gatchell, “High-energy and high-peak-power nanosecond pulse generation with beam quality control in 200-μm core highly multimode Yb-doped fiber amplifiers,” *Opt. Lett.*, vol. 30, no. 4, p. 358, 2005.

[52] R. Kashyap and K. J. Blow, “Observation of catastrophic self-propelled self-focusing in optical fibres,” *Electron. Lett.*, vol. 24, no. 1, pp. 47–49, 1988.

[53] J. Limpert, F. Röser, T. Schreiber, and A. Tünnermann, “High-power ultrafast fiber laser systems,” *IEEE J. Sel. Top. Quantum Electron.*, vol. 12, no. 2, pp. 233–244, 2006.

[54] J. Limpert *et al.*, “High-power rod-type photonic crystal fiber laser,” *Opt. Exp.*, vol. 13, no. 4, pp. 1055–1058, 2005.

[55] C. D. Brooks and F. Di Teodoro, “Multimegawatt peak-power, single-transverse-mode operation of a 100 μm core diameter, Yb-doped rodlike photonic crystal fiber amplifier,” *Appl. Phys. Lett.*, vol. 89, no. 11, 2006.

[56] X.-H. Fang, M.-L. Hu, B.-W. Liu, L. Chai, C.-Y. Wang, and A. M. Zheltikov, “Generation of 150 MW, 110 fs pulses by phase-locked amplification in multicore photonic crystal fiber.,” *Opt. Lett.*, vol. 35, no. 14, pp. 2326–2328, 2010.

[57] Y.-H. Cha *et al.*, “High-power single-frequency pulsed laser based on a Yb-doped large-pitch photonic crystal fiber,” *J. Korean Phys. Soc.*, vol. 70, no. 11, pp. 973–978, 2017.

[58] X. Su, T. Hoang, P. Long, Y. Zheng, and D. Strickland, “A Compact High-Average-Power Femtosecond Fiber-Coupled Two-Color CPA System,” *IEEE J. Sel. Top. Quantum Electron.*, vol. 24, no. 5, pp. 1–5, 2018.

[59] P. Yang *et al.*, “Highly stable Yb-fiber laser amplifier of delivering 32-μJ, 153-fs pulses at 1-MHz repetition rate,” *Appl. Phys. B Lasers Opt.*, vol. 124, no. 8, pp. 1–6, 2018.

[60] A. Zaytsev, Y. J. You, S. W. Huang, and C. L. Pan, “Spectrally shaped chirped pulse amplification of an all-normal dispersion Yb-doped fibre laser,” *Laser Phys. Lett.*, vol. 15, no. 8, 2018.

[61] R. Paschotta, “https://www.rp-photonics.com/slab_lasers.html.” .

[62] G. Guo, Y. Lang, W. Lin, Z. Kang, H. Zhang, and Z. Fan, “Experimental Study of a Diode-Pumped Nd:YAG Slab Laser Amplifier,” *J. Russ. Laser Res.*, vol. 38, no. 2, pp. 199–203, 2017.

[63] P. Russbueldt *et al.*, “Innoslab Amplifiers,” *IEEE J. Sel. Top. Quantum Electron.*, vol. 21, no. 1, 2015.

[64] R. Paschotta, “https://www.rp-photonics.com/regenerative_amplifiers.html.”

[65] A.Giesen, H.Hugel, A.Voss, K.Wittig, U.Brauch, and H.Opower, “Scalable Concept for diode-pumped high power solid-state lasers,” *Appl. Opt. B, Phototypes Laser Chem*, vol. 58, p. 365, 1994.

[66] A. Giesen and J. Speiser, “Fifteen years of work on thin-disk lasers: Results and scaling laws,” *IEEE J. Sel. Top. Quantum Electron.*, vol. 13, no. 3, pp. 598–609, 2007.

[67] Y. Jeong, J. K. Sahu, D. N. Payne, and J. Nilsson, “Ytterbium-doped large-core fiber laser with 1 . 36 kW continuous-wave output power,” vol. 12, no. 25, pp. 6088–6092, 2004.

[68] T. Li *et al.*, “Power Scaling of Narrow-Linewidth Fiber Amplifier Seeded by Yb-Doped Random Fiber Laser,” *IEEE J. Sel. Top. Quantum Electron.*, vol. 24, no. 5, 2018.

[69] J. Kim, P. Dupriez, C. Codemard, J. Nilsson, and J. K. Sahu, “Suppression of stimulated Raman scattering in a high power Yb-doped fiber amplifier using a W-type core with fundamental mode cut-off.,” *Opt. Express*, vol. 14, no. 12, pp. 5103–5113, 2006.

[70] J. O. N. Ilsson and S. E. Y. Oo, “Bendable large-mode-area fiber with a non-circular core,” *Appl. Opt.*, vol. 57, no. 22, pp. 6388–6395, 2018.

[71] S. Liu *et al.*, “Multi-kW Yb-doped aluminophosphosilicate fiber,” *Opt. Mater. Express*, vol. 8, no. 8, pp. 9924–9932, 2018.

[72] P. Russbueldt, T. Mans, J. Weitenberg, H. D. Hoffmann, and R. Poprawe, “Compact diode-pumped 1.1 kW Yb: YAG Innoslab femtosecond amplifier,” *Opt. Lett.*, vol. 35, no. 24, pp. 4169–4171, 2010.

[73] Y. Ma *et al.*, “High-power continuous-wave dual-wavelength diode-pumped Yb:YAG slab amplifier with temperature-dependent effects,” *Appl. Phys. B Lasers Opt.*, vol. 123, no. 10, pp. 1–7, 2017.

[74] M. Li *et al.*, “High Power Continuous Wave Yb:YAG Composite Crystal Zigzag Slab Amplifier at Room Temperature,” *IEEE Photonics J.*, vol. 9, no. 6, 2017.

[75] L. X. U. Iu *et al.*, “High brightness laser based on Yb : YAG MOPA chain and adaptive optics system at room temperature,” vol. 26, no. 11, pp. 3906–3911, 2018.

[76] I. V Obronov, A. S. Demkin, and D. V Myasnikov, “Solid-state Yb : YAG amplifier pumped by a single- mode laser at 920 nm Solid-state Yb : YAG amplifier pumped by a single-mode laser at 920 nm,” pp. 48–51, 2018.

[77] I. Kuznetsov, I. Mukhin, O. Palashov, and K.-I. Ueda, “Thin-rod Yb:YAG amplifiers for high average and peak power lasers,” *Opt. Lett.*, vol. 43, no. 16, p. 3941, 2018.

[78] I. I. Kuznetsov, I. B. Mukhin, E. A. Perevezentsev, M. Volkov, and O. V. Palashov, “High-Power Laser Based on Amplifiers with Yb : YAG Elements of Advanced Geometries,” *Talk ALT17*, vol. 2, no. September, pp. 2–3, 2017.

[79] I. I. Kuznetsov, I. B. Mukhin, and O. V Palashov, “Yb : YAG thin-rod laser amplifier with a high pulse energy for a fibre oscillator,” *Quantum Electron.*, vol. 46, no. 4, pp. 375–378, 2016.

[80] M. Kienel *et al.*, "Coherent beam combination of Yb:YAG single-crystal rod amplifiers.," *Opt. Lett.*, vol. 39, no. 11, pp. 3278–81, 2014.

[81] R. Jung, J. Tümmler, and I. Will, "Regenerative thin-disk amplifier for 300 mJ pulse energy," *Opt. Express*, vol. 24, no. 2, p. 883, 2016.

[82] H. Fattahi *et al.*, "High-power, 1-ps, all-Yb:YAG thin-disk regenerative amplifier," *Opt. Lett.*, vol. 41, no. 6, p. 1126, 2016.

[83] J. Novák *et al.*, "Thin disk amplifier-based 40 mJ, 1 kHz, picosecond laser at 515 nm," *Opt. Express*, vol. 24, no. 6, p. 5728, 2016.

[84] I. I. Kuznetsov, I. B. Mukhin, O. L. Vadimova, and O. V Palashov, "Thin-disk laser based on an Yb:YAG / YAG composite active element," *Quantum Electron.*, vol. 45, no. 3, pp. 207–210, 2015.

[85] J. P. Negel *et al.*, "Thin-disk multipass amplifier for fs pulses delivering 400 W of average and 2.0 GW of peak power for linear polarization as well as 235 W and 1.2 GW for radial polarization," *Appl. Phys. B Lasers Opt.*, vol. 123, no. 5, pp. 1–8, 2017.

[86] B. A. Reagan *et al.*, "Scaling diode-pumped, high energy picosecond lasers to kilowatt average powers," *High Power Laser Sci. Eng.*, vol. 6, p. e11, 2018.

[87] T. Nubbemeyer *et al.*, "1 kW, 200 mJ picosecond thin-disk laser system," *Opt. Lett.*, vol. 42, no. 7, p. 1381, 2017.

[88] T. Y. Fan, "Heat generation in Nd:YAG and Yb:YAG," *IEEE J. Quantum Electron.*, vol. 29, no. 6, pp. 1457–1459, 1993.

[89] P. Lacovara, H. K. Choi, C. A. Wang, R. L. Aggarwal, and T. Y. Fan, "Room-temperature diode-pumped Yb : YAG laser," vol. 16, no. 14, pp. 1089–1091, 1991.

[90] P. Yang, P. Deng, and Z. Yin, "Concentration quenching in Yb:YAG," *J. Lumin.*, vol. 97, no. 1, pp. 51–54, 2002.

[91] J. K. Neeland and V. Evtuhov, “Measurement of the laser transition cross section for Nd+3 in yttrium aluminum garnet,” *Phys. Rev.*, vol. 156, no. 2, pp. 244–246, 1967.

[92] Y. Sato and T. Taira, “Spectroscopic properties of neodymium-doped yttrium orthovanadate single crystals with high-resolution measurement,” *Japanese J. Appl. Physics, Part 1 Regul. Pap. Short Notes Rev. Pap.*, vol. 41, no. 10, pp. 5999–6002, Oct. 2002.

[93] X. Peng, A. Asundi, Y. Chen, and Z. Xiong, “Study of the mechanical properties of Nd:YVO4 crystal by use of laser interferometry and finite-element analysis.,” *Appl. Opt.*, vol. 40, no. 9, pp. 1396–403, 2001.

[94] M. Siebold *et al.*, “A high-average-power diode-pumped Nd: YVO4regenerative laser amplifier for picosecond-pulses,” *Appl. Phys. B Lasers Opt.*, vol. 78, no. 3–4, pp. 287–290, 2004.

[95] D. K. Sardar and R. M. Yow, “Stark components of 4F3/2, 4I9/2 and 4I11/2 manifold energy levels and effects of temperature on the laser transition of Nd3+in YVO4,” *Opt. Mater. (Amst).*, vol. 14, no. 1, pp. 5–11, 2000.

Chapter Two

Laser Amplifier Theory and Model

2.1 Introduction

This chapter introduces the basic theory of laser gain in the context of a low power and low heat load laser amplifier, in order to construct a model of the Nd:YVO_4 amplifier behaviour. This model will provide a starting point in order to gain an understanding of the amplifiers that will be constructed and tested. The model will then be compared to empirical data for validation and will provide an improved understanding of what level of complexity may be required to achieve amplification to 100 W, at least with the assumptions made for the low power and low temperature regime. The end of the chapter begins to address the issues that a high temperature regime starts to present.

The theory explores: small-signal gain; the importance of pump beam shape; the saturated gain regime; and lifetime quenching processes and their effects in a Nd:YVO_4 laser amplifier. The small-signal regime is examined before moving onto the saturated regime where depletion of the upper laser level by an input seed beam is considered. The small-signal and saturated regimes are examined with both Gaussian and top-hat pump beam shapes. Lifetime quenching processes are discussed and the most important of these, energy transfer up-conversion, is incorporated into the model but through a simplified method that breaks down in the highly saturated amplifier regime.

Nd:YVO_4 rod amplifier experiments are then discussed and the results compared with data extracted from the model in order to validate it. Three variations of the Nd:YVO_4 laser amplifier model were used: with a Gaussian pump beam profile, with a top-hat pump beam profile and with a top-hat pump beam profile but also

including the effects of the lifetime quenching process, energy-transfer up-conversion. The experiments were performed with 0.5 atm % and 1 atm % Nd:YVO_4 rods at different pump and seed beam radii to explore a broad range of input intensities. These experiments confirm that the models, with the various simplifying assumptions made, make accurate predictions of the amplifier performance in their appropriate regimes.

2.2 Laser amplifier theory

The purpose of examining the theory of laser amplifiers was to create a model that could accurately predict the behaviour a Nd:YVO_4 laser amplifier. An accurate model would also help in understanding the performance obtained experimentally and set limits on the performance levels that are realistically achievable with this laser amplifier. The level of complexity, in the number of the passes of the seed beam required to reach 100 W, can also be estimated with an accurate model.

It can be very difficult to incorporate every aspect of a laser system into a model and often counter-productive to spend too much time adding features to a model which may make little difference to the output. The purpose of the model presented here is to understand the main factors affecting amplifier performance in order to achieve the optimum design. In this section, the theory of laser gain will be explored with some simplifying assumptions made. The theory begins with small-signal gain and examines the importance of the pump beam profile. Saturated gain is then considered where the effects of the depletion of the upper-state population are included and lifetime quenching processes are discussed.

2.2.1 Small-signal gain

A signal beam, I_l, propagating through a laser amplifier will experience gain. The total gain of the amplifier is given by the expression [1],

$$\boldsymbol{G = \frac{I_{out}}{I_{in}}} \qquad \text{Equation 2.1}$$

where I_{out} is the signal intensity at the output of the amplifier and I_{in} is the input signal intensity. The change in a signal beam, dI_l, propagating through the amplifier, through a distance, dz, can be described by the following equation,

$$\boldsymbol{\frac{dI_l}{dz} = g(r,z)I_l(z)} \qquad \text{Equation 2.2}$$

Where $g(r,z)$ is the gain coefficient and is given by,

$$\boldsymbol{g(r,z) = \sigma_{21} n_2(r,z)} \qquad \text{Equation 2.3}$$

where σ_{21} is the stimulated-emission cross-section of the transition from the upper laser level to the lower laser level in the gain material, as in a four-level laser system, and n_2 is the population density of the upper laser level of the gain medium. In Equation 2.2 and 2.3, the gain coefficient, g(r,z), contains a radial component, r, because the population density of the upper laser level of the gain medium contains a radial dependence. This is because the incident pump power at each radial position determines the population density of the upper state and the radial pump profile is not necessarily uniform radially. The pump profile can vary from a top-hat shape, where it would be uniform radially, to a gaussian, as shown in Figure 2.1.

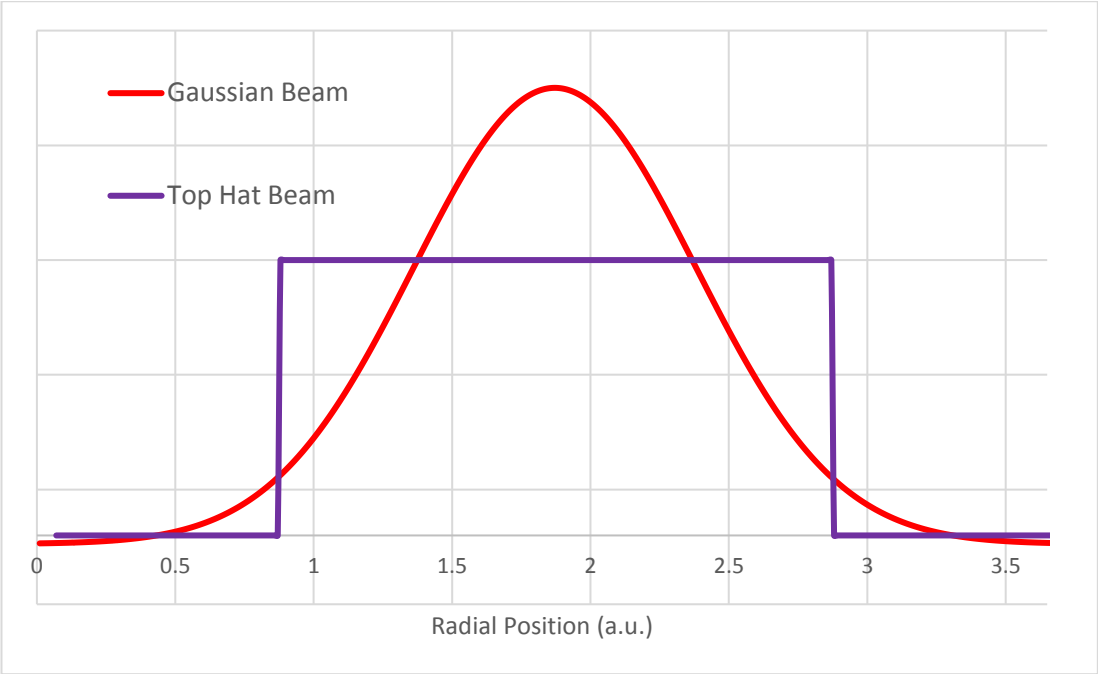

Figure 2.1 – Where the top hat pump is incident, the pump power is distributed uniformly in the radial dimension. However, for a gaussian pump beam, the pump power varies radially.

With no lifetime quenching processes considered, the rate of change of the upper-state population is given by,

$$\frac{dn_2}{dt} = R(r,z) - \frac{n_2(r,z)\sigma_{21}I_l(z)}{h\nu_l} - \frac{n_2(r,z)}{\tau} \qquad \text{Equation 2.4}$$

where R is the pump rate per unit volume, h is Planck's constant, ν_l is the laser frequency and τ is the fluorescence lifetime of the gain material. Stimulated-emission is represented by the $\frac{n_2(r,z)\sigma_{21}I_l(z)}{h\nu_l}$ term and spontaneous-emission by the $\frac{n_2(r,z)}{\tau}$ term. With continuous wave pump and signal beams, the population inversion, and therefore the gain, will reach a steady state within the amplifier so that,

$$\frac{dn_2}{dt} = 0 \qquad \text{Equation 2.5}$$

This means Equation 2.4 can be rearranged to give,

$$\boldsymbol{n_2(r,z) = \frac{R(r,z)\tau}{\left(\frac{\sigma_{21}\tau}{h\nu_l}\right)I_l(z)+1}} \qquad \text{Equation 2.6}$$

In the small-signal regime, where it is assumed the signal beam has a negligible effect on the upper-state population so that $\left(\frac{\sigma_{21}\tau}{h\nu_l}\right) I_l(z) \ll 1$, the population density is then simply given by,

$$\boldsymbol{n_2(r,z) = R(r,z)\tau} \qquad \text{Equation 2.7}$$

In the small-signal regime, using the n_2 from Equation 2.7, the gain coefficient, g, now becomes the small-signal gain coefficient, g_0.

The pump rate per unit volume is related to the incident pump intensity, I_p, and the absorption coefficient, α_p, of the gain material at the pump frequency, ν_p. $R(r,z)$, when end pumping the gain material, can then be described by the following equation,

$$\boldsymbol{R(r,z) = \frac{\alpha_p I_p(r)}{h\nu_p}\exp(-\alpha_p z)} \qquad \text{Equation 2.8}$$

With the assumption that the pump beam is free from diffraction within the gain medium, $R(r,z)$ can be integrated over the length of the gain medium, l, and the longitudinal variation of the pump can be averaged to give the fraction of the pump beam absorbed. The fraction of the pump beam absorbed is given by,

$$\boldsymbol{\eta_{abs} = \int_0^l \alpha_p \exp\left(-\alpha_p z\right) dz = 1 - \exp(\alpha_p l)} \qquad \text{Equation 2.9}$$

The pump rate per unit volume, $R(r)$, is now averaged along the length of the gain medium and becomes,

$$\boldsymbol{R(r)l = \frac{\eta_{abs} I_p(r)}{h\nu_p}} \qquad \text{Equation 2.10}$$

From Equation 2.7, the population density can then be written as,

$$\boldsymbol{n_2(r)l = \frac{\eta_{abs} I_p(r) \tau}{h\nu_p}} \quad \text{Equation 2.11}$$

If both sides of Equation 2.11 are multiplied by σ_{21} then,

$$\boldsymbol{g_0(r)l = \frac{\eta_{abs} I_p(r) \tau \sigma_{21}}{h\nu_p}} \quad \text{Equation 2.12}$$

Going back to Equation 2.2, which described the rate of change of a signal beam travelling through an amplifier, it can be rearranged and integrated over both the total length of the amplifier, l, and the output, I_{out}, and input, I_{in}, seed intensities,

$$\boldsymbol{\int_{I_{in}}^{I_{out}} \frac{1}{I_l(z)} dI_l = \int_0^l g_0(z)\, dz} \quad \text{Equation 2.13}$$

Integrating Equation 2.13 gives [2],

$$\boldsymbol{\frac{I_{out}}{I_{in}} = G_0 = exp(g_0 l)} \quad \text{Equation 2.14}$$

where G_0 is the total small-signal gain. Substituting Equation 2.12 into Equation 2.14 now gives the expression,

$$\boldsymbol{G_0(r) = exp\left(\frac{\eta_{abs} I_p(r) \tau \sigma_{21}}{h\nu_p}\right)} \quad \text{Equation 2.15}$$

2.2.2 Gaussian and top-hat pump profiles

In the experiments discussed within this thesis, the laser amplifiers are pumped by various laser diodes coupled into multimode fibres. The pump profiles incident on the gain medium are, therefore, defined by the multimode fibres. They produce a profile that is neither a Gaussian nor a top-hat but somewhere in between, yet, for simplicity, it is Gaussian and top-hat beams that are modelled. A Gaussian intensity profile can be described by the following expression,

$$\boldsymbol{I_p(r) = \frac{2P_p}{\pi\omega_p^2}\exp\left(\frac{-2r^2}{\omega_p^2}\right)} \quad \text{Equation 2.16}$$

where P_p is the pump power and ω_p is the $1/e^2$ pump beam radius. A top-hat intensity profile, where the power is radially constant until r is greater than the beam radius where it is zero, is given by,

$$\boldsymbol{I_p(r) = \frac{P_p}{\pi\omega_p^2},\ where\ \ r \leq \omega_p} \quad \text{Equation 2.17}$$

$$\boldsymbol{I_p(r) = 0,\ where\ \ r > \omega_p} \quad \text{Equation 2.18}$$

The signal beam is always assumed to have a Gaussian intensity profile and is described as,

$$\boldsymbol{I_l(r) = \frac{2P_l}{\pi\omega_l^2}\exp\left(\frac{-2r^2}{\omega_l^2}\right)} \quad \text{Equation 2.19}$$

where ω_l is the $1/e^2$ signal beam radius. For a top-hat intensity profile and using Equation 2.12, the small-signal gain coefficient, $g_0(r)$, can then be represented as,

$$\boldsymbol{g_0(r) = \left(\frac{P_p\eta_{abs}\sigma_{21}\tau}{lh\nu_p\pi\omega_p^2}\right),\ where\ \ r \leq \omega_p} \quad \text{Equation 2.20}$$

$$\boldsymbol{g_0(r) = 0,\ where\ \ r > \omega_p} \quad \text{Equation 2.21}$$

In Equation 2.20 and Equation 2.21, the gain still contains a radial dependence. An effective small-signal gain coefficient, g_{eff}, can be found with the following equation [2],

$$\boldsymbol{g_{eff} = \frac{\int g_0(r)I_l(r)2\pi r dr}{\int I_l(r)2\pi r dr}} \quad \text{Equation 2.22}$$

The profile of the signal beam is also taken into account which weights the gain with respect to the signal beam, as the pump and signal beam can have different radii. If the signal beam radius was greater than the pump beam radius, the effective

small-signal gain would be reduced compared to the case where the signal beam radius was smaller than the pump beam radius. By substituting Equation 2.20 and Equation 2.21 into Equation 2.22 for the top-hat case, g_{eff} becomes,

$$\boldsymbol{g_{eff} = \frac{P_p \eta_{abs} \sigma_{21} \tau}{l h \nu_p \pi \omega_p^2} \left[1 - exp\left(\frac{-2\omega_p^2}{\omega_l^2}\right)\right]} \qquad \text{Equation 2.23}$$

The total small-signal gain for a top-hat pump beam can then be given by,

$$\boldsymbol{G_{0,T} = exp\left(\frac{P_p \eta_{abs} \sigma_{21} \tau}{h \nu_p \pi \omega_p^2} \left[1 - exp\left(\frac{-2\omega_p^2}{\omega_l^2}\right)\right]\right)} \qquad \text{Equation 2.24}$$

The same process can be applied to a pump beam with a Gaussian profile. The expression for the small-signal gain coefficient for a Gaussian pump is,

$$\boldsymbol{g_0(r) = \frac{2P_p \eta_{abs} \sigma_{21} \tau}{l h \nu_p \pi \omega_p^2} exp\left(\frac{-2r^2}{\omega_p^2}\right)} \qquad \text{Equation 2.25}$$

The effective small-signal gain coefficient then becomes,

$$\boldsymbol{g_{eff} = \frac{2P_p \eta_{abs} \sigma_{21} \tau}{l h \nu_p \pi (\omega_p^2 + \omega_l^2)}} \qquad \text{Equation 2.26}$$

And so the total small-signal gain for a Gaussian pump beam is,

$$\boldsymbol{G_{0,G} = exp\left(\frac{2P_p \eta_{abs} \sigma_{21} \tau}{h \nu_p \pi (\omega_p^2 + \omega_l^2)}\right)} \qquad \text{Equation 2.27}$$

2.2.3 Saturation effects

In the previous section, the gain in a laser amplifier was considered in the small-signal regime where the signal does not significantly deplete the upper-state population. This section will consider the performance of a laser amplifier when the signal intensity is large enough to deplete the upper-state population [3].

Equation 2.6 describes the upper-state population and in the small-signal regime, it was assumed that the signal beam was negligible, in that it had no effect on the population. When considering saturation effects, the potential for the upper-state population to be reduced in the presence of the signal beam can no longer be neglected. From Equation 2.6, it can be seen that if the signal intensity is equal to $\left(\frac{h\nu_l}{\sigma_{21}\tau}\right)$ then the upper-state population will be reduced to half its value in the presence of no signal beam. This intensity is referred to as the saturation intensity [1],

$$\boldsymbol{I_{sat} = \frac{h\nu_l}{\sigma_{21}\tau}} \qquad \text{Equation 2.28}$$

This can be substituted into Equation 2.6 to give,

$$\boldsymbol{n_2(r,z) = \frac{R(r,z)\tau}{1+\left(\frac{I_l(z)}{I_{sat}}\right)}} \qquad \text{Equation 2.29}$$

Multiplying both sides of Equation 2.29 by σ_{21} gives,

$$\boldsymbol{g(z) = \frac{g_0}{1+\frac{I_l(z)}{I_{sat}}}} \qquad \text{Equation 2.30}$$

The rate of change of the signal beam as it propagates along the z-axis through the gain material can now be expressed as,

$$\boldsymbol{\frac{dI_l}{dz} = \frac{g_0}{1+\frac{I_l(z)}{I_{sat}}} I_l(z)} \qquad \text{Equation 2.31}$$

Equation 2.31 can be rearranged to give,

$$\boldsymbol{\left(\frac{1}{I_l(z)} + \frac{1}{I_{sat}}\right) dI_l = g_0(z)dz} \qquad \text{Equation 2.32}$$

Equation 2.32 can then be integrated over the length of the gain medium, l, and over the input and output signal intensities, I_{in} and I_{out},

$$\int_{I_{in}}^{I_{out}} \left[\frac{1}{I_l(z)} + \frac{1}{I_{sat}}\right] dI_l = \int_0^l g_0(z)\, dz \qquad \text{Equation 2.33}$$

Solving Equation 2.33 produces,

$$ln\left(\frac{I_{out}}{I_{in}}\right) + \frac{I_{out} - I_{in}}{I_{sat}} = g_0 l \qquad \text{Equation 2.34}$$

Using Equation 2.1 and Equation 2.14, Equation 2.34 can be rearranged to give,

$$\frac{I_{in}}{I_{sat}} = \frac{1}{G-1} ln\left(\frac{G_0}{G}\right) \qquad \text{Equation 2.35}$$

It is this expression that is used to model the output power of a Nd:YVO_4 laser amplifier although it cannot be rearranged to give an analytical solution for G and must be solved numerically. Figure 2.2 shows how the gain and extraction efficiency vary with input seed power for various absorbed pump powers, with a pump and seed spot size of 150 µm. Extraction efficiency is a measure of what fraction of available power, given by $P_{available} = \left({\nu_l}/{\nu_p}\right) P_p \eta_{abs}$, the signal beam extracts from the amplifier, $\eta_{extracted} = {P_{out} - P_{in}}/{P_{available}}$. The largest available power that can be extracted from an amplifier is the absorbed pump power minus the pump power that is lost to the quantum defect, as discussed in section 1.7. If a signal beam extracts this maximum available power in its entirety then the extraction efficiency would be 1.

The different pump powers in Figure 2.2 effectively represent different values for the small-signal gain. For different gain materials, other parameters such as stimulated-emission cross-section and fluorescence lifetime would also vary the small-signal gain. As only Nd:YVO_4 is considered here, and at one doping concentration of 0.5 atm %, different absorbed pump powers serve to show the variation in behaviour of the gain as a function of input seed power for different small-signal gain values.

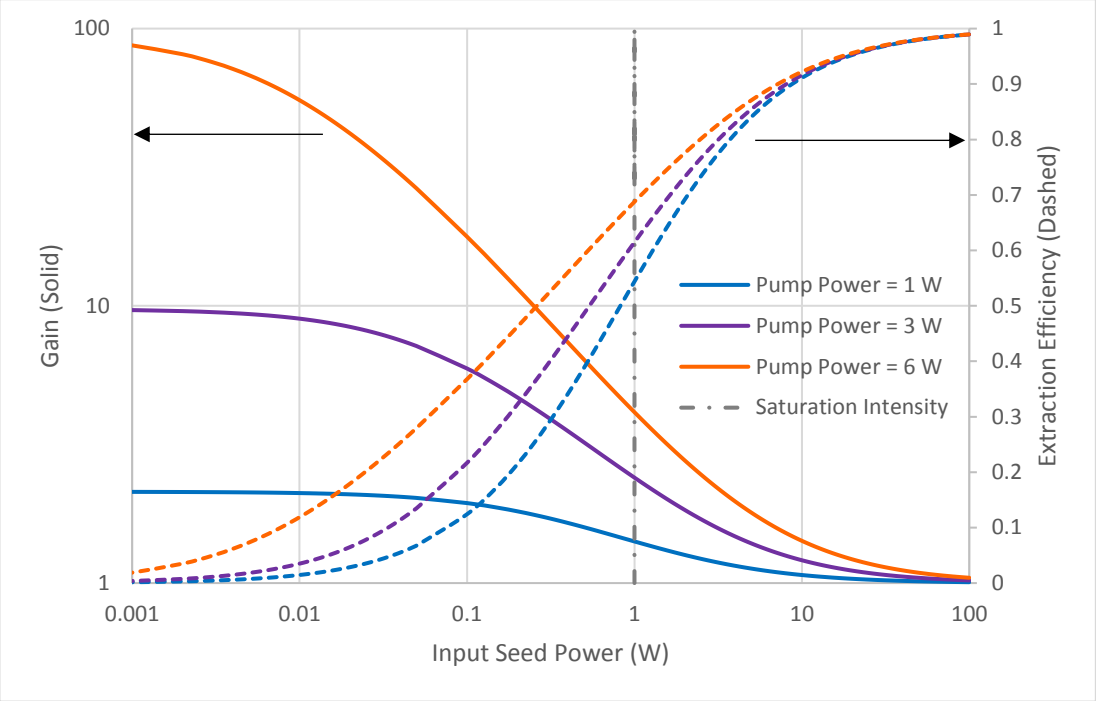

Figure 2.2 – Gain and extraction efficiency as a function of input seed power for three different absorbed pump powers of 1, 3 and 6 W. The gain, G, (solid lines) corresponds to the left axis and the extraction efficiency (dashed lines) to the right. The dashed vertical line represents the power at which the saturation intensity is reached for a signal beam with a radius of 150 µm. For the parameters used to create this graph, the saturation intensity occurs at an input seed power of 1 W. The graph is produced using data from the model with a pump and seed beam radii of 150 µm, chosen arbitrarily. The parameters used for 0.5 atm % Nd:YVO_4 are $12x10^{-19}$ cm^{-2} [4] for the stimulated-emission cross-section and 108 µs for the fluorescence lifetime which is inferred from fluorescence lifetimes taken for other doping concentrations, described in a later section of this chapter.

At low input seed powers, the gain is closest to the small-signal gain value and is at its highest. The extraction efficiency is also low, close to zero, in this regime as the low intensity seed beam does not interact with most of the ions in the upper laser level but can still be amplified to many times its original power. In the highly saturated regime at high input seed powers, the gain tends to a value of 1 as does the extraction efficiency. Here, the seed beam reduces almost all of the ions in the

upper laser level to the ground state but as the power gained by the seed beam is small in comparison to the initial input power, the gain is low. This is the linear regime as the input beam power increases linearly with increasing absorbed pump power. Saturation makes it difficult to extrapolate the effects on the output power of an amplifier from an increased number of passes of the seed beam using data gleaned from one double pass of the seed beam. If the seed beam were to double its number of passes through the gain material, it would not simply double the gain as the intensity of the seed beam would be greater on those extra passes, changing the degree of saturation. Further still, the gain of the first pass would also be reduced in the presence of subsequent passes. This effect will be discussed further in the next chapter, where it is incorporated into the model.

So far, in this simplified model of a laser amplifier, ignoring spontaneous-emission, only the seed beam has been able to extract ions from the upper laser level. There are, however, other, unwanted affects that can also extract energy from the amplifier that are not conducive to amplification called lifetime quenching processes and these will be discussed next.

2.2.4 Lifetime quenching processes

Solid-state lasers and amplifiers can suffer from a deterioration in performance caused by lifetime quenching processes. These processes provide alternative routes to the ground-state for excited ions in the upper laser level other than spontaneous-emission and so decrease the effective lifetime of the upper laser level. These processes can also often be non-radiative and can contribute to further heating of the gain medium. The lifetime quenching processes that will be examined here are cross-relaxation, excited-state absorption and energy-transfer up-conversion (ETU).

Cross-relaxation begins with an excited ion in the upper laser level as shown in Figure 2.3 a). The excited ion transfers some of its energy to an ion in the ground state, Figure 2.3 b). Both ions then lie in an intermediate level where they then

decay to the ground state, Figure 2.3 c). This process decreases the effective lifetime of the upper laser level and can add additional heating in Nd:YVO_4 [5]. Cross-relaxation relies on ions being in close proximity to one another and can be more problematic at higher doping concentrations.

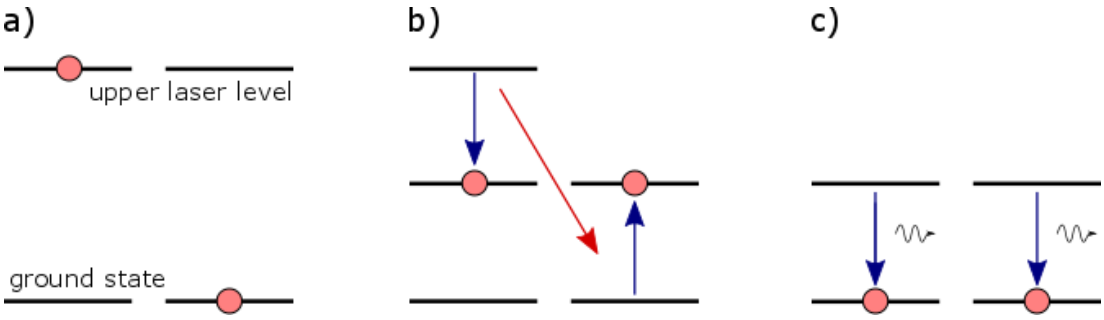

Figure 2.3 – Diagram of cross-relaxation. Part a) shows the excited ion in the upper laser level and an ion in the ground state. Part b) shows the transfer of energy from the excited ion to the ion in the ground state with both ions reaching an intermediate state. Part c) shows both ions decaying to the ground state where the energy can be lost as additional heating in the lattice or via an emitted photon.

Excited-state absorption again begins with an excited ion in the upper laser level, Figure 2.4 a). The excited ion then may absorb a pump or seed photon and be excited to an energy level above the upper laser level, Figure 2.4 b). The ion then decays back down to a lower energy level in Figure 2.4 c). The transition does not necessarily have to be back down to the upper laser level but could be to the ground state or some other energy level, where the energy can be lost via heating of the crystal lattice or photon emission. Fornasiero et al [6] have shown that the effect of excited-state absorption is negligible in Nd:YVO_4, hence it is not included in the models presented in this thesis.

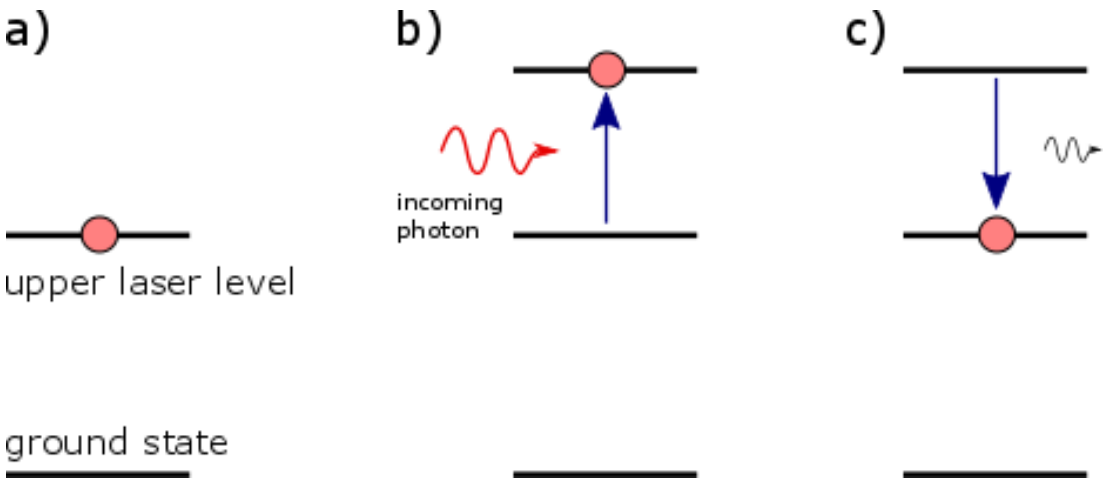

Figure 2.4 – Diagram of excited-state absorption. Part a) shows an excited ion lying in the upper laser level. Part b) shows the ion being raised to a higher energy level because it absorbs an incoming photon. Part c) show the ion decaying back down to the upper laser level and emitting radiation which could be via lattice heating or an emitted photon. The ion does not have to necessarily decay back to the upper laser level but could decay to the ground state or some other intermediate level.

Energy transfer up-conversion (ETU) occurs when there are two excited ions in the upper laser level that are close enough to interact with one other, Figure 2.5 a). When they interact, one ion gives some of its energy to the other, dropping down to an intermediate energy level while the other ion rises to a higher level as shown in Figure 2.5 b). The ion in the higher level decays back down to a lower energy level and the ion in the intermediate state also decays to a lower energy level, in both cases either by heating the lattice or emitting photons, Figure 2.5 c) [7]. This process can increase the heat load within the gain medium and reduces the effective lifetime of the upper laser level. For Nd:YVO_4, the ions in the higher levels above the upper laser level can also decay straight to the ground state, emitting photons of yellow light. However, this transition is negligible compared to the non-radiative decays back to the upper laser level [8].

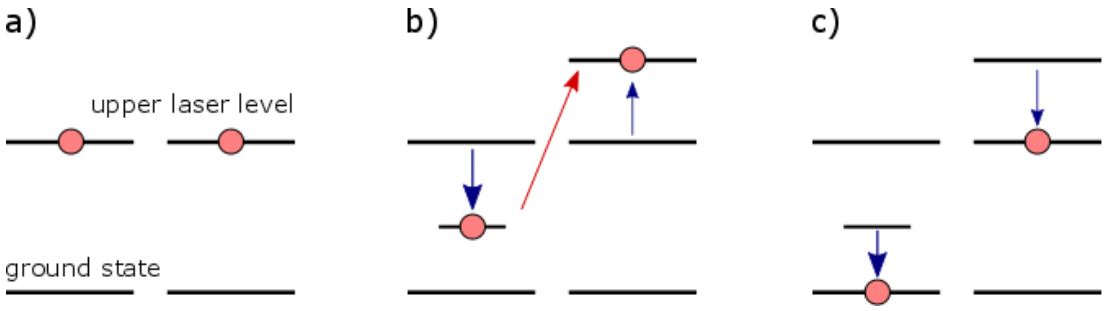

Figure 2.5 – Diagram of energy-transfer up-conversion. Part a) shows two excited ions close to each other in the upper laser level. Part b) shows one ion decaying to an intermediate level by giving part of its energy to the other ion which rises to a higher energy level. Part c) shows the lower energy ion decaying to a lower energy level and the higher energy ion also decaying to a lower energy level.

The rate of ETU is proportional to the square of the upper-state population (n_2^2), which means that the effects of ETU are worse when the concentration of excited ions is more dense. So under low pump intensities, the effect of ETU will be very small but under high pump intensities it may be very detrimental. In the literature, fluorescence lifetime measurements have been taken for 1 and 2 atm % Nd:YVO_4 under low pump intensities [9] which would render the effects of ETU negligible. However, even in the absence of ETU, the lifetimes measured drop from 97 µs for 1 atm % to 63 µs for 2 atm %. Similar values are given in other papers [10]–[12] so it was assumed that they are also carried out under low pump intensities, although this was not explicitly stated. The fluorescence lifetimes vary with respect to doping concentration in these cases because of other quenching effects, such as cross-relaxation [5], and not ETU.

Without the effects of ETU, the model accounts for these other quenching effects by using a fluorescence lifetime based on the empirical measurements for a given doping concentration. However, to add the effects of ETU, the total small-signal gain must be reassessed. As ETU reduces the upper-state population, Equation 2.4, which describes the rate of change of the upper-state population, now becomes [13],

$$\frac{dn_{2,ETU}}{dt} = R(r,z) - \frac{n_{2,ETU}(r,z)\sigma_{21}I_l(z)}{h\nu_l} - \frac{n_{2,ETU}(r,z)}{\tau} - Wn_{2,ETU}^2 \quad \text{Equation 2.36}$$

where W is the upconversion parameter. The $Wn_{2,ETU}^2$ term describes the rate of reduction in the upper-state population due to ETU and is proportional to the square of the upper-state population. Assuming continuous wave pump and signal beams, the rate of change in the population can be set to zero and the equation for the upper-state population becomes,

$$n_{2,ETU}(r,z) = \frac{-\left(1+\frac{I_l(z)}{I_{sat}}\right)+\sqrt{\left(1+\frac{I_l(z)}{I_{sat}}\right)^2+4R(r,z)W\tau^2}}{2W\tau} \quad \text{Equation 2.37}$$

For the small-signal regime, assuming negligible depletion of the upper-state by the signal beam, the equation for the upper-state population is simplified by setting I_l to zero and becomes [14],

$$n_{2,ETU}(r,z) = \frac{-1+\sqrt{1+4R(r,z)W\tau^2}}{2W\tau} \quad \text{Equation 2.38}$$

The pump rate per unit volume for a top-hat pump beam can be expressed as,

$$R(r,z) = \frac{\alpha_p P_p}{h\nu_p \pi\omega_p^2} e^{-\alpha_p z} \ \ where\ r \leq \omega_p \quad \text{Equation 2.39}$$

$$R(r,z) = 0 \ \ where\ r \geq \omega_p \quad \text{Equation 2.40}$$

Substituting Equation 2.39 into Equation 2.38 and then also using Equation 2.3, the small-signal gain coefficient when ETU is considered is [8],

$$g_{o,ETU}(r,z) = \frac{\sigma_{21}}{2W\tau}\left(-1+\sqrt{1+4\left(\frac{\alpha_p P_p}{h\nu_p\pi\omega_p^2}e^{-\alpha_p z}\right)W\tau^2}\right) \quad \text{Equation 2.41}$$

The effective small-signal gain coefficient with ETU can be calculated with the same method used previously using Equation 2.22. $g_{eff,ETU}$ then becomes,

$$\boldsymbol{g_{eff,ETU}(z) = \frac{\sigma_{21}}{2W\tau}\left(-1 + \sqrt{1 + \frac{4\alpha_p P_p W\tau^2}{h\nu_p \pi\omega_p^2} e^{-\alpha_p z}}\right)\left(1 - exp\left(\frac{-2\omega_p^2}{\omega_l^2}\right)\right)} \quad \text{Equation 2.42}$$

$g_{eff,ETU}(z)$ can then be integrated over the length of the gain medium to find the total small-signal gain with ETU, $G_{0,ETU} = \exp(g_{eff,ETU} l)$,

$$\boldsymbol{lnG_{o,ETU} = \frac{\sigma_{21}}{2W\tau}\left[1 - exp\left(\frac{-2\omega_p^2}{\omega_l^2}\right)\right]\left[-\int_0^l dz + \int_0^l \sqrt{1 + \frac{4\alpha_p P_p W\tau^2}{h\nu_p \pi\omega_p^2} exp(-\alpha_p z)}\, dz\right]} \quad \text{Equation 2.43}$$

Following the same method as Yarrow [15], where the integral can be simplified by letting,

$$\boldsymbol{\kappa = \frac{4\alpha_p P_p W\tau^2}{h\nu_p \pi\omega_p^2}} \quad \text{Equation 2.44}$$

The total small-signal gain with ETU finally becomes,

$$\boldsymbol{lnG_{o,ETU} = \frac{\sigma_{21}}{2W\tau}\left(1 - exp\left(\frac{-2\omega_p^2}{\omega_l^2}\right)\right)\left\{-l + \frac{-2}{\alpha_p}\left[\sqrt{\kappa exp(-\alpha_p l) + 1} - \sqrt{\kappa + 1} + ln\left(\frac{1+\sqrt{\kappa+1}}{\sqrt{\kappa}}\right) - ln\left(\frac{1+\sqrt{\kappa exp(-\alpha_p l)+1}}{\sqrt{\kappa exp(-\alpha_p l)}}\right)\right]\right\}} \quad \text{Equation 2.45}$$

The total small-signal gain with ETU, $G_{0,ETU}$, then replaces the total small-signal gain, G_0, in Equation 2.35 to calculate the output power for a given set of amplifier parameters.

In this case, because only the total small-signal gain has been altered to account for ETU, the model does not take into account the variation in ETU when large signal intensities significantly reduce the upper-state population. For the model to accurately simulate the amplifier in the saturated regime, the steps taken in section 2.2.3 would have to be repeated but with the much more complex expression for the total small-signal gain. Therefore, the model with ETU should

accurately simulate the empirical data for low seed intensities and gradually diverge from the empirical data as the seed intensity grows larger. In the saturated regime, the model without ETU should better match the empirical data because, in the saturated regime, the upper-state population has been reduced and is smaller than in the small-signal regime. As ETU is proportional to the square of the population inversion, the effects of ETU will be reduced.

2.3 Low power experiments

The experiments performed in this chapter were deliberately simplified, compared to the setup that would be used to try and achieve more significant amplification of the seed laser. This low complexity experimental setup was used to test the model in the regime that it was most applicable to, which in this case was at relatively low pump powers, about 10 W absorbed pump power, with Nd:YVO_4 rods. Low pump powers were used in order to minimise the deleterious effects of large increases in temperature as the high power regime will be discussed in the next chapter. A rod architecture was chosen so that the pump and seed beams could pass straight through the gain material without being reflected back again as this would entail altering the model to consider multi-pass amplification which will, again, be considered in the next chapter. The results from these simplified experiments were used to confirm the efficacy of the model in the low power regime which provided a baseline that would help in understanding deviations from the basic amplifier physics caused by higher temperatures and multi-passing of the seed beam.

In order to provide a comparison with the experimental results, data was extracted from three variations of the model: a Gaussian pump beam with no ETU, a top-hat pump beam with no ETU and a top-hat pump beam with the effects of ETU included. These three variations of the model will be referred to as the Gaussian, top-hat and ETU models respectively. As will be discussed in Chapter 3, the effect of temperature on a Nd:YVO_4 amplifier is significant at higher pump powers, where multiple tens of Watts are absorbed. However, the experiments discussed in the

following sections were deliberately conducted in a regime where such effects were not significant, although they can begin to be seen. The experiments were conducted with a wide range of input seed intensities to enable the small-signal gain and the highly saturated regimes to be reached.

2.3.1 Experimental setup

Two Nd:YVO_4 rods were used, one with 1 atm % of Nd^{3+} and the other 0.5 atm %. Both rods were a-cut with dimensions of 3 x 3 x 5 mm, where the 5 mm dimension was the length along the direction of propagation. The rods were anti-reflection (AR) coated on both facets for 808 nm and 1064 nm.

The rods were mounted in an aluminium block which was actively cooled with chilled water. A sheet of 250 µm thick indium foil lay between the cooled aluminium block and the rod to improve the thermal contact. The gain medium was pumped using a diode laser, with a maximum output power of 10 W, coupled into a 100 µm core-diameter multimode fibre and operating at a wavelength of 808 nm. The incident pump power was varied by changing the current supplied to the diode pump laser. The diode laser was not temperature tuned as the current was varied and so the central wavelength of the pump light also varied as the current changed. This would alter the absorption of the pump light within the gain medium but, by how much, was not measured. The absorbed pump power was calculated for each data point by subtracting the measured transmitted pump power from the incident pump power.

The experimental setup, shown in Figure 2.6, began with the pump beam, which was collimated using a 50 mm focal length, plano-convex lens then focused using another plano-convex lens. Two different focal length lenses were used to focus the pump beam in order to achieve different pump spot sizes within the gain medium, and both the collimating and focussing lenses were AR coated at the pump wavelength. The first pump focussing lens was a 100 mm focal length lens which produced a measured pump beam radius of 160 µm. The second pump spot radius

was measured to be 420 µm created with a 300 mm focal length lens. After the pump focusing lens, the pump beam passed through a flat, dichroic mirror, transparent for the pump wavelength and reflective for the seed wavelength. This dichroic mirror was used to direct the seed beam into the gain medium. The unabsorbed pump light that passed through the gain medium then passed through another, identical dichroic mirror to separate the pump and seed beams. The residual pump beam was then collected and measured on a Thorlabs S322C thermal power sensor, so that the absorbed pump light could be calculated.

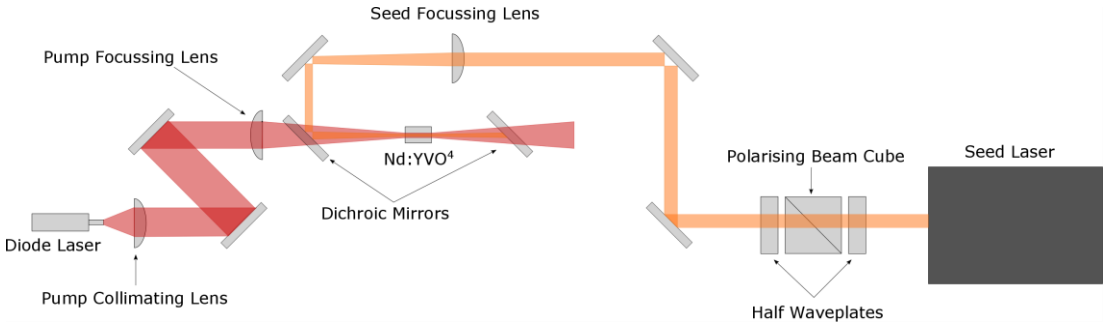

Figure 2.6 – A diagram of the experimental setup for the Nd:YVO_4 rod amplifier experiment.

The seed beam source was the mode-locked picosecond laser discussed in Chapter 1, emitting a collimated beam of linearly polarised light at a wavelength of 1064 nm with an M^2 value of 1.3. The pulses were less than 15 ps long at a repetition rate of 1 MHz. The seed beam was passed through a half-wave plate and a polarising beam splitter cube to attenuate the power. It was then passed through another half-wave plate to allow the polarisation to be adjusted so it was parallel with the c-axis of the Nd:YVO_4 gain medium in order to achieve the highest gain in the amplifier. The seed beam was then focused using a plano-convex lens and, like the pump, two different spot sizes were obtained. A 300 mm focal length lens was used to obtain a measured beam radius of 110 µm and a 750 mm focal length lens for a measured beam radius of 330 µm. Both lenses were AR coated at the seed wavelength. The seed beam was steered into the gain medium by the first dichroic

mirror that the pump beam passes through. The amplified seed beam was then reflected using a second dichroic mirror to separate it from the unabsorbed pump beam. The amplified seed power is then measured using a power meter. A wide range of output seed values were expected in this experiment so two different power meters were used to measure the seed output. For powers up to 500 mW the Thorlabs S121C standard photodiode power sensor was used which is a silicon photodetector. For powers greater than 500 mW, the Thorlabs S310C thermal power sensor was used.

The seed beam radii were chosen to provide a range of intensities around the saturation intensity. The smallest seed beam radii, with the lowest average seed power, provided a seed beam intensity that was 0.01 times the saturation intensity for 0.5 atm % Nd:YVO_4. The largest seed beam radii, with the highest average seed power, provided a seed beam intensity that was 54 times the saturation intensity for 0.5 atm Nd:YVO_4.

2.3.2 Model parameters

The experimental data from these experiments was compared with the results of the model constructed using the theory outlined in section 2.2. Three variations of the model were used; with Gaussian pump profile, with a top-hat pump profile and a top-hat pump profile but also including ETU. To obtain data from the models, values had to be attributed to the parameters used.

For the pump and seed wavelengths, 808 and 1064 nm were used respectively. The values for absorbed pump power that were measured in the experiments described above were used for the Gaussian and top-hat models. For the ETU model, the same absorbed pump power was used to infer the absorption coefficient. Since the diode pump laser was not temperature tuned as the current was varied, the wavelength of the pump light also varied with current. This meant that the absorption coefficient was different for each data point, sometimes by as much as 12 %. For simplicity, a single value for the absorption coefficient was used for each

doping concentration with the top-hat, ETU model. Values of 44 and 58 cm^{-1} were used for the 0.5 atm % and 1 atm %, respectively, as these were the median values measured for each doping concentration.

For the stimulated-emission cross-section of the c-axis of Nd:YVO_4, many papers use the value of $14.4x10^{-19}$ cm^{-2} [10]; however, the value of $12x10^{-19}$ cm^{-2} [4] was found to give results closer to the empirical data. The fluorescence lifetime varied between the two different crystal doping concentrations. For 1 atm % Nd:YVO_4, the value given by Blows et al. [9] of $97\ \mu s$ was used as they stated that this value was found under low pump intensities. A specific value for 0.5 atm % Nd:YVO_4 was not found in the literature but values of $110\ \mu s$ [16] and $105\ \mu s$ [12] were found for 0.4 atm % and 0.58 atm % respectively. Along with other lifetimes found for various doping concentrations [10], these fluorescence lifetimes were plotted against doping concentration and a straight line was fitted to the data, as shown in Figure 2.7. This fit was used to estimate a fluorescence lifetime of $108\ \mu s$ for 0.5 atm % Nd:YVO_4.

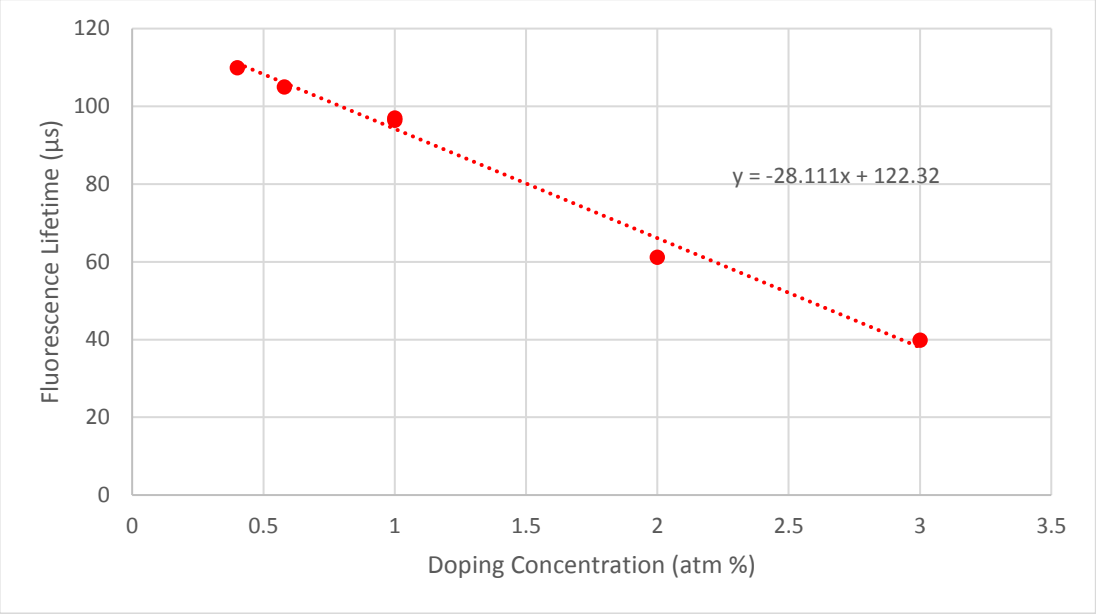

Figure 2.7 – The fluorescence lifetimes of Nd:YVO_4 is plotted against doping concentration and a linear line of best fit is applied to the data. The fluorescence lifetime varies with doping concentration and the fluorescence lifetime of 0.5 atm % Nd:YVO4 is calculated using the linear fit in this graph. The data points in the graph were from various sources [9], [10], [12], [16].

2.4 Results

In order to obtain data from the small-signal to the highly saturated regime, two different spot sizes were used, as described in section 2.3.1, with input seed powers ranging from 50 mW to 30 W in both cases. With these values, the input seed intensities ranged from 1.46×10^5 W/m^2, 0.01 times the saturation intensity for 0.5 atm % Nd:YVO_4, to 7.89×10^8 W/m^2, fifty four times the saturation intensity. Figure 2.8 and Figure 2.9 contain a selection of the power transfers taken over the range of input powers.

Figure 2.8 shows power transfers for the smaller pump and seed radii with a pump beam radius of 160 µm and a seed beam radius of 110 µm. The power transfers in Figure 2.9 are with larger spot sizes, with pump and seed beam radii of 420 µm and 330 µm respectively. In Figure 2.8, plots a), b) and c), the power transfers are taken with 0.5 atm % Nd:YVO_4 as the gain medium. Figure 2.8, plots d), e) and f) are with a 1 atm % Nd:YVO_4 crystal. The same is also true for Figure 2.9, where plots a) and b) are power transfers for 0.5 atm % Nd:YVO_4 and plots c) and d) are power transfers for 1 atm % Nd:YVO_4. The rationale behind using two different doping concentrations for the Nd:YVO_4 gain medium was to illustrate the effects of energy transfer up-conversion which should be more pronounced for the 1 atm % doping concentration compared to the 0.5 atm % doping concentration.

For Figure 2.8, the top two plots, a) and d), have an input seed power of 50 mW. The two plots in the second row, b) and e), have an input seed power of 5 W and the two bottom plots, c) and f), have an input seed power of 30 W. For Figure 2.9, the top two plots, a) and c), have an input seed power of 50 mW and the bottom two plots, b) and d), have an input seed power of 30 W. The change in input seed power serves to illustrate the transition from the small-signal gain regime, at lower input seed powers, to the saturated regime, at higher input seed powers. Each graph contains the empirical data (blue dots) taken from the experiments described in Section 2.3.1 along with the data from the Gaussian (orange line), top-hat (purple line) and ETU (blue line) models.

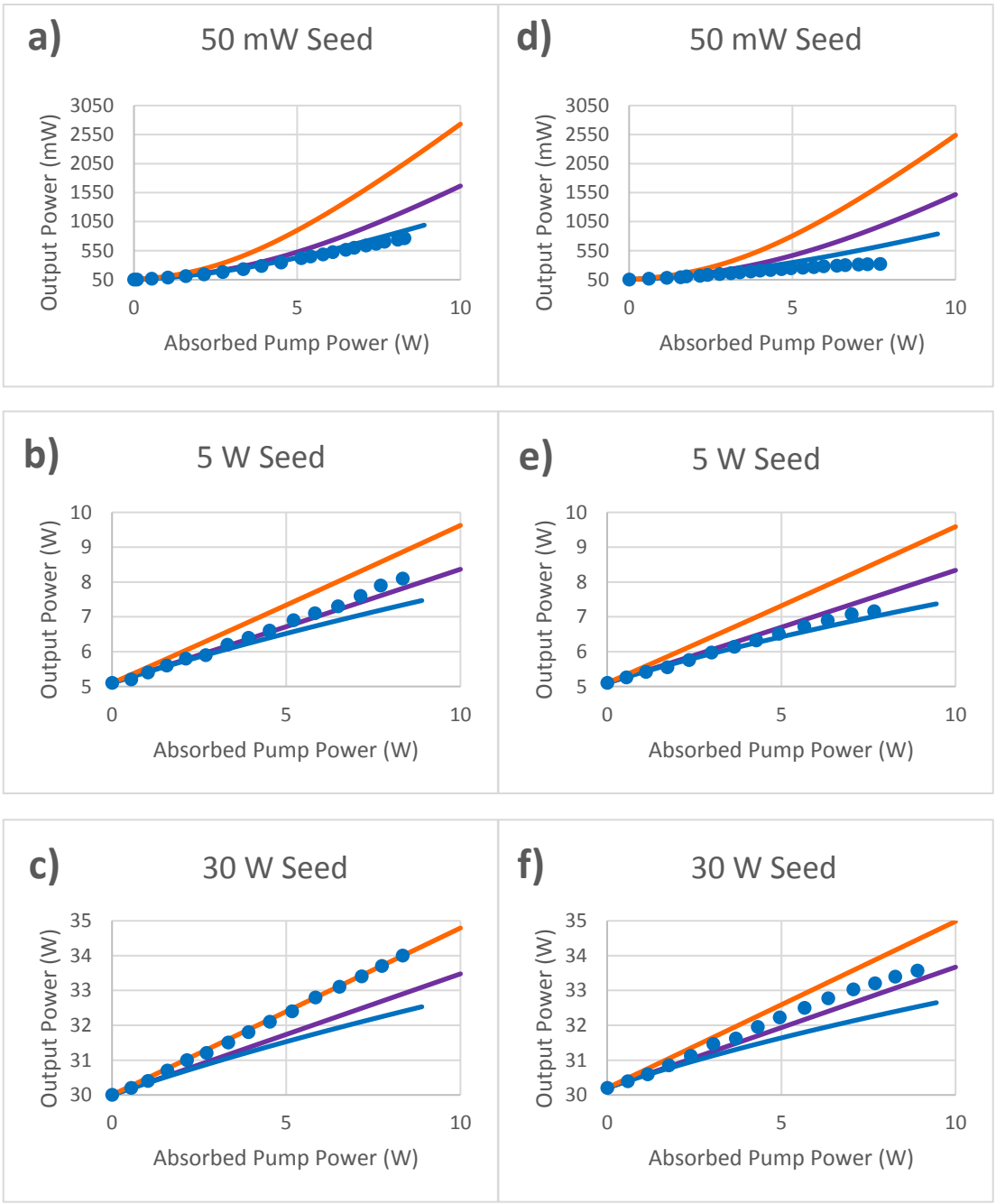

Figure 2.8 – All the plots in this figure show power transfers where the pump radius is 160 µm and the seed radius is 110 µm. Plots a), b) and c) are for a gain medium of 0.5 atm % Nd:YVO_4 and plots d), e) and f) are for a gain medium of 1 atm % Nd:YVO_4. In each plot the blue dots represent the empirical data taken from the experiments described in section 2.3.1, the orange line is the modelled data for a Gaussian pump beam, the purple line is the modelled data for a top-hat pump beam and the blue line is the modelled data for a top-hat pump beam with the effects of ETU included.

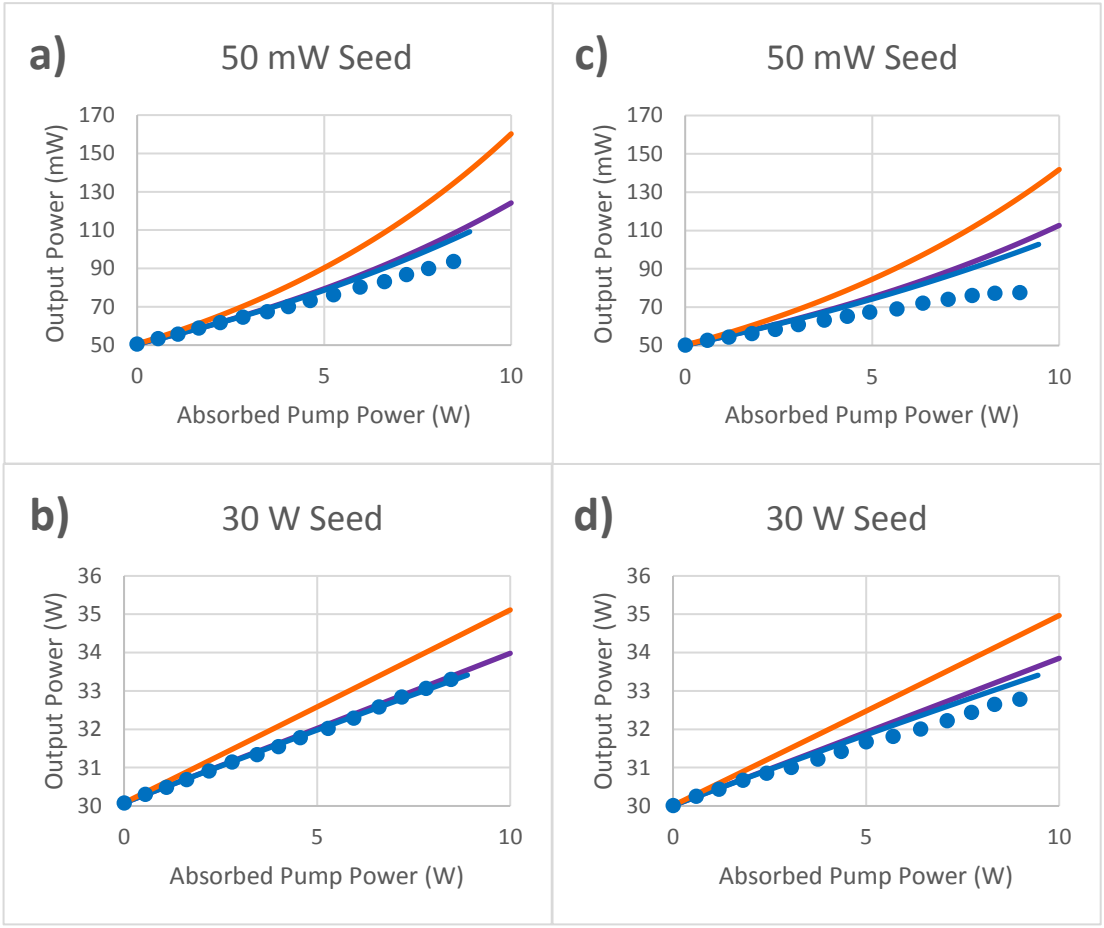

Figure 2.9 - All the plots in this figure show power transfers where the pump radius is 420 µm and the seed radius is 330 µm. Plots a) and b) are for a gain medium of 0.5 atm % Nd:YVO_4 and plots c) and d) are for a gain medium of 1 atm % Nd:YVO_4. In each plot the blue dots represent the empirical data taken from the experiments described in section 2.3.1, the orange line is the modelled data for a Gaussian pump beam, the purple line is the modelled data for a top-hat pump beam and the blue line is the modelled data for a top-hat pump beam with the effects of ETU included.

2.4.1 Saturation

As many simplifying assumptions are made in the models, no one set of modelled data should fit the empirical data across all the different regimes. The pump beam is neither a Gaussian nor a top-hat shape, but somewhere between the two and is also assumed to be free from diffraction within the gain medium; however, there is

some divergence of the beam within the crystal. For the smaller beam size, the pump radius was 138 µm at its smallest and 190 µm at its largest, across the length of the rod. For the larger beam size, the pump radius was 390 µm at its smallest and 440 µm at its largest. The model that takes into account the effects of ETU does not consider the depopulation of the upper laser level by the seed beam and so it is expected that at low seed input intensities, the ETU model should be the closest to the empirical data. At the high seed input intensity, the empirical data should be somewhere between the top-hat and Gaussian models.

Indeed, where the input seed power is lowest, in Figure 2.8, plots a) and d), and in Figure 2.9, plots a) and c), the ETU model (in blue) best matches the empirical data. The relevant plots have been shown again in Figure 2.10 below. The match is especially good for the 0.5 atm % gain material for both the small and large spot sizes, in Figure 2.10. In the 1 atm % case, for both the small and large spot sizes in Figure 2.10, the agreement between the data and the ETU model is worse at higher absorbed pump powers. This is true for all the 1 atm % plots [Figure 2.8, plots d), e) and f), and Figure 2.9, plots c) and d)] as they all exhibit a slight rollover in output power. This is due to adverse effects that are present at higher temperatures but that are not accounted for in the simple models. They can only be seen in the 1 atm % data because the peak temperatures reached are higher than in the 0.5 atm % case due to the higher absorption coefficient. The absorbed power is more concentrated at the front of the 1 atm % crystal and so the temperature rise is higher. In the 0.5 atm % crystal the absorbed power is more evenly spread along the length of the crystal. The heating is also made worse still in the 1 atm % case as the ETU leads to greater heating per unit of absorbed pump power.

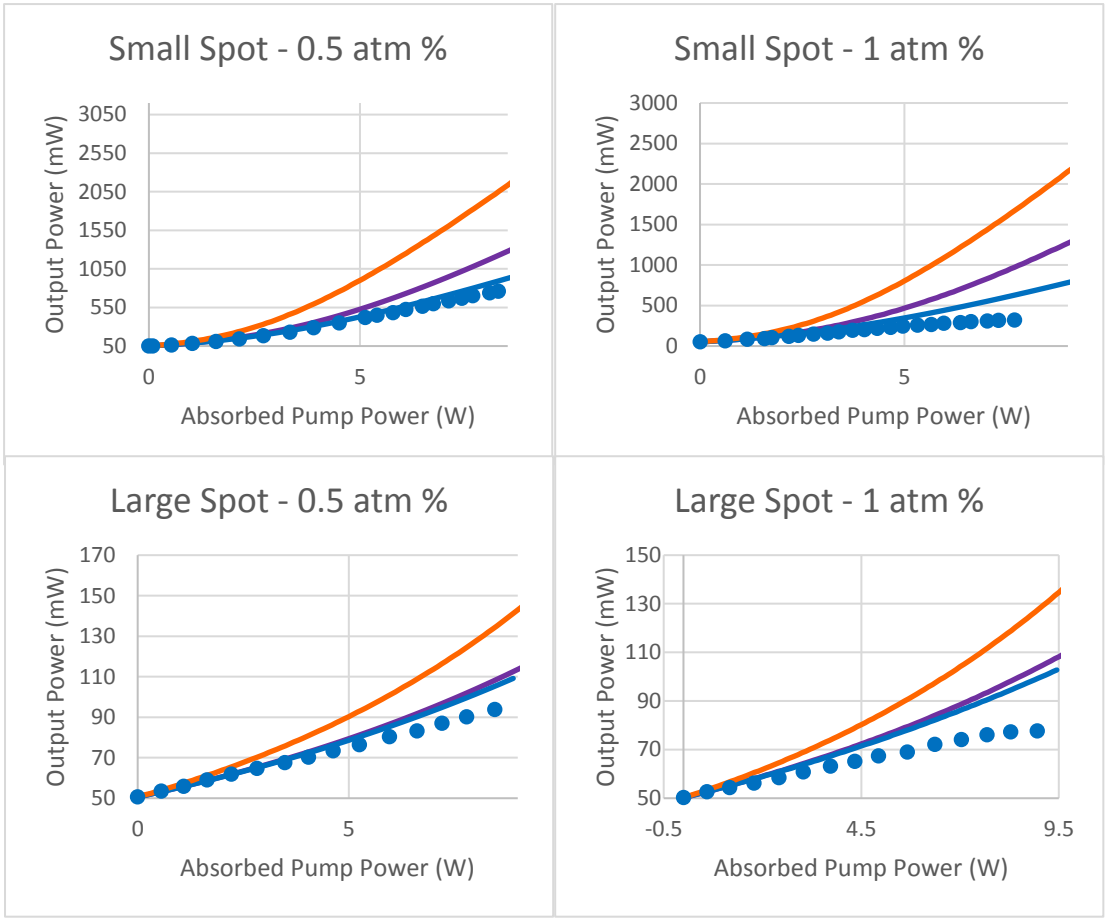

Figure 2.10 – In each power transfer, the input seed power is 50 mW. The small spot sizes are presented in the top two graphs for 0.5 atm % and 1 atm % Nd:YVO_4, with the same doping concentrations presented in the bottom two graphs but for the larger spot sizes. The blue dots represent the empirical data taken from the experiments described in Section 2.3.1, the orange line is the modelled data for a Gaussian pump beam, the purple line is the modelled data for a top-hat pump beam and the blue line is the modelled data for a top-hat pump beam with the effects of ETU included. These plots illustrate that at low seed intensities, the top-hat pump model that includes the effects of ETU best matches the empirical data.

The power transfers with the intermediate input seed power of 5 W are shown in Figure 2.8, plots b) and e), and are replicated in Figure 2.11 below. For the smaller seed beam radius, 5 W of input seed power corresponds to an input intensity that is greater than the saturation intensity. The saturation intensity differs slightly

between the 0.5 atm % and 1 atm % Nd:YVO_4 as the fluorescence lifetime is different. The saturation intensity is lower for the 0.5 atm % Nd:YVO_4 so for the same input intensity, the 0.5 atm % Nd:YVO_4 should be more saturated than the 1 atm % Nd:YVO_4. This can be seen when comparing the two plots for both doping concentrations in Figure 2.11. In the 0.5 atm % plot, on the left in Figure 2.11, the empirical data closely matches the top-hat model whereas in the 1 atm % plot, on the right in Figure 2.11, the empirical data still lies between the top-hat and ETU models.

It should be expected that as the input seed intensity is increased, the empirical data should move from closely matching the ETU data, to lying somewhere between the Gaussian and top-hat models and this is what is observed when comparing the graphs from Figure 2.10 and Figure 2.11. The empirical data in the graphs in Figure 2.10, where the input seed intensity was lower, most closely matched the ETU model. The graphs in Figure 2.11, where the input seed intensity had been increased compared to Figure 2.10, moved away from the ETU model and closer to the top-hat and Gaussian models. The two graphs in Figure 2.11 have the same input seed intensity, but the 0.5 atm % gain medium has a lower saturation intensity compared to the 1 atm % crystal and so it would be expected that the empirical data for the 0.5 atm % graph has a steeper gradient than the 1 atm % graph. This is what is observed in Figure 2.11 where the 0.5 atm % empirical data lies between the Gaussian and top-hat models and the 1 atm % empirical data is between the top-hat model and the ETU model.

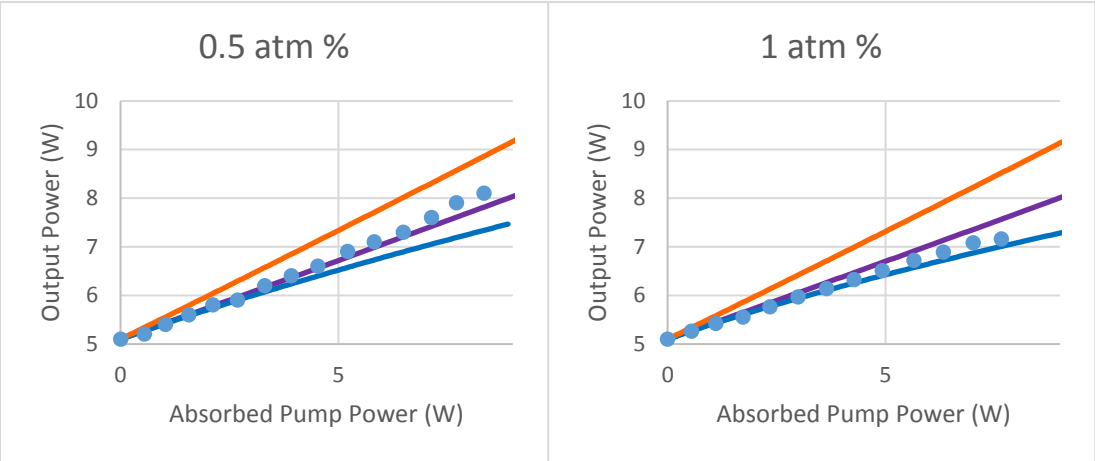

Figure 2.11 - In each power transfer the input seed power is 5 W and for both graphs the small spot sizes are used. The graph on the left is for 0.5 atm % Nd:YVO_4 and the graph on the right for 1 atm % Nd:YVO_4. The blue dots represent the empirical data taken from the experiments described in Section 2.3.1, the orange line is the modelled data for a Gaussian pump beam, the purple line is the modelled data for a top-hat pump beam and the blue line is the modelled data for a top-hat pump beam with the effects of ETU included.

At the highest input seed power of 30 W [show in Figure 2.8, c) and f), and Figure 2.9, b) and d), and replicated in Figure 2.12 below] the empirical data mostly matches the top-hat or Gaussian model or is somewhere in between. The 1 atm % Nd:YVO_4 with the small beam radii, shown in Figure 2.12 in the top right graph, lay between the Gaussian and top-hat models. For the larger beam radii, both the 0.5 atm % and 1 atm % Nd:YVO_4 empirical data agreed well with the top-hat model with the exception of the rollover in the 1 atm % case.

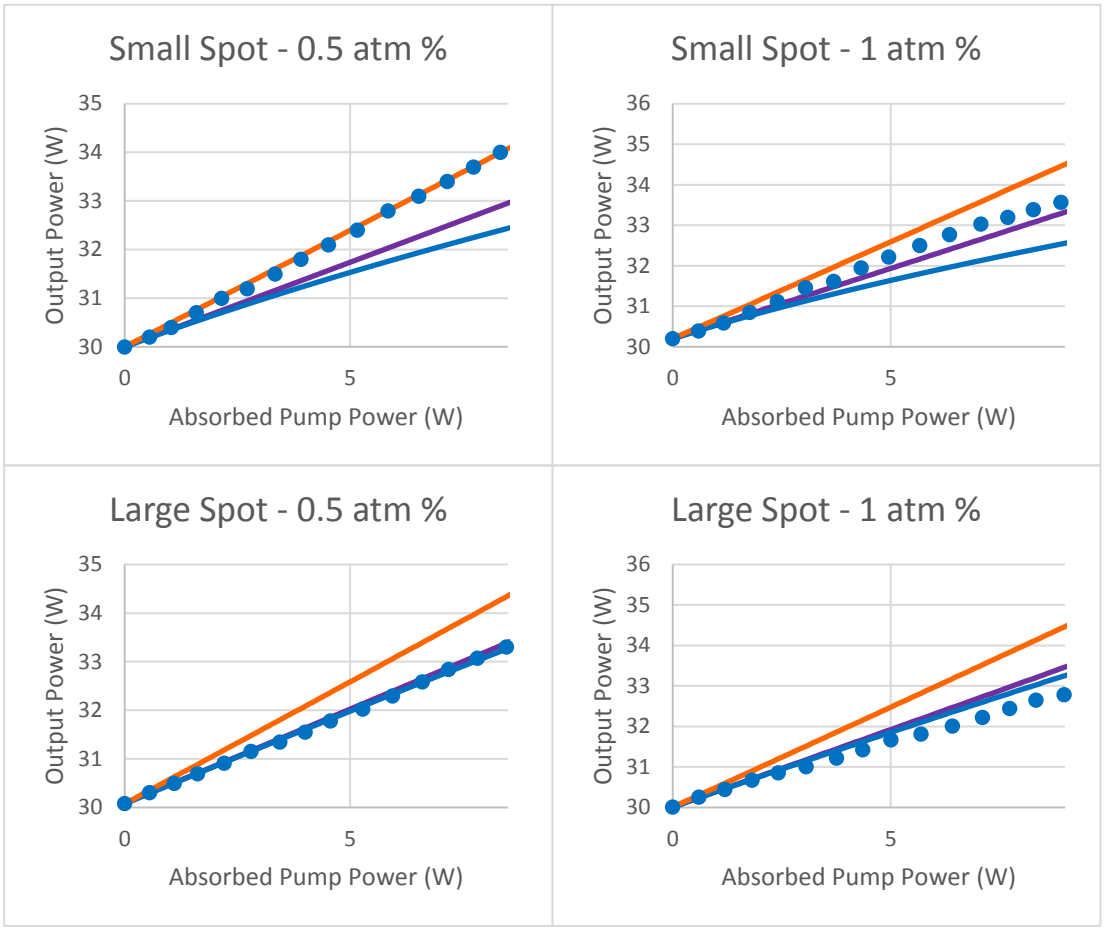

Figure 2.12 - In each power transfer the input seed power is 30 W. The small spot sizes used were 160 µm for the pump radius and 110 µm for the seed radius (top graphs). The large spot sizes 420 µm for the pump radius and 330 µm for the seed radius (bottom graphs). The graphs on the left display the power transfers for 0.5 atm % Nd:YVO_4 and the graphs on the right for 1 atm % Nd:YVO_4. The blue dots represent the empirical data taken from the experiments described in Section 2.3.1, the orange line is the modelled data for a Gaussian pump beam, the purple line is the modelled data for a top-hat pump beam and the blue line is the modelled data for a top-hat pump beam with the effects of ETU included.

2.4.2 Energy transfer up-conversion

The effects of ETU should be greatest for the smaller pump beam radius with the 1 atm % $Nd:YVO_4$, as the density of ions in the upper laser level will be highest in this regime, whilst the larger pump radius with the 0.5 atm % $Nd:YVO_4$ will be the least affected by ETU. This can be seen by comparing the difference between the top-hat and ETU models in Figure 2.8 (all graphs), which has the smaller pump radius, with those in Figure 2.9 (all graphs), which has the larger pump radius. This is also evident in Figure 2.13, below, which shows the top-hat (blue line) and ETU (red line) models for an input seed power of 50 mW. The graph on the left of Figure 2.13 is for a small pump radius (160 µm) with 1 atm % $Nd:YVO_4$ and the graph on the right is for a pump radius of 420 µm with 0.5 atm %. The two models are much more closely aligned for the larger spot with the lower doping concentration than the smaller spot with the larger doping concentration.

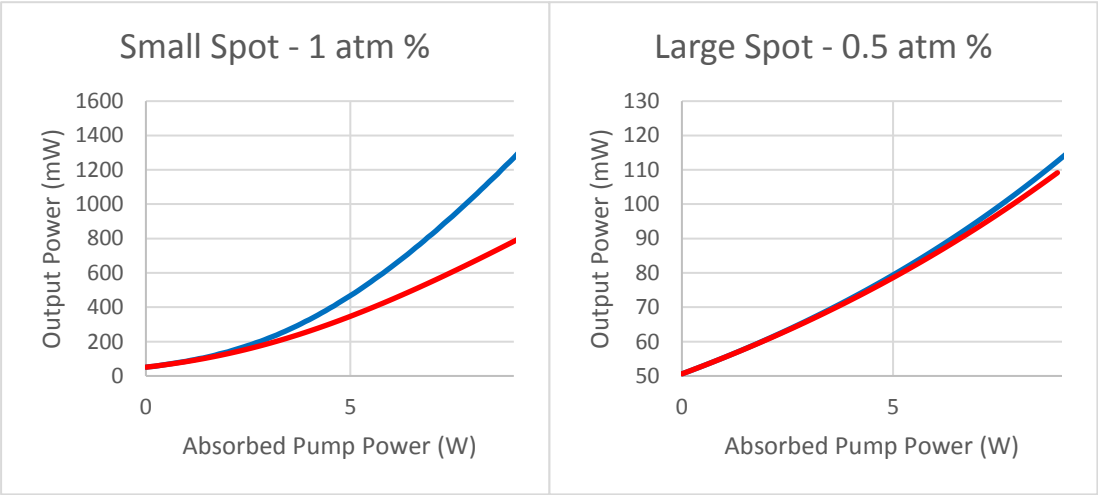

Figure 2.13 – all the plots on both graphs are for an input seed power of 50 mW. The top-hat model is represented by the blue line and the ETU model is represented by the red line. The graph on the left has the smaller pump radius and a doping concentration of 1 atm %. The graph on the right has the larger pump radius and a doping concentration of 0.5 atm %.

It is also expected that the 0.5 atm % $Nd:YVO_4$ should outperform the 1 atm % $Nd:YVO_4$ as it has a greater fluorescence lifetime and in the low saturation regime, the effects of ETU are not as deleterious. The difference in performance between the 0.5 atm % and 1 atm % is more pronounced for lower input seed intensity and this can be seen in Figure 2.14 which compares two power transfers, one for a doping concentration of 0.5 atm % (blue dots) and the other for a doping concentration of 1 atm % (red dots). The input seed power for both power transfers is 100 mW and the pump and seed radii are 160 µm and 110 µm, respectively. From Figure 2.14, it can be clearly seen that the 0.5 atm % $Nd:YVO_4$ outperforms the 1 atm % $Nd:YVO_4$. The graph also shows a rollover in output power for the 1 atm % data. This rollover effect has a significant impact on amplifier performance and will be discussed in great detail in Chapter 3.

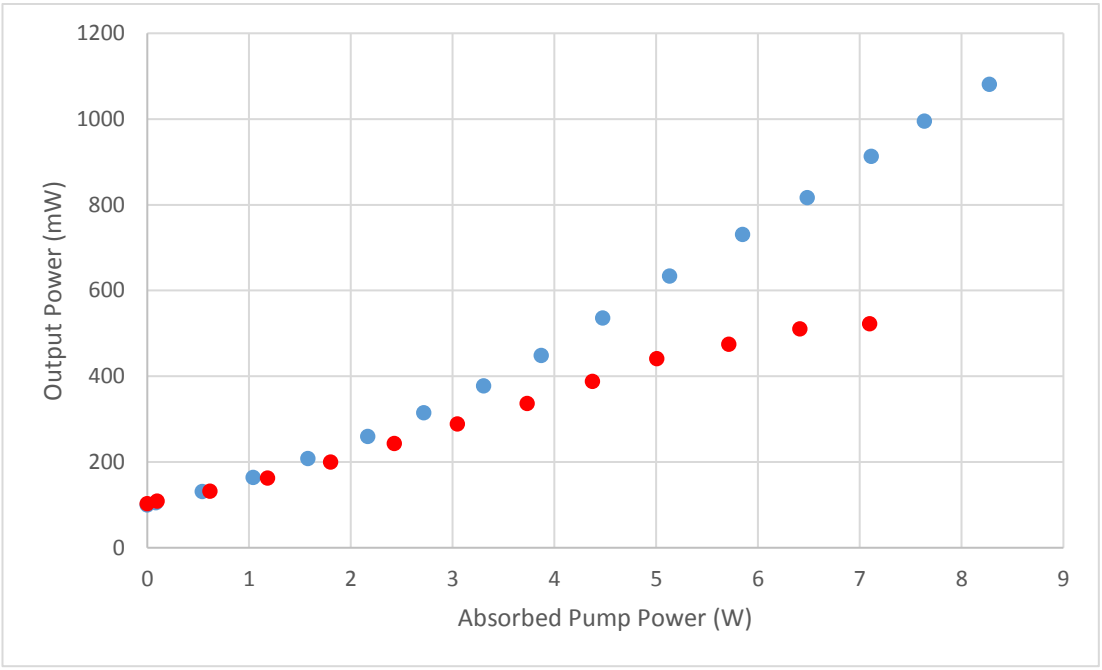

Figure 2.14 – Two power transfers, both with an input seed power of 100 mW, a pump beam radius of 160 µm and a seed beam radius of 110 µm. The blue dots are for a doping concentration of 0.5 atm % and the red dots for a doping concentration of 1 atm %. The rollover behaviour exhibited in the 1 atm % data is very important and will be discussed in great detail in the next chapter.

2.5 Conclusions

The theory behind laser amplifier gain was explored from the small-signal gain to the highly saturated regime. The importance of pump beam profile was explored and the data from the low pump power rod experiments showed that, in reality, the output from a fibre-coupled diode pump laser cannot be accurately described by either a Gaussian or a top-hat beam shape.

The effects of energy transfer up-conversion were added to the model but only accurately described the behaviour in the low saturation regime, as was expected as increasing saturation of the amplifier gain reduces the effects of ETU, but this was not accounted for in the model. The low power experiments served to confirm the understanding of the laser amplifier performance in the absence of significant thermal effects and provided a baseline from which to understand the thermal effects to be discussed in Chapter 3.

The limitations of the variations of the models presented, which result from the simplifying assumptions made, were also explored and better understood. Some of the negative effects of temperature were already becoming apparent with the 1 atm % Nd:YVO_4 due to the higher absorption coefficient, and these will be discussed in detail in the next chapter as these temperature effects severely limit the use of Nd:YVO_4 in the high power regime.

2.6 References

[1] O. Svelto, *Principles of Lasers*, Fifth. Springer, 2009.

[2] W. Koechner and M. Bass, *Solid-State Lasers*. 2003.

[3] A. E. Siegman, *Lasers*. University Science Books, 1986.

[4] A. W. Tucker, M. Birnbaum, C. L. Fincher, and J. W. Erler, “Stimulated-emission cross section at 1064 and 1342 nm in Nd:YVO4,” *J. Appl. Phys.*, vol. 48, no. 12, pp. 4907–4911, 1977.

[5] X. Délen *et al.*, "Characteristics of laser operation at 1064 nm in Nd : YVO4 under diode pumping at 808 and 914 nm," *J. Opt. Soc. Am. B*, vol. Vol. 28, no. 1, pp. 52–57, 2012.

[6] L. Fornasiero, S. Kück, T. Jensen, G. Huber, and B. H. T. Chai, "Excited state absorption and stimulated emission of Nd3+in crystals. Part 2: YVO4, GdVO4, and Sr5(PO4)3F," *Appl. Phys. B Lasers Opt.*, vol. 67, no. 5, pp. 549–553, 1998.

[7] J. W. Kim, J. K. Sahu, and W. A. Clarkson, "Impact of energy-transfer-upconversion on the performance of hybrid Er:YAG lasers," *Solid State Lasers XVII Technol. Devices*, vol. 6871, p. 68710W, 2008.

[8] I. O. Musgrave, "Study of the Physics of the Power-Scaling of End-Pumped Solid-State Laser Sources Based on Nd:YVO4," 2003.

[9] J. L. Blows, T. Omatsu, J. Dawes, H. Pask, and M. Tateda, "Heat generation in Nd:YVO4 with and without laser action," *IEEE Photonics Technol. Lett.*, vol. 10, no. 12, pp. 1727–1729, 1998.

[10] Y. Sato and T. Taira, "Spectroscopic properties of neodymium-doped yttrium orthovanadate single crystals with high-resolution measurement," *Japanese J. Appl. Physics, Part 1 Regul. Pap. Short Notes Rev. Pap.*, vol. 41, no. 10, pp. 5999–6002, Oct. 2002.

[11] J. G. Sliney, K. M. Leung, M. Birnbaum, and a. W. Tucker, "Lifetimes of the 4F3/2 state in Nd:YVO4," *J. Appl. Phys.*, vol. 50, no. 5, p. 3778, 1979.

[12] O. Guillot-Noël, B. Viana, B. Bellamy, D. Gourier, G. B. Zogo-Mboulou, and S. Jandl, "Spectroscopic evidence of inhomogeneous distribution of Nd3+in YVO4, YPO4and YAsO4crystals," *Opt. Mater. (Amst).*, vol. 13, no. 4, pp. 427–437, 2000.

[13] S. Cante, S. J. Beecher, and J. I. Mackenzie, "Characterising energy transfer upconversion in Nd: YVO4 at elevated temperatures," *Opt. InfoBase Conf. Pap.*, vol. Part F75-A, no. 6, pp. 11935–11943, 2017.

[14] Ş. A. Amarande, “Influence of energy transfer upconversion on thermal lens of Nd:YVO_4 bounce laser amplifier,” *J. Opt. Soc. Am. B*, vol. 29, no. 8, p. 2138, 2012.

[15] M. J. Yarrow, “Power Scaling of Laser Oscillators and Amplifiers Based on Nd:YVO4,” 2006.

[16] T. S. Lomheim and L. G. DeShazer, “Optical-absorption intensities of trivalent neodymium in the uniaxial crystal yttrium orthovanadate,” *J. Appl. Phys.*, vol. 49, no. 11, pp. 5517–5522, 1978.

Chapter Three

Development and Experimental Testing of a Model for Low-Complexity Thin-Disk Amplifiers

---

3.1 Introduction

In the previous chapter, a model of a Nd:YVO_4 laser amplifier was constructed and the results compared with the data taken from Nd:YVO_4 rod amplifier experiments. These experiments were performed at relatively low pump intensities, never exceeding 10 W of absorbed pump power with a minimum pump radius of 160 µm, providing a maximum pump intensity of 1.24×10^8 W/m^2. This was to establish the efficacy of the model in the absence of any deleterious thermal effects and to provide a baseline to explore if there were any deviations from this performance for higher thermal loads. In this chapter, the experiments performed move to higher absorbed pump powers, of multiple 10s of Watts, in order to achieve significant amplification of the seed beam. The gain material geometry is also changed from a rod to a thin-disk for improved thermal management.

This chapter will first explore the alterations made to the amplifier model in order to incorporate a double-pass of both the pump and seed beams that are brought about by the thin-disk geometry. The deleterious effects of increased temperatures within the gain material will then be examined and incorporated into the model before moving onto attempts at mitigating this increase in temperature, involving the use of heat-spreaders and improving extraction efficiency by using a seed laser with a greater input seed power and exploring multiple passes of the seed beam. A method of measuring the temperature rise within the gain material will also be explored, where the wavelength shift of the fluorescence spectrum that occurs

when the temperature is varied is measured. Temperature rises within the crystal were found to be very important to the performance of the laser amplifier and so a lot of effort was expended to better understand and model temperature rises. This chapter then briefly considers the importance of beam quality and looks at experiments that measured the beam quality of the laser amplifier output beam.

3.2 Double-pass model

In the rod experiments in the previous chapter, the pump and seed beams each passed through the gain material only once and this greatly simplified the implementation of the model. To incorporate a double-pass of both the pump and seed beams, some parameters had to be adjusted.

3.2.1 Pump double-pass

Firstly, the pump rate is altered by the double-pass of the pump beam. For a single-pass, the pump rate, R, is described by the following,

$$R(r,z) = \frac{\alpha_p I_p(r)}{h\nu_p}\exp(-\alpha_p z) \qquad \text{Equation 3.1}$$

Where ν_p is the pump frequency, α_p is the pump absorption coefficient, I_p is the incident pump intensity and h is Planck's constant. For a double-pass of the pump, Equation 3.1 becomes,

$$R(r,z) = \frac{\alpha_p I_p(r)}{h\nu_p}\left[exp(-\alpha_p z) + exp(-\alpha_p l)exp\left(-\alpha_p(l-z)\right)\right] \qquad \text{Equation 3.2}$$

Where l is the length of the gain medium. This, in turn, alters the small-signal gain coefficient as the small-signal gain coefficient is a function of the pump rate.

3.2.2 Double-pass saturation effects

With regards to the seed beam, the key difference between the single-pass and double-pass models comes when considering the depletion of the upper-state population due to saturation effects in the amplifier. The gain coefficient is proportional to the upper-state population, which is reduced in the presence of a seed beam due to saturation effects, as shown in the following equation [1],

$$n_2(r,z) = \frac{R(r,z)\tau}{1+\left(\frac{I_l(z)}{I_{sat}}\right)} \qquad \text{Equation 3.3}$$

Where τ is the fluorescence lifetime of the gain material, I_l is the seed beam intensity and I_{sat} is the saturation intensity. In the single-pass model, the saturation of the upper-state population, and therefore the reduction in gain, is dependent only on the seed beam, assuming the pump rate is constant. In the double-pass model, the seed beam can be split into two parts, the forward propagating beam, I_f, and the reverse propagating beam, I_r. The level of saturation in the amplifier is determined by both the forward and reverse propagating seed beams as they overlap in the amplifier [2]. Therefore, the saturation effects are larger and the gain is reduced more than if there was a single-pass of the seed beam. Equation 3.3, for an overlapping, double-pass amplifier becomes,

$$n_2(r,z) = \frac{R(r,z)\tau}{1+\left(\frac{I_{f+r(z)}}{I_{sat}}\right)} \qquad \text{Equation 3.4}$$

Where the reduction in the upper-state population is now determined by the combined forward propagating and reverse propagating seed beam intensities, I_{f+r}. Now, the rate of change of the seed beam as it propagates along the z-axis is expressed as,

$$\frac{dI_l}{dz} = \frac{g_0(z)}{1+\frac{I_{f+r(z)}}{I_{sat}}} I_l(z) \qquad \text{Equation 3.5}$$

Here, I_l is the intensity of the seed beam as it propagates through the amplifier, first in the forward direction and then backwards through the amplifier again. The integration performed in the previous chapter can no longer be solved. In order to

understand the gain the seed beam experiences, the saturation of the amplifier must be understood. However, in order to understand the level of saturation, the gain must be known and so on. To solve this problem, an iterative approach is used.

Firstly, the amplifier is split into slices that each span a distance, dz, as shown in Step 1 in Figure 3.1. In the figure, the dimensions of the slices are exaggerated for the purposes of the diagram and there are also many more slices than shown. The small-signal gain coefficient, $g_0(z)$, is calculated for each slice. For the first step, the intensities of the forward and reverse propagating seed beams are unknown and they, therefore, cannot be added together to find the level of saturation at each slice. Instead, the saturation is determined using the intensity of the seed beam at each slice which underestimates the level of saturation and leads to an output intensity that is too large in magnitude.

In the simplified example shown in Step 1 in Figure 3.1, the amplifier is split into three slices, each with a length, dz. The small-signal gain coefficient, $g_0(z)$, is calculated for each slice. The input seed beam, $I_l(in)$, enters the amplifier at the first slice and the intensity of the seed beam after the first slice, $I_l(1)$, is found by multiplying the input intensity by the small-signal gain coefficient and then dividing by $1 + {I_l(z)}/{I_{sat}}$. Normally, $1 + {I_{f+r}(z)}/{I_{sat}}$ would be used but, as the forward and reverse seed intensities are unknown at this point, $I_l(z)$ is used to calculate the level of saturation. The output intensity of the first slice is then used as the initial seed intensity for the next slice in order to calculate $I_l(2)$ and so on. After the third slice, the forward propagation of the seed beam is complete and the seed intensity here is then used as the initial seed intensity, $I_l(3)$, for the first slice of the reverse propagating beam. In reality, the model had 10,000 slices, rather than three.

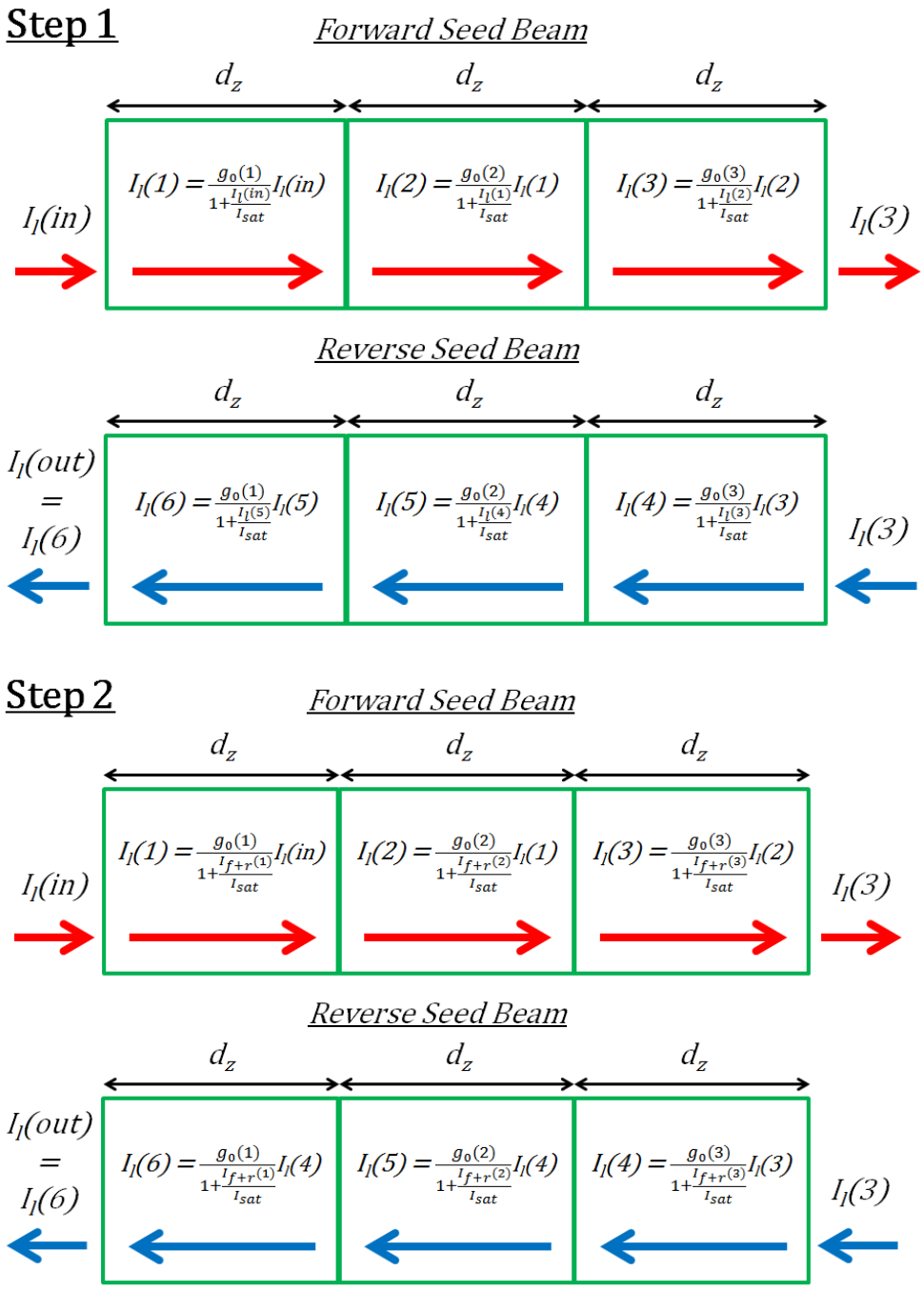

Figure 3.1 – Steps 1 and 2 both show a simplified example of the model. In Step 1, the saturation only from one beam at a time, either the forward or reverse. Step 2 then uses the results from Step 1 to simulate the saturation effects with both the forward and reverse beams, although it is known that the saturation is exaggerated. Step 2 is then repeated with the new data and a smaller than expected level of saturation. This is repeated until the model converges on a consistent level of saturation.

The reverse propagating beam starts at slice 3 and follows the same process as the forward propagating beam until there is an output seed intensity, $I_l(6)$. The small-signal gain coefficient is the same at each slice as it was for the forward propagating beam. Importantly, there is now a value for the forward and reverse propagating seed beams at each slice. These values are then used in the next step of the model.

In the next step, Step 2 in Figure 3.1, for each slice of the amplifier, the intensity of the forward and reverse seed beams that were calculated in the previous step are added together, $I_{f+r}(z)$, and are used to find the level of saturation at that particular slice. The seed beam intensity is then calculated at each slice, as previously, but this time the previous seed intensity is multiplied by the small-signal gain coefficient and then divided by, $1 + {I_{f+r}(z)}/{I_{sat}}$.

It is important to note that the level of saturation modelled in the amplifier is now too high at this step. The level of saturation from the forward and reverse propagating seed beams was taken from the results of the model in Step 1, where the amplification was greater than expected as there was a reduced level of saturation taken into account. This means that the level of saturation in Step 2 is now greater than expected as the forward and reverse seed beam intensities should not be as large. The seed beam is then modelled travelling through the amplifier, as per the previous step, but now with this new saturation at each slice. As the level of saturation is greater than expected, this now leads to an output intensity that is too small in magnitude.

New values for the forward and reverse propagating seed beams at each slice of the amplifier have now been obtained and they can be used to repeat Step 2 with a level of saturation that is lower than in Step 1 but is still not high enough. This same process is repeated with the saturation flipping from being too high to too low until it converges to a constant intensity profile, giving the correct level of saturation for the multi-pass amplifier. A summary of this process is displayed in Figure 3.2.

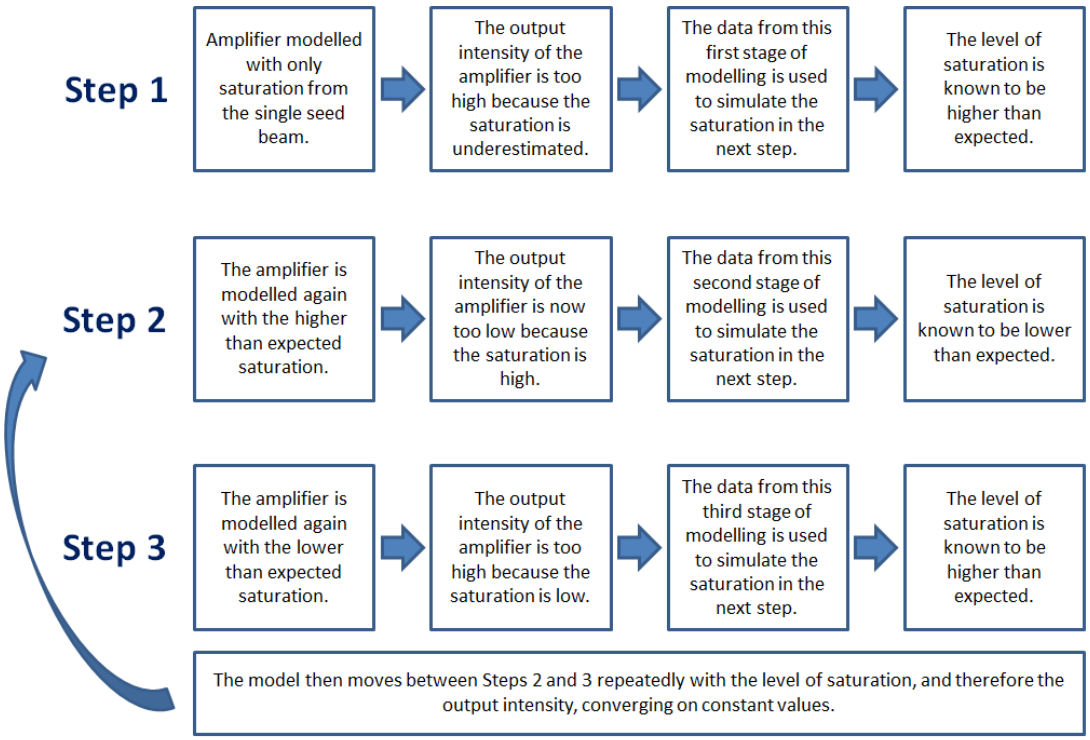

Figure 3.2 – A summary outline of the process undergone in modelling a double-pass laser amplifier with saturation effects taken into account. In Step 1 the amplifier is modelled with saturation effects from either the forward or reverse propagating seed beam, not both simultaneously, which initially leads to an output intensity that is higher than expected. The output from Step 1 is then used to simulate the saturation in Step 2 with both the forward and reverse seed beams simultaneously but now the output intensity is known to be lower than expected. Step 3 then uses the output from Stage 2. This process is repeated until the model converges on a consistent level of saturation.

The number of slices used to model the gain medium was 10,000 and, with a total length of 250 µm, this meant that each slice was 25 nm in length. The stimulated-emission cross-section and fluorescence lifetime used in this modelling were the same as those outlined in Section 2.3.2. The uncertainty in the stimulated-emission cross-section can range from $12x10^{-19}$ cm^{-2} to $14.4x10^{-19}$ cm^{-2} based on values given in the literature whereas the uncertainty in

the fluorescence lifetime appears to be smaller based on Figure 2.7 in the previous chapter. Variations in these values can affect the predicted output of the modelled amplifier, however, even with variation in these parameters, the general trends predicted hold true when examining the impact of other variables such as pump and seed beam radii, doping concentration, gain medium length and the number of passes of the seed beam.

The model program, which was written in MATLAB, was run until the difference between the output power of two iterations was less than 0.01 mW. Due to the iterative nature of this model, when it was run on a computer, it took approximately 20 to 30 minutes to complete and reach this difference between iterations.

3.2.3 Double-pass model with energy transfer up-conversion

To incorporate the effects of energy transfer up-conversion (ETU) in the double-pass model, the small-signal gain coefficient and the equation that determines the reduction in the upper-state population due to saturation effects must both be altered.

The small-signal gain coefficient in the presence of ETU is found for the double-pass model in the same way as it was in the single-pass model, which is discussed in Section 2.2.4. The equation for the upper-state population is different for the non-ETU and ETU cases and the pump rate, R, is also adjusted to incorporate the double-pass of the pump beam. Unlike in Chapter 2, for the single-pass model, the equation for the small-signal gain coefficient is not integrated over the length of the gain medium but is considered for each slice at position z in the double-pass model.

The equation for the rate of change of the upper-state population in the presence of ETU with respect to time [3] can be rearranged to give the upper-state population in the presence of ETU in the steady state as,

$$n_{2,ETU}\left(I_{f+r}\right)=\frac{-\left(1+\frac{I_{f+r}(z)}{I_{sat}}\right)+\sqrt{\left(1+\frac{I_{f+r}(z)}{I_{sat}}\right)^{2}+4R(r,z)W\tau^{2}}}{2W\tau} \quad \text{Equation 3.6}$$

Where W is the up-conversion parameter. Equation 3.6 is then simplified for the small-signal regime, where it is assumed that the seed intensity is small enough that it causes no appreciable reduction in the upper-state population, by setting I_{f+r} to zero. Equation 3.6 then becomes [1],

$$n_{2,ETU}\left(I_{f+r}=0\right)=\frac{-1+\sqrt{1+4R(r,z)W\tau^{2}}}{2W\tau} \quad \text{Equation 3.7}$$

Multiplying both sides of equation 3.7 by σ_{21} gives the small-signal gain coefficient in the presence of ETU. By dividing equation 3.6, the upper-state population with no saturation, by equation 3.7, the upper-state population which has been reduced by a seed beam intensity, I_{f+r}, the following equation is produced,

$$\frac{n_{2,ETU}\left(I_{f+r}\right)}{n_{2,ETU}\left(I_{f+r}=0\right)}=\frac{-\left(1+\frac{I_{f+r}(z)}{I_{sat}}\right)+\sqrt{\left(1+\frac{I_{f+r}(z)}{I_{sat}}\right)^{2}+4R(r,z)W\tau^{2}}}{-1+\sqrt{1+4RW\tau^{2}}} \quad \text{Equation 3.8}$$

Equation 3.8 gives the fraction of the original upper-state population that remains after the upper-state population has been reduced by a seed beam, I_{f+r}. When this fraction is multiplied by the small-signal gain coefficient, it gives the gain coefficient when saturation effects and ETU are considered,

$$g(z)=g_{0}\left[\frac{-\left(1+\frac{I_{f+r}(z)}{I_{sat}}\right)+\sqrt{\left(1+\frac{I_{f+r}(z)}{I_{sat}}\right)^{2}+4R(r,z)W\tau^{2}}}{-1+\sqrt{1+4RW\tau^{2}}}\right] \quad \text{Equation 3.9}$$

The gain coefficient can then be used to calculate the variation in the seed beam over a distance, dz,

$$\frac{dI_l}{dz} = g_0 \left[\frac{-\left(1+\frac{I_{f+r}(z)}{I_{sat}}\right)+\sqrt{\left(1+\frac{I_{f+r}(z)}{I_{sat}}\right)^2+4R(r,z)W\tau^2}}{-1+\sqrt{1+4RW\tau^2}} \right] I_l(z) \qquad \text{Equation 3.10}$$

As I_{f+r} must be known to calculate the output intensity, but I_{f+r} cannot be known until the output intensity has been calculated, Equation 3.10 must be solved iteratively, as described in Section 3.2.2.

3.3 Diamond heat-spreader amplifier experiment

The first double-pass experiments were performed with a thin-disk geometry and all crystals had a highly reflective (HR) coating on the rear surface to reflect both the pump and seed beams. The seed laser for these experiments was a picosecond mode-locked laser with a wavelength of 1064 nm producing linearly polarised light. The pulse duration was around 10 ps with a repetition rate of 200 kHz and the laser could provide an average power of 16 W. The repetition rate of 200 kHz means that the time between pulses was 5 µs, which is significantly shorter than the fluorescence lifetime of the gain material, which varies from $97\ \mu s$ for 1 atm % Nd:YVO_4 [4] to $110\ \mu s$ for 0.4 atm % Nd:YVO_4 [5]. This means that the pulsed seed beam can be treated as a continuous wave (CW) beam for the purposes of the model [6].

The pump source for the thin disk amplifier was a 70 W, 808 nm fibre coupled diode laser (Dilas IS30). The fibre had a core diameter of 200 µm. The pump was not temperature tuned to the optimum absorption wavelength and so, as the incident pump power was varied, the wavelength of the pump beam was varied. This is taken into account in the double-pass model by calculating the variation in absorption coefficient as a function of incident pump power, taken from empirical data. For each set of variables, the experimental data was used to calculate the percentage of pump power that was absorbed and, subsequently, the pump absorption co-efficient. This provided an equation representing the pump

absorption co-efficient as a function of incident pump power and this was implemented in the model.

3.3.1 Diamond heat-spreaders

The first set of experiments were performed with two wedged diamond heat-spreaders, one bonded to the front of the Nd:YVO_4 crystal and another bonded onto the back as shown in Figure 3.3. The diamond heat-spreader on the front of the Nd:YVO_4 crystal was not anti-reflection coated for either the pump or seed wavelengths on either the front or rear surface, therefore wedged diamond was used to stop an etalon being formed within the diamond. The rear diamond heat-spreader was also wedged and uncoated on both surfaces but this wedge was simply due to the availability of a wedged diamond heat-spreader and not for practical purposes as the rear face of the Nd:YVO_4 crystal had a highly-reflective (HR) coating for both the pump and seed wavelengths. This meant that no pump or seed light should have been incident upon the rear diamond heat-spreader.

The Nd:YVO_4 crystals measured 6 mm x 5 mm x 0.25 mm and were purchased from Castech Inc. The crystals were HR coated for both the pump and seed wavelengths on the rear surface. The front surface of the Nd:YVO_4 crystals were not coated as they were bonded to diamond heat-spreaders with a similar refractive index (Nd:YVO_4 with a refractive index of approximately 2.2 [7] and diamond with a refractive index of approximately 2.4 [8]). From top to bottom, the coated (or uncoated surfaces) were as follows: the top, wedged diamond heat-spreader was uncoated on both surfaces; the Nd:YVO_4 crystal's front face, which was bonded to the top heat-spreader, was uncoated; the rear surface of the Nd:YVO_4 crystal was HR coated for both the pump and seed wavelengths; and finally, the rear, diamond heat-spreader was uncoated on both surfaces.

Both heat-spreaders were chemical vapour deposition grown, single crystal diamond with a diameter of 4 mm. At the thickest side, the thickness of the diamond was 0.52 mm, and at the thinnest side the thickness was 0.41 mm. The

wedge angle of the diamond heat-spreaders was calculated to be 1.57 degrees. This wedge angle was not chosen specifically, it was merely due to the availability of diamond heat-spreaders. They were bonded to the Nd:YVO_4 crystal using a liquid-assisted capillary bonding technique [9].

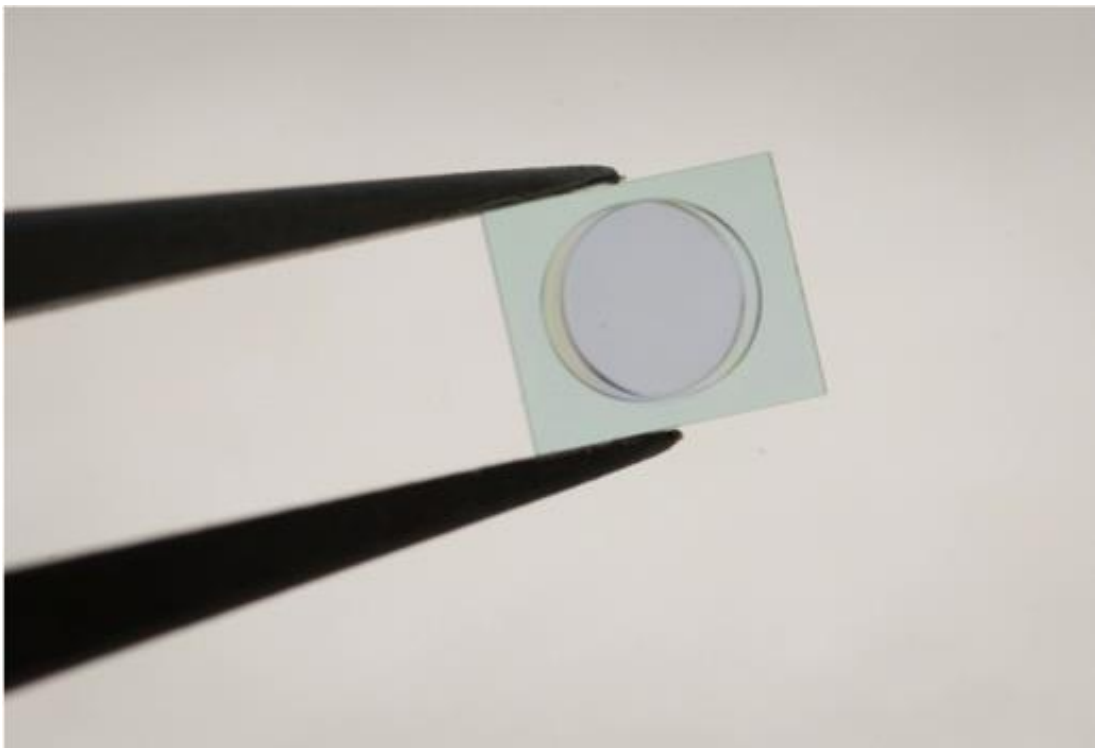

Figure 3.3 – The Nd:YVO_4 crystal with two wedged, diamond heat-spreaders, one bonded to the front and the other to the back. The larger, square crystal is the Nd:YVO_4 and the two circular samples are the diamond heat-spreaders.

The crystal/heat-spreader sandwich was then mounted in a brass mount. Figure 3.4 shows a schematic diagram of this brass mount. The brass mount had a chamber beneath the area the crystal sat on through which chilled water was flowed to aid heat extraction. The crystal sat on top of a layer of indium foil and had another layer of foil on the top side with an aperture to allow the pump and seed beams to pass through. The brass mount had an annulated cap that, when tightened, compressed

the crystal/heat-spreader sandwich and the indium foil to provide a better thermal contact.

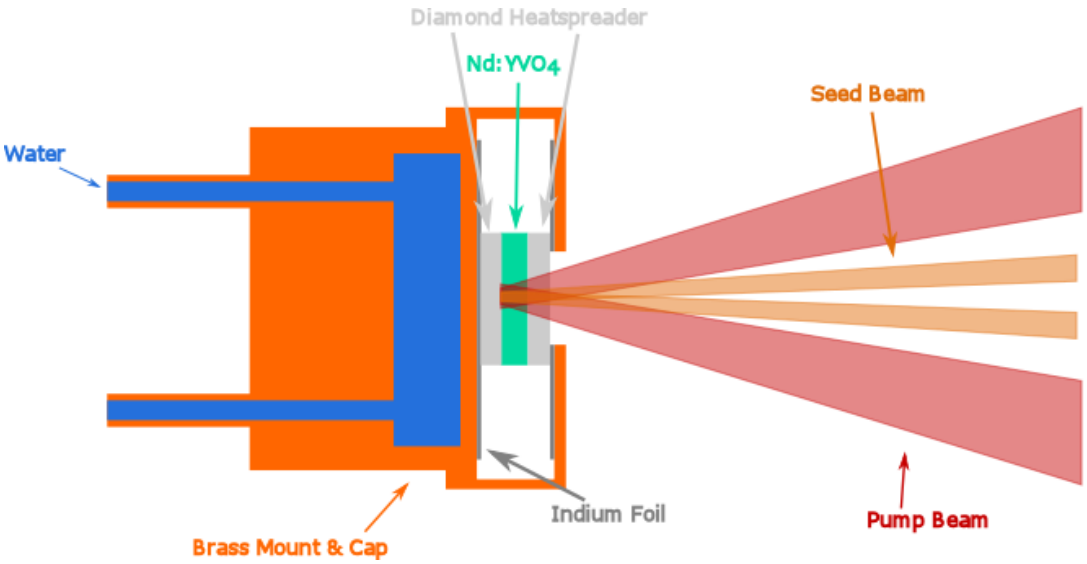

Figure 3.4 – A diagram of the crystal mount. The diagram shows how the Nd:YVO_4 crystal and heat-spreaders sat in the mount between layers of indium foil.

The experimental setup of the amplifier is shown in Figure 3.5. The pump beam was delivered though a fibre and the beam was collimated and then focussed onto the crystal and the unabsorbed, reflected beam was collected on a power meter. The seed beam passed through a half wave-plate then a polarising beam cube to control and vary the incident seed power incident upon the crystal. The seed beam then passed through another half wave-plate in order to adjust the polarisation to achieve the maximum gain. The amplified seed beam was then collected by another power meter.

Due to availability, the front diamond heat-spreader did not have an anti-reflection (AR) coating and so, due to Fresnel reflections, the diamond reflected approximately 17 % of the incident pump and seed beams from the front surface. This 17 % of the pump and seed beam that was reflected never passed through the gain material. As the absorbed pump power was calculated by subtracting the

measured reflected pump power from the incident pump power, this did not affect the calculation of the absorbed pump power as long as all of the unabsorbed pump power was measured. The seed beam also suffered multiple reflections as a fraction of any beams exiting the front diamond heat-spreader were reflected back into the gain material, with each reflection offset from the last due to the wedge in the diamond. The first and second beams were measured and added together to find the output of the amplifier and the subsequent reflections were neglected. The complications that arose from the use of the uncoated wedged diamond heat-spreaders reduce the expected accuracy of comparisons of the experimental data with the double-pass model.

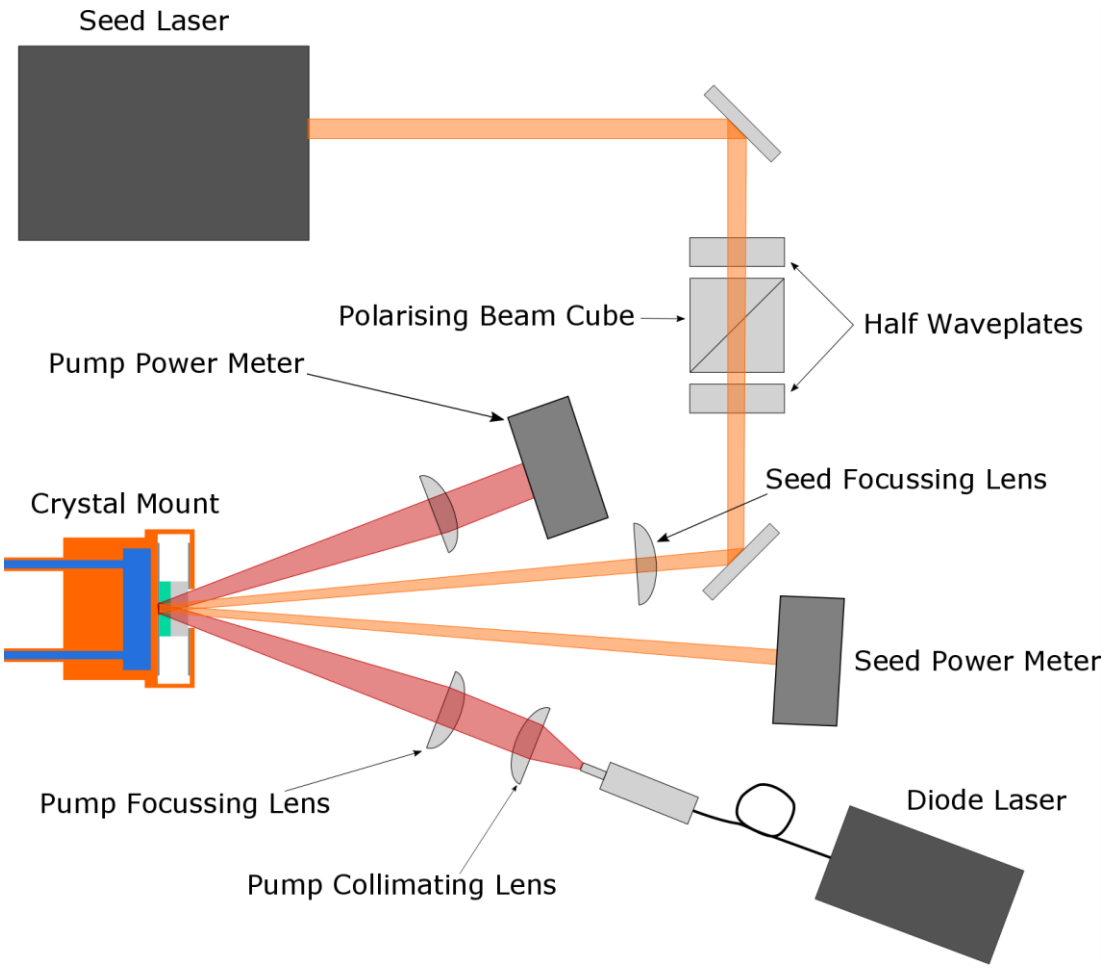

Figure 3.5 – A diagram of the experimental set-up used in the Nd:YVO_4 amplifier experiments.

Figure 3.6 and Figure 3.7 show power transfers for three different beam radii using 2 atm % and 1 atm % Nd:YVO_4 respectively. For all of the power transfers, the pump and seed radii were approximately equal and the initial seed power was approximately 13 W. The maximum incident pump power for each spot size varies. The incident pump power was no longer increased once the output power of the amplifier began to rollover as, in previous experiments, rollover of the output power preceded the destruction of the gain material. Many crystals were destroyed when the incident pump power of the amplifier was increased after the output power had rolled over, so, in order to preserve the gain material, the maximum incident pump power was set by the rollover and this rollover varied when different amplifier parameters were used.

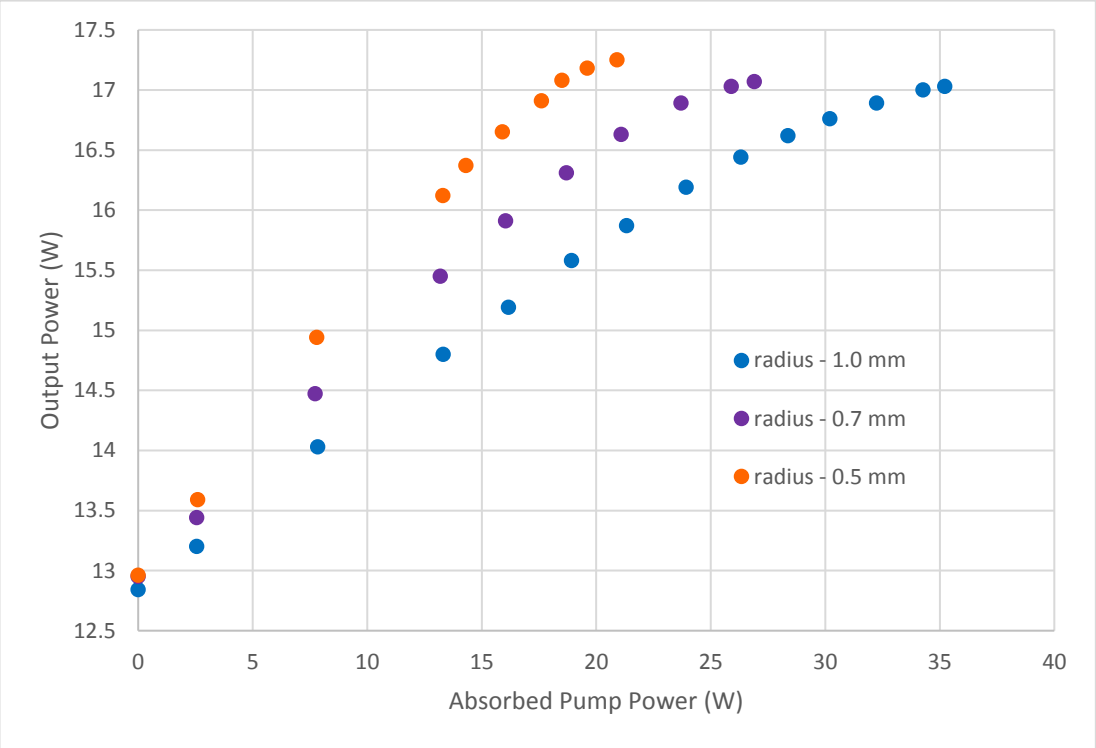

Figure 3.6 – Power transfers taken with 2 atm % Nd:YVO_4. The pump and seed radii are approximately equal and three different radii are shown.

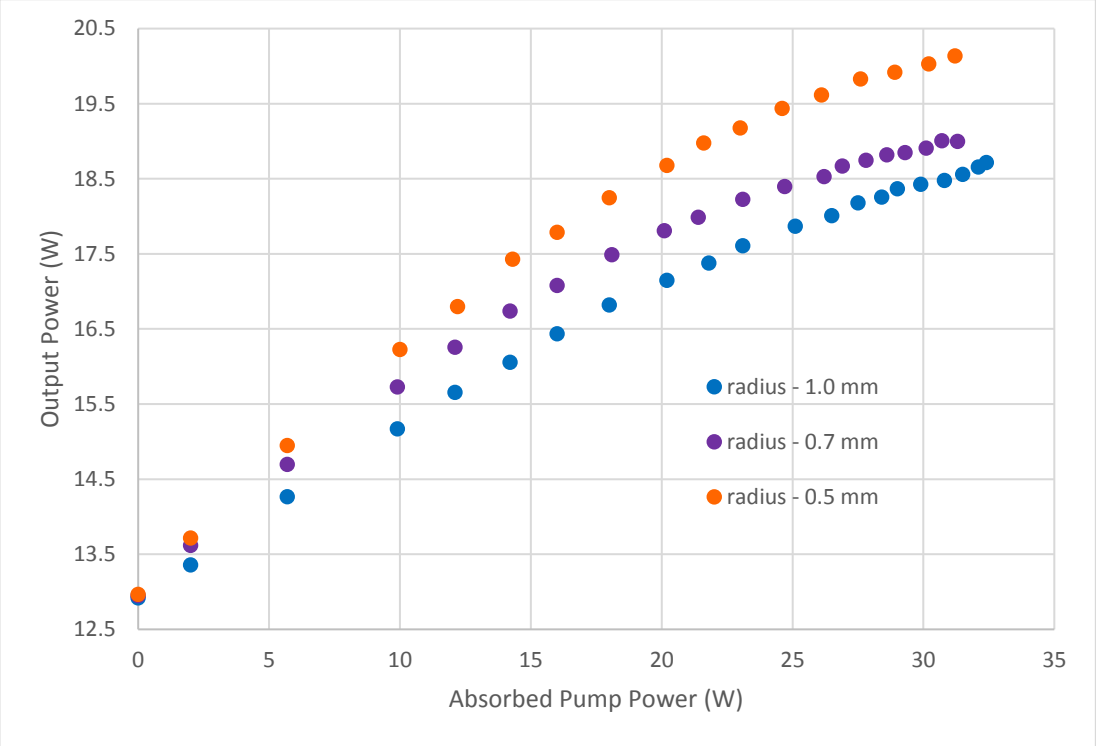

Figure 3.7 – Power transfers taken with 1 atm % Nd:YVO_4. The pump and seed radii are approximately equal and three different radii are shown.

In both Figure 3.6 and Figure 3.7, the power transfer with the smallest pump and seed spot size, 500 µm, has the steepest gradient and the power transfer with the largest pump and seed spot size, 1000 µm, has the shallowest gradient, with the power transfer for the 700 µm spot size in between the two. For the 2 atm % Nd:YVO_4, used in Figure 3.6 the effects of ETU will be greater than for the 1 atm % Nd:YVO_4, used in Figure 3.7, due to the higher doping concentration. The intensity of the pump beam is greater when the pump spot size is smaller, for a given absorbed pump power, and this can negatively impact the amplifier by increasing the temperature of the gain material and increasing the effects of ETU. However, the smaller seed spot size allows for higher saturation of the laser amplifier, which also reduces the effects of ETU. All of this means that it is difficult to predict just how varying one parameter can affect the overall performance of the laser amplifier as when some parameters are changed, the effects can be positive and negative.

In Figure 3.6, which displays the power transfers for the 2 atm % Nd:YVO_4, the final output power for each spot size does not differ greatly: the 500 µm spot size delivering a final output power of 17.3 W at an absorbed pump power of 20.9 W; the 700 µm spot size delivered an output power of 17.1 W at an absorbed pump power of 26.9 W; and the 1000 µm spot size delivering a final output power of 17.0 W at an absorbed pump power of 35.2 W. Even though the final output power of the three power transfers was similar, taken when the output power began to rollover, the smaller spot sizes achieved this output power at a lower absorbed pump power. The difference in absorbed pump power, taken at the maximum output power, between the 500 µm and the 1000 µm cases was 14.3 W.

For the 1 atm % Nd:YVO_4 power transfers, shown in Figure 3.7, the output powers did differ somewhat: the 500 µm spot size delivering a final output power of 20.1 W at an absorbed pump power of 31.2 W; the 700 µm spot size delivered an output power of 19.0 W at an absorbed pump power of 31.3 W; and the 1000 µm spot size delivering a final output power of 18.7 W at an absorbed pump power of 32.4 W. The output power was greater as the spot size was reduced and each power transfer began to rollover at approximately the same absorbed pump power. For the 1000 µm power transfer, the output power of the amplifier appears to rollover before it starts to increase again. This phenomenon will be discussed further later in the chapter.

Figure 3.8, Figure 3.9 and Figure 3.10 show the same data as in Figure 3.6 and Figure 3.7 but each figure displays power transfers for both doping concentrations, 1 atm % and 2 atm %, on the same graph for a single pump and seed beam radius. For Figure 3.8, Figure 3.9 and Figure 3.10, each graph shows two power transfers, one for 1 atm % Nd:YVO_4 and one for 2 atm % Nd:YVO_4. Both power transfers in Figure 3.8 are taken with a pump and seed spot size of approximately 500 µm. The power transfers in Figure 3.9 are with pump and seed spot sizes of approximately 700 µm and Figure 3.10 with spot sizes of approximately 1000 µm. These figures better illustrate the difference in performance between the 1 atm % and 2 atm % Nd:YVO_4.

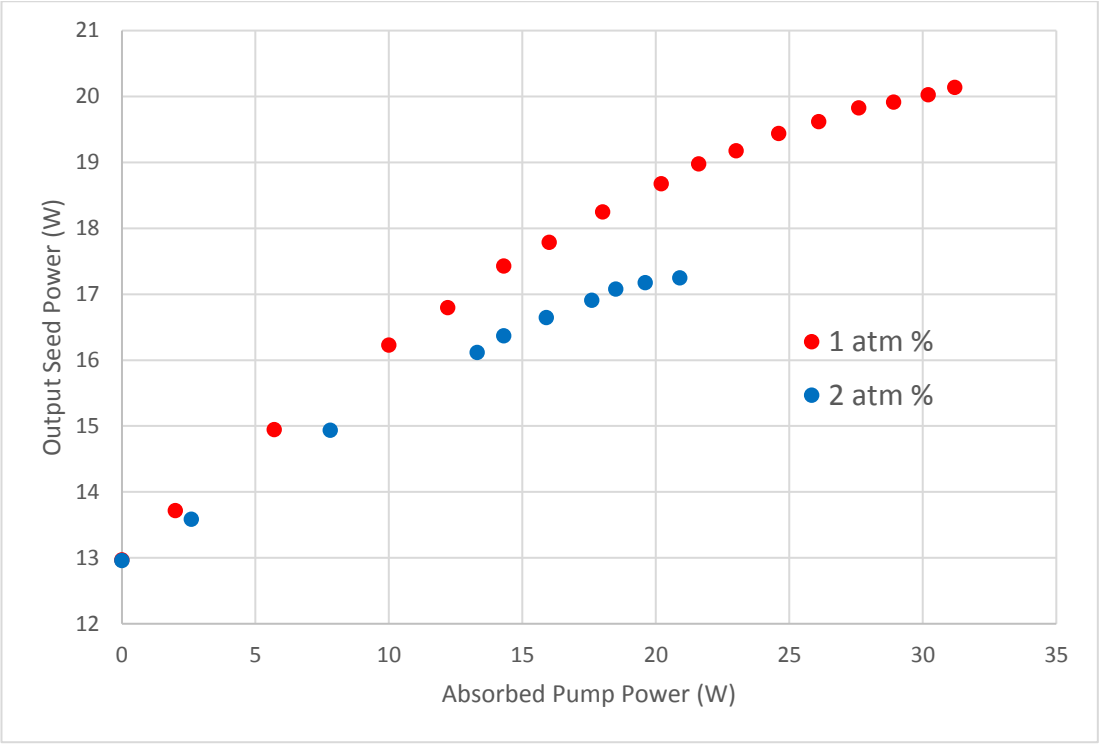

Figure 3.8 - Power transfers taken with 1 atm % and 2 atm % Nd:YVO_4. The pump and seed beam radii are approximately 500 µm for both power transfers.

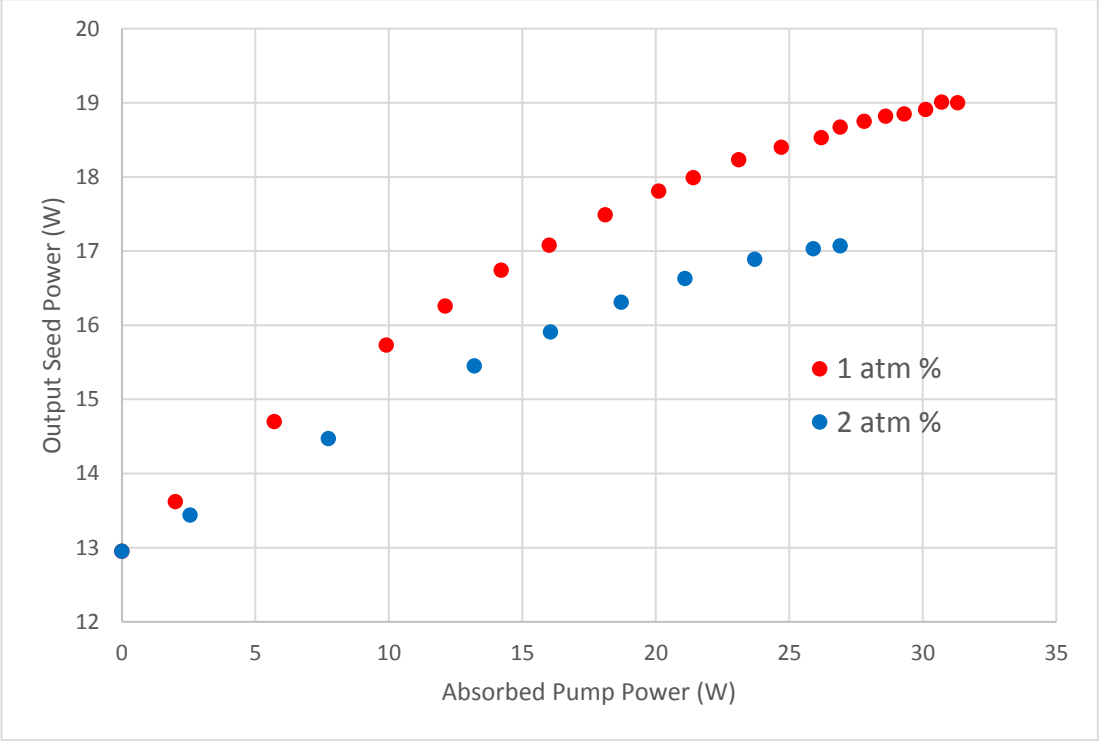

Figure 3.9 - Power transfers taken with 1 atm % and 2 atm % Nd:YVO_4. The pump and seed beam radii are approximately 700 µm for both power transfers.

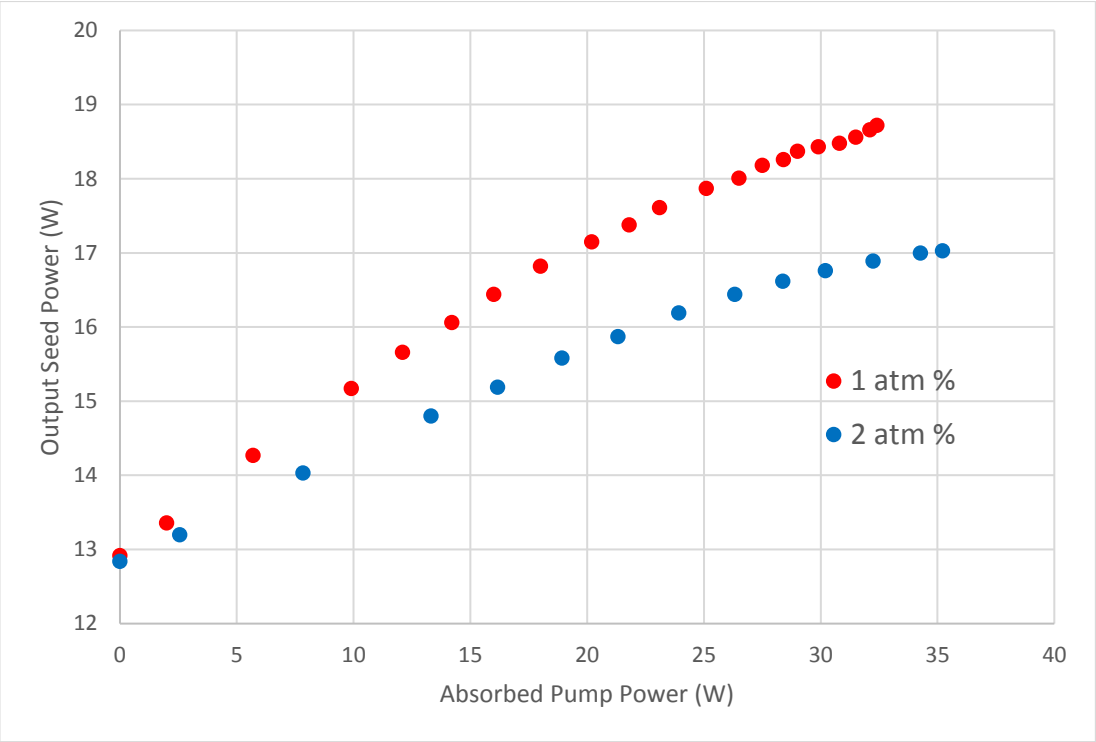

Figure 3.10 - Power transfers taken with 1 atm % and 2 atm % Nd:YVO_4. The pump and seed beam radii are approximately 1000 µm for both power transfers.

Figure 3.8 displays the two power transfers taken with a pump and seed beam radii of approximately 500 µm for both doping concentrations. The 1 atm % doping concentration achieved a higher maximum output power of 20.1 W compared to the 2 atm % doping concentration, which was 17.3 W, although the 1 atm % doping concentration had a maximum absorbed pump power that was more than 10 W greater than the 2 atm % doping concentration, which had a maximum absorbed pump power of 20.9 W. When comparing the two power transfers at a similar absorbed pump power, the 1 atm % doping concentration reached an output power of 19.0 W at an absorbed pump power of 21.6 W, approximately 2 W greater than the 2 atm % doping concentration.

In Figure 3.9, where the pump and seed beam radii for both power transfers were approximately 700 µm, the trends were similar to those in Figure 3.8. The 1 atm % doping concentration achieved a higher maximum output power of 19.0 W at an

absorbed pump power of 31.3 W, compared to the 2 atm % doping concentration, which achieved a maximum output power of 17.1 W at an absorbed pump power of 26.9 W. The 1 atm % doping concentration also had a higher output power, 18.7 W, at the same absorbed pump power of 26.9 W, 1.6 W greater than the 2 atm % doping concentration.

The power transfers for the 1 atm % and 2 atm % doping concentrations with a pump and seed beam radii of approximately 1000 µm are shown in Figure 3.10. The maximum output powers for the two doping concentrations were 18.7 W at an absorbed pump power of 32.4 W for the 1 atm % doping and 17.0 W at an absorbed pump power of 35.2 W for the 2 atm % doping. Again, the 1 atm % doping concentration outperforms the 2 atm % doping concentration but for this spot size, the 2 atm % case reaches higher absorbed pump powers, unlike the other spot sizes. In Figure 3.10, the output power of the 1 atm % doping concentration power transfer does begin to rollover but then starts increasing again just as the power transfer ends. It may be the case that the power transfer was terminated prematurely and the absorbed pump power could have been increased beyond this point without damage to the gain material but a comparison between the two doping concentrations can still be made at an absorbed pump power of approximately 32 W. At an absorbed pump power of 32.4 W, the 1 atm % doping concentration case achieved an output power of 18.7 W, 1.8 W greater than the output power of 16.9 W reached by the 2 atm % amplifier at an absorbed pump power of 32.2 W.

From these experiments, it can be seen that the 1 atm % doping concentration outperforms the 2 atm % for all pump and seed spot sizes, and this is expected as the effects of ETU should be worse for the higher doping concentration. In Figure 3.6 and Figure 3.7 it can be seen that the power transfers for the smaller beam radii have steeper gradients. This is due to the larger intensity of the seed beam when the beam radius is smaller leading to an improved extraction efficiency over the larger radii. Overall, the best results were achieved with the 1 atm % doping concentration with a pump and seed beam radius of 500 µm. Every power

transfer also exhibits a rollover and this is due to the effects of increased temperature on the stimulated-emission cross-section of Nd:YVO_4 which will be discussed in detail in the next section.

3.4 Stimulated-emission cross-section as a function of temperature

The laser transition in Nd:YVO_4 that emits photons at a wavelength of 1064 nm is subject to a thermal shift and thermal broadening. The processes behind this broadening and shift are described in detail by Sardar and Yow [10] and Sato and Taira [11]. These processes mean that the stimulated-emission cross-section of Nd:YVO_4 is not constant with respect to temperature but as the temperature of the crystal is increased, the peak stimulated-emission cross-section decreases as the stimulated-emission spectrum is broadened. The peak stimulated-emission cross-section is also shifted to longer wavelengths. This can have a great effect on the performance of Nd:YVO_4 amplifiers [11]–[13]. An experiment was set-up to test the hypothesis that the gain in the thin-disk amplifier is affected by this process.

3.4.1 Nd:YVO_4 amplifier seeded by a semiconductor disk laser

Delen et al [12] show that over a temperature range of 16 °C to 80 °C, the peak of the stimulated-emission cross-section for Nd:YVO_4 varies by approximately 0.2 nm. In order to test this phenomenon, an experiment was devised where the temperature of a thin-disk amplifier was varied and a tunable seed beam was used to probe the variation in gain with varying temperature.

A 1 atm % Nd:YVO_4 thin-disk, with dimensions of 6 mm x 5 mm x 0.25 mm, was glued onto a microscope slide to provide minimum cooling to ensure a sufficient temperature rise within the crystal. The thin-disk was pumped with a pulsed diode laser at a wavelength of 808 nm. The pump pulse duration was 3 ms. To provide a tunable, continuous wave seed source, a 1 µm InGaAs semiconductor disk laser (SDL) was constructed. The laser cavity had three mirrors: a Bragg mirror on the

rear surface of the semiconductor; a concave, HR fold mirror with a radius of curvature of 100 mm; and a flat, 91 % reflective output coupler. The SDL was pumped using an 808 nm diode laser coupled into a 100 µm core diameter fibre and then collimated and focussed onto the SDL. A birefringent filter (BRF) was inserted into the cavity and used to tune the wavelength of the laser to two different wavelengths, 1064.4 nm and 1064.8 nm. These two wavelengths were chosen simply as they were easily achievable with the setup being used. The experimental setup is shown in Figure 3.11.

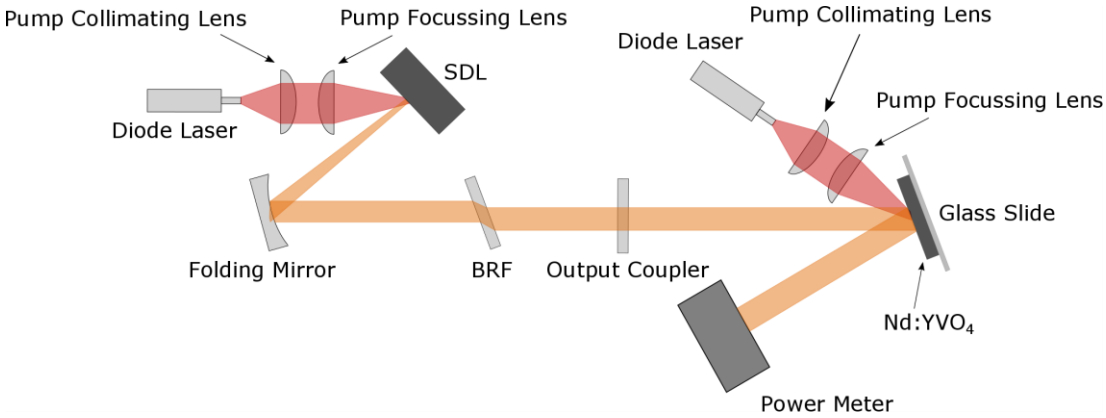

Figure 3.11 - The experimental setup showing the SDL laser cavity seeding the Nd:YVO_4 amplifier.

Figure 3.12 shows the results of the experiment with the 1064.4 nm seed beam on the left and the 1064.8 nm seed beam on the right. The yellow trace is the pump pulse that is switched on from zero and then switched off again after 3 ms. The green trace is the seed beam. The seed begins at the unamplified level and is then amplified by some amount and returned to its unamplified level after the pump pulse is switched off. It can be assumed that because of the limited cooling of the gain material, a significant temperature rise should occur over the 3 ms that the pump pulse is present. If there were no change in the stimulated-emission cross-section whilst the pump pulse was present, it would be expected that the shape of the gain in the seed beam would match the shape of the pump since the gain would be determined only by the upper-state population of the gain material.

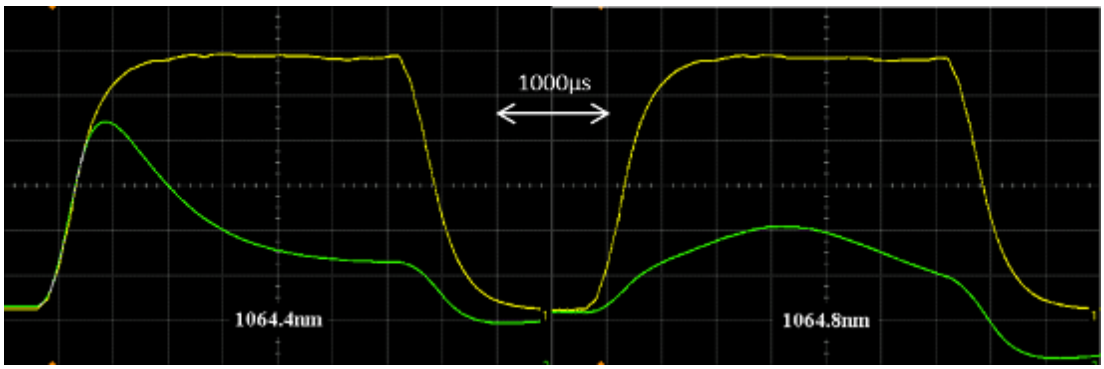

Figure 3.12 - Amplification of two seed lasers (green), tuned to different wavelengths, using a pulsed pump source (yellow).

What is observed in Figure 3.12 is that, for the 1064.4 nm seed beam, the gain peaks near the beginning of the pump pulse and then decreases even with the pump pulse still present. For the 1064.8 nm seed beam, the gain in the seed beam peaks closer to the middle of the pump pulse and the peak is significantly smaller than for the 1064.4 nm case. This indicates that the gain in the amplifier is not consistent over the duration of the pump pulse and therefore not consistent as the temperature is increased. The next step was to incorporate this temperature effect into the double-pass model and see if this variation in the stimulated-emission cross-section explains the rollover observed in the diamond heat-spreader experiments, as seen in Figure 3.6 and Figure 3.7.

3.4.2 The effects of temperature incorporated into the model

In lasers and laser amplifiers, the reduction in the peak stimulated-emission cross-section is deleterious as it reduces the gain, but the wavelength shift of the peak emission cross-section is particularly concerning for the performance of laser amplifiers. The wavelength of a laser has the ability to drift with the peak emission cross-section shift, but an amplifier has a fixed seed wavelength and, therefore, experiences a larger, relative reduction in the stimulated-emission cross-section. Delen et al. [12] measured the relative reduction in the stimulated-emission

cross-section of 0.1 atm % Nd:YVO4 at a fixed wavelength, λ_0, where λ_0 is the wavelength of the peak stimulated-emission cross-section at a temperature of 16 °C, which is 1064.1 nm in this case. These measurements provide a relationship between the stimulated-emission cross-section and temperature for a seed wavelength of 1064.1 nm that is described by,

$$\sigma_{21,T} = 1.2213\ \sigma_{21,0}\ exp(-0.012T) \qquad \text{Equation 3.11}$$

Where $\sigma_{21,T}$ is the stimulated-emission cross-section at temperature, T in °C, and $\sigma_{21,0}$ is the stimulated-emission cross-section at 16 °C. This is for a fixed seed wavelength of 1064.1 nm and includes the contributions from both the reduction in the peak value of the emission cross-section with temperature and the shift of the peak with temperature. Figure 3.13 is a graphical representation of Equation 3.11, showing how the stimulated-emission cross-section for a fixed wavelength varies with temperature. This can be added to the amplifier model in order to alter the stimulated-emission cross-section with respect to temperature.

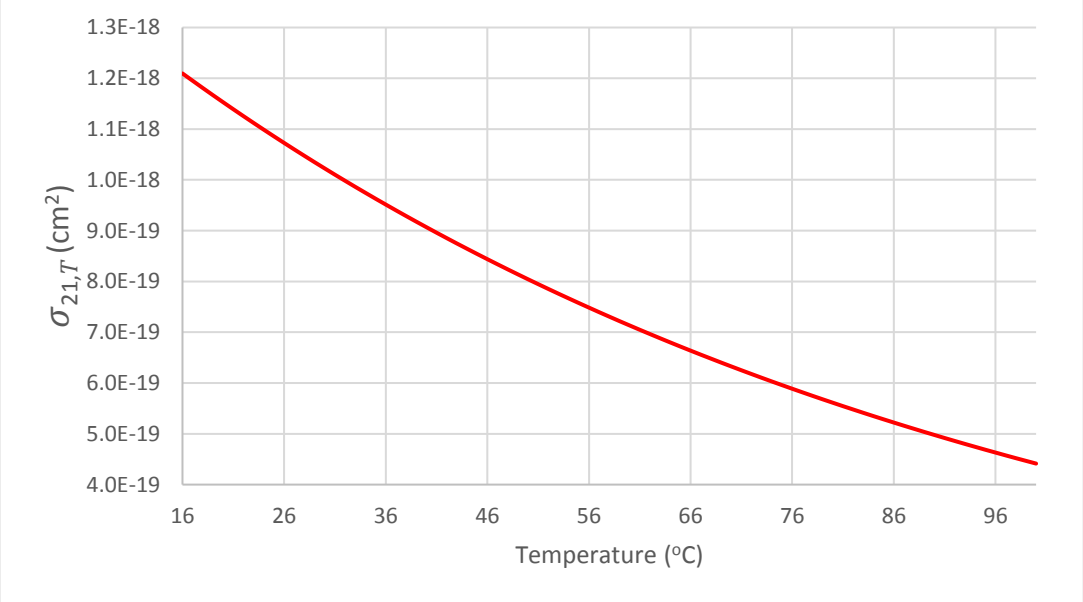

Figure 3.13 – This graph shows how the stimulated-emission cross-section varies with temperature using Equation 3.11, for the seed wavelength, λ_0, which in this case is 1064.1 nm.

The main source of heating in the amplifier experiments performed in this chapter is from the quantum defect between the pump and seed wavelengths. As discussed in Section 1.7 in Chapter 1, if the amplifier pump laser has a wavelength of approximately 808 nm then the ion is excited to the $^4F_{5/2}$ level in Nd:YVO_4. It then undergoes a non-radiative decay to the $^4F_{3/2}$ level before emitting a photon with a wavelength of 1064 nm as it decays further to the $^4I_{11/2}$ level. The rest of the energy is lost as heat when the ion decays to the ground level, $^4I_{9/2}$. This is shown in Figure 3.14. If all the ions decay through the 1064 nm transition, via stimulated-emission, then 24 % of the pump energy is converted to heat [14].

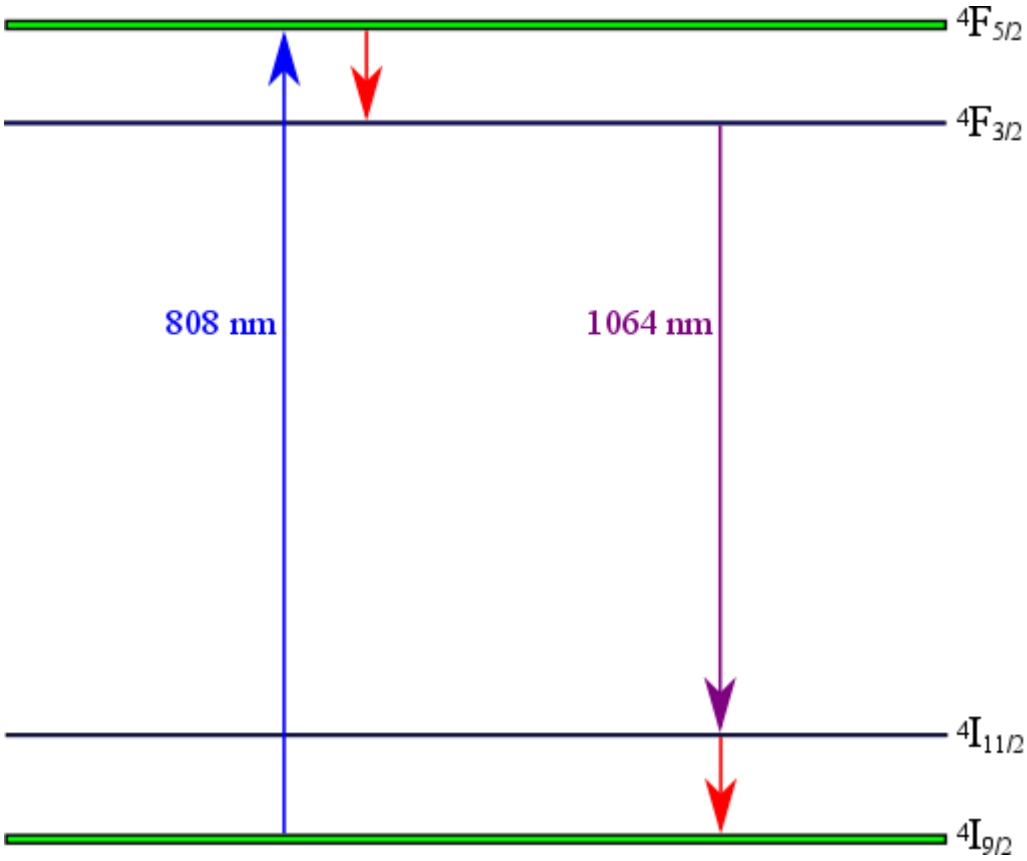

Figure 3.14 – An energy level diagram of Nd:YVO_4 showing the main pump transition (808 nm) in blue and the stimulated-emission transition (1064 nm) in purple. The red arrows in the diagram indicate non-radiative transitions where the energy becomes heat.

If the ions are allowed to decay through spontaneous-emission, with the assumption that no lifetime quenching processes occur, then the heat generated is slightly decreased, compared with the case where all the ions decay through the 1064 nm transition via stimulated-emission. There are four fluorescent transitions from the $^4F_{3/2}$ energy level and they are shown in Figure 3.15. From the $^4F_{3/2}$ level, the ion can decay to the $^4I_{15/2}$, $^4I_{13/2}$, $^4I_{11/2}$ or $^4I_{9/2}$ levels which correspond to photons emitted with wavelengths of 1890 nm, 1342 nm, 1064 nm and 914 nm, respectively [15], [16]. The branching ratios for these transitions are as follows: 0.003 for 1890 nm; 0.110 for 1342 nm; 0.467 for 1064 nm; and 0.422 for 914 nm [5], [17].

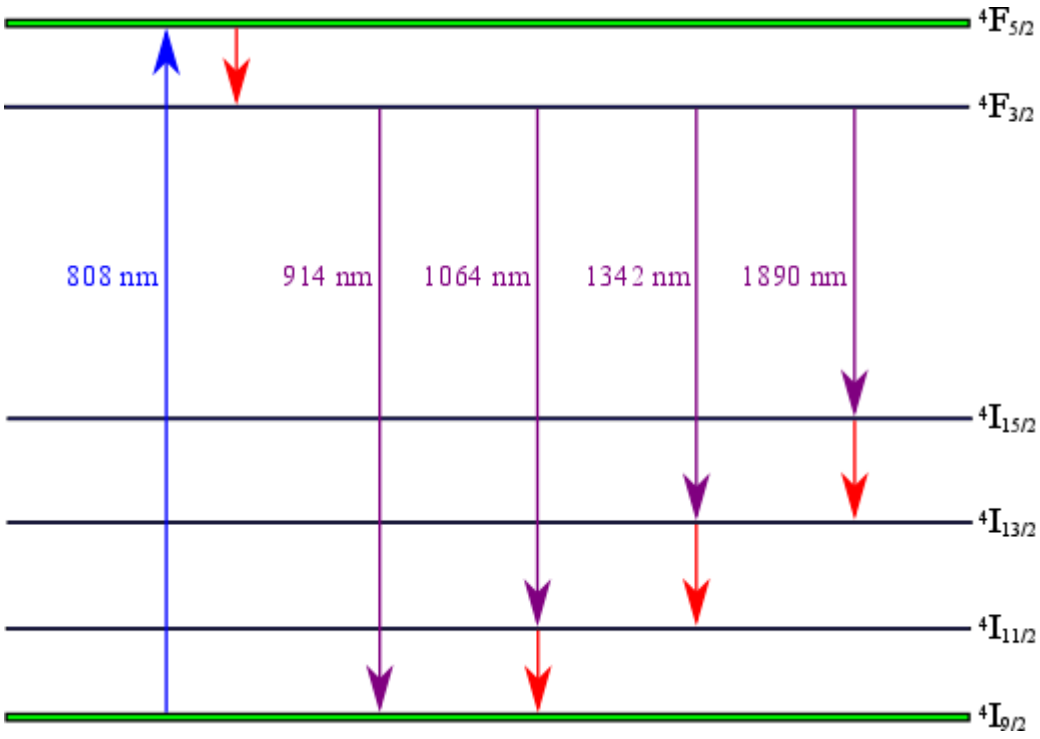

Figure 3.15 – An energy level diagram of Nd:YVO_4 showing the main pump transition (808 nm) in blue. The four fluorescent transitions (914 nm, 1064 nm, 1342 nm and 1890 nm) are shown in purple. The red arrows in the diagram indicate non-radiative transitions where the energy becomes heat.

The percentage of pump energy converted to heat, due to spontaneous-emission to these four levels, is calculated to be approximately 21 %, which is less than the 24 % for the case where all ions decay through stimulated-emission via the 1064 nm transition. The 914 nm transition has a branching ratio 0.422 which is only slightly smaller than the branching ratio of 0.467 for the 1064 nm transition and, as the 914 nm emission is closer in wavelength to the pump wavelength of 808 nm, the fraction of pump energy transferred to heat is decreased. The 1342 nm and 1890 nm transitions each contribute greater heating per ion that decays through these transitions but their branching ratios are smaller than for the 1064 nm and 914 nm transitions.

Whether or not the ions decay through spontaneous-emission or stimulated-emission, heat is generated when they do so, therefore, the heat generated in the gain medium is a function of the absorbed pump power. As the stimulated-emission cross-section is a function of the temperature of the gain medium, the stimulated-emission cross-section is also a function of the absorbed pump power. Additional heating comes from ETU, which is a function of the upper-state population and so is also a function of the absorbed pump power in the absence of saturation of the amplifier gain. If saturation of the amplifier gain does occur, then the additional heating from ETU is reduced. This means that saturation of the amplifier adds additional heat in the gain medium through forcing all ions to decay through the 1064 nm transition rather than spontaneously decay through the various fluorescent transitions, but it also reduces the heat generated in the gain medium through ETU. The extra heating generated by ETU in the absence of any stimulated-emission is the dominant factor, outweighing the reduction in heat from the different fluorescence branching ratios. The increase in thermal loading between the non-lasing and lasing cases can be greater than double [4].

For the purposes of the double-pass model, it is assumed that the temperature increases linearly with absorbed pump power. Due to this assumption, the model will not accurately model the heating from ETU or other processes that may occur, such as changes to the heat flow between the crystal and the crystal mount due to

bowing of the crystal at higher temperatures. Nonetheless, this provides a baseline from which to begin to understand the effect of heat on amplifier performance and to begin to understand the likely of importance of different processes.

With the information provided by Delen et al. [12], the rise in temperature as a function of absorbed pump power is all that needs to be measured in order to incorporate the effects of temperature on the stimulated-emission cross-section into the double-pass model. The first attempt at determining the rise in temperature of the gain medium measured the peak fluorescence wavelength shift as a function of absorbed pump power to infer the temperature rise and will be described in detail in the following section.

3.4.3 Peak fluorescence wavelength shift in Nd:YVO_4

Delen et al. [12] observed a shift in the peak wavelength of the fluorescence spectrum as a function of temperature and measured the rate of the shift as 3 pm/°C in Nd:YVO_4. This information was used to infer a temperature rise in the Nd:YVO_4 gain medium by measuring the shift in the peak wavelength of the fluorescence spectrum as the Nd:YVO_4 gain material was pumped using a laser diode, inducing a temperature rise in the crystal.

The experimental setup for these experiments is shown in Figure 3.16. The same 250 µm thick, Nd:YVO_4 crystals were used as in the diamond heat-spreader experiments, described in Section 3.3, but only for a doping concentration of 1 atm %. The Nd:YVO_4 had an HR coating for the pump wavelength, 808 nm, and the seed wavelength, 1064 nm, on the rear surface and was uncoated on the front surface. Rather than being bonded to diamond heat-spreaders, the crystals were bonded to plane-parallel silicon carbide (SiC) heat-spreaders which were AR coated on their front surfaces for wavelengths of 808 nm and 1064 nm and had no coating on their rear surfaces, the side which was bonded to the Nd:YVO_4. These heat-spreaders were obtained from Cree, Inc. As the SiC heat-spreaders were AR coated on the front surface, this meant that the complications of the multiple

reflections that arose using the uncoated, wedged diamond were no longer present. The SiC heat-spreaders had dimensions of 7 mm x 6 mm x 0.35 mm. As the SiC dimensions were slightly bigger than the Nd:YVO_4 dimensions, trying to bond a heat-spreader to the front and back of the crystal using the liquid-assisted capillary bonding technique became very difficult and so a single SiC heat-spreader was bonded to the uncoated side of the Nd:YVO_4. In summary, this provided an AR coating, at the pump and seed wavelengths, on the front face of the SiC heat-spreader. The rear of the SiC was uncoated and was bonded to the uncoated face of the Nd:YVO_4. The rear of the Nd:YVO_4 was HR coated at both the pump and seed wavelengths.

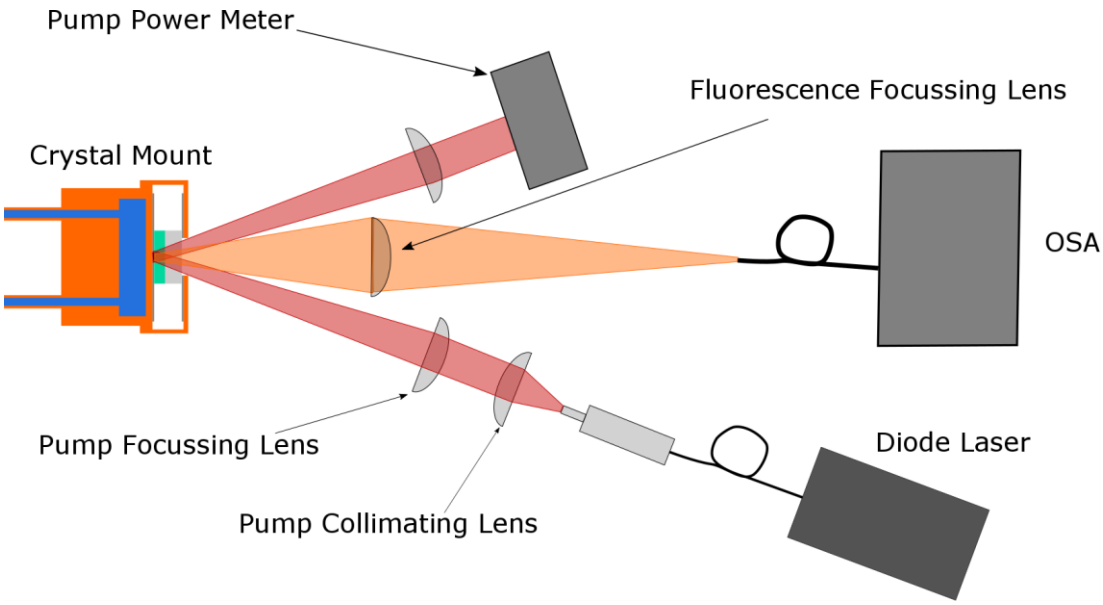

Figure 3.16 – The experimental setup used to measure the shift in the peak of the fluorescence spectrum as a function of temperature for 1 atm % Nd:YVO_4. The gain medium was pumped using an 808 nm diode laser and the fluorescence was captured and focussed into an optical spectrum analyser.

The gain crystal was mounted in the same mount described in the diamond heat-spreader experiments. Again, the mount was water cooled and the chiller set

to a temperature of 15 °C. It is therefore reasonable to assume that, with no incident pump power, the crystal is also at a temperature of 15 °C. Due to the mounting configuration of the gain medium, it was not possible to collect the fluorescence spectrum from the side of the crystal and so it had to be viewed head on, as shown in Figure 3.16, using a lens to focus the fluorescence into a fibre that was connected to an optical spectrum analyser (OSA). There were no etalon effects observed possibly as the front surface of the SiC had an AR coating at the seed wavelength. As the fluorescence was measured head on, this meant that the amplifier could not be seeded when the fluorescence was measured. A consequence of the amplifier being unseeded was that the temperature increase that was inferred for a given absorbed pump power would inevitably be higher than if the amplifier was seeded.

The crystal was pumped using the same diode laser used in the diamond heat-spreader experiments and the peak of the fluorescence spectrum was measured using the OSA. The pump wavelength was not tuned to the peak absorption wavelength of the gain material but the incident pump power and unabsorbed pump power were measured and used to calculate the absorbed pump power. The variation in the absorption coefficient with pump wavelength will alter the profile of the absorbed pump power within the crystal but this is the same setup that is used in the power transfer experiments and so best represents what will occur during those experiments. Three different pump radii were used: 0.43 mm, 0.57 mm and 0.80 mm. These sizes were chosen as they were the beam radii used for the power transfer experiments described in the next section.

Figure 3.17 shows the results of the experiment. It was difficult to accurately measure the changes in the peak wavelength of the fluorescence as the changes in wavelength were on the order of the resolution of the OSA, which was 0.1 nm. The broadening of the fluorescence spectrum as the pump power increased also made it difficult to determine the peak of the fluorescence accurately. The OSA was the only instrument available at the time and, due to its age, the only method of extracting the spectrum data was by printing it on a dot matrix printer. The peak was then

determined by judging where the peak in the spectrum was by eye and then using a ruler to calculate the wavelength of the peak, hence why it was it more difficult as the fluorescence spectrum broadened.

The dashed lines in Figure 3.17 are linear fits to the data that were used to determine the temperature rise as a function of absorbed pump power using the fluorescence shift of 3 pm/°C described by Delen et al [12]. The gradient of each fit can be multiplied by the absorbed pump power at a given point and divided by 3 picometers to give the temperature increase at that point.

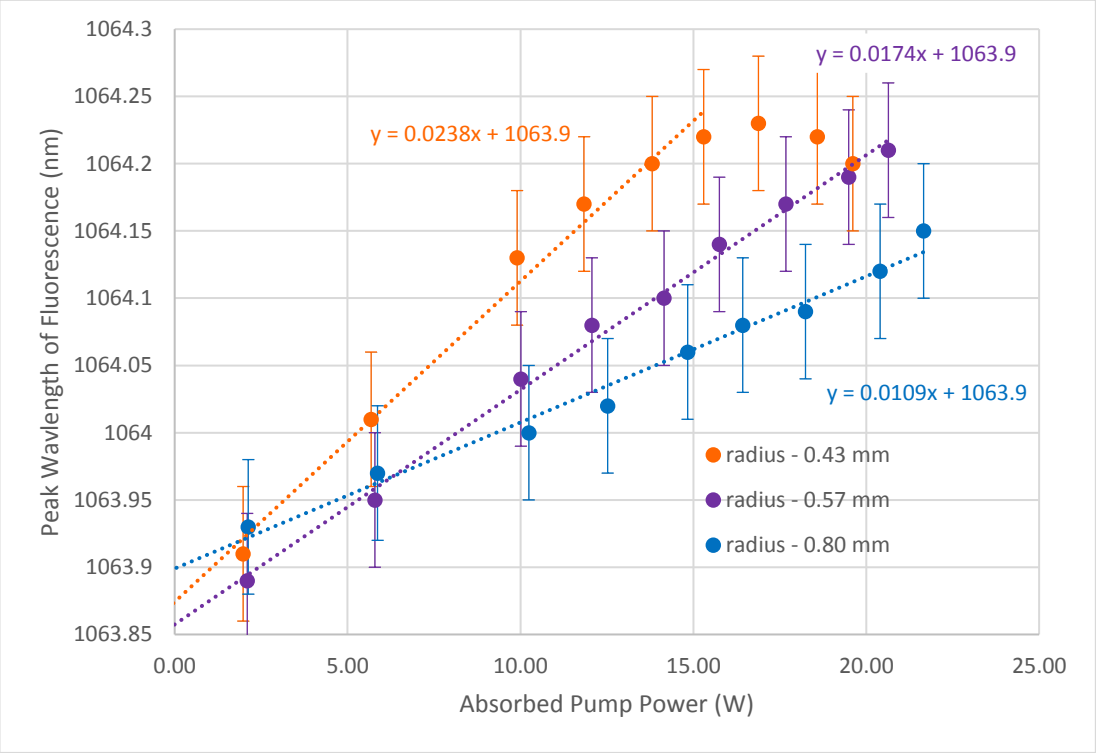

Figure 3.17 – The peak wavelength of the fluorescence emitted from 1 atm % Nd:YVO_4 was plotted against the absorbed pump power in the gain medium. The data was plotted for a pump beam radius of three different sizes, shown in the graph in different colours. A linear line of best fit was added to the linear portion of each data set.

It would be expected that at zero absorbed pump power, the peak wavelength of the fluorescence would be the same regardless of the pump beam radius. This is the case within the experimental uncertainty due to the resolution of the OSA being 0.1 nm, but this technique for measuring the peak of the fluorescence emission is limited in regards to measuring the absolute temperature of the crystal. The graph can, however, be used to show the general trend of the temperature rise as a function of absorbed pump power. The graph shows that the smallest beam radius, corresponding to the largest pump intensity, has the largest temperature increase, at an absorbed pump power of approximately 15 W, of 115 °C, whilst the largest radius, corresponding to the smallest pump intensity, has the smallest temperature increase, at an absorbed pump power of approximately 15 W, of 53 °C. The caveat is that the technique, as it is used here, is limited as the temperature increase is likely to be overestimated in the absence of a seed beam that extracts energy from the amplifier. A seed beam will reduce the heating in the crystal by reducing the lifetime quenching effects that can lead to greater than double the amount of thermal loading [4].

Figure 3.18, below, shows the results of a similar experiment but this time conducted with a 2 atm % Nd:YVO_4 crystal. Both sets of data in Figure 3.18 are for a pump radius of 0.7 mm but the red data is taken with two diamond heat-spreaders bonded to the gain medium, one on the rear of the gain medium and one on the front. The blue data is the gain medium without any heat-spreader at all.

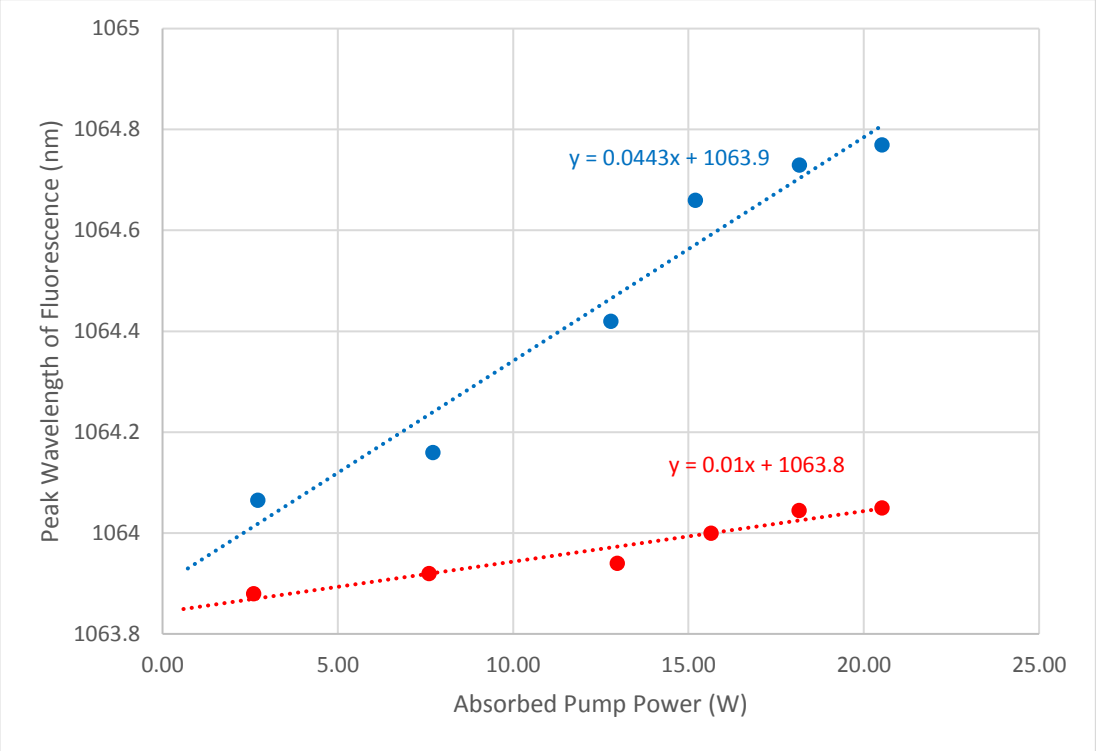

Figure 3.18 – The peak wavelength of the fluorescence emitted from 2 atm % Nd:YVO_4 was plotted against the absorbed pump power in the gain medium. The data was plotted for a pump beam radius of 0.7 mm. The red data shows the results for a diamond heat-spreaders bonded to the gain medium and the blue data is for the gain medium with no heat-spreader.

The main purpose of the graph in Figure 3.18 is to illustrate the significant difference in the gradient when there is a much larger difference in temperature, as there is between the diamond heat-spreader and no heat-spreader cases. The temperature increase when there is no heat-spreader, for an absorbed pump power of 20.5 W, is approximately 290 °C. For the configuration with the diamond heat-spreaders, the temperature increase, at an absorbed pump power of 20.5 W, is approximately 70 °C. The temperature difference between the two cases is 220 °C, which means that the heat-spreaders reduce the temperature by a factor greater than 4. This is a significant difference and demonstrates the efficacy of heat-spreaders.

To compare diamond heat-spreaders with SiC heat-spreaders, the temperature for the two diamond heat-spreader case, at an absorbed pump power of 15 W, was calculated as 57 °C. This compares to the SiC heat-spreader case where the temperature increase, at an absorbed pump power of 15 W, was 53 °C. The two temperature increases are similar but the comparison is not straightforward, however. In the diamond heat-spreader the gain material used was 2 atm % $Nd:YVO_4$, whereas, the SiC case used 1 atm % $Nd:YVO_4$. The temperature increase should be greater for the 2 atm % $Nd:YVO_4$, due to ETU. The diamond heat-spreader case also has two heat-spreaders, one on the front and one on the rear of the gain medium.

With the differences between the two cases, it is difficult to make a fair comparison between the two materials. The thermal conductivity of both materials is very different, with SiC having a thermal conductivity of approximately 500 W/mK and diamond a thermal conductivity of approximately 2000 W/mK. Therefore, it should be expected that diamond would perform better as a heat-spreader, however, Higurashi et al have shown that for thermal conductivities above 500 W/mK, there is little improvement in heat extraction [18]. One advantage of SiC was its availability as, at the time, it was difficult to procure suitable diamond with the optical properties required. In experiments discussed later in this chapter, the use of SiC heat-spreaders, with suitable AR coatings, eliminated the problems with stray reflections that arose using the uncoated diamond heat-spreader experiments but still provided similar performance to diamond heat-spreaders.

3.4.4 Amplified spontaneous emission and parasitic lasing

The 0.43 mm radius data in Figure 3.17 shows the peak wavelength of fluorescence starting to decrease as the absorbed pump power is increased past 17 W. This implies that the temperature of the crystal was decreasing at this point as the absorbed pump power was increased. A possible explanation for the temperature of the crystal decreasing with greater absorbed pump power could be amplified

spontaneous-emission (ASE) or parasitic lasing, both mechanisms by which the upper laser level population could be reduced through stimulated-emission, therefore reducing the heating that is associated with other lifetime quenching effects.

ASE occurs when the fluorescence within a laser gain medium, that has an inverted population, is amplified to higher power levels, reducing the stored energy in the gain medium and, therefore, the gain for the seed beam in an amplifier [19]–[22]. It can occur in laser media with a large gain, such as Nd:YVO_4, and can be highly directional when the gain crystal has a large aspect ratio, such as in a thin-disk. This is because the high aspect ratio provides a much longer amplification length for the ASE than for the intended seed amplification. To power scale thin-disk amplifiers, the pump spot size is made larger, to better manage the heat within the gain medium, but this can exacerbate the problem of ASE as it makes the amplification length for ASE even longer [23].

Parasitic lasing is similar to amplified spontaneous-emission but the effect is compounded as an unintentional laser cavity is formed within the gain medium. This cavity is usually a result of Fresnel reflections at the surfaces and edges of the gain material and redirects the amplified spontaneous-emission back into the pumped region of the gain material [24]–[26]. If the gain and amplification length are large enough then a parasitic laser can reach threshold which reduces the gain for the intentional amplification of the amplifier seed beam.

ASE and parasitic lasing are detrimental to the performance of both lasers and laser amplifiers and much research has been conducted with the goal of characterising and minimising their affects [27]–[34]. Reflections from the top surface of the gain medium can increase the path length for amplified spontaneous-emission, trapping the ASE inside the active gain medium. To mitigate these reflections from the top surface, an un-doped end cap, with a refractive index that is the same as, or similar, to the refractive index of the gain medium, can be placed on the top surface of the gain medium. This un-doped end cap reduces reflections back into the active gain

medium and provides an alternative path for the ASE to travel that is not back into the active gain medium.

The primary purpose of the diamond and SiC heat-spreaders, used in the previous experiments discussed in this chapter, was to reduce the temperature within the gain medium; however, it is feasible that the heat-spreaders may also act as end caps to suppress ASE. The refractive index of Nd:YVO_4 is approximately 2.2 [7] while diamond has a refractive index of approximately 2.4 [8]. With no heat-spreader, the reflection between the Nd:YVO_4/air surface would be approximately 13.6 % but with a diamond heat-spreader, the reflection between the Nd:YVO_4/diamond surface would be approximately 0.3 %, a reduction of 13.3 %. There would, however, be a reflection of approximately 17.2 % between the diamond/air surface. Therefore, Fresnel reflections would be reduced at the Nd:YVO_4/diamond surface compared to the Nd:YVO_4/air surface. This end cap function of the diamond heat-spreader was not considered when conducting the experiments outlined in this thesis but it may be an idea to consider in future work.

In Figure 3.17, for each case, the gain medium is being pumped but there is no seed beam to extract any of the energy, so the temperature increase within the gain medium will be maximised because of the lifetime quenching effects that occur [4]. If ASE or parasitic lasing were to occur within the amplifier gain medium, it would reduce the effects of lifetime quenching processes by causing more ions to decay via the fluorescent transitions and, therefore, decrease the temperature within the gain medium. For the 0.43 mm pump beam radius case in Figure 3.17, the peak wavelength of fluorescence began to decrease whilst the absorbed pump power increased, implying that the temperature of the crystal was also decreasing. It is feasible that this may have been caused by a parasitic laser reaching threshold.

Parasitic lasing was never observed during these experiments but it was not explicitly looked for either. It was only after performing these experiments that the possibility of parasitic lasing was considered. It would be of interest to repeat the experiment described in Section 3.4.3 and to try to observe parasitic lasing within

the gain medium. This would involve measuring the fluorescence spectrum emitted from the long axis of the gain medium. If a parasitic laser was to reach threshold, a narrowing of the fluorescence spectrum would be expected.

The results from the peak wavelength of fluorescence as a function of absorbed pump power experiment were used to estimate the temperature rise for further amplifier experiments performed with SiC heat-spreaders described in Section 3.5. The temperature rise was used in the double-pass model to calculate the reduction in the stimulated-emission cross-section and subsequently, the output power of the amplifier. As mentioned previously, the use of SiC heat-spreaders, with suitable AR coatings, eliminated the problems with stray reflections that arose using the uncoated diamond heat-spreader experiments but still provided similar performance to diamond heat-spreaders.

3.5 Laser amplifier experiments using silicon carbide heat-spreaders

The experiments performed in this section used the same experimental setup as shown in Figure 3.5 but with a single, plane-parallel SiC heat-spreader bonded to the 250 µm thick, Nd:YVO_4 crystal rather than two wedged diamond heat-spreaders. The SiC heat-spreader was uncoated on the surface that was in contact with the Nd:YVO_4 but AR coated for the pump and seed wavelengths on the air interface side, therefore eliminating the issues with Fresnel reflections that arose using the uncoated wedged diamond heat-spreaders. Only 1 atm % Nd:YVO_4 was used as it provided better amplification than 2 atm % Nd:YVO_4 in the diamond experiments. Again, three different beam radii were used with the pump and seed radii being approximately equal. The initial seed power used for these experiments was approximately 16 W, which was slightly higher than for the previous experiments. The results from the experiments are shown in Figure 3.19 below, where the three power transfers are plotted for each spot radii: 430 µm, 570 µm and 800 µm. The incident pump power was increased until the power transfer began to exhibit rollover effects in order to prevent damage to the amplifier gain

medium, as in previous experiments, which meant that the power transfers terminated at varying absorbed pump powers.

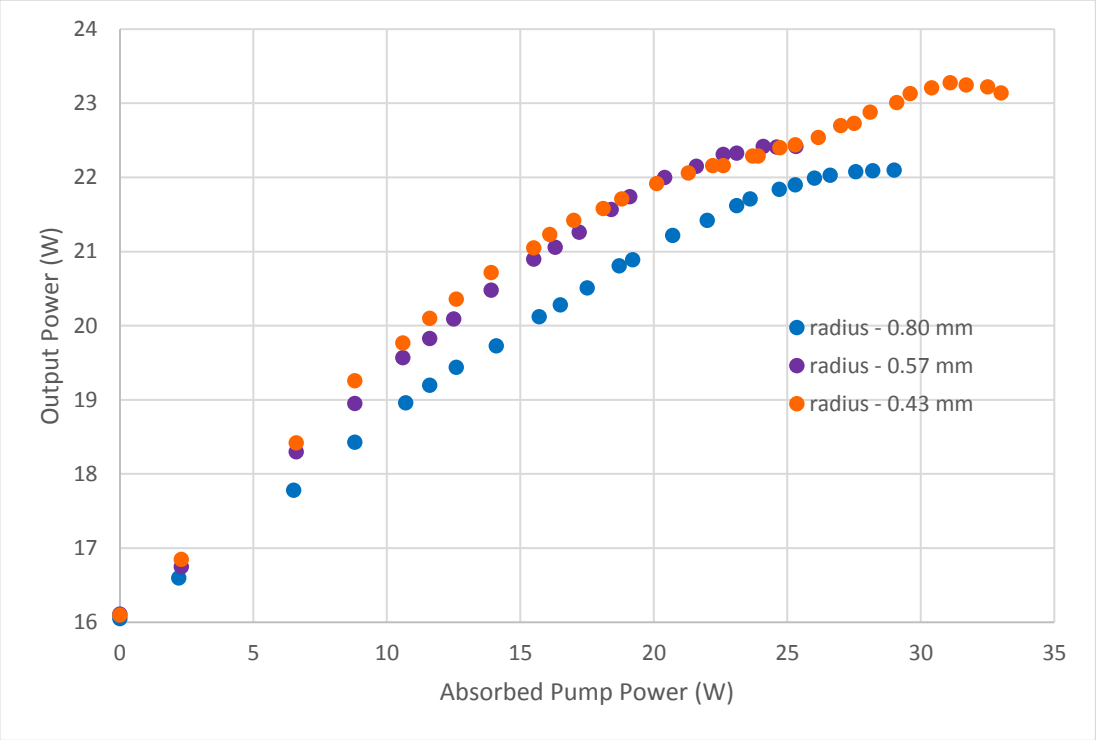

Figure 3.19 - Power transfers for the three different pump and seed beam radii used. The blue data represents the data taken with a pump and seed beam radius of 800 µm. The purple data is for a pump and seed radius of 570 µm and the orange data for pump and seed radii of 430 µm.

A summary of the results presented in Figure 3.19 is given in Table 3.1 below. The table highlights the maximum output power of the amplifier for each different spot size with the corresponding absorbed pump power for that maximum output power. The table then also displays the gain and the extraction efficiency of the amplifier for the given maximum output power at each spot size. The anomalous behaviour of the 430 µm amplifier results, which will be discussed later, leads to the amplifier output increasing again after it initially appears to rollover, however, if the output power was taken at the initial rollover, the output power would be 22.2 W

at an absorbed pump power of 22.6 W with a gain of 1.39 and an extraction efficiency of 36.1 %. The gain for the three different spot sizes is broadly the same whereas the extraction efficiency decreases as the spot size increases, as expected, as the saturation of the amplifier is slightly greater for the smaller beam radii.

Spot Size (µm)	Maximum Output Power (W)	Absorbed Pump Power at Maximum Output Power (W)	Gain	Extraction Efficiency (%)
430	23.3	31.1	1.46	30.9
570	22.4	24.1	1.4	34.9
800	22.1	27.6	1.38	29.1

Table 3.1 - The maximum output power for three different spot sizes is given alongside the absorbed pump power, the gain and the extraction efficiency of the amplifier, all at the corresponding maximum output power.

3.5.1 Delayed rollover in laser amplifier power transfer

In Figure 3.19, the power transfer for the 430 µm spot size data differs from the power transfers for 570 µm and 800 µm at absorbed pump powers above 25 W. For the two larger spot sizes, the data exhibits a smoother rollover. The 570 µm power transfer rolls over between an absorbed pump power of 20 W to 25 W and the 800 µm power transfer rolls over at an absorbed pump power of between 25 W to 30 W. For the 430 µm case, between absorbed pump powers of 17 W to 23 W, the rollover looks similar to the other power transfers but above absorbed pump powers of 24 W, the power transfer is more erratic as the output power of the amplifier begins to increase again. Above absorbed pump powers of 31 W, the power transfer rolls over once more.

The origins of this extended rollover phenomenon was not explored during the experiment; however, one hypothesis is that the behaviour could possibly be

explained by parasitic lasing, similar to the behaviour of the 430 µm pump radius in Figure 3.17, where the peak wavelength of the fluorescence is plotted against absorbed pump power, especially as the pump beam radius is the same in both cases. Figure 3.20 shows the power transfer taken with a pump and seed beam radii of 430 µm, from Figure 3.19, on its own. In this figure, the power transfer has been split into two parts, to illustrate the how parasitic lasing may be a possible explanation for the abnormal power transfer.

Figure 3.20 shows the power transfer for the 430 µm pump and seed beam radii again but splits the power transfer into two parts. The first part, displayed in red, shows the power transfer up to an absorbed pump power of 22.6 W. The second part, in blue shows the rest of the power transfer for absorbed pump powers above 22.6 W. The graph has been split as such because, after an absorbed pump power of 22.6 W, the gradient of the power transfer changes. At the end of the red section of the graph, it appears that the power transfer is beginning to rollover, as observed with the 570 µm and 800 µm data in Figure 3.19. In the blue section of the graph, the gradient of the power transfer begins to increase again until it reaches another rollover point at 31.1 W of absorbed pump power.

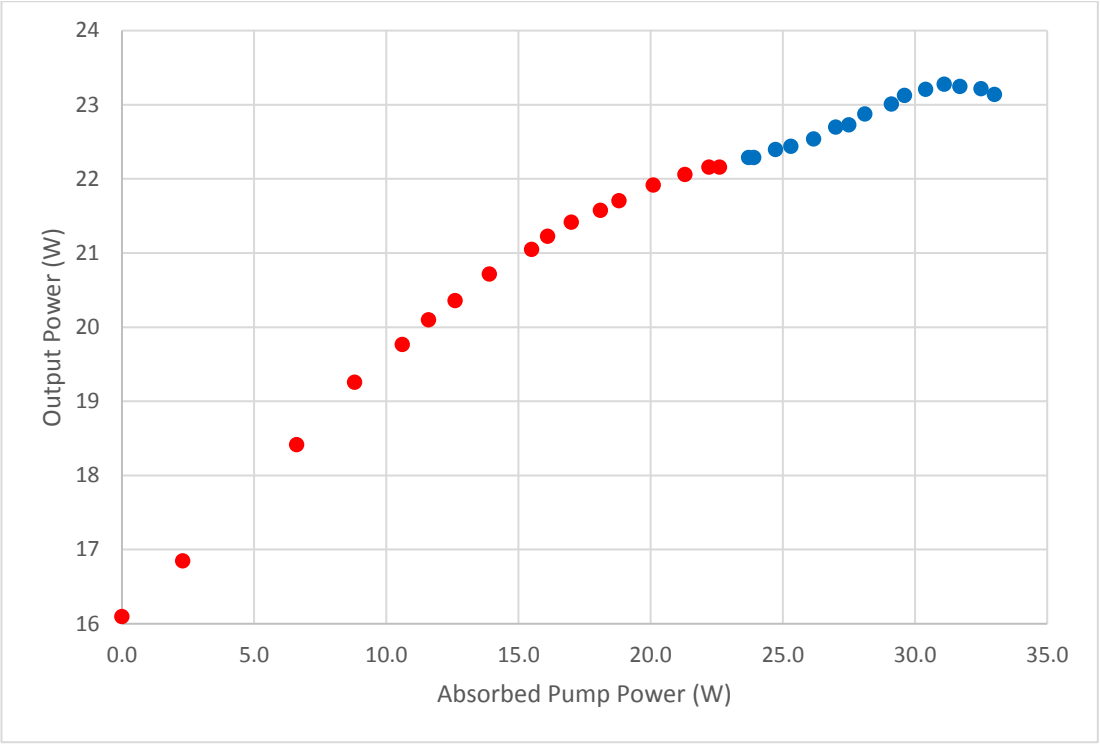

Figure 3.20 – A power transfer for a pump and seed beam radii of 430 µm. The power transfer is split into two sections. The red section shows the power transfer for absorbed pump powers up to 22.6 W. The blue section shows the power transfer for absorbed pump powers above 22.6 W. The red section of the power transfer is consistent with other power transfers taken at larger spot sizes, however, the blue section is abnormal as the gradient of the power transfer begins to increase again.

It has been observed that there are distinct transitions in the peak small-signal gain as a function of pump power due to ASE and parasitic lasing [35]. In Figure 3.20, there is an obvious change in the power transfer between the red and blue sections. A parasitic laser reaching threshold at the point between the red and blue sections could lead to a reduction in the temperature within the gain medium, due to fewer ions decaying through lifetime quenching processes, and the change in gradient for the power transfer due to the small-signal gain as a function of the pump power changing. A decrease in temperature would lead to a larger stimulated-emission cross-section, however, any parasitic laser would reduce the small-signal gain for the amplifier at the same time.

Figure 3.17 shows how the peak wavelength of fluorescence shifts with absorbed pump power, and in this figure, for the 430 µm pump beam radius, the change in the trend of the graph occurs at an absorbed pump power of approximately 16 W; however, in Figure 3.20 the change in trend appears at a higher absorbed pump power of approximately 23 W. If these changes in the trends of both graphs were caused by parasitic lasing, the variation in absorbed power could be explained by the fact that when the amplifier is being seeded, as is the case in Figure 3.20, the stored energy within the gain medium is reduced by the seed beam, which would lead to a smaller gain for the parasitic laser, therefore increasing the threshold of the parasitic laser.

3.5.2 Modelling temperature rise in laser amplifier power transfers

Figure 3.21, Figure 3.32 and Figure 3.33 display the power transfers from Figure 3.19 individually, for spot radii of 430 µm, 570 µm and 800 µm, respectively. Alongside this data is the predicted power transfer from the double-pass model, using the fluorescence peak shift data from Figure 3.17 to predict the temperature, and therefore the stimulated-emission cross-section, at each absorbed pump power. In Figure 3.21, Figure 3.22 and Figure 3.23, the curves modelled in this way are labelled as “Model – Inferred Temperature Shift” as it is expected that the temperature rise as a function of absorbed pump power will be over-estimated as the gain medium was not seeded when the fluorescence spectrum was measured.

The other power transfer shown in each figure, labelled “Model – Adjusted Temperature”, displays the output from the double-pass model, but the temperature rise as a function of absorbed pump power has been adjusted to provide a better fit to the data. The fit was judged to be better by performing a standard estimate of error (SEOE) analysis with each model and the empirical data. In each figure, the SEOE was better for the “Model – Adjusted Temperature” data. In Figure 3.21, the SEOE for the “Inferred Temperature Shift” model was 1.93, compared to a value of 1.16 for the SEOE in the “Adjusted Temperature model. In Figure 3.22, the “Inferred Temperature Shift” model had an SEOE value of 1.84,

whereas the "Adjusted Temperature" model had a better value of 0.28. In Figure 3.23, the SEOE for the "Inferred Temperature Shift" model was 1.57, compared to a value of 0.13 for the SEOE in the "Adjusted Temperature model. In each case, the SEOE was better for the "Adjusted Temperature" model.

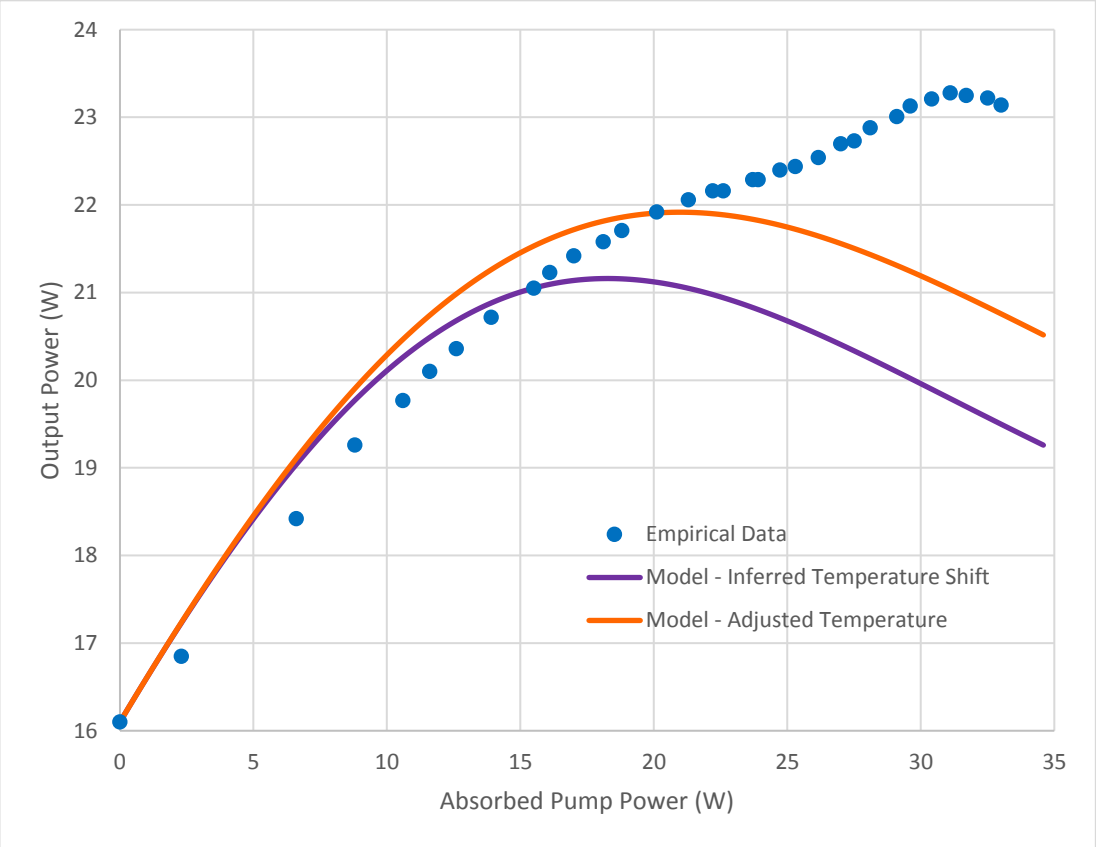

Figure 3.21 – Power transfers with pump and seed beam radii of 430 µm. The blue dots represent the experimental data. The purple line is from the double-pass model with the temperature increase as a function of absorbed pump power taken from the fluorescence spectra measurements shown in Figure 3.17*, and the orange line is from the double-pass model with the temperature increase as a function of absorbed pump power adjusted to provide an improved fit to the data.*

For Figure 3.21, at absorbed pump powers above 22.6 W, there is poor agreement between the models and the empirical data. It is believed that this might possibly be due to ASE or parastic lasing, as discussed in Section 3.5.1. The model does not incorporate the effects of ASE or parasitic lasing so cannot adequately predict the

behaviour of the laser amplifier if it is experiencing these phenomena. Future work would require exploring whether ASE or parasitic lasing was actually present and causing this lack of initial rollover in the power transfer and then, if that were the case, to incorporate it into the model to better predict amplifier performance.

In Figure 3.21, Figure 3.22 and Figure 3.23 it can be seen that the addition to the double-pass model of the temperature dependent stimulated-emission cross-section predicts a rollover in the power transfer. The purple power transfers displayed in Figure 3.21, Figure 3.22 and Figure 3.23, which show the data from the double-pass model where the temperature increase as a function of absorbed pump power was taken from the fluorescence spectrum shift data in Figure 3.17, underestimate the output power of the amplifier and predict the rollover to be more severe than it was in the empirical data. This is expected as the data taken from Figure 3.17 was taken in the unseeded case where the temperature increase should be higher than it would be if the amplifier were seeded. Seeding the amplifier reduces the temperature rise as fewer ions in the upper-state decay via lifetime quenching processes, such as ETU, which generate more heat.

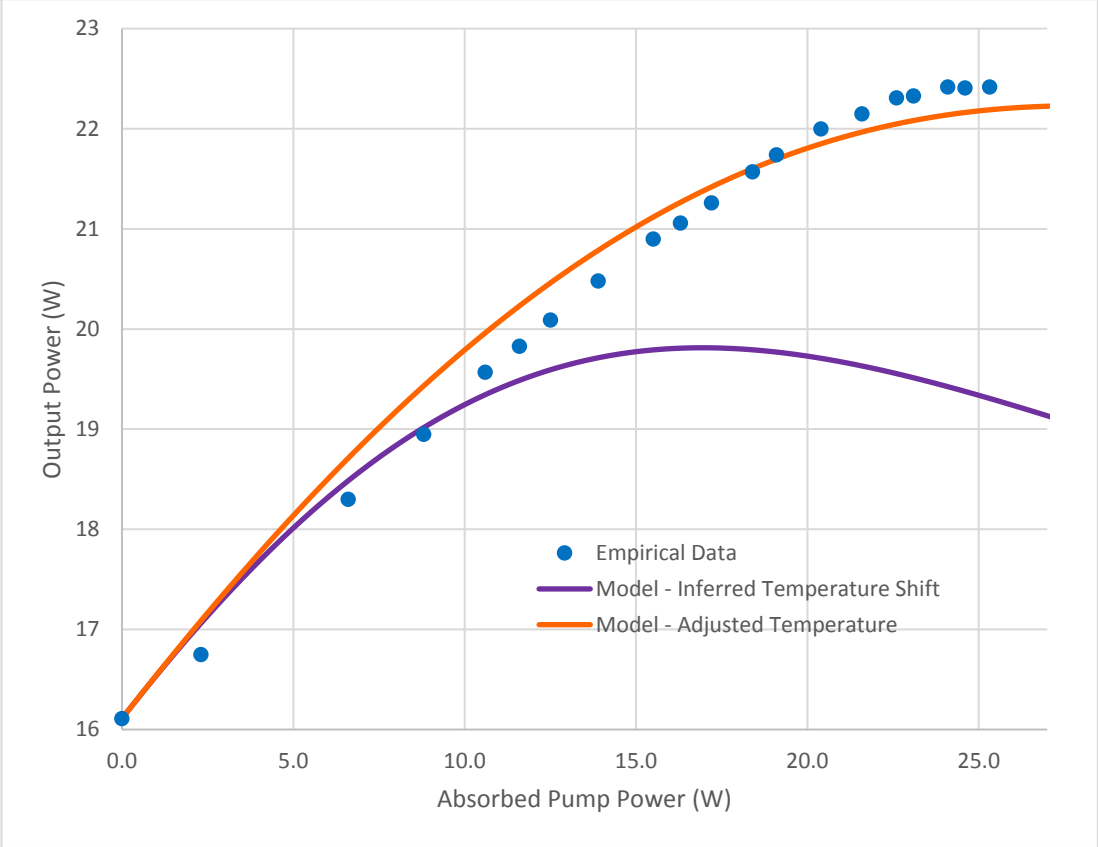

Figure 3.22 - Power transfers with pump and seed beam radii of 570 µm. The blue dots are the empirical data taken from the experiment. The purple line is from the double-pass model with the temperature increase as a function of absorbed pump power taken from the fluorescence spectra measurements shown in Figure 3.17, and the orange line is from the double-pass model with the temperature increase as a function of absorbed pump power adjusted to provide an improved fit to the data.

The double-pass model was adjusted by changing the gradient of the function of the temperature against absorbed pump power until it better matched the empirical data and is displayed in Figure 3.21, Figure 3.22 and Figure 3.23 as the orange line. In Figure 3.21, the model is adjusted to match the power transfer at the initial rollover, before the amplifier output power begins to increase again, which may be caused by other processes such as ASE or parasitic lasing which are not included in the amplifier model. Table 3.2 shows the gradients used based on the data from Figure 3.17, labelled “Inferred Temperature Shift”, and the orange curves, labelled “Adjusted Temperature” for each spot radius.

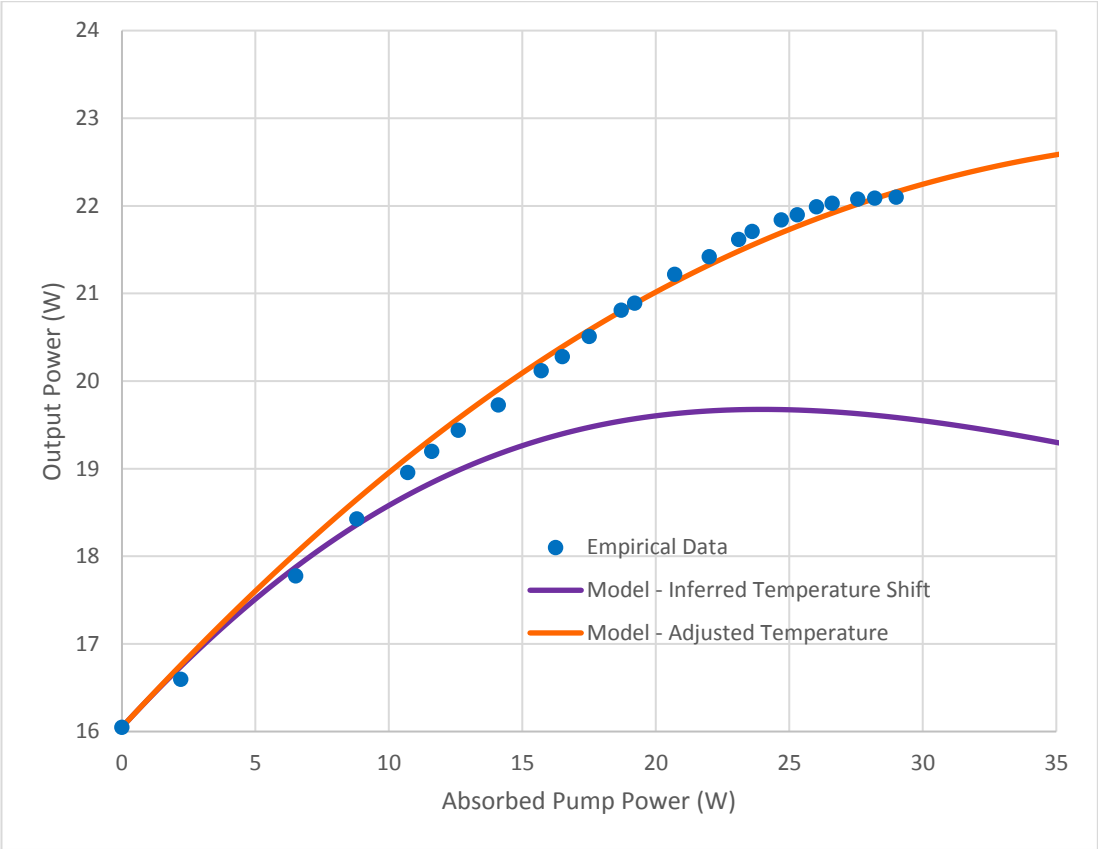

Figure 3.23 - Power transfers with pump and seed beam radii of 800 µm. The blue dots are the empirical data taken from the experiment. The purple line is from the double-pass model with the temperature increase as a function of absorbed pump power taken from the fluorescence spectra measurements shown in Figure 3.17 and the orange line is from the double-pass model with the temperature increase as a function of absorbed pump power adjusted to provide an improved fit to the data.

The adjusted model data provides an SEOE value of 0.32, 0.28 and 0.13 for the 430 µm, 570 µm and 800 µm cases, respectively. For the 430 µm case, this is ignoring the anomolyous data after the first rollover. This is a reasonable agreement with the empirical data and is evidence that the stimulated-emission cross-section shift and reduction with increased temperature is the source of the rollover in output power in the laser amplifiers discussed here. This would mean that significant increases in temperature are severely deleterious to the performance of

Nd:YVO_4 amplifiers and that high power amplification with this gain medium in a thin-disk configuration faces serious challenges in thermal management.

In Section 3.4.3, Figure 3.18 displays the peak wavelength of fluorescence as a function of absorbed pump power for a 2 atm % Nd:YVO_4 amplifier with and without a heat-spreader. Two diamond heat-spreaders were used in the experimental setup for Figure 3.18 and the pump beam radius was 0.7 mm. The gradient of the peak wavelength of fluorescence as a function of absorbed pump power is more than four times larger for the case without a heat-spreader in Figure 3.18, compared to the case with a heat-spreader.

Whilst the experimental setup used for Figure 3.18 was different from the experimental setup used in this section, the effects of the single SiC heat-spreader used in this section should not differ greatly from the two diamond heat-spreaders used in Figure 3.8. The performance of SiC and diamond as heat-spreaders should not differ greatly, as was explained at the end of Section 3.4.3 [18], and the secondary heat-spreader between the gain medium and the heat-sink should not perform as crucial a role in the system as the front heat-spreader. It is, therefore, reasonable to conclude that the use of a heat-spreader reduces the increase in temperature as a function of absorbed pump power considerably, enabling the amplifier to reach greater output powers before rolling over.

Some of the discrepancies between the empirical data and the adjusted double-pass model data can be explained by the simplifying assumptions made in the model. The model does not account for the effects of ASE and parasitic lasing. The model also assumes that the temperature increase as a function of absorbed pump power is linear which may not be the case. If the Nd:YVO_4 disk began to buckle, so as to impede heat-sinking, or if there was an increase in non-radiative decay with temperature then there may be deviation between the model and the experimental data. Such effects could account for the sharper rollover seen in the experimental data compared with the more gentle rollover predicted by the model.

		Inferred Temperature Shift		Adjusted Temperature	
Spot Size	Absorbed Pump Power at Rollover (W)	Gradient (nm/W)	Temperature at Rollover (°C)	Gradient (nm/W)	Temperature at Rollover (°C)
430 µm	23.9	0.0238	205	0.013	119
570 µm	25.3	0.0174	162	0.01	99
800 µm	29.0	0.0109	120	0.0055	68

Table 3.2 – The absorbed pump power at rollover is given for the three different beam radii, taken from the experimental data presented in Figure 3.21, Figure 3.22 and Figure 3.23, along with the gradients that describe the fluorescence shift as a function of absorbed pump power and the accompanying temperatures of the gain medium at those absorbed pump powers for that gradient. The "Inferred Temperature Shift" columns show the gradients and temperatures when using the data obtained from Figure 3.17. The "Adjusted Temperature" columns display the gradients that were adjusted to provide the best fit to the empirical data and the accompanying temperature at the rollover absorbed pump power.

Table 3.2 displays the absorbed pump power at rollover for varying spot sizes, taken from Figure 3.21, Figure 3.22 and Figure 3.23. It also shows the rate of change in the peak wavelength of the fluorescence of 1 atm % Nd:YVO_4 as a function of the pump power for both the "Inferred Temperature Shift" and "Adjusted Temperature" cases. Using both the absorbed pump power at rollover and the gradient, the temperature of the 1 atm % Nd:YVO_4 gain medium at rollover is inferred. From Table 3.2 it can be seen that the temperature at which rollover occurs varies for each spot size with the rollover occurring at lower temperatures for larger spot sizes. The rollover should occur when increasing the absorbed pump power leads to the amplifier gain decreasing rather than increasing. Increasing the absorbed pump power simultaneously increases the gain by increasing the inverted population within the gain medium but the temperature within the gain medium is also

increased causing a reduction in the stimulated-emission cross-section, which reduces the gain. The rollover occurs when the deleterious effects are greater than the beneficial effects, which will be different for differing amplifier parameters.

The discrepancy between the "Inferred Temperature Shift" and the "Adjusted Temperature" data was expected. The "Inferred Temperature Shift" data was created using the gradient for the peak wavelength of fluorescence as a function of absorbed pump power for each spot size, from Figure 3.17. For reasons discussed in Section 3.4.3, the amplifier in that instance was not seeded. Lifetime quenching effects are greatest in the absence of any energy extraction and, therefore, the temperature rise in the gain material is also at its greatest. It is a reasonable assumption that the "Inferred Temperature Shift" model would overestimate the heating within the gain medium in the presence of a laser seed beam, as is the case for Figure 3.21, Figure 3.22 and Figure 3.23. From Table 3.2, it can be seen that, for all three spot sizes, the peak wavelength of fluorescence as a function of absorbed pump power gradient is greater for the "Inferred Temperature Shift" compared to the "Adjusted Temperature" case, as expected. For the 430 µm beam radii, the "Inferred Temperature Shift" gradient is 1.8 times greater than the "Adjusted Temperature" gradient. For the 570 µm and 800 µm radii, the "Inferred Temperature Shift" gradients are greater than the "Adjusted Temperature" gradients by factors of 1.7 and 2.0, respectively.

It has been shown that, for 1 atm % Nd:YVO_4, the difference in the temperature increase between the lasing and non-lasing cases is approximately a factor of two [4]. For the amplifier parameters used in these experiments the gain is not saturated, as is the case for a laser, therefore, the difference in the temperature between the seeded and non-seeded gain media should not be as great as it is between a non-seeded gain medium and a laser. The saturation intensity for 1 atm % Nd:YVO_4, assuming a fluorescence lifetime of $97\,\mu s$ [4] and a stimulated-emission cross-section of $12x10^{-19}$ cm^{-2} [36], is $1.61x10^7$ W/m^2. The intensity of the 430 µm, 570 µm and 800 µm radii seed beams were $2.75x10^7$ W/m^2, $1.57x10^7$ W/m^2 and $0.80x10^7$ W/m^2, respectively. The

differences between the “Inferred Temperature Shift” and “Adjusted Temperature” gradients, shown in Table 3.2, appear to be reasonable when considering the limitations of the model discussed earlier.

In particular, the model highlights the importance of temperature for a Nd:YVO_4 thin-disk amplifier, due to the sensitivity of the stimulated-emission cross-section to changes in temperature. The model accurately predicts the rollover behaviour of the amplifier, showing the effects of varying various amplifier parameters, such as spot size. In order to achieve a higher output power from the laser amplifier, the next section describes an experiment where the seed beam was passed through the amplifier twice again, providing four passes through the gain medium with the added benefit of increased saturation of the gain and the subsequent decrease in temperature that it brings.

3.6 Multiple passes of the seed beam

This section describes an experiment that was performed utilising another double pass of the seed beam, providing four passes of the seed beam in total. By increasing the number of passes of the seed beam, the output power of the amplifier was increased. The increase in the seed intensity also provided an increase in the saturation of the amplifier and potentially a decreased heat load.

3.6.1 Power transfers with four passes of the seed beam

A rise in temperature leads to a reduction in the gain of the Nd:YVO_4 laser amplifier and, therefore, a reduction in extraction efficiency. This means there are more ions left in the upper-state, increasing heating through lifetime quenching processes, such as ETU. This compounds the problem in a vicious cycle. If there is greater saturation of the amplifier, there should be less heating and less reduction in the laser gain. With this in mind, an experiment was performed utilising another double pass of the seed beam, providing four passes of the seed beam in total. These four

passes serve to increase the seed intensity incident upon the amplifier and, therefore, increase the saturation of the amplifier and the output power.

In the experiments described in Section 3.5, the seed beam underwent a double-pass. In this section, the seed beam undergoes this double-pass and is then redirected and refocussed back onto the gain medium for another double-pass. This provides four passes in total, as seen in Figure 3.24, which shows the experimental setup used.

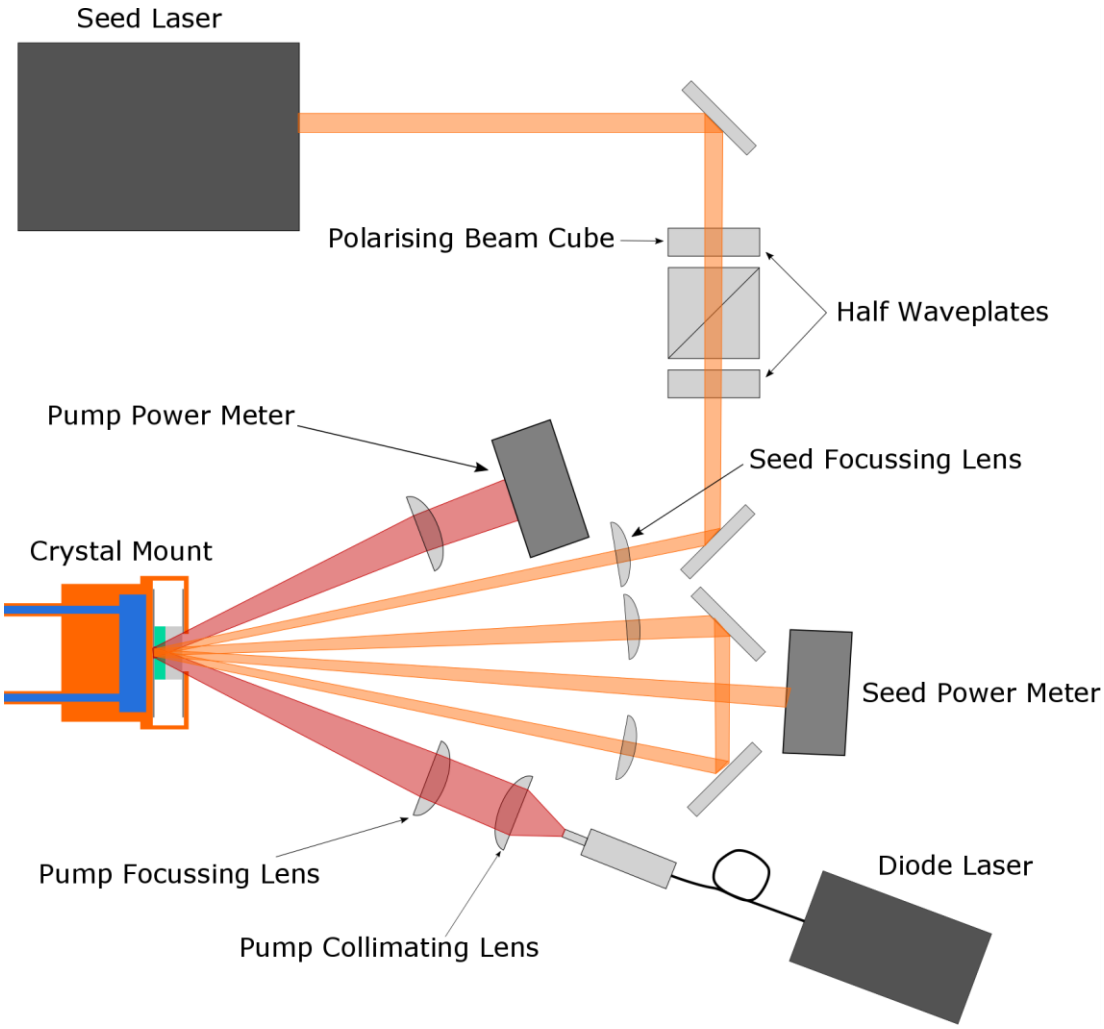

Figure 3.24 – Experimental setup for the 1 atm % Nd:YVO_4 amplifier with four passes of the seed beam.

The multiple, four-pass, experiment was conducted using the same seed beam radius of 430 µm for both the first double-pass and the second double-pass of the seed beam. The pump beam was also focussed to a radius of 430 µm. The gain medium was 250 µm thick, 1 atm % Nd:YVO_4, bonded to a SiC heat-spreader. The input seed power was 16 W. Figure 3.25 shows the power transfer for the four-pass experiment and also includes the power transfer from Figure 3.21, where a pump and seed beam radii of 430 µm was used and the seed beam underwent a double-pass within the 250 µm thick, Nd:YVO_4 gain medium.

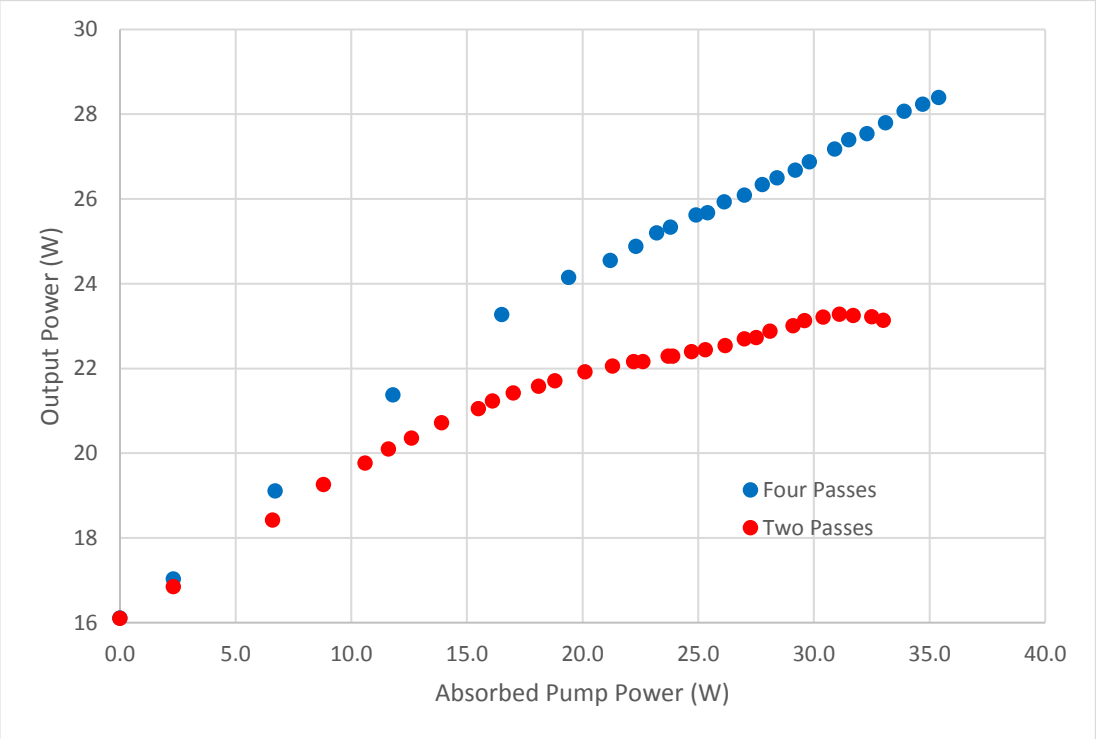

Figure 3.25 – Power transfers for four and two passes of the seed beam, both using a pump and seed beam radius of 430 µm.

The extra two passes through the gain medium, compared with the experiments in the previous section, doubles the length of the amplifier which leads to the power transfer being in the linear regime for longer and a higher output power, as can be seen from Figure 3.25. The higher saturation of the amplifier should also contribute

to the steeper gradient due to a reduction in the temperature rise in the gain medium, compared with the double-pass case. The four pass case has a maximum output power of 28.4 W at an absorbed pump power of 35.4 W, providing a gain of 1.78 and an extraction efficiency of 46 %. This is compared to the maximum output power of the two pass case, which is 23.3 W at an absorbed pump power of 31.1 W, providing a gain of 1.46 and an extraction efficiency of 31 %. The output power for the four pass amplifier was 5.1 W greater than the output power of the double pass amplifier and the extraction efficiency was greater by 15 %. In the double-pass data, rollover occurred at approximately 33.0 W of absorbed pump power. Rollover did not occur for the four-pass data before the maximum available incident pump power was reached.

Figure 3.26 shows the same empirical data as shown in Figure 3.25 but includes the modelled data for both the two and four-pass cases. For the power transfer with two passes of the seed beam, the modelled data is the same as that displayed in the "Adjusted Temperature" data in Figure 3.21. The laser amplifier model was adapted to add in another two passes of the seed beam, making four passes in total, which allowed the four-pass data to be modelled. The gradient of the fluorescence shift as a function of absorbed pump power for the four-pass case was 0.013 nm/W, the same as that used in the two-pass case in the same graph.

The four-pass modelled data does not fit the empirical data particularly well in Figure 3.26. At an absorbed pump power of 21.2 W, the power transfer for the four-pass amplifier changes in gradient and it is possible that other factors, such as ASE and parasitic lasing, that are not included in this model are affecting the power transfer. It might also be expected that the gradient of the fluorescence shift as a function of absorbed pump power might be smaller for the four-pass case when compared to the two-pass case due to the higher saturation of the laser amplifier, which would reduce the heating caused by lifetime quenching processes. This would serve to delay the rollover effect in the power transfer which would better match the empirical data, however, this would also make the discrepancies between the model and the empirical data worse when considering the non-

rollover portion of the power transfer, as shown in Figure 3.27. It is unclear why the modelled data does not agree well with the empirical data before rollover and this would require further exploration in any future work.

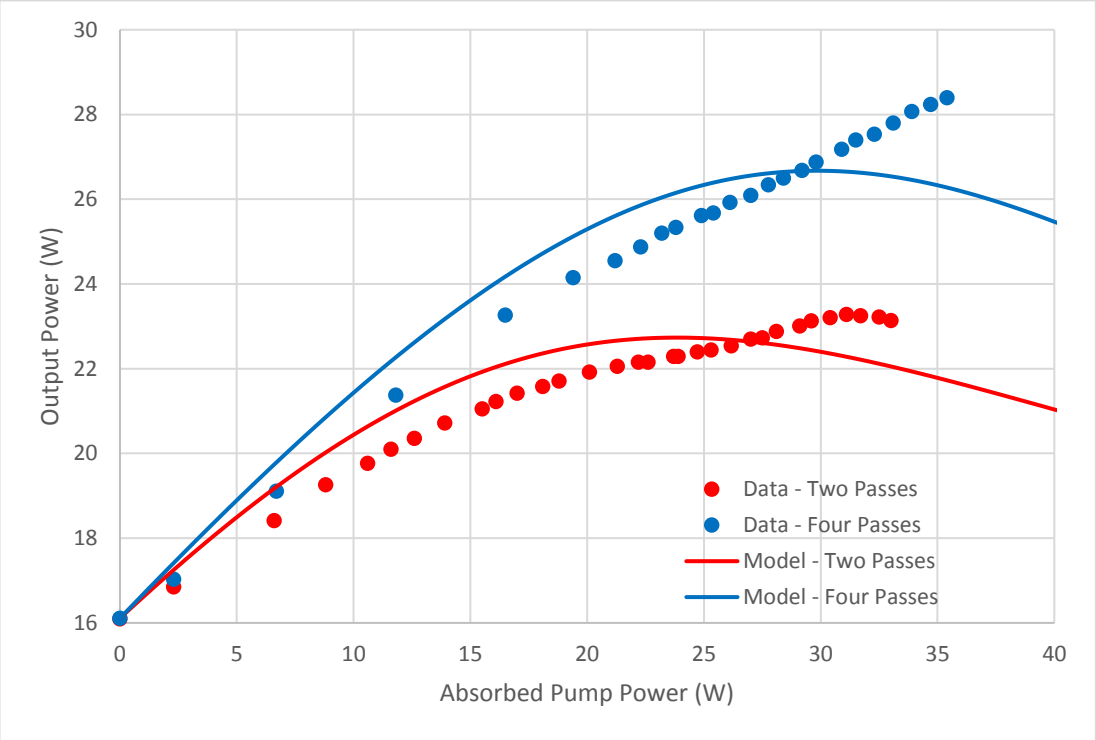

Figure 3.26 - Power transfer data for four and two passes of the seed beam, both using a pump and seed beam radius of 430 µm, shown in dots. The lines shown in the graph display the modelled power transfers for four and two passes of the seed beam at the same beam radius.

Figure 3.27 shows the empirical data for the four-pass power transfer again but here, the modelled power transfers have various values for the gradient of the fluorescence shift as a function of absorbed pump power. The fluorescence shift as a function of absorbed pump power with a value of 0.013 nm/W is the same gradient that is used in Figure 3.26 and can be seen again in Figure 3.27 as the lightest blue line, which has the lowest peak output power. None of the modelled data in Figure 3.27 adequately describes the empirical data, however, the modelled

data with fluorescence shifts that are smaller than in the two-pass case appear to agree more with the empirical data in terms of modelling the rollover behaviour, supporting the theory that the temperature increase is reduced with more passes and greater saturation of the amplifier. The modelled data with fluorescence shifts that are larger appear to better match the data at lower absorbed pump powers.

With the model adapted to incorporate four passes of the seed beam, more passes can be added to better understand the number of passes required to reach an output power of 100 W for different pump and seed radii.

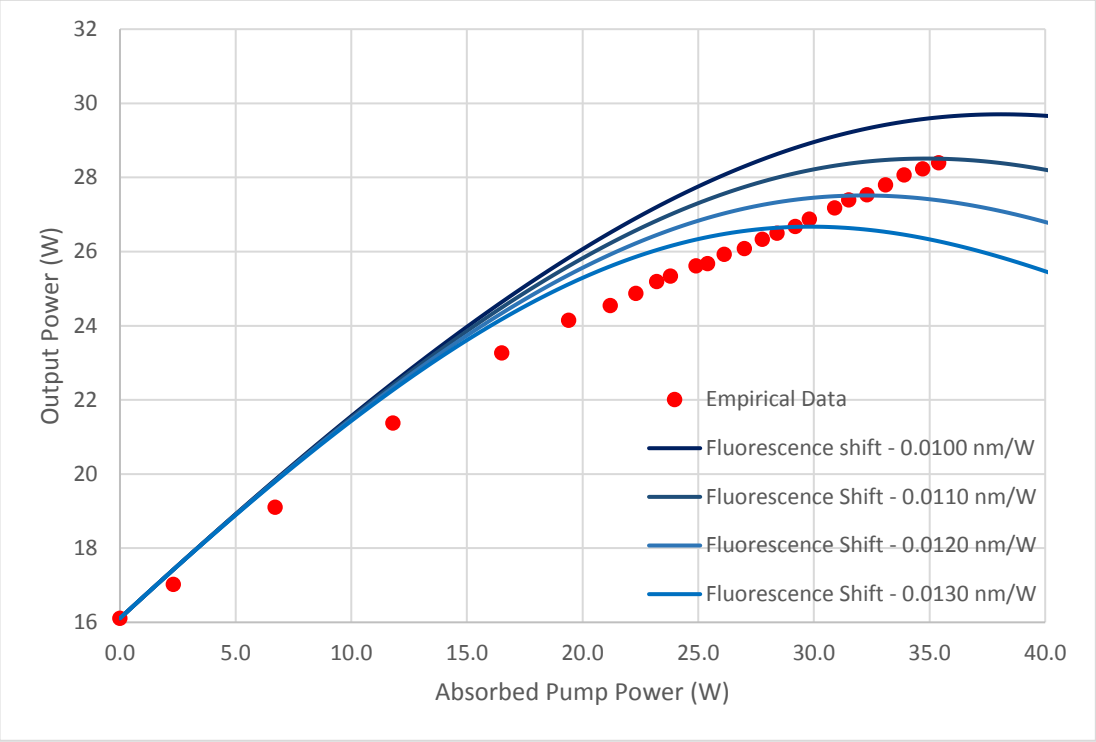

Figure 3.27 – A power transfer with four passes of the seed beam and a pump and seed radius of 430 µm. The empirical data is shown as red dots. The various lines are the modelled data taken with various gradients for the fluorescence shift as a function of absorbed pump power, shown in the graph legend.

3.6.2 Modelling many passes of the seed beam

The initial goal of the industrially led project that drove most of the work presented in this thesis was to achieve an amplifier output power of 100 W. To better understand the degree of complexity required to reach an output power of 100 W with an initial seed power of 16 W, the model used in the previous sections was adapted to provide any number of passes of the seed beam. Figure 3.28, Figure 3.29 and Figure 3.30 show power transfers for pump and seed radii of approximately 430 µm, 570 µm and 800 µm, respectively with various numbers of passes of the seed beam. The number of passes range from two to twenty four. To model the effects of temperature, a gradient for the fluorescence shift as a function of pump power was used for each model. The gradient for each spot size was taken from the "Fitted Temperature" column in Table 3.2 which should be an overestimation of the fluorescence shift as a function of absorbed pump power for a greater number of passes as discussed previously. The greater the number of passes of the seed beam, the greater the saturation of the amplifier and, therefore, the temperature rise should decrease. This means that the modelling in Figure 3.28, Figure 3.29 and Figure 3.30 could be an underestimation of the output power when the seed beam is passed through the amplifier multiple times.

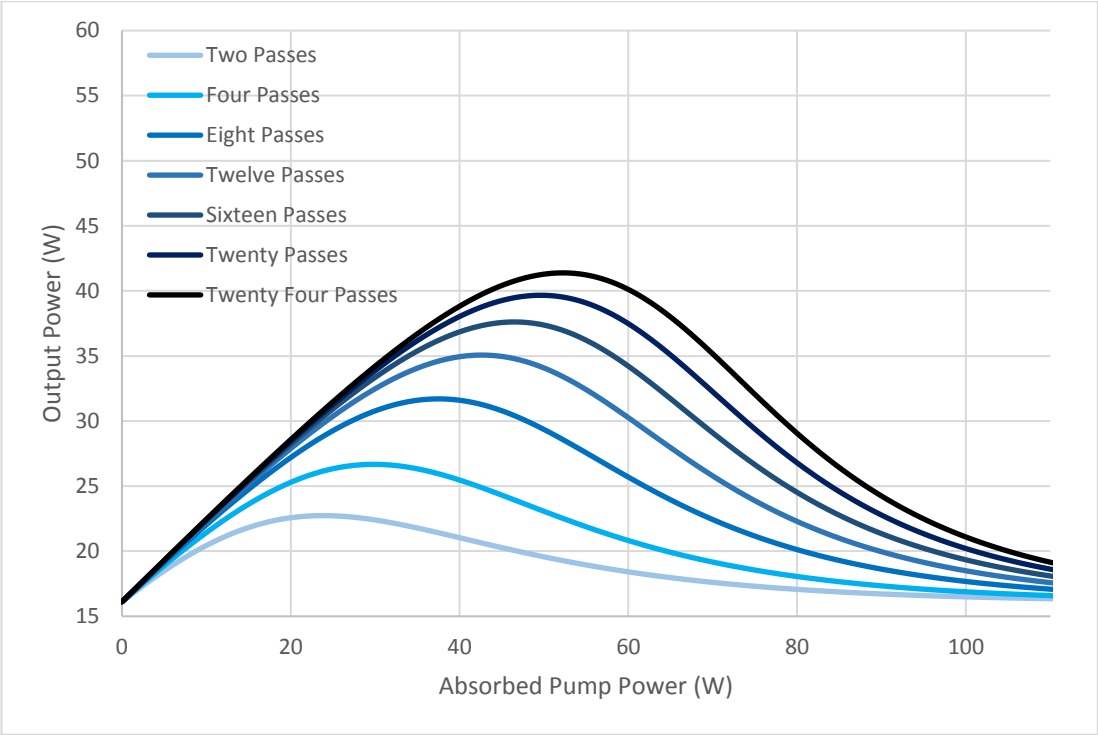

Figure 3.28 – Modelled power transfers, with a pump and seed beam radii of 430 µm, for various passes of the seed beam.

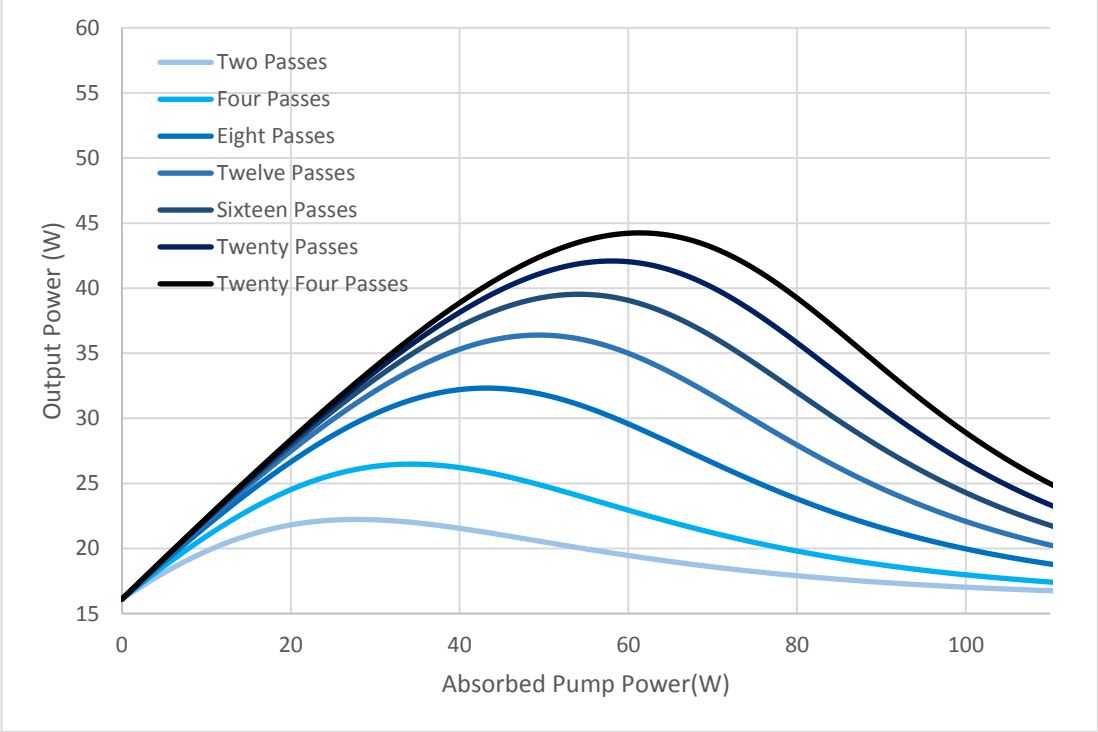

Figure 3.29 - Modelled power transfers, with a pump and seed beam radii of 570 µm, for various passes of the seed beam.

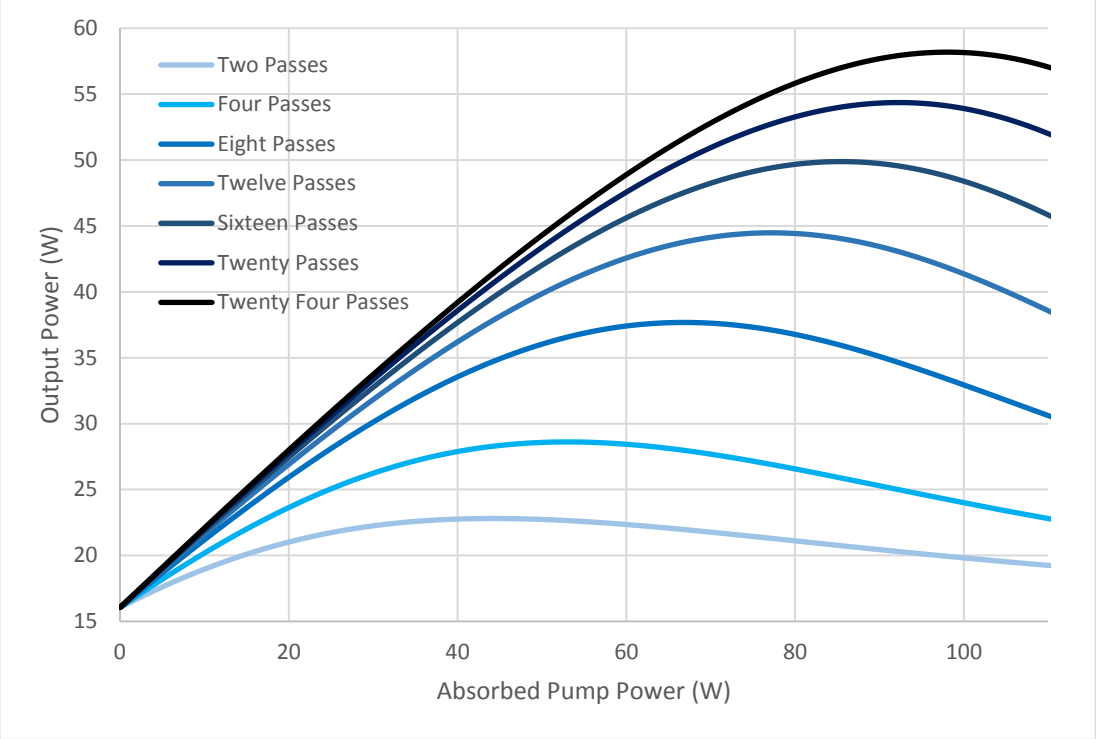

Figure 3.30 - Modelled power transfers, with a pump and seed beam radii of 800 µm, for various passes of the seed beam.

In all three figures, it can be seen that, for each extra pass of the seed beam added to the amplifier, there are diminishing returns with regards to output power. In Figure 3.28, after twenty four passes, the largest output power modelled was 41.4 W, providing a theoretical gain of 2.6. In Figure 3.29, after the same number of passes, the largest output power modelled was 44.2 W, with a gain of 2.7. In Figure 3.30, the largest output power modelled was 58.2 W, with a theoretical gain of 3.6. Figure 3.31 shows the theoretical gain of the laser amplifiers as a function of the number of passes of the seed beam for the three different pump and seed beam radii. A line of best fit has been added to each spot size in Figure 3.31. Extrapolating these lines of best fit, it would require approximately 900 passes of the seed beam for the 430 µm spot size case to reach an output power of 100 W. For the 570 µm spot size, approximately 440 passes would be required and, for the 800 µm spot size, 99 passes would be needed to reach an output power of 100 W.

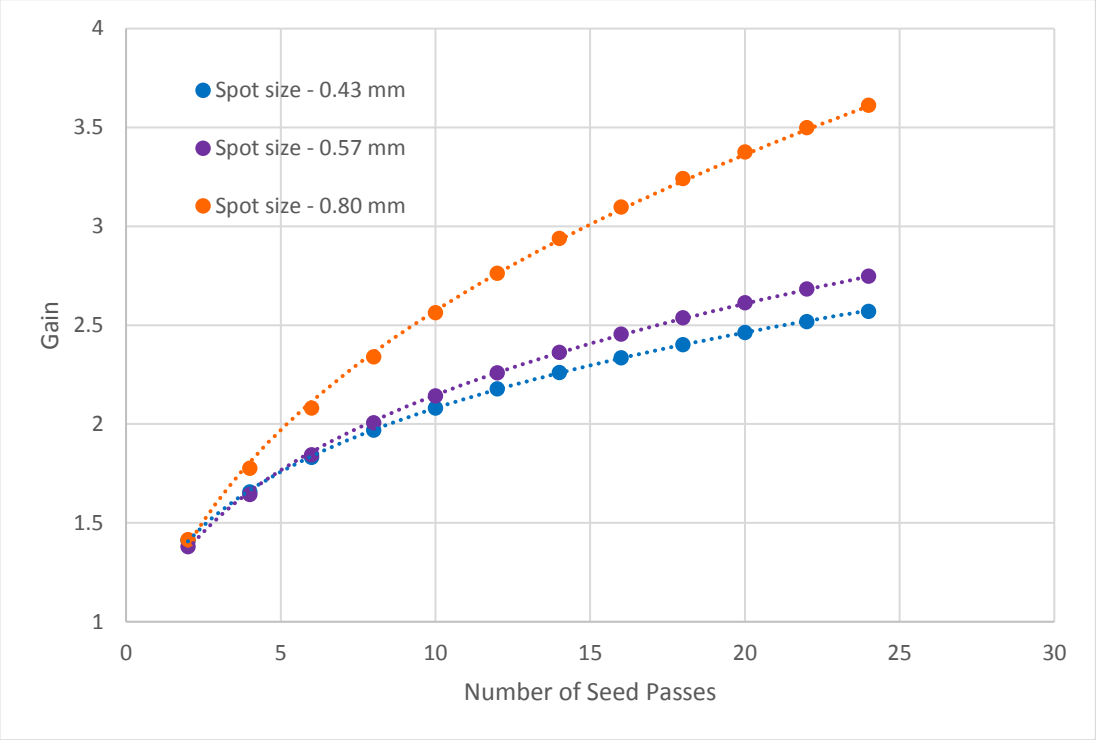

Figure 3.31 – The peak amplifier gain for various numbers of passes of the seed beam for three different pump and seed beam radii: 430 µm, 570 µm and 800 µm.

The modelling may underestimate the output power due to the gradient of the fluorescence shift as a function of absorbed pump power being too large but the model also does not take into account any deleterious effects that may arise from ASE or parasitic lasing. The number of passes of the seed beam required to realise an amplifier output power of 100 W, extrapolated from the data in Figure 3.31, should provide an estimate of the level of complexity required in the laser amplifier. Even the best case, using a pump and seed beam radius of 800 µm, requires almost 100 passes of the seed beam which would be difficult to manufacture. A higher power seed laser was acquired which should reduce the complexity required to reach an output power of 100 W and this is discussed in the next section.

3.7 Higher power input seed beam

This section describes experiments performed with a higher power input seed beam, supplying an average power of up to 34 W, more than double the input seed beam of approximately 16 W used for the previous experiments. This new seed source also operated at a higher repetition rate of 1 MHz. A higher power diode pump laser (DILAS IS11) was used as well, enabling an incident pump power of up to 300 W at a wavelength of 808 nm. This pump laser delivered the pump beam to the experiment via a 200 µm fibre and both the diode laser itself and the fibre ends were water cooled with a chiller.

3.7.1 Double-pass power transfers with varying spot sizes

Power transfers were taken again using the same setup as the previous experiments, described in Section 3.5, with a 250 µm thick, 1 atm % Nd:YVO_4 gain medium. Again, the gain medium was bonded to a SiC heat-spreader and the pump and seed beams were directed onto the gain medium once, which provides a double pass of both beams due to the reflection off the HR reflector at the back of the gain medium. For each power transfer, the pump and seed radii were the same size and four different pump and seed beam radii were used. Figure 3.32 shows the results of these experiments.

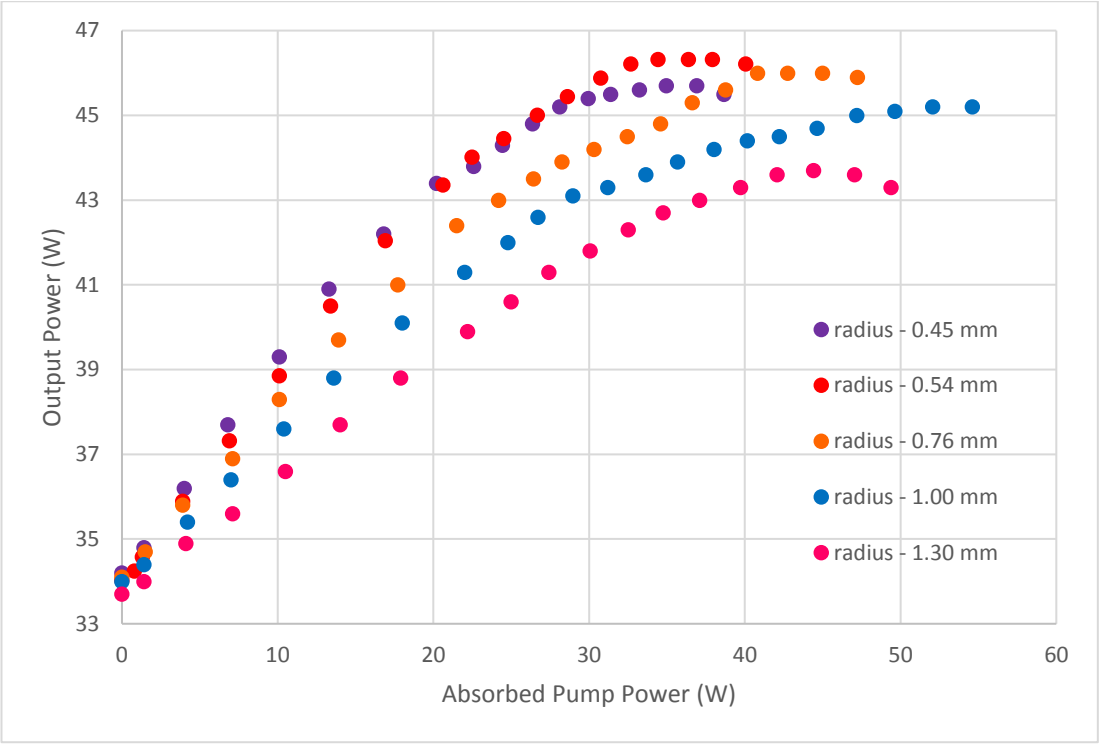

Figure 3.32 - Power transfers for the five different pump and seed beam radii used. The purple data represents the data taken with a pump and seed beam radius of 450 µm. The red data is for a pump and seed beam radius of 540 µm and the orange data is for a pump and seed radius of 760 µm. The blue data is for radii of 1000 µm and the pink data for 1300 µm.

A summary of the results presented in Figure 3.32 is given in Table 3.3 below. The table highlights the maximum output power of the amplifier for each different spot size with the corresponding absorbed pump power for that maximum output power. The table then also displays the gain and the extraction efficiency of the amplifier for the given maximum output power at each spot size.

Similar trends are observed from Figure 3.32 as were observed in Figure 3.19, where the gain achieved for each spot size was similar and the extraction efficiency generally decreased as the spot size increased. The 450 µm and 540 µm spot radii are relatively close together compared to the other spot radii, therefore the trends observed from Figure 3.32 break down slightly between these two cases which may be due to small experimental differences.

Spot Size (µm)	Maximum Output Power (W)	Absorbed Pump Power at Maximum Output Power (W)	Gain	Extraction Efficiency (%)
450	45.7	35	1.34	44
540	46.3	34.4	1.36	47
760	46.0	40.8	1.35	38.7
1000	45.2	52.1	1.33	28.3
1300	43.7	44.4	1.29	28.7

Table 3.3 - The maximum output power for five different spot sizes is given alongside the absorbed pump power, the gain and the extraction efficiency of the amplifier, all at the corresponding maximum output power.

In Figure 3.32, it can be seen that the absorbed pump power at rollover is larger as the spot size gets larger, which is the same as in Figure 3.19 which shows three power transfers at different spot sizes for the 16 W seed laser. The rollover also occurs at higher absorbed pump powers in Figure 3.32 when compared to Figure 3.19. The greater input seed power used for the experiments presented in Figure 3.32 means there is more saturation of the amplifier gain which should reduce the temperature within the gain medium by reducing the effects of lifetime quenching processes. This delays the onset of the amplifier rollover, similar to what was observed in Figure 3.25, where the saturation was increased by doubling the number of passes of the seed beam. In Figure 3.32, the largest spot size, 1.3 mm, seems to defy the trend that larger spot sizes exhibit rollover at larger absorbed pump powers as the rollover occurs at an absorbed pump power of 44.4 W for the 1.3 mm spot size. It may be that for the 760 µm and 1000 µm spot sizes, there is some ASE or parasitic lasing occurring as there appears to be a change in the gradient of these power transfers, with the possibility that the rollover is delayed in these cases. The smallest spot sizes have the steepest gradients in Figure 3.32, which is also seen in Figure 3.19. This is because the higher pump beam intensity,

which is because of the smaller pump beam radius, leads to a greater increase in the gain of the amplifier per unit of absorbed pump power when compared with a larger pump beam radius.

Some comparison can be made between the data presented in Figure 3.19 and Figure 3.32, for the spot radii that are similar. The 430 µm radii, from Figure 3.19, can be compared with the 450 µm radii from Figure 3.32. The 570 µm radii, from Figure 3.19, can be compared with the 540 µm radii from Figure 3.32 and the 800 µm, from Figure 3.19, with the 760 µm, from Figure 3.32. While the output powers from Figure 3.32 are all larger than the output powers from Figure 3.19, due to the higher incident seed power, the gain and extraction efficiency can be compared. For the higher input seed powers, the extraction efficiency is greater for all cases when compared with the lower input seed powers. The extraction efficiency is greater by 8 % for the 430 µm and 450 µm comparison, greater than 9.6 % for the 760 µm and 800 µm comparison and 12 % greater for the 570 µm and 540 µm comparison. This trend is expected as the higher input seed power leads to a greater saturation of the amplifier gain. For the lower input seed powers, the gain is slightly greater when compared to the gain for the higher input seed powers. The gain is greater for the lower input seed powers by: 0.05 for the 430 µm and 450 µm comparison; 0.04 for the 570 µm and 540 µm comparison; and 0.03 for the 800 µm and 760 µm comparison.

Figure 3.33 displays the same power transfers that are presented in Figure 3.32 but with additional, modelled power transfers. Each spot size was modelled with the gradient of the fluorescence shift as a function of absorbed pump power adjusted to provide the best fit to the empirical data. All the modelled power transfers fit quite well to the empirical data with the exception of the 1300 µm spot size. The rollover always appeared at larger absorbed pump powers for the modelled data in comparison with the empirical data. This modelling meant that an estimate of the gradient for the fluorescence shift as a function of absorbed pump power could be found for each spot size and these are shown in Figure 3.34. Using this information, multiple passes of the seed beam were modelled to provide an indication of the

level of complexity required in the laser amplifier to reach an output power of 100 W. Power transfers with various seed passes, from two passes to twenty four, were modelled for the various pump and seed spot sizes shown in Figure 3.33.

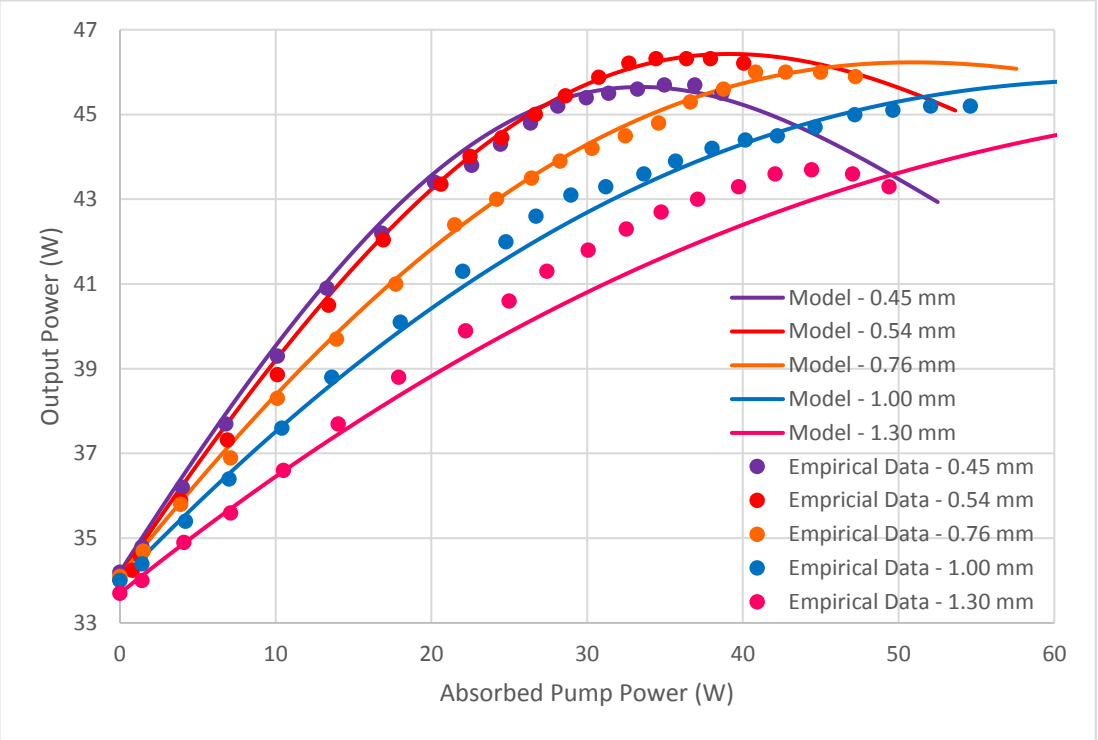

Figure 3.33 – The same power transfers displayed in Figure 3.32 with the addition of a modelled power transfer for each spot size.

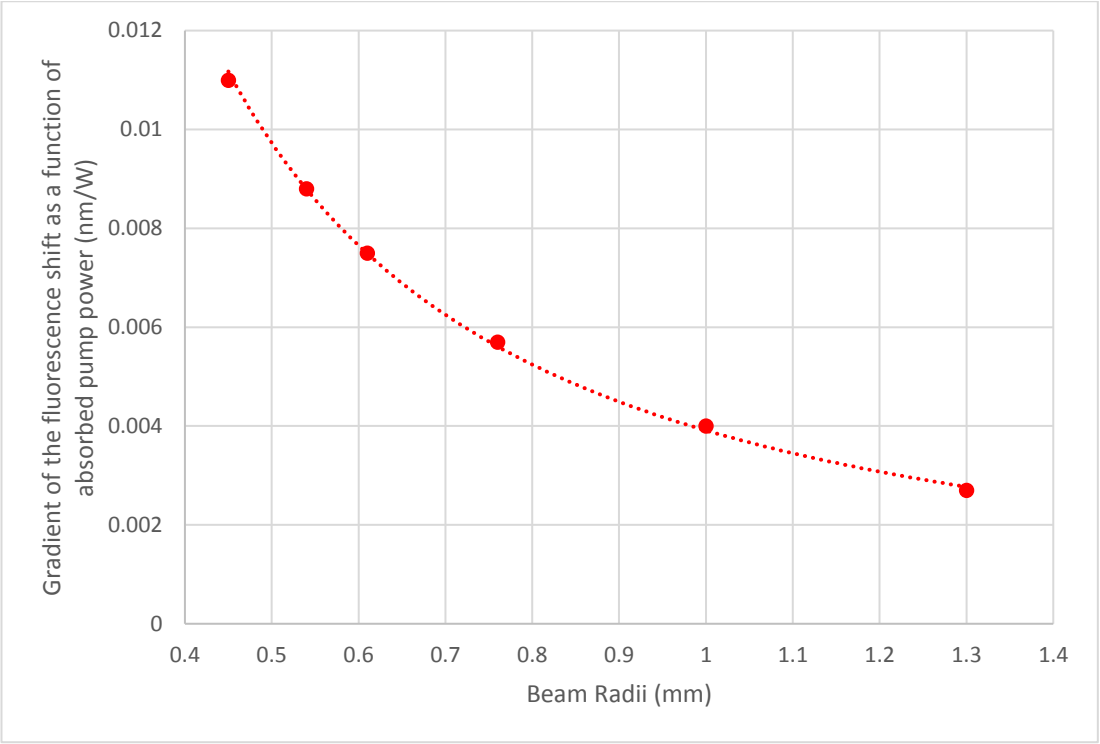

Figure 3.34 – The gradients of the fluorescence shift as a function of absorbed pump power are displayed for various pump and seed beam radii.

The multi-pass power transfers are displayed in the five graphs below, from Figure 3.35 to Figure 3.39. Figure 3.35 displays the multi-pass power transfers for a pump and seed beam radii of 450 µm and Figure 3.36 displays similar data for spot sizes of 540 µm. The pump and seed beam radii for Figure 3.37, Figure 3.38 and Figure 3.39 were 760 µm, 1000 µm and 1300 µm, respectively. As observed previously in Figure 3.28, Figure 3.29 and Figure 3.30, for a greater the number of passes of the seed beam, the returns diminish in terms of output power. The greatest number of passes of the seed beam in each graph is twenty four and, for this number of passes, the greatest output powers are: 69.5 W, with a gain of 2.0 for the 450 µm spot size; 74.9 W, with a gain of 2.2 for the 540 µm spot size; 85.8 W, with a gain of 2.5 for the 760 µm spot size; 96.5 W, with a gain of 2.8 for the 1000 µm spot size and; 112.1 W, with a gain of 3.3 for the 1300 µm spot size.

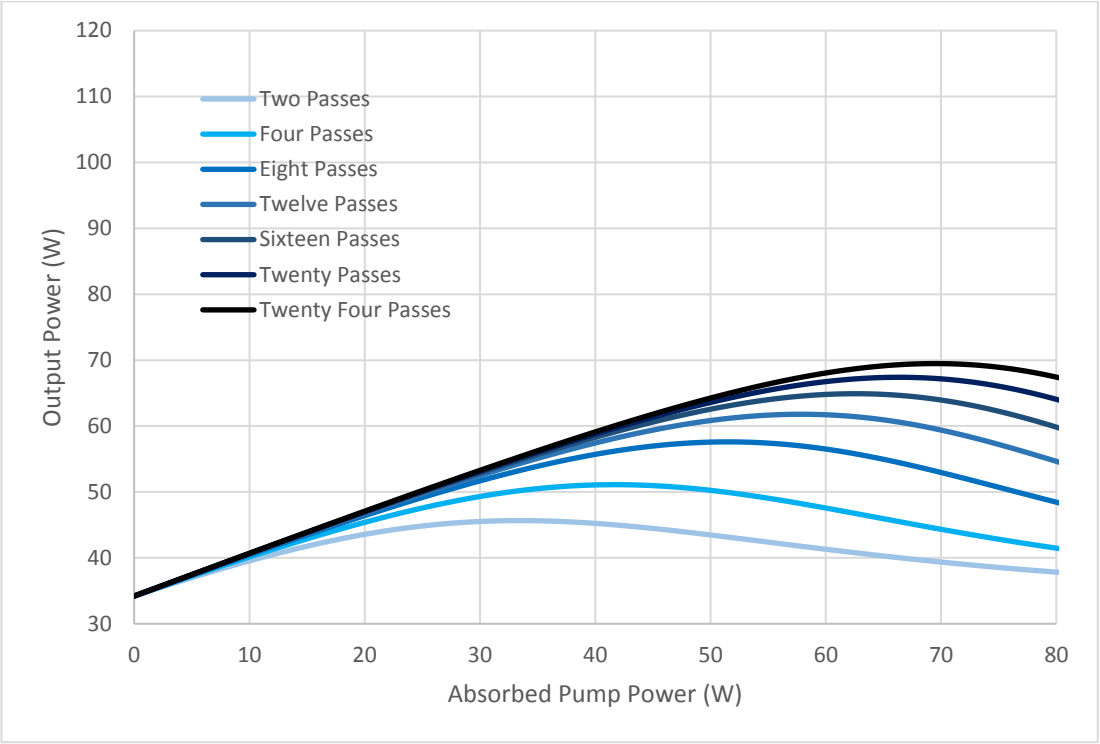

Figure 3.35 – Modelled power transfers, with pump and seed beam radii of 450 µm, with a varying number of passes of the seed beam.

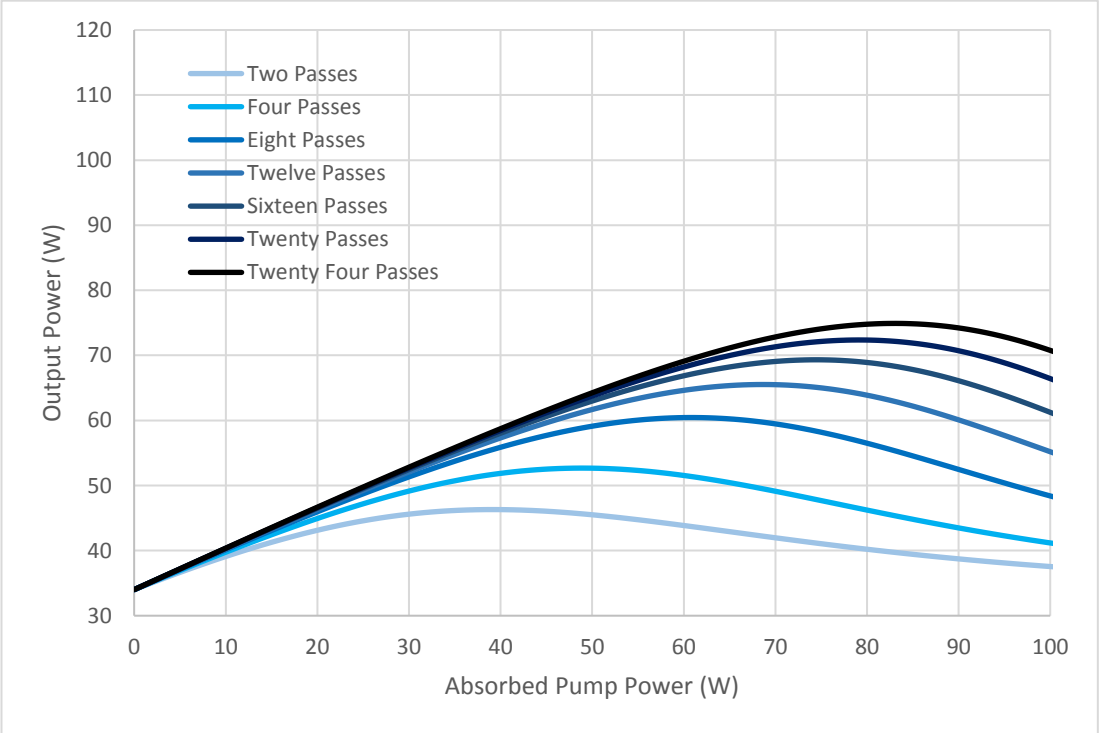

Figure 3.36 - Modelled power transfers, with pump and seed beam radii of 540 µm, with a varying number of passes of the seed beam.

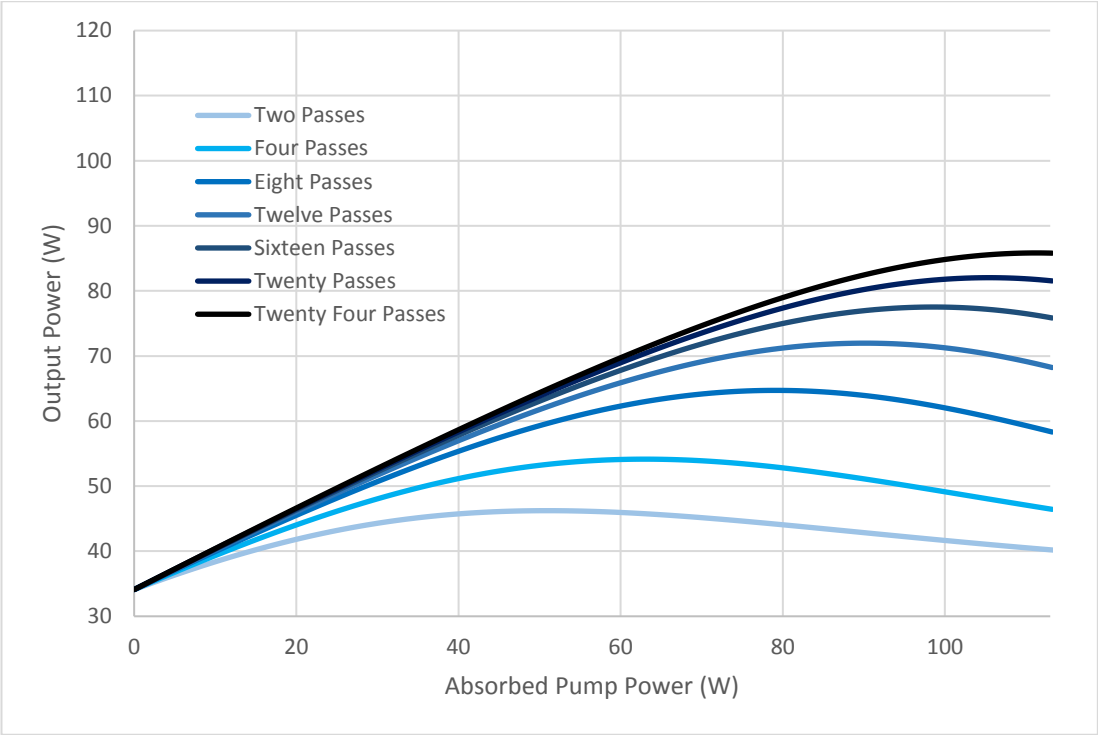

Figure 3.37 - Modelled power transfers, with pump and seed beam radii of 760 µm, with a varying number of passes of the seed beam.

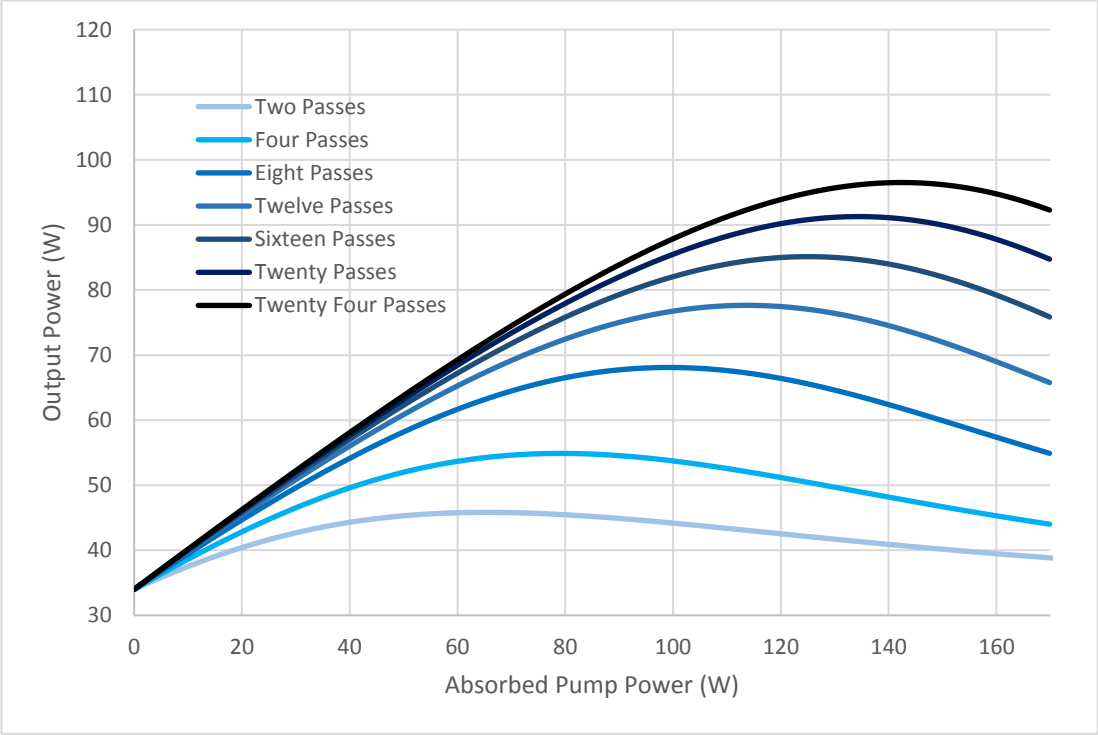

Figure 3.38 - Modelled power transfers, with pump and seed beam radii of 1000 µm, with a varying number of passes of the seed beam.

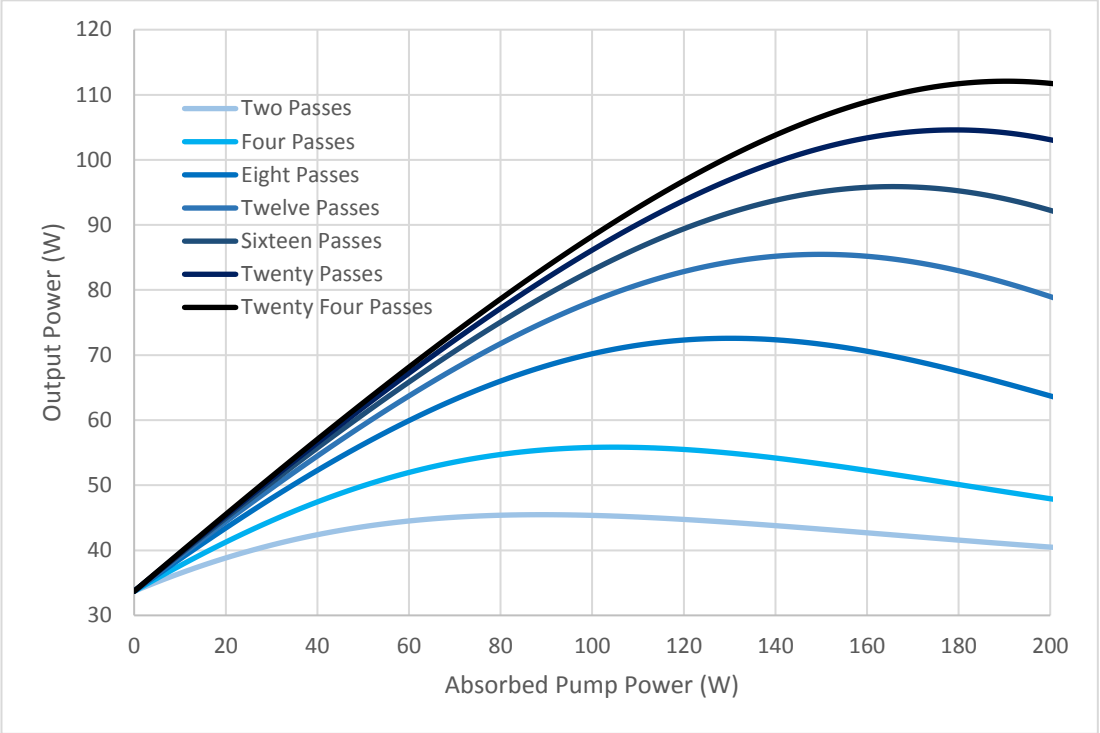

Figure 3.39 - Modelled power transfers, with pump and seed beam radii of 1300 µm, with a varying number of passes of the seed beam.

The peak amplifier gain as a function of the number of seed passes was plotted for each of the different spot sizes and is displayed in Figure 3.40. A line of best fit was added to each data set and the number of passes required to reach an output power of 100 W was, again, extrapolated from this line of best fit. For the case with the pump and seed beam radii of 450 µm, over 200 passes of the seed beam would be required to reach an output power of 100 W. The number of passes reduces to slightly over 100 for the 540 µm spot size and 45 for the 760 µm spot size. The spot size of 1000 µm would require 29 passes and the modelling of the 1300 µm pump and seed beam radii achieves an output power of 100 W within the parameters modelled, at 19 passes of the seed beam. The greater input seed power greatly reduces the number of passes required of the seed beam to reach an output power of 100 W. The larger spot sizes also show promise as they require fewer passes to reach the required output power.

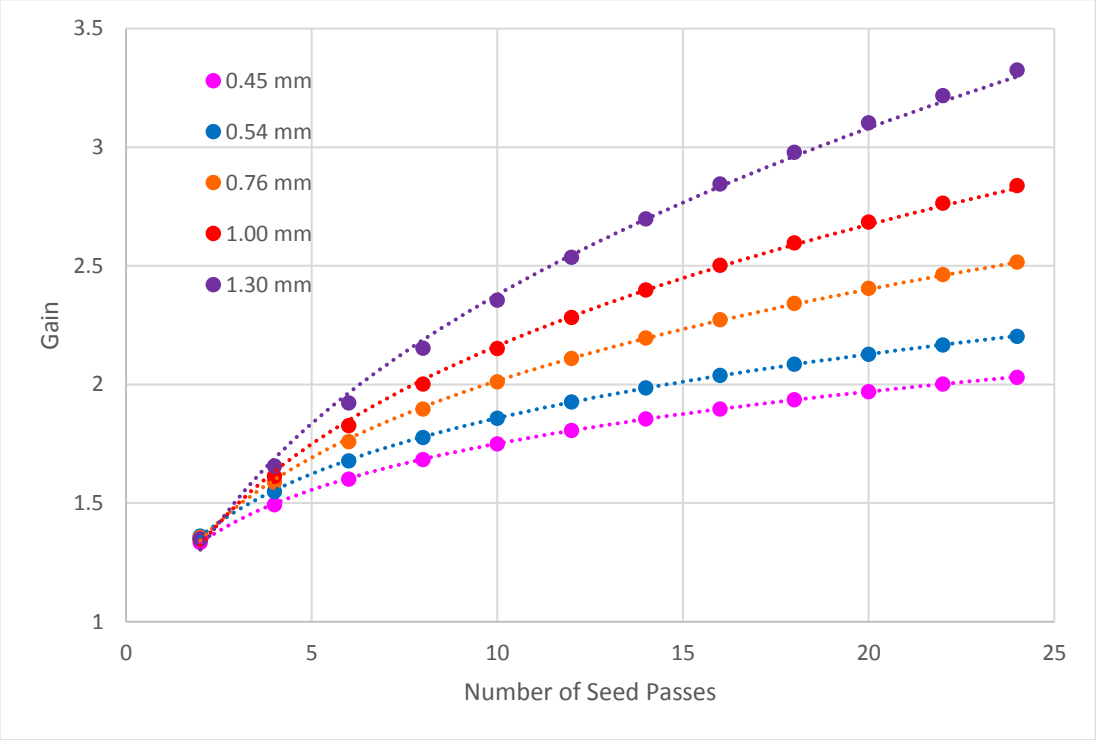

Figure 3.40 – The peak amplifier gain for various numbers of passes of the seed beam for various different pump and seed beam radii.

Whilst the laser amplifier model does not perfectly describe all aspects of the laser amplifier performance, it provides a good indication of which part of the parameter space to explore in future work, with the goal of achieving an output power of 100 W. Some appropriate next steps would be to implement more passes of the seed beam in order to corroborate the modelled data. The model may require more features to be added in order to correctly predict the performance of the laser amplifier, such as the addition of ASE. If the model performs well then the optimum pump and seed beam radii can be found to deliver an output power of 100 W in the fewest number of passes of the seed beam. The model suggests that with pump and seed beam radii of 1300 µm, 100 W of output power may be achievable in 19 passes of the seed beam. The modelling also suggests that larger pump and seed beam radii than 1300 µm may lead to an output power of 100 W in fewer passes. An interesting alternative amplifier architecture to explore would be to use multiple amplifier stages. The model shows the importance of the input seed power and so,

with multiple amplifier stages, the input seed power of each stage could be increased by the amplifier stage before it. This would have the benefit of decreasing the number of seed passes in each stage, therefore reducing the manufacturing complexity of each individual amplifier stage.

After exploring these options, it would then be the prerogative of the industrial partner in this project to decide if the complexity required in the laser amplifier is appropriate to their manufacturing capabilities. The output power and complexity, however, is are not the only consideration for the amplifier. The output beam must have a high brightness which means that beam quality is also very important and this will be discussed in the next section.

3.7.2 Beam quality measurements

The pump beam is neither a Gaussian nor a top-hat beam shape, as shown in Figure 3.41. The blue data in Figure 3.41 shows a 1.00 mm radius pump beam measured using a knife-edge measurement. The noise in this measurement comes from uncertainties in the position of the knife-edge and in the output from the power meter. The red line is a modelled Gaussian beam with a radius of 1.00 mm and the purple line is a modelled top-hat beam, also with a radius of 1.00 mm. The measured pump beam is closer to the modelled Gaussian beam but it is not quite a Gaussian shape. Figure 3.42 shows the measured seed beam, also measured with a knife-edge measurement, in blue. The red line is a modelled Gaussian curve, fitted to the empirical data. The seed beam in this figure has a radius of 0.95 mm. Figure 3.43 displays the measured pump beam from Figure 3.41, in red, and the measured seed beam from Figure 3.42, in blue, overlapped with each other.

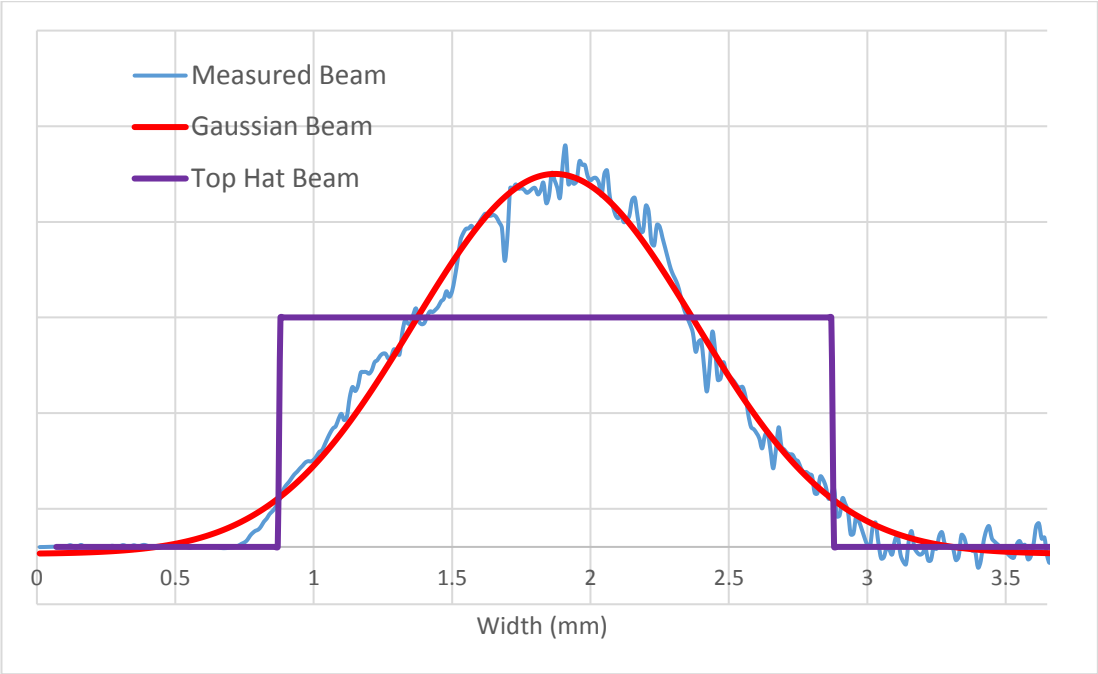

Figure 3.41 – a diagram of the pump beam with a radius of 1.00 mm. The blue line is the data taken from the knife-edge measurement. The red and purple lines show modelled Gaussian and top-hat beams, respectively, both with a radius of 1.00 mm.

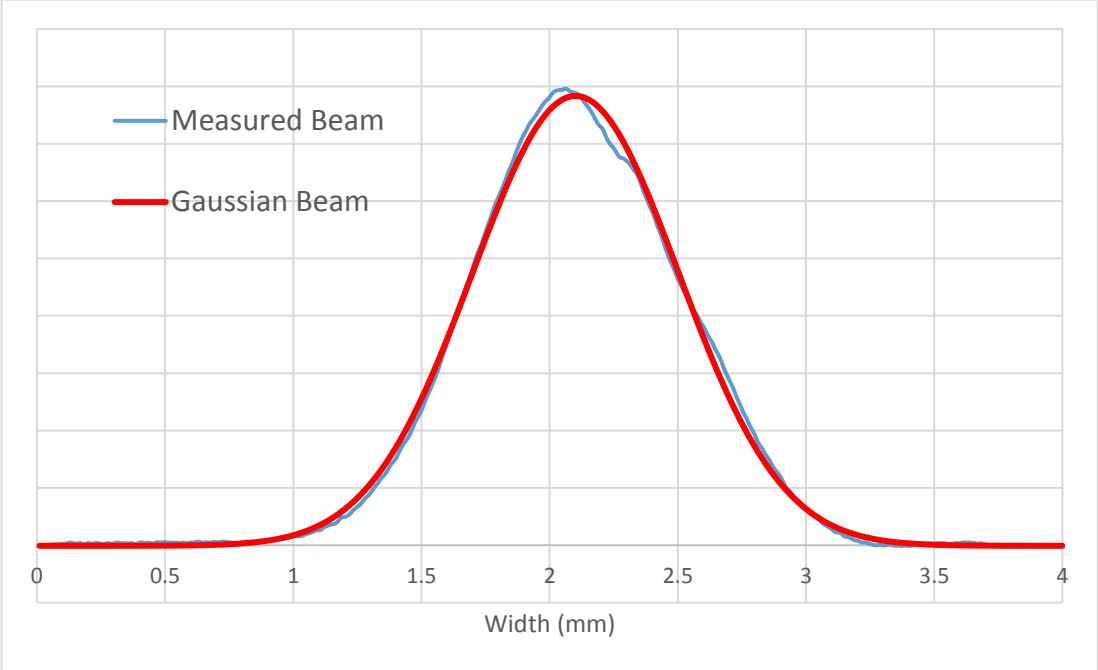

Figure 3.42 – a diagram of the seed beam with a radius of 0.95 mm. The blue line is the measured beam, the data taken using the knife-edge measuring method. The red line is a modelled Gaussian curve fitted to the empirical data.

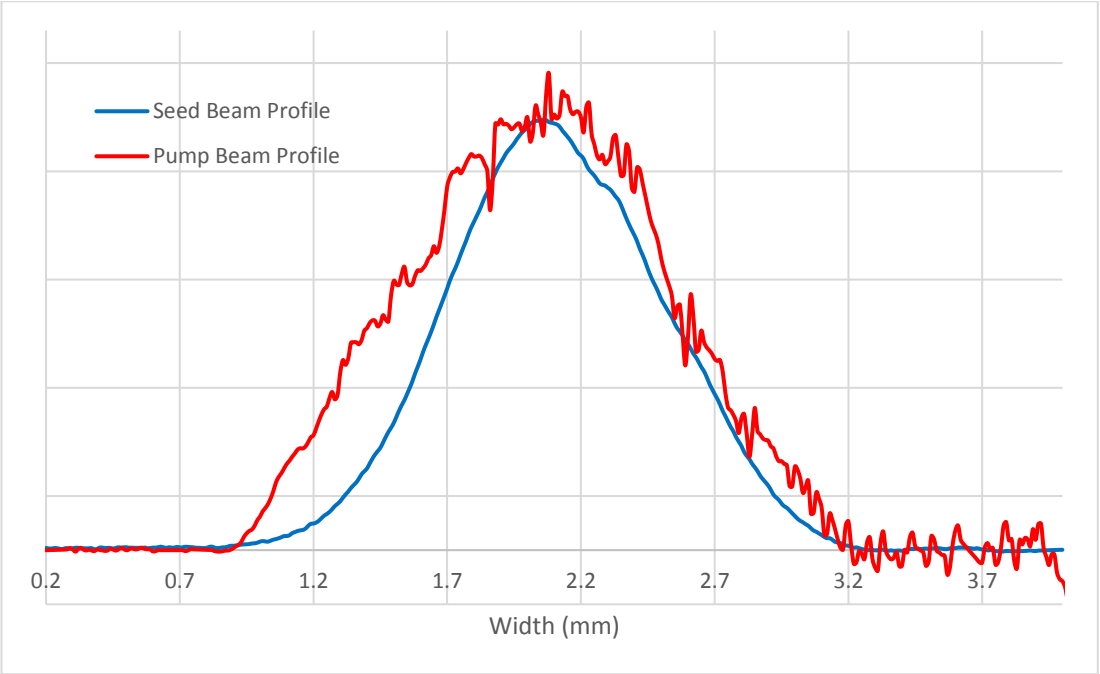

Figure 3.43 – a diagram of the pump and seed beams, overlapped with each other. The pump beam is in red, with a radius of 1.00 mm. The seed beam is in blue, with a radius of 0.95 mm.

When conducting the power transfer experiments discussed in Section 3.7.1, seed beam quality measurements were taken, using a Spiricon M^2-200, at three separate points in the power transfer, for each spot size with the exception of the 450 µm radii. The seed beam quality was measured after it had made a double-pass through the amplifier. The first beam quality measurement for each spot size was taken with no pump power incident upon the amplifier, so the amplifier was un-pumped. The second measurement was taken approximately in the middle of the power transfers and the third at the end of the power transfers, where the output power of the amplifier was beginning to rollover.

Initially, the pump and seed beams were maintained at the same radii and the results are shown in Figure 3.44 and Figure 3.45. Figure 3.44 shows the beam quality as a function of absorbed pump power and Figure 3.45 shows the beam quality as a function of output seed power. When measuring the beam quality, M^2

values were calculated for both the x and y axis and, for both Figure 3.44 and Figure 3.45, the geometric mean was calculated to give a single M^2 value for the beam quality. The beam quality of the seed beam before it entered the amplifier was 1.5 or less so, for the 1.0 mm and 1.3 mm spot sizes, the beam quality has already worsened without any pump power incident upon the amplifier, as can be seen in Figure 3.44 and Figure 3.45. The M^2 squared value for the 1.0 mm spot size is 1.63 at an absorbed pump power of 0 W and it is 2.17 for the 1.3 mm spot size, also at an absorbed pump power of 0 W.

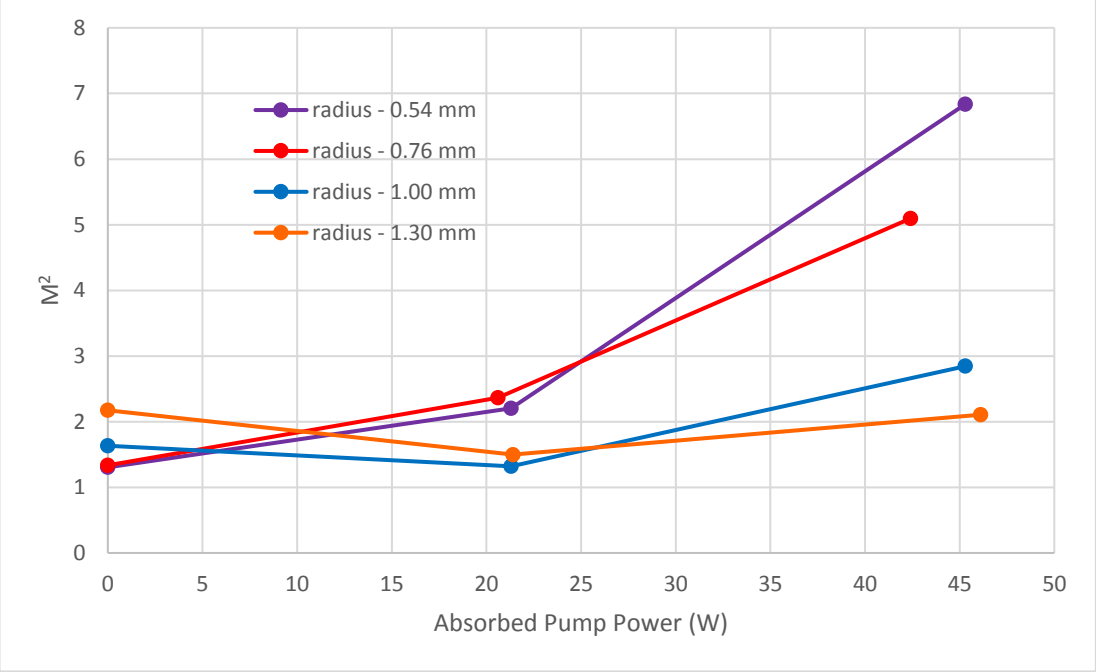

Figure 3.44 – this graph shows beam quality measurements, for four different pump and seed spot sizes, as a function of absorbed pump power. The pump and seed beam radii were the same for each case.

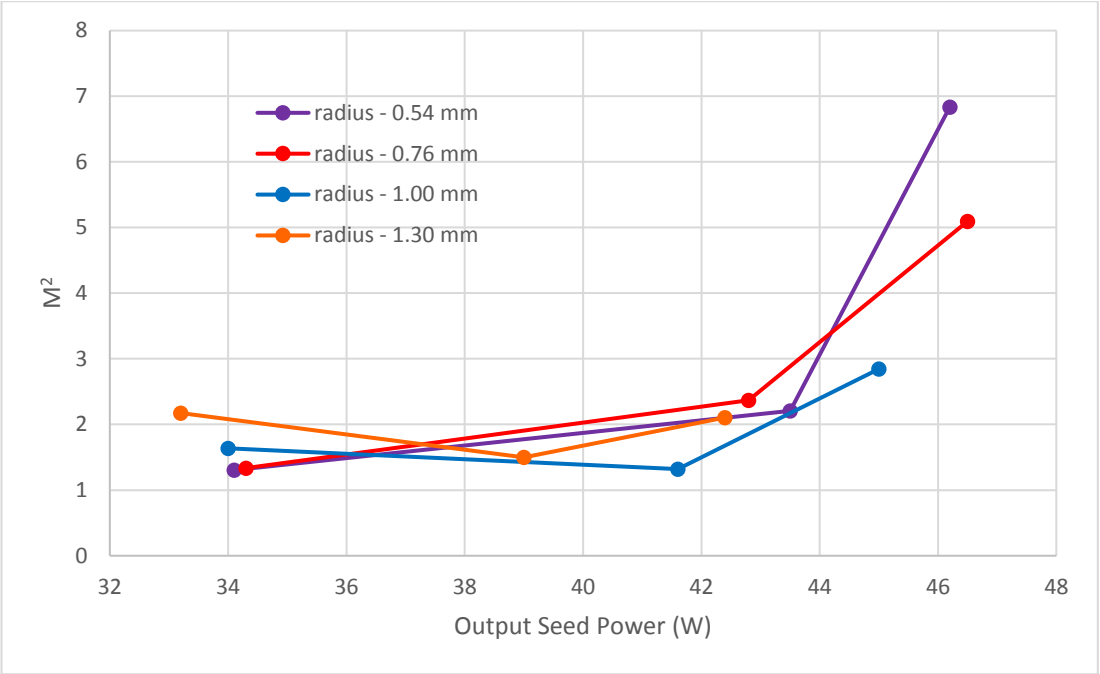

Figure 3.45 – this graph shows beam quality measurements, for four different pump and seed spot sizes, as a function of output seed power. The pump and seed beam radii were the same for each case.

For the 0.54 mm and 0.76 mm spot sizes, with no absorbed pump power, the beam quality is 1.30 and 1.34, respectively. For these two spot sizes, the beam quality deteriorates as the absorbed pump power is increased with the M^2 value of the 0.54 mm spot size case increasing to 2.20 at an absorbed pump power of 21.3 W and the M^2 value of 0.76 mm case increasing to 2.37 at an absorbed pump power of 20.6 W. The two larger spot sizes of 1.00 mm and 1.30 mm have a poorer beam quality than the smaller beam sizes for the un-pumped case, with M^2 values of 1.63 and 2.17, respectively. However, unlike the two smaller beam sizes, the M^2 values for the two larger beams actually improve when measured in the middle of the power transfer. The 1.00 mm spot size case has an M^2 value of 1.32 at an absorbed pump power of 21.3 W and the 1.30 mm case has an M^2 value of 1.5 at an absorbed pump power of 21.4 W. For the M^2 values measured around rollover, every spot size gets worse. The 0.54 mm spot case has an M^2 value of 6.84 at an absorbed pump power of 45.3 W and the 0.76 mm case has an M^2 value of 5.10 at an

absorbed pump power of 42.4 W. The 1.00 mm spot size case has an M^2 value of 2.84 at an absorbed pump power of 45.3 W and the 1.30 mm case has an M^2 value of 2.11 at an absorbed pump power of 46.1 W.

The beam quality degrades for all spot sizes when taken at rollover but the two smaller spot sizes experience the worse degradation. The beam quality for the 0.54 mm spot size case, from the un-pumped M^2 measurement to the M^2 measurement taken at rollover, goes from 1.30 to 6.84, changing by 5.54, which is the largest degradation in beam quality. The 0.76 mm spot size case undergoes a similar degradation, although by a smaller value, with the M^2 value changing by 3.76 from 1.34 to 5.10. The two larger spot sizes do not experience as great a change in beam quality, with the beam quality of the largest spot size case, of 1.30 mm, actually improving.

The beam quality of the 1.00 mm case changes from 1.63 to 2.84, giving a change of 1.21. The beam quality of the 1.30 mm spot size case improves by 0.06, changing from 2.17 for the un-pumped amplifier case to 2.11 at rollover. The beam quality degradation for the larger spot sizes with an un-pumped gain medium could be due to possible stresses induced in the gain medium during the bonding and mounting process of the crystal. The larger beam radii would experience a greater distortion from stresses in the gain medium than the smaller beam radii and this would appear to be alleviated when the gain medium is pumped, although nearly all of the spot size cases experience a deterioration in beam quality when the amplifier rolls over.

As the absorbed pump powers in the amplifier increase, the thermal effects will get stronger and this leads to poorer beam quality. For the same unit of absorbed pump power absorbed, the smaller pump sizes will experience a greater increase in pump intensity and, subsequently, greater temperature increases per unit of absorbed pump power, as well as more transverse heat flow leading to stronger and more aberrated thermal lensing, which explains the greater deterioration in beam quality.

The same setup was then used to measure the beam quality of the output beam as the seed beam radius was varied, with a constant pump beam radius. This experiment was performed to investigate if the beam quality of the output beam could be improved. The pump beam was kept at a constant radius of 1 mm and two absorbed pump powers of approximately 22 W and 42 W were used as these absorbed pump powers were similar to those used in Figure 3.44 and Figure 3.45. The seed beam radius was varied from approximately 0.45 mm to 1.3 mm for the absorbed pump power of 22 W and from approximately 0.5 mm to 0.9 mm for the absorbed pump power of 42 W. The seed beam radius was varied by a reduced range for the absorbed pump power of 42 W to ensure that the energy extraction from the amplifier was never too low in an attempt to ensure the temperature within the gain medium did not get too high which could lead to the fracture of the Nd:YVO_4 crystal. The output power of the amplifier was also measured for each point. Figure 3.46 and Figure 3.47 show the results of these experiments for absorbed pump powers of approximately 22 W and 42 W, respectively.

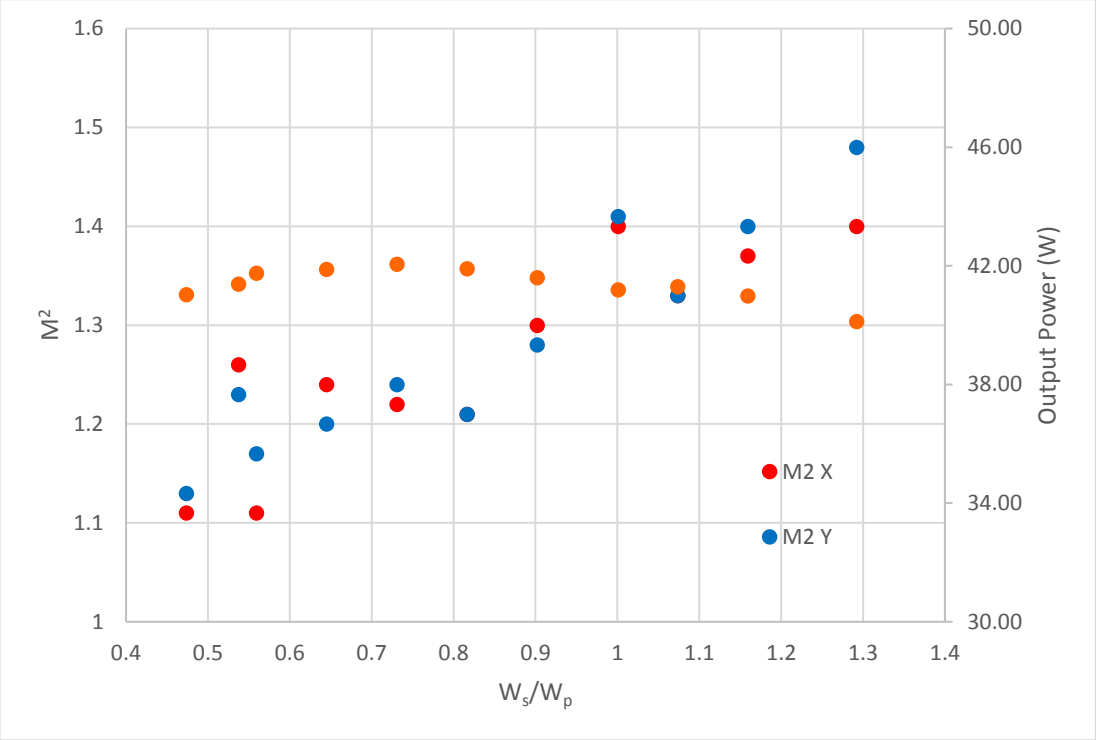

Figure 3.46 – The M_2 values for the X and Y axis are shown as a function of the ratio of the seed beam radius (w_s) to the pump beam radius (w_p). The pump beam radius was kept at a constant value of 1 mm. The M_2 values correspond to the left hand vertical axis. The output power is also shown on the right hand vertical axis and every measurement was taken for an absorbed pump power of approximately 22 W.

In Figure 3.46, where the data was taken with an absorbed pump power of approximately 22 W, it can be seen that the beam quality gets worse as the ratio of the seed beam radius over the pump beam radius gets larger. The geometric mean of the M^2_X and M^2_Y beam quality measurements, at a seed/pump beam ratio of 0.47, was 1.12. At a seed/pump beam ratio of 1.29, the beam quality was 1.44. This is an increase in the average M^2 value of 0.32. The same trend is observed in Figure 3.47, with an absorbed pump power of 42 W, where the average beam quality changes by 0.68, going from an average M^2 value of 1.22, at a seed/pump ratio of 0.56, to 1.90, at a seed/pump ratio of 0.9. The output power of the amplifier remains fairly constant in both Figure 3.46 and Figure 3.47. In Figure 3.46, the

minimum output power is 41.0 W, at a seed/pump ratio of 1.16, and the maximum output power is 42.1 W, at a seed/pump ratio of 0.73. The difference between the maximum and minimum output powers is 1.1 W. In Figure 3.47, the minimum output power is 44.9 W, at a seed/pump ratio of 0.47, and the maximum output power is 46.5 W, at a seed/pump ratio of 0.65. The difference between the maximum and minimum output powers is 1.6 W.

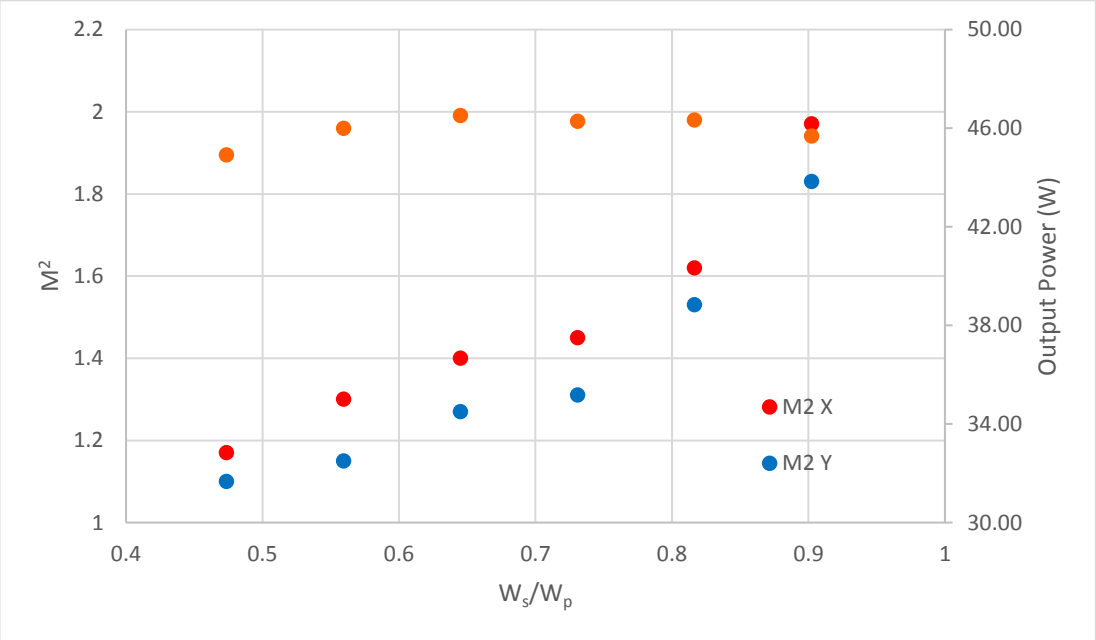

Figure 3.47 – The M_2 values for the X and Y axis are shown as a function of the ratio of the seed beam radius (w_s) to the pump beam radius (w_p). The pump beam radius was kept at a constant value of 1 mm. The M_2 values correspond to the left hand vertical axis. The output power is also shown on the right hand vertical axis and every measurement was taken for an absorbed pump power of approximately 42 W.

This does suggest that, with the careful selection of pump and seed spot sizes, good beam quality can be maintained which is important to maintain high brightness. By reducing the ratio of the seed beam radius over the pump beam radius, beam quality can be improved, even when the amplifier output power is rolling over. This is shown in Figure 3.47, where the M^2 value is below 1.5 for seed/pump beam ratios

of 0.73 and below, with a pump beam radius of 1.00 mm. It may be the case that, in order to maintain the beam quality and reach an output power of 100 W, the pump and seed spot sizes have to be larger than is optimal for simply power extraction. Making the pump and seed beam larger requires more passes of the seed beam in order to extract the required energy, which increases the complexity of manufacturing the amplifier.

3.8 Conclusions

This chapter explored the thin-disk laser amplifier architecture for the first time, with a double-pass of both the pump and seed beams. In order to incorporate the double-pass of both beams, the model had to be altered and the necessary theory required to update the model was introduced at the beginning of this chapter. The iterative, numerical approach utilised by the model was outlined before going onto the first experiments involving a thin-disk, Nd:YVO_4 laser amplifier that utilised two diamond heat-spreaders, to amplify a 16 W seed beam.

The experiments with the two diamond heat-spreaders were problematic as the front diamond heat-spreader was not anti-reflection coated for either the pump or seed wavelengths. This led to multiple reflections within the amplifier which made the collection of data more difficult; however, useful and informative results were still gleaned. The experiments were performed with both 1 atm % and 2 atm % Nd:YVO_4 crystals at three different pump and seed beam radii, showing that the 1 atm % Nd:YVO_4 consistently produced the highest output powers. It was observed that, for all the different parameters, each power transfer exhibited a rollover in output power.

This rollover in output power was caused by the stimulated-emission cross-section's dependence on temperature. As the temperature of the gain medium increased, the peak wavelength of the stimulated-emission cross-section moved to longer wavelengths and the cross-section became broader. An experiment was conducted that confirmed this was the phenomenon being observed in the Nd:YVO_4 gain

medium and the temperature dependence of the stimulated-emission cross-section was added to the model. In order to model the temperature rise as a function of absorbed pump power, an experiment was devised that measured the peak wavelength of fluorescence as a function of absorbed pump power. This data was taken in the absence of a seed beam due to the limitations of the experimental apparatus. Because of this, it was assumed that the temperature rise as a function of pump power taken from this data would overestimate the heating within the gain medium. This overestimation of the temperature rise was observed in the next set of experiments that were performed.

Power transfers were taken with the laser amplifier for three different pump and seed beam sizes, with 1 atm % Nd:YVO_4 as the gain medium. Instead of using two diamond heat-spreaders, as used previously, these experiments utilised a single SiC heat-spreader, bonded to the front of the gain medium, which was anti-reflection coated at the pump and seed wavelengths. This removed the previous issues caused by stray reflections. The data taken from these power transfers was compared with the modelled amplifier power transfers using the inferred temperature rise from the peak wavelength of fluorescence experiment. A second set of data was taken from the model but with the temperature rise as a function of pump power adjusted until the model data best fit the empirical data. This fitted data better matched the empirical data when compared with the inferred temperature rise data, with the temperature rise as a function of absorbed pump power being approximately half that of the inferred temperature case. This confirmed that the peak wavelength of fluorescence technique for measuring the temperature rise of the amplifier did overestimate the temperature rise as the amplifier was unseeded when measuring the change in the peak wavelength of fluorescence. The highest output power achieved in this group of experiments was 23.3 W from a 16 W input power, at an absorbed pump power of 31.1 W. That is a gain of 1.46 with an extraction efficiency of 30.9 %.

Another interesting observation was made during these experiments where, for the 430 µm pump and seed beam radii case, the output power appeared to rollover

before increasing again and undergoing a second rollover. It is not known for certain what the cause of this behaviour is, but one hypothesis is that it may be the effects of ASE or parasitic lasing within the gain medium. If ASE or parasitic lasing reduced the temperature within the gain medium, through the process of depopulating ions that would otherwise contribute greater temperature rises through lifetime quenching processes, then rollover could perhaps be delayed. This hypothesis could be tested in future work by adding the effects of ASE and parasitic lasing to the amplifier model and comparing the results with the empirical results that observe this secondary rollover behaviour.

Two additional passes of the seed beam were added to the experimental setup, to provide four passes of the seed beam in total, with pump and seed beam radii of 430 µm. As this doubled the amplification length of the amplifier, a greater output power of 28.4 W was achieved, at an absorbed pump power of 35.4 W. This gave the laser amplifier a gain of 1.78 and an extraction efficiency of 46.0 %. This was an increase in output power of 5.1 W over the double-pass amplifier. Importantly, there was no rollover in the output power before the available incident pump power was exhausted. The amplifier model was adapted to incorporate the four passes of the seed beam and the four-pass power transfer was modelled. The shift in the peak of the stimulated-emission cross-section shift as a function of absorbed pump power was adjusted to provide a better fit to the empirical data and, whilst none of the modelled data fit the empirical data as well as previous examples, the modelled data with a reduced gradient was closer which supports the idea that greater saturation of the amplifier gain reduces the temperature within the gain medium as fewer ions decay through lifetime quenching processes which produce more heat.

The laser amplifier model was adapted again to apply an even greater number of passes of the seed beam. Various numbers of passes were modelled at different pump and seed beam radii. This modelled data showed that there are diminishing returns in terms of output power when adding more passes of the seed beam and that allowing more passes benefits the larger spot sizes more than the smaller ones.

For the 430 µm spot size, the largest, theoretical output power, with twenty four passes of the seed beam, was 41.4 W, whereas, for the 800 µm spot size, the largest, theoretical output power with twenty four passes of the seed beam was 58.2 W. The data obtained was extrapolated to find the approximate number of seed passes that would be required to reach an output power of 100 W with 99 passes required with a spot size of 800 µm.

The previous experiments utilised an input seed laser that had a maximum output power of 16 W but a new seed laser was provided with a maximum output power of 34 W, which would provide greater saturation of the amplifier gain. These experiments used a double-pass of the seed beam. The cooling effect of higher saturation was observed again as the power transfers taken with the higher power seed beam reached higher absorbed pump powers than those with the lower power seed beam, for similar spot sizes. The highest output power achieved with this experimental setup was 46.3 W, with pump and seed beam radii of 540 µm, at an absorbed pump power of 34.4. This was a gain of 1.36 with an extraction efficiency of 47.0 %.

These power transfers were modelled and the shift in the peak of the stimulated-emission cross-section shift as a function of absorbed pump power was adjusted to provide the best fit to the data. Using this information, the laser amplifier was modelled at different spot sizes with many different numbers of passes of the seed beam, up to twenty four passes. For the pump and seed beam radii of 1300 µm, a theoretical output power over 100 W was predicted with twenty passes of the seed beam. While the model has many simplifying assumption inherent within it, this shows evidence of a pathway to an output power of 100 W with a reasonable number of passes of the seed beam.

With the same experimental setup, beam quality measurements were also recorded as beam quality is a key component in achieving a high brightness laser amplifier. Beam quality measurements were taken at various stages of the power transfers: whilst the amplifier has no pump power incident upon it; in the middle at an

absorbed pump power of approximately 21 W; and at the rollover section, near the end, which varied in absorbed pump power for the various spot sizes. For the two larger spot sizes, the beam quality was degraded as it passed through the un-pumped amplifier but improved for the middle beam quality measurements. The two smaller spot sizes had a moderate degradation in beam quality in the middle of the power transfers. At rollover, the beam quality of the two smaller spot sizes was significantly worsened, both with M^2 values above 5. The beam quality for the larger spot sizes were only marginally worse or approximately the same as they were at the beginning of the power transfers.

Changes in the beam quality were also observed as the ratio of the seed beam radius to the pump beam radius was adjusted. The pump beam radius was maintained at a size of 1.0 mm for two different absorbed pump powers. The first absorbed pump power was 22 W, in the middle of the power transfer, and the seed beam radius was changed from 0.45 mm to 1.30 mm. The second absorbed pump power was 42 W, at the rollover part of the power transfer, and the seed beam radius was changed from 0.50 mm to 0.90 mm. The clear trend in both experiments was that the beam quality was poorer as the seed to pump radii ratio was increased. For the rollover case, the beam quality was below an M^2 value of 1.5 for seed to pump radii ratios of 0.8 with very little change in the output power of the amplifier.

This work has made progress towards developing a roadmap to the industrial sponsor's target of achieving an output seed power of 100 W. A greater understanding of the amplifier dynamics was also developed, especially the susceptibility of the Nd:YVO_4 gain medium to changes in temperature. The model was used to predict that an output power of 100 W would be achievable with a pump and seed beam radii of 1300 µm and twenty passes of the seed beam. Future work would involve adding more passes of the seed beam to the physical laser amplifier in order to confirm that the model adequately describes the laser amplifier performance. The model may have to incorporate new features, such as ASE, but if it can reasonably predict the performance of the laser amplifier then a

pathway to achieving 100 W can be laid out with the optimised pump and seed beam radii and the minimum number of passes of the seed beam. It would then be for the industrial partner to assess the level of complexity and manufacturability of the subsequent design and the prospect of power scaling to even higher output powers.

3.9 References

[1] I. O. Musgrave, "Study of the Physics of the Power-Scaling of End-Pumped Solid-State Laser Sources Based on Nd:YVO_4," 2003.

[2] S. Pearce, C. L. M. Ireland, and P. E. Dyer, "Simplified analysis of double-pass amplification with pulse overlap and application to Nd:YVO_4 laser," *Opt. Commun.*, vol. 255, no. 4–6, pp. 297–303, 2005.

[3] S. Hooker and C. E. Webb, *Laser Physics*. Oxford University Press, 2010.

[4] J. L. Blows, T. Omatsu, J. Dawes, H. Pask, and M. Tateda, "Heat generation in Nd:YVO_4 with and without laser action," *IEEE Photonics Technol. Lett.*, vol. 10, no. 12, pp. 1727–1729, 1998.

[5] T. S. Lomheim and L. G. DeShazer, "Optical-absorption intensities of trivalent neodymium in the uniaxial crystal yttrium orthovanadate," *J. Appl. Phys.*, vol. 49, no. 11, pp. 5517–5522, 1978.

[6] M. J. Yarrow, "Power Scaling of Laser Oscillators and Amplifiers Based on Nd:YVO_4," 2006.

[7] T. Taira, A. Mukai, Y. Nozawa, and T. Kobayashi, "Single-mode oscillation of laser-diode-pumped Nd:YVO_4 microchip lasers," *Opt. Lett.*, vol. 16, no. 24, pp. 1955–1957, 1991.

[8] J. Fontanella, R. L. Johnston, J. H. Colwell, and C. Andeen, "Temperature and pressure variation of the refractive index of diamond," *Appl. Opt.*, vol. 16, no. 11, p. 2949, 1977.

[9] Z. L. Liau, “Semiconductor wafer bonding via liquid capillarity,” *Appl. Phys. Lett.*, vol. 77, no. 5, pp. 651–653, 2000.

[10] D. K. Sardar and R. M. Yow, “Stark components of $^4F_{3/2}$, $^4I_{9/2}$ and $^4I_{11/2}$ manifold energy levels and effects of temperature on the laser transition of Nd^{3+} in YVO_4,” *Opt. Mater. (Amst).*, vol. 14, no. 1, pp. 5–11, 2000.

[11] Y. Sato and T. Taira, “Temperature dependencies of stimulated emission cross section for Nd-doped solid-state laser materials,” *Opt. Mater. Express*, vol. 2, no. 8, p. 1076, 2012.

[12] X. Délen, F. Balembois, and P. Georges, “Temperature dependence of the emission cross section of Nd:YVO_4 around 1064 nm and consequences on laser operation,” *J. Opt. Soc. Am. B*, vol. 28, no. 5, p. 972, Apr. 2011.

[13] G. Turri, H. Jenssen, F. Cornacchia, M. Tonelli, and M. Bass, “Temperature-dependent stimulated emission cross section in Nd^{3+}:YVO_4 crystals,” *Josa B*, vol. 26, no. 11, p. 2084, Oct. 2009.

[14] V. Lupei, N. Pavel, and T. Taira, “Highly efficient laser emission in concentrated Nd:YVO_4 components under direct pumping in the emitting level,” *Opt. Commun.*, vol. 201, no. 4–6, pp. 431–435, 2002.

[15] L. Fornasiero, S. Kück, T. Jensen, G. Huber, and B. H. T. Chai, “Excited state absorption and stimulated emission of Nd^{3+} in crystals. Part 2: YVO_4, $GdVO_4$, and $Sr_5(PO_4)_3F$,” *Appl. Phys. B Lasers Opt.*, vol. 67, no. 5, pp. 549–553, 1998.

[16] H. R. Xia, X. L. Meng, M. Guo, L. Zhu, H. J. Zhang, and J. Y. Wang, “Spectral parameters of Nd-doped yttrium orthovanadate crystals,” vol. 88, no. 9, pp. 5134–5137, 2000.

[17] T. S. Lomheim and L. G. Deshazer, “New procedure of determining neodymium fluorescence branching ratios as applied to 25 crystal and glass hosts.,” *Opt. Commun.*, vol. 24, no. 1, pp. 89–94, 1978.

[18] E. Higurashi, K. Okumura, K. Nakasuji, and T. Suga, “Surface activated bonding of GaAs and SiC wafers at room temperature for improved heat dissipation in high-power semiconductor lasers,” *Jpn. J. Appl. Phys.*, vol. 54, no. 3, pp. 1–5, 2015.

[19] L. Allen, “Amplified Spontaneous Emission and External Signal Amplification in an Inverted Medium,” *Phys. Rev.*, vol. 8, no. 4, 1973.

[20] I. Okuda and M. J. Shaw, “Gain depletion due to amplified spontaneous emission in multi-pass laser amplifiers,” *Appl. Phys. B Photophysics Laser Chem.*, vol. 54, no. 6, pp. 506–512, 1992.

[21] D. D. Lowenthal and J. M. Eggleston, “ASE Effects in Small Aspect Ratio Laser Oscillators and Amplifiers with Nonsaturable Absorption,” *IEEE J. Quantum Electron.*, vol. 22, no. 8, pp. 1165–1173, 1986.

[22] J. Speiser, “Scaling of thin-disk lasers—influence of amplified spontaneous emission,” *J. Opt. Soc. Am. B*, vol. 26, no. 1, p. 26, 2008.

[23] A. Giesen and J. Speiser, “Fifteen years of work on thin-disk lasers: Results and scaling laws,” *IEEE J. Sel. Top. Quantum Electron.*, vol. 13, no. 3, pp. 598–609, 2007.

[24] F. G. Patterson, J. Bonlie, D. Price, and B. White, “Suppression of parasitic lasing in large-aperture Ti:sapphire laser amplifiers,” *Opt. Lett.*, vol. 24, no. 14, p. 963, 2008.

[25] F. Soyer *et al.*, “Suppression of parasitic lasing in high energy, high repetition rate Ti:sapphire laser amplifiers,” *Opt. Lett.*, vol. 37, no. 11, p. 1913, 2012.

[26] F. Ple, M. Pittman, G. Jamelot, and J.-P. Chambaret, “Design and demonstration of a high-energy booster amplifier for a high-repetition rate petawatt class laser system,” *Opt. Lett.*, vol. 32, no. 3, p. 238, 2007.

[27] D. C. Brown, S. D. Jacobs, and N. Nee, “Parasitic oscillations, absorption, stored energy density and heat density in active-mirror and disk amplifiers,” *Appl. Opt.*, vol. 17, no. 2, pp. 211–224, 1978.

[28] D. Albach, J. C. Chanteloup, and G. Touz, “Influence of ASE on the gain distribution in large size , high gain Yb^{3+}:YAG slabs,” *Opt. Express*, vol. 17, no. 5, pp. 431–437, 2009.

[29] G. I. Peters and L. Allen, “Amplified spontaneous emission I. The threshold condition,” *J. Phys. A Gen. Phys.*, vol. 4, pp. 238–243, 1971.

[30] G. J. Linford, E. R. Peressini, W. R. Sooy, and M. L. Spaeth, “Very Long Lasers,” *Appl. Opt.*, vol. 13, no. 2, pp. 379–390, 1974.

[31] E. C. Harvey *et al.*, “Picosecond gain and saturation measurements in a KrF laser amplifier depumped by amplified spontaneous emission,” *J. Appl. Phys.*, vol. 70, no. 10, pp. 5238–5245, 1998.

[32] A. M. Hunter and R. Hunter, “Bidirectional Amplification with Nonsaturable Absorption and Amplified Spontaneous Emission,” *IEEE J. Quantum Electron.*, vol. 17, no. 9, pp. 1879–1887, 1981.

[33] G. Kuhnle, U. Teubncr, and S. Szatmfiri, “Amplified Spontaneous Emission in Short-Pulse Excimer Amplifiers,” *Appl. Phys. B Photophysics Laser Chem.*, vol. 51, pp. 71–74, 1990.

[34] N. P. Barnes and B. M. Walsh, “Amplified Spontaneous Emission — Application to Nd:YAG Lasers,” *IEEE J. Quantum Electron.*, vol. 35, no. 1, pp. 101–109, 1999.

[35] H. Furuse, H. Chosrowjan, J. Kawanaka, N. Miyanaga, M. Fujita, and Y. Izawa, “ASE and parasitic lasing in thin disk laser with anti-ASE cap,” *Opt. Express*, vol. 21, no. 11, pp. 13118–13124, 2013.

[36] A. W. Tucker, M. Birnbaum, C. L. Fincher, and J. W. Erler, “Stimulated-emission cross section at 1064 and 1342 nm in Nd:YVO_4,” *J. Appl. Phys.*, vol. 48, no. 12, pp. 4907–4911, 1977.

Chapter Four

Multi-stage Amplification of a Q-Switched Laser for the Generation of Sub-Nanosecond Pulses at Higher Average Powers

---

4.1 Introduction

The motivation for amplifying picosecond pulses, as discussed in this thesis, has been in the context of laser machining as an application. In chapter 1, the benefits of using picosecond pulses in laser machining, as opposed to nanosecond pulses, were discussed. Due to the short pulse durations required, lasers for precision machining are typically mode-locked, producing pulses in the picosecond and femtosecond regimes. Mode-locked lasers can be expensive and complex to build whereas Q-switched lasers are often simpler and cheaper, although they generally produce nanosecond pulses. Q-switched microchip lasers, however, can operate with pulse durations of 10s to 100s of picoseconds and still maintain their simplicity and lower cost [1], [2]. As well as laser machining, a smaller and less complex source for picosecond pulses also has applications in nonlinear frequency conversion [3], [4], time-of-flight range-finding and coherent anti-Stokes Raman spectroscopy [2].

In previous chapters, it has been demonstrated that Nd:YVO_4, when used as a gain material in a high power regime, is not as effective as its intrinsic parameters might suggest due to the reduction in its stimulated-emission cross-section as its temperature increases. However, the characteristics of Nd:YVO_4, its high gain and high absorption, make it a good choice as a laser gain material for Q-switched microchip lasers, operating at lower powers and, consequently, lower temperatures [2]. Amplification of the Q-switched pulses is required to reach

suitable average powers for machining applications. Average powers provided by current, commercially available Q-switched microchip lasers are quite low. A larger, more powerful Q-switched laser could be used to simply increase average powers at the laser source but this would lead to longer pulse lengths that are not compatible with precision machining. Amplification of a low average power Q-switched microchip laser, with the desired pulse properties, can provide a solution.

This chapter will first give a brief description of the basic principles behind both Q-switching and Q-switched microchip lasers before going on to describe experiments performed using a commercially available Nd:YVO_4, Q-switched microchip laser. The output of this laser required amplification and so three subsequent amplifier stages were built. The aim of the three amplifier stages used in this work was to take the tens of milli-Watts average output power of the Q-switched microchip laser and to amplify it into multiple Watts, suitable for machining applications. The work set out in this chapter had strict time and material constraints. The time constraints required that this work was not a full characterisation and optimisation of the Q-switched microchip laser and its amplifier stages but a 'first-pass' to assess what might be possible with further research. The doping concentrations used were chosen based on the Nd:YVO_4 gain material available, meaning that the design of the amplifier stages was not optimised for performance. However, the experiments were designed to gain a better understanding of amplifier design, through the modelling of each amplifier stage after the experimental work was completed.

After building the Q-switched microchip laser and the subsequent amplifier stages, it was discovered that a similar work had been completed by A.Agnesi et al [3]. To corroborate the learning taken from the experiments discussed in this chapter, the amplifiers produced by Agnesi et al were also modelled and compared with the results presented here. Agnesi et al utilised Nd:YVO_4 crystals with lower doping concentrations than was available for this work, in a similar amplifier architecture, to achieve multiple Watts of output power from an input seed power of mW from a

Q-switched microchip laser and thus the two sets of results are strongly complementary.

4.2 Q-switching

Q-switching is a technique that is used to achieve pulsed operation of a laser by modulating the intra-cavity losses in the resonator. Initially, the gain medium is pumped but the laser cavity has high losses so that it cannot oscillate. The energy stored in the gain medium then builds up as it is being pumped. The loss in the cavity is quickly switched (by either active or passive means) into a low-loss state and, from spontaneous emission, a pulse is formed as high intra-cavity powers build up. The high intra-cavity powers begin to saturate the gain and the peak of the pulse is achieved when the gain equals the losses of the low-loss state of the cavity, as in the threshold level of continuous wave (CW) operation [5].

Active Q-switching is achieved by using an active element to modulate the losses such as an acousto-optic modulator or an electro-optic modulator. The Q-switched microchip laser described in this chapter uses an alternative form of Q-switching called passive Q-switching, where the losses are automatically modulated using a saturable absorber.

A saturable absorber is an optical component that has a loss that is reduced at high optical intensities. In the Q-switched microchip laser used in this work, the saturable absorber takes the form of semiconductor saturable absorber mirror (SESAM) at one end of the optical cavity [1]. When the intra-cavity intensity of the laser mode is sufficiently low, the SESAM losses are high, it is in an unbleached state. As the gain medium is pumped, the gain increases until it becomes high enough to overcome the high losses in the cavity from the SESAM's unbleached state and the laser begins to oscillate, although very weakly. As the laser pulse intensity increases, it becomes large enough to bleach the absorption of the SESAM and the cavity losses switch from a high state to a low state.

At this point, the intra-cavity power grows more rapidly, depleting the gain, and reaches a peak when the gain equals the losses in the cavity in the low loss regime, which is the same as the CW threshold level. After this moment, energy is still extracted but the net gain is negative and the intra-cavity power beings to decay as seen in Figure 4.1.

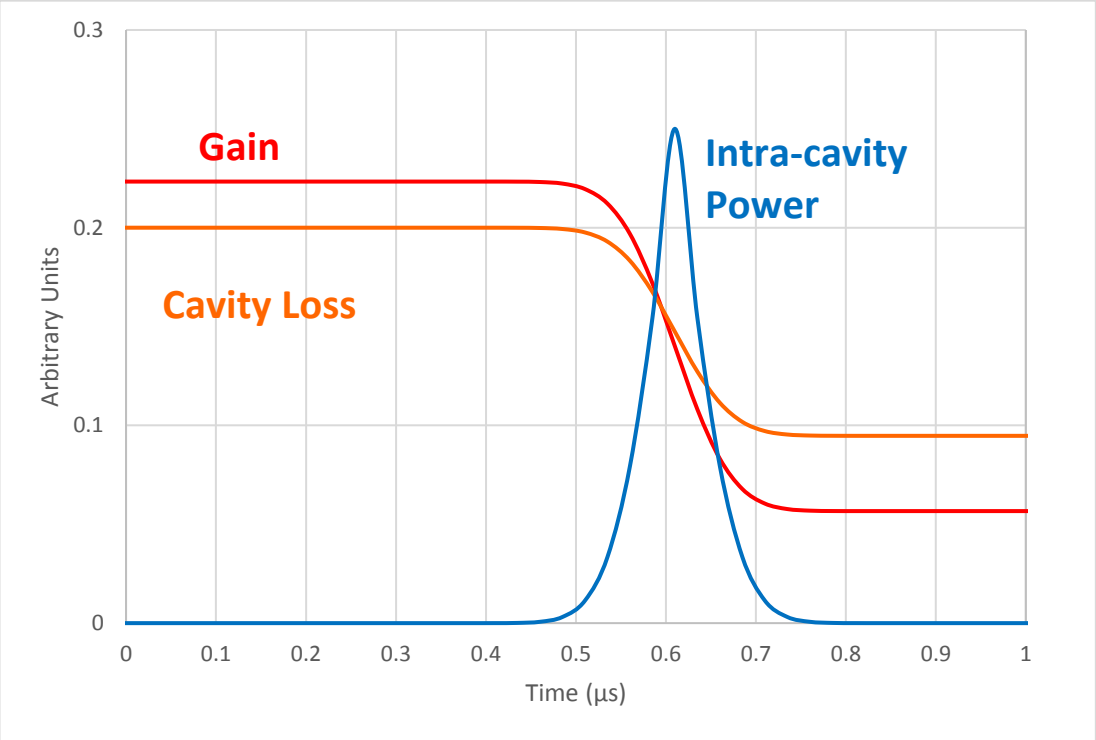

Figure 4.1 – As the intra-cavity power increases, intra-cavity loss begins to decrease. When the SESAM has been bleached, the cavity loss switches to a low loss regime and intra-cavity power begins to build up much more rapidly, depleting the gain. After the pulse, the SESAM begins to recover, increasing the cavity loss once more [6].

This trailing edge of the pulse is largely defined by the cavity decay time. The cavity decay time is a function of both the round-trip loss in the cavity and the cavity length. A Q-switched pulse has to be longer than the passive cavity decay time because the pulse first has to build up to the peak before decaying away in

approximately the cavity decay time. Therefore, the pulse length is the cavity decay time with the additional time it takes for the pulse to build up to the peak. This is the reason that shorter cavity lengths lead to shorter pulse durations and is why a Q-switched microchip laser can offer pulses in the picosecond regime whereas a more standard laser cavity has Q-switched pulse lengths on the order of nanoseconds due to cavity lengths being centimetres to tens of centimetres in length.

The beginning of the pulse is triggered when the gain equals the unbleached losses, and this gain is achieved when a certain population inversion is obtained in the gain medium. A consequence of this is that increasing the pump power only serves to achieve this required population inversion more quickly but does not affect the pulse energy or duration. What increasing the pump power does do, since it allows the laser to reach a certain gain threshold more quickly, is to increase the repetition rate of the laser [1].

4.3 Microchip lasers

Q-switched microchip lasers are typically made up from the following components: a gain crystal, output coupler, SESAM and a heat sink, as shown in Figure 4.2. The majority of the cavity is comprised of the gain medium, which is typically less than 2mm and often only 100s of microns in length [2]. The gain medium often has flat surfaces, providing a plane-parallel cavity, with the SESAM acting as an end mirror. The cavity length, and therefore the length of the gain medium, is one of the main parameters that determine pulse duration. For Q-switched lasers, the minimum pulse width that can be obtained is determined by t_{rt}, the round trip time of the cavity, and G_{rt}, the round trip, small-signal gain of the cavity [7].

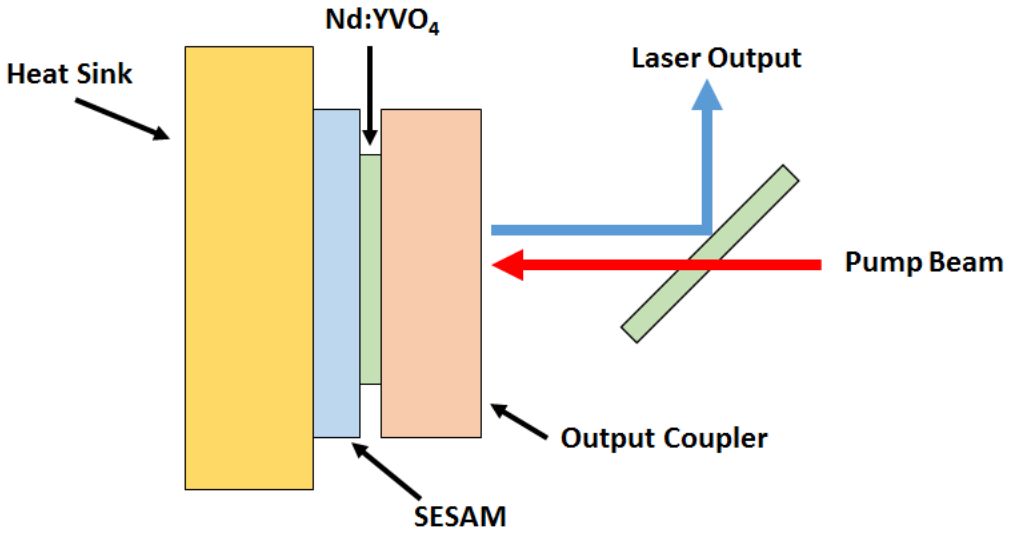

Figure 4.2 – Schematic of a typical Q-switched microchip laser. The Nd:YVO₄ crystal is sandwiched between the output coupler and the SESAM, which is all mounted on a heat sink.

The Q-switched microchip laser used in the experiments described in this chapter was purchased from Batop Optoelectronics (MCT-1064_90ps). This microchip laser had a different architecture from the typical Q-switched microchip laser, shown in Figure 4.2. In this instance, the laser did not have a separate output coupler and SESAM but had a saturable output coupler (SOC). Unlike with a conventional SESAM, the DBR stack here was not designed to be highly reflective but for a particular reflectivity. The Nd:YVO₄ gain medium had an anti-reflection coating at the pump wavelength of 808 nm and a high-reflection coating at the laser wavelength of 1064 nm and was bonded to the SOC. This was then mounted onto a heat sink with an aperture in its centre as shown in Figure 4.3. The pump beam was incident on the gain medium from one side and the laser output emitted from the other. This removed the need for a dichroic mirror to separate the laser output from the pump beam. The BATOP Q-switched microchip laser provided pulses at a wavelength of 1064 nm with a pulse duration of approximately 90 ps.

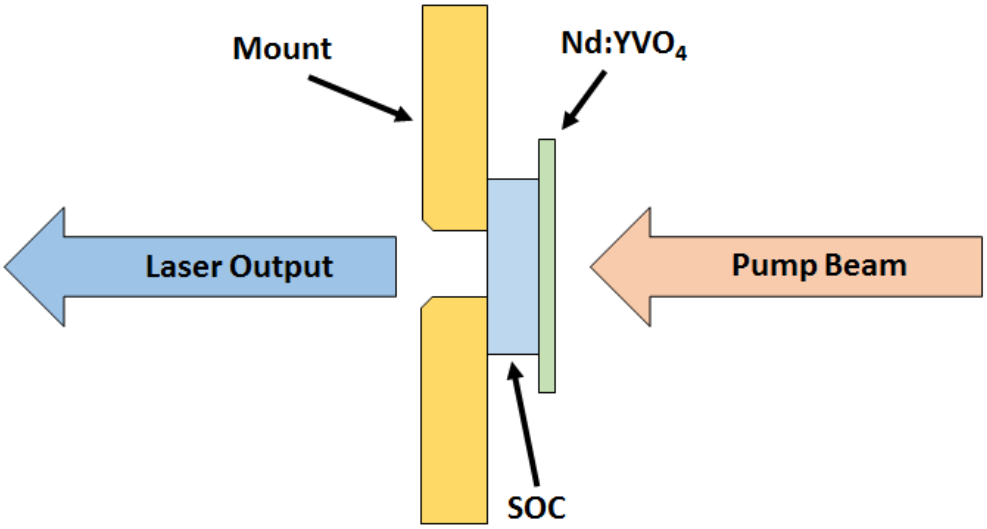

Figure 4.3 – A schematic diagram of the Q-switched microchip laser showing the Nd:YVO_4 crystal bonded to the saturable output coupler. The microchip laser here works in transmission mode where the pump beam enters on one side, striking the Nd:YVO_4 crystal first and the laser output exits from the opposing side, through the saturable output coupler (SOC).

4.3.1 Experimental setup

The experimental setup for the microchip laser is shown in Figure 4.4. The microchip laser gain medium was a 3 atm % Nd:YVO_4 crystal, with dimensions of 2 mm x 2 mm x 0.4 mm, bonded to a saturable output coupler which was attached to a mount, as in Figure 4.3. This mount was further mounted on a metal cooling block that had chilled water flowing through it to extract heat. As the SESAM also acted as the output coupler for the cavity, the microchip laser was pumped from one side while the laser output was emitted from the opposite side as in Figure 4.3. As the microchip laser output was on the same side as the cooling block, the block had an aperture where the microchip laser was mounted to allow the laser beam through to be collimated by a lens.

The microchip laser was pumped with a 1000 mW diode laser operating at 808 nm. The datasheet provided by the microchip laser manufacturer recommended a pump beam diameter of between 40 µm and 80 µm. The diode laser beam was delivered by an optical fibre, with a core diameter of 100 µm, before being approximately collimated using a 50 mm focal length lens. The pump beam was then focussed onto the microchip using a 15 mm focal length, aspherical lens. To optimise the pump diameter on the microchip, the pump collimating lens was mounted on a translatable stage and adjusted to achieve the maximum power from the output of the microchip laser; however, the pump beam diameter was not measured.

The datasheet provided by the microchip laser manufacturer stated that with a pump beam diameter of 40 µm, the microchip laser would have a threshold pump power of 70 mW. From this data, the pump density at threshold was calculated. Experimentally, a threshold pump power of 72.3 mW was determined and, with assuming the same pump density at threshold, the pump beam diameter was calculated to be 44 µm. The output of the laser was incident on a semiconductor power meter to record the output power. To measure the repetition rate of the laser, the output of the power meter was viewed on an oscilloscope.

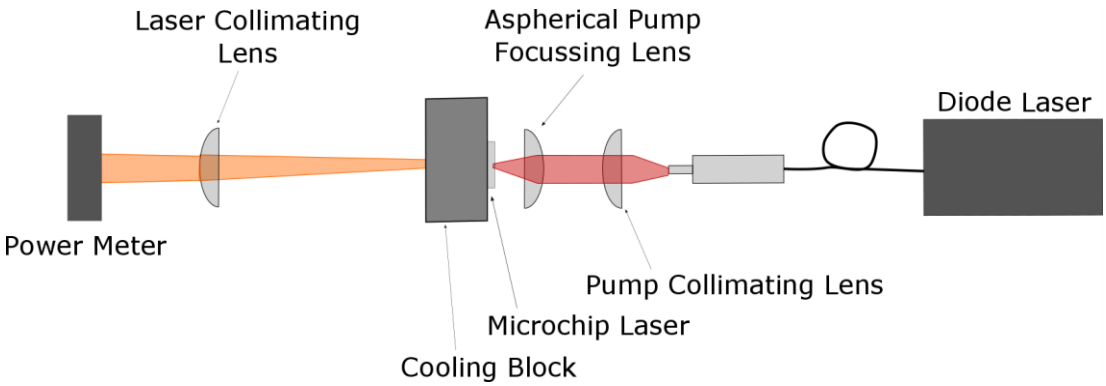

Figure 4.4 – A diagram of the experimental setup used for the microchip laser.

4.3.2 Microchip laser output

Figure 4.5 shows a power transfer for the microchip laser. The graph plots the output power against the incident pump power as any unabsorbed pump light could not be measured to determine the absorbed pump power. It was not possible to measure the unabsorbed light due to the unabsorbed pump beam's divergence angle. As the pump beam was focussed to such a small beam diameter, it quickly diverged and another short focal length, aspheric lens would have been needed to collimate it but none were available at the time. There was no spectral filtering of the pump and laser beams after the output, however, it was assumed, as the divergence of the pump was large and the collimating lens of the laser beam was sufficiently far away, that any pump light incident on the power meter was negligible.

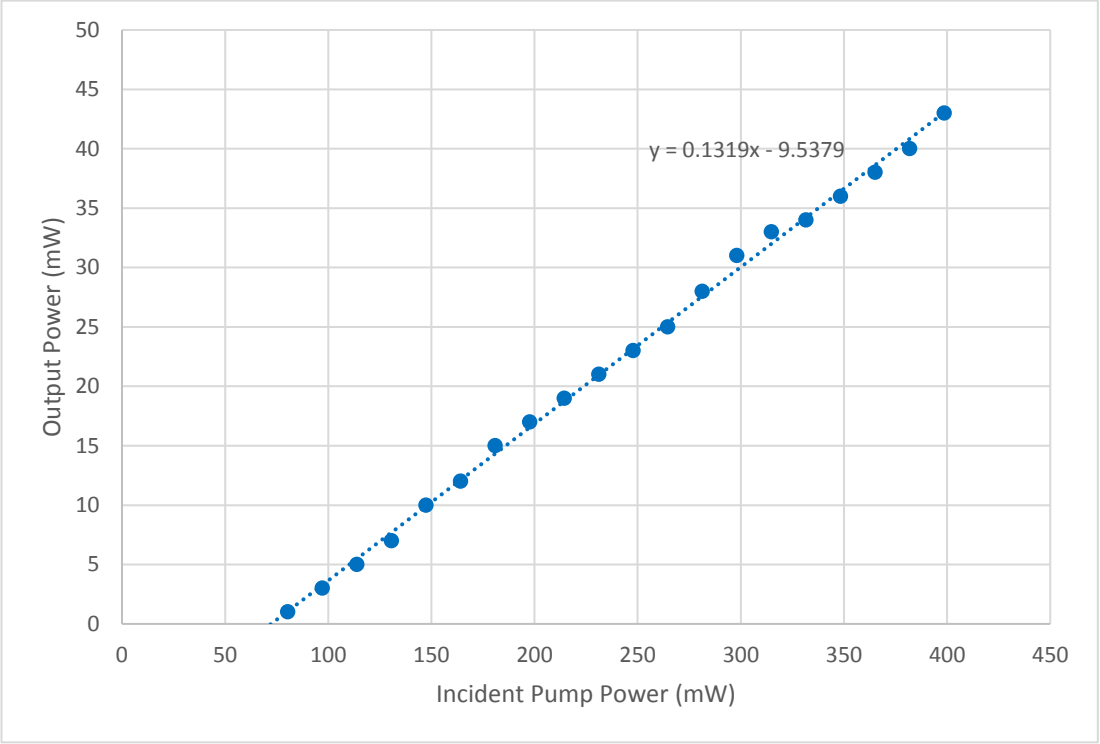

Figure 4.5 – Power transfer for the microchip laser.

The threshold incident pump power was 72 mW with a slope efficiency of 13 %. These numbers are expected from the specifications given by the microchip laser

manufacturer. For a pump beam diameter of 40 µm, the manufacturer's specifications state a threshold pump power of 70 mW and a slope efficiency of 10 %. The manufacturer's specifications also show that larger pump beam diameters lead to higher pump threshold powers and increased slope efficiencies. Using the threshold pump power of 72 mW, the pump beam diameter is calculated as 44 µm, assuming the same pump density at threshold given by the data sheet.

The maximum output power reached was 43 mW at an incident pump power of 399 mW. The manufacturer's specifications only provide an output power at a pump power of 200 mW which, for a 40 µm beam diameter, is 17 mW. In this experiment, the microchip laser output was 22 mW for the same incident pump power of 200 mW. Figure 4.6 shows the pulse repetition rate of the microchip laser as a function of incident pump power. It can be seen from the graph in Figure 4.6 that the repetition rate increases as the incident pump power is increased. The reason that the repetition rate increases as the incident pump power is increased is because the beginning of each pulse is triggered when the gain equals the losses in the cavity when the SESAM is unbleached. The gain reaches this level when there is an adequate population inversion and this is driven by the pump power. By increasing the incident pump power, the gain is increased more quickly but when it equals the cavity losses, a pulse is formed. Therefore, the greater the incident pump power, the greater the repetition rate of the laser. The manufacturer's specifications also provide a graph of pulse repetition rate against incident pump power and it similar to Figure 4.6.

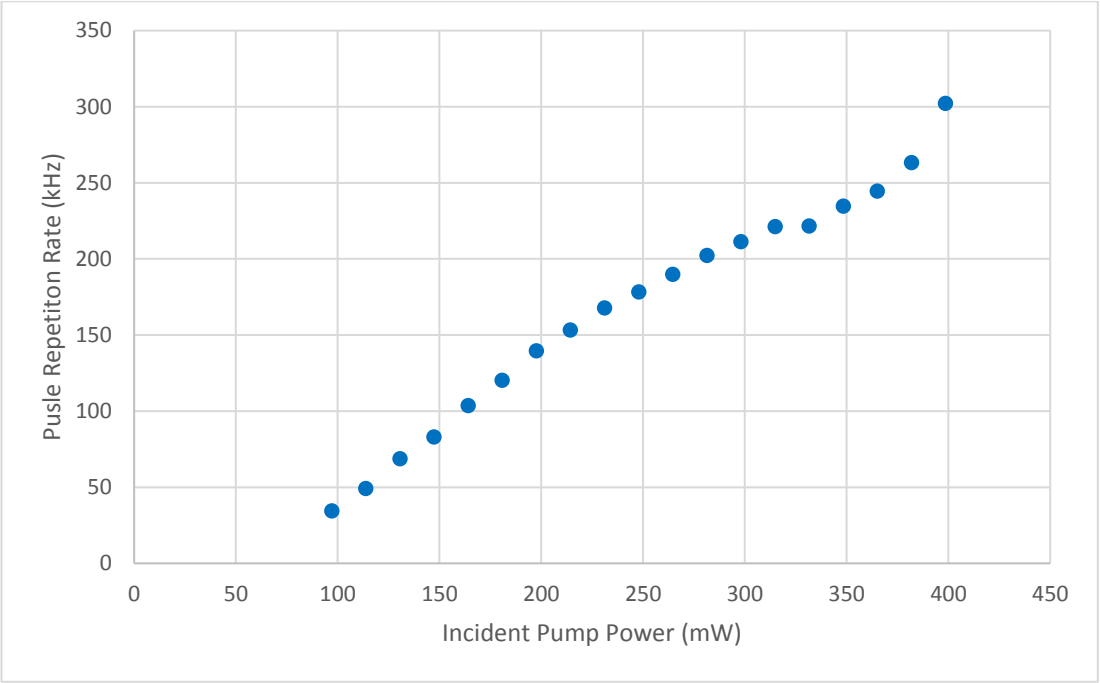

Figure 4.6 – The pulse repetition rate of the microchip laser as a function of incident pump power.

The beam quality of the microchip laser was measured using an Ophir Spiricon. The Spiricon equipment focuses the beam using a lens and the beam travels along a beam path of variable length before it is incident on a camera. The beam path is varied so that varying parts of the beam caustic are incident of the camera and the software determines the M^2 value by fitting to the measured beam diameters. For this microchip laser, the beam quality was measured as 1.09 in the horizontal x-axis and 1.40 in the vertical y-axis.

Whilst the pulse duration was not measured here, the manufacturer did provide some specifications. The manufacturer quotes a pulse duration, for a pump beam diameter of 40 µm, of 80 ps. The pulse duration increases as the pump beam diameter increases, up to 110 ps for a pump diameter of 100 µm, according to the specification. It is assumed then that the pulse duration would be close to, but slightly greater, than 80 ps. The pulse energy was calculated by dividing the output

power by the repetition rate, yielding a value of 130 nJ. The microchip laser output was then used as the input seed beam into an amplifier chain.

4.4 Amplifier stages

This section deals with the amplifier chain that was used to amplify the microchip laser, with an average output power of 43 mW, to multiple Watts of average output power. The amplifier chain consisted of three amplifier stages. The first amplifier stage was a high-gain amplifier with a rod shaped gain medium with a higher doping concentration of 1 atm % Nd:YVO_4. The second and third amplifier stages also had a gain medium with a rod architecture but utilised a lower doping concentration of 0.5 atm % Nd:YVO_4 for both stages and achieved output powers of 1.08 W and 3.00 W, respectively. Each amplifier stage was modelled and the empirical results compared with those predicted by the model.

These amplifier stages had a, somewhat, similar design to that which was used by Agnesi et al [3] where a picosecond microchip laser, with an output power of 3.5 mW, was amplified to 6 W in two amplifier stages. The first amplifier stage used by Agnesi et al had a 0.5 atm % Nd:YVO_4 crystal for the gain medium and the second used a 0.2 atm % Nd:YVO_4 crystal. The amplifier model was used again to simulate the two amplifier stages used by Agnesi et al and was then used again to provide a comparison between the different doping concentrations.

4.4.1 First amplifier stage

The first amplifier stage utilised a rod architecture for the gain medium and incorporated a double pass of the seed beam to increase the amplifier gain. The doping concentration of the gain medium was 1 atm %, higher than that of the second and third amplifier stages. Similar to the microchip laser, a power transfer was taken but now the unabsorbed pump power was measured so the absorbed

pump power could be calculated. The beam quality was measured again at the output of the amplifier.

4.4.1.1 Experimental setup

The experimental setup is shown below in Figure 4.7. The laser output of the microchip laser was used as the seed beam for the amplifier after passing through a half wave-plate, to enable control over the polarisation of the seed beam. This control over the polarisation allowed for the optimisation of the gain of the amplifier, as Nd:YVO_4 is a birefringent material with polarised gain. An a-cut, 1 atm % Nd:YVO_4 crystal, with dimensions of 3 x 3 x 5 mm, was used and the gain material was mounted in a water cooled mount. The 5 mm dimension ran along the direction of propagation of the pump and seed beams and both facets of the gain material were anti-reflection (AR) coated at the pump and seed wavelengths of 808 nm and 1064 nm, respectively.

The seed beam was focussed to a radius of 130 µm using a 750 mm focal length lens and the seed beam radius was uniform throughout the whole of the rod. The seed beam was directed through the gain medium and then reflected back through for a second pass using a dichroic mirror. The dichroic mirror allowed the pump beam to pass through and onto the gain medium. In Figure 4.7, the angle of the dichroic mirror and the first and second pass of the seed beam are exaggerated. In reality, the first and second passes were overlapped with only a slight deviation, an angle of less than 2 degrees, to allow them to be separated further along the beam path.

A 10 W, unpolarised, diode laser, operating at a wavelength of 808 nm, was used to pump the first amplifier stage. The pump beam was delivered through a fibre with a core diameter of 100 µm, then collimated using a 25.4 mm focal length lens. The beam was then focussed onto the gain material, using a 50 mm focal length lens, after passing through a dichroic mirror. The pump beam radius at the centre of the gain medium, along the beam axis, was approximately 130 µm; however, the pump beam radius was not uniform throughout the gain medium.

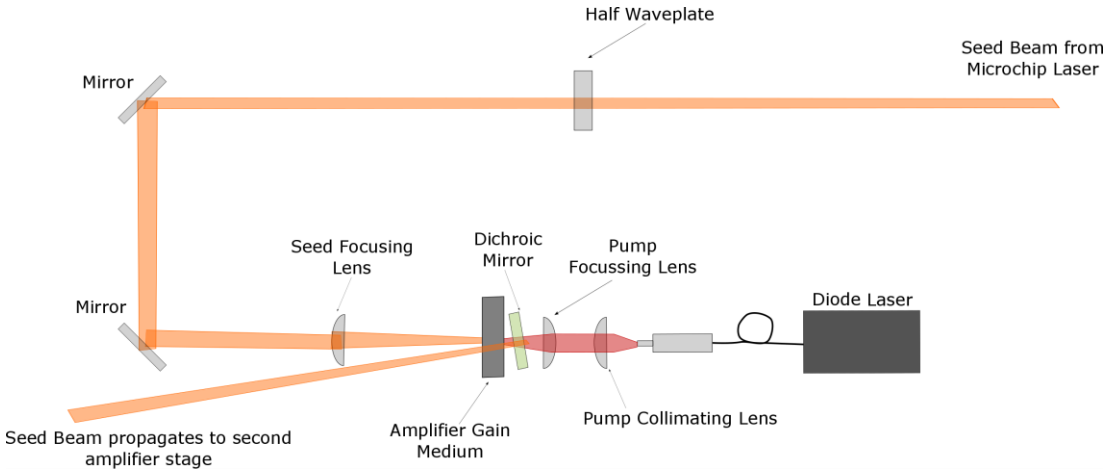

Figure 4.7 – A schematic diagram of the first laser amplifier setup.

4.4.1.2 First amplifier stage output

Figure 4.8 shows the power transfer for the first amplifier stage. The power of the seed beam, without any pump light incident on the amplifier stage, was measured as 35 mW, after passing through all the various optics present in the amplifier stage. This power is slightly lower than the output of the microchip laser due to losses present in the amplifier stage. At an absorbed pump power of 7.8 W, an output power of 130 mW was achieved, which was a gain of 3.7.

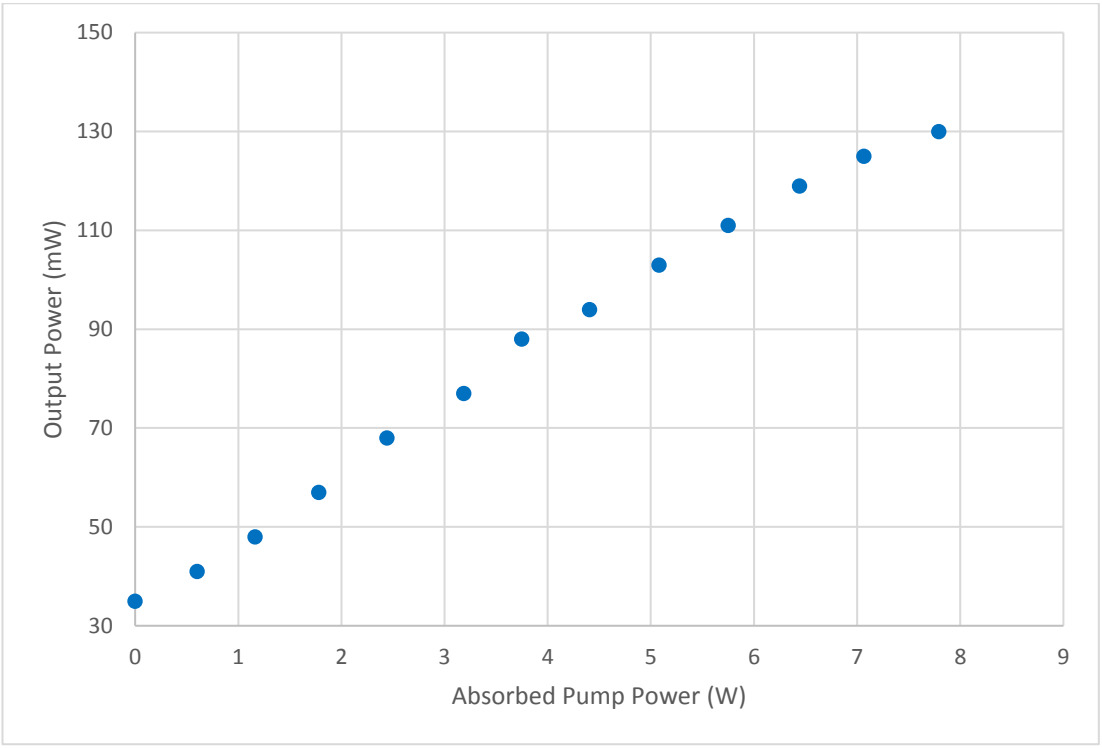

Figure 4.8 – Power transfer for the first amplifier stage.

The same multi-pass laser amplifier model that was discussed in the previous chapter was utilised again, modelling the double-pass of the seed beam. As the pump beam radius was not uniform throughout the rod shaped gain medium, an average of the pump beam radii that were measured throughout the length of the gain medium was used and, in this case, the average pump beam radius was 240 µm. The seed beam was approximately the same radius of 130 µm throughout the whole gain medium.

Figure 4.9 displays the same power transfer as in Figure 4.8 but with the addition of modelled data. The modelled data displayed is for a Gaussian and a top-hat pump beam shape, both without the effects of temperature or ETU incorporated into the model. However, it is clear from Figure 4.9 that these models do not accurately represent the empirical data as the output power is considerably lower for the empirical data.

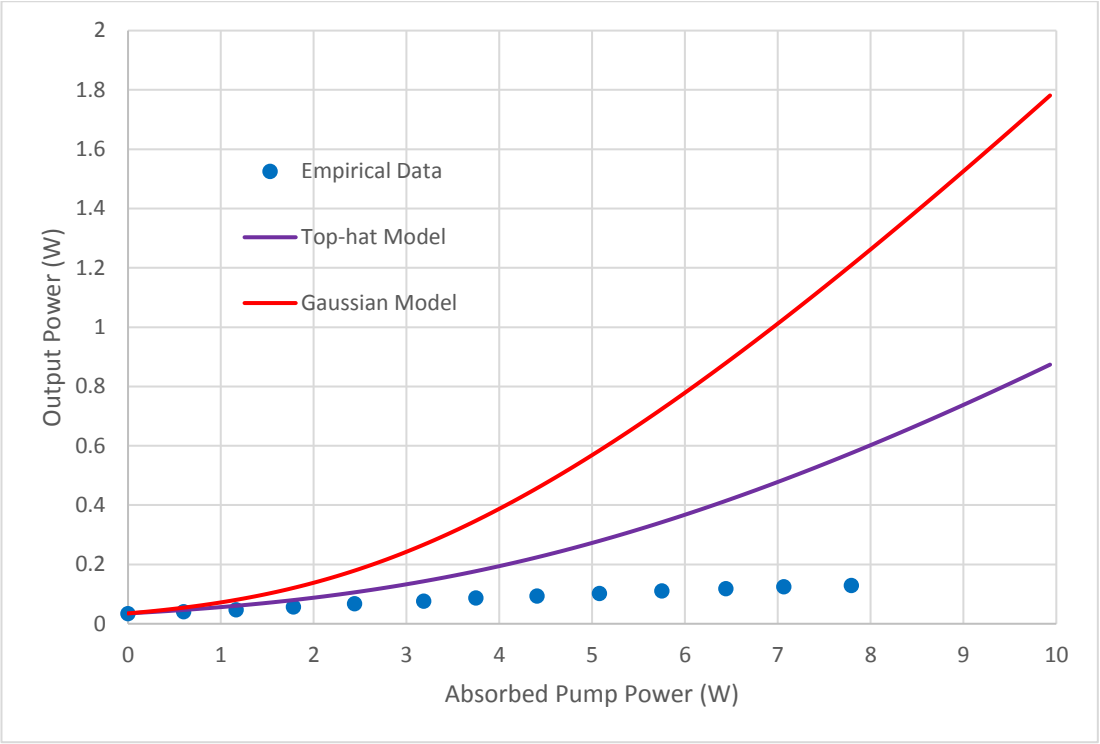

Figure 4.9 - Empirical data for the power transfer for the first amplifier stage alongside modelled data of the same power transfer. The red line is the modelled data with a Gaussian shaped pump beam and the purple line is the modelled data with a top-hat shaped pump beam.

The power transfer was modelled again, this time with a top-hat pump beam shape and the effects of temperature and ETU included, and the results are shown in Figure 4.10. The gradient of the stimulated-emission cross-section shift as a function of absorbed pump power was set to 0.03 nm/W, which is a reasonable value for the pump beam radius when compared to the gradients of the stimulated-emission cross-section shift as function of absorbed pump power used in the previous chapter. Whilst there is some discrepancy between the modelled and empirical data, this modelled data provides a much closer match to the empirical data than in Figure 4.10. This is evidence that the deleterious effects of temperature are significant within this particular amplifier design.

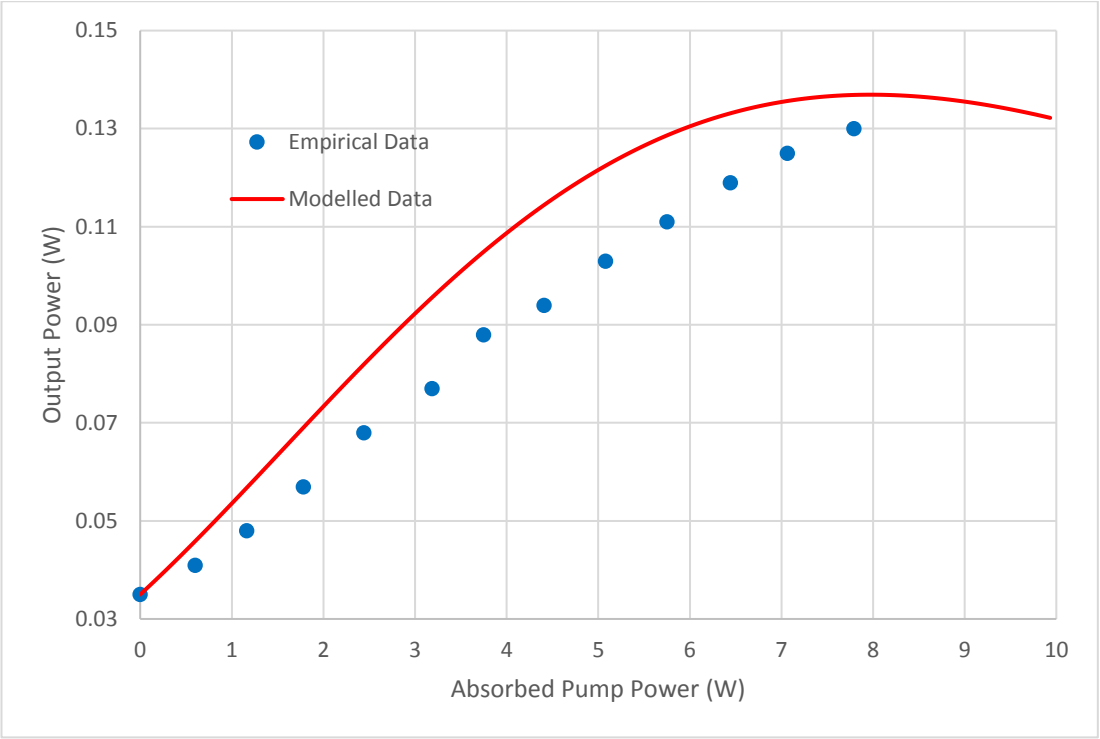

Figure 4.10 – Empirical data for the power transfer for the first amplifier stage alongside modelled data of the same power transfer. The modelled data is for a top-hat pump beam and includes the effects of temperature and ETU.

The beam quality was measured after the amplifier stage using the Spiricon and the M^2 parameter was found to be 1.46 in the x-axis and 1.29 in the y-axis. The beam quality after the first amplifier stage was worse than that from the microchip laser output but no effort was made to improve beam quality due to a lack of time.

Agnesi et al [3] provided data on their first amplifier stage for a picosecond, Q-switched, Nd:YVO_4, microchip laser and this was, somewhat, comparable to the first amplifier stage described in this section. Similar to the amplifier setup described in Section 4.4.1.1, the first stage of the Agnesi amplifier chain also utilised a 5 mm long Nd:YVO_4 gain medium. The input seed beam underwent a double pass through the gain medium and the input seed power was also 3.5 mW. The main difference between the two amplifier setups was the doping concentration of the Nd:YVO_4 gain medium. Agnesi et al used a doping concentration of 0.5 atm %, as opposed to

a doping concentration of 1 atm %. Other differences between the amplifier described in Section 4.4.1.1 and the Agnesi amplifier were that the pump beam was focussed to a radius of 100 μm. A higher absorbed pump power was also used with an absorbed pump power of 11 W, from an incident pump power of 15 W, at the maximum output power of 650 mW.

The paper only provided two data points for the power transfer and these are shown in Figure 4.11. Figure 4.11 also displays two modelled power transfers of this amplifier, one with a top-hat pump beam profile and one with a Gaussian pump beam profile. Some assumptions were made due to a lack of information in the Agnesi paper. The seed beam radius was not provided so it was assumed to be the same size as the focussed pump beam radius of 100 μm. It was also assumed that the pump beam would not be a uniform radius within the gain medium. An average pump beam radius of 230 μm was modelled as this was similar to the average pump beam radius used to generate the modelled data used in Figure 4.9 and Figure 4.10.

The modelled results shown in Figure 4.11, while somewhat approximate due to the assumptions made, show that the output power of the amplifier lies between the top-hat and Gaussian models. This is in contrast to the modelled data in Figure 4.9, where the top-hat and Gaussian models were a poor fit for the empirical data from the 1 atm % Nd:YVO_4 amplifier. The model that incorporated the effects of ETU and temperature was a better fit to the 1 atm % Nd:YVO_4 amplifier, as shown in Figure *4.**10***. This is evidence that the lower doping concentration improves amplifier performance by ameliorating the effects of ETU and decreasing the temperature within the gain medium.

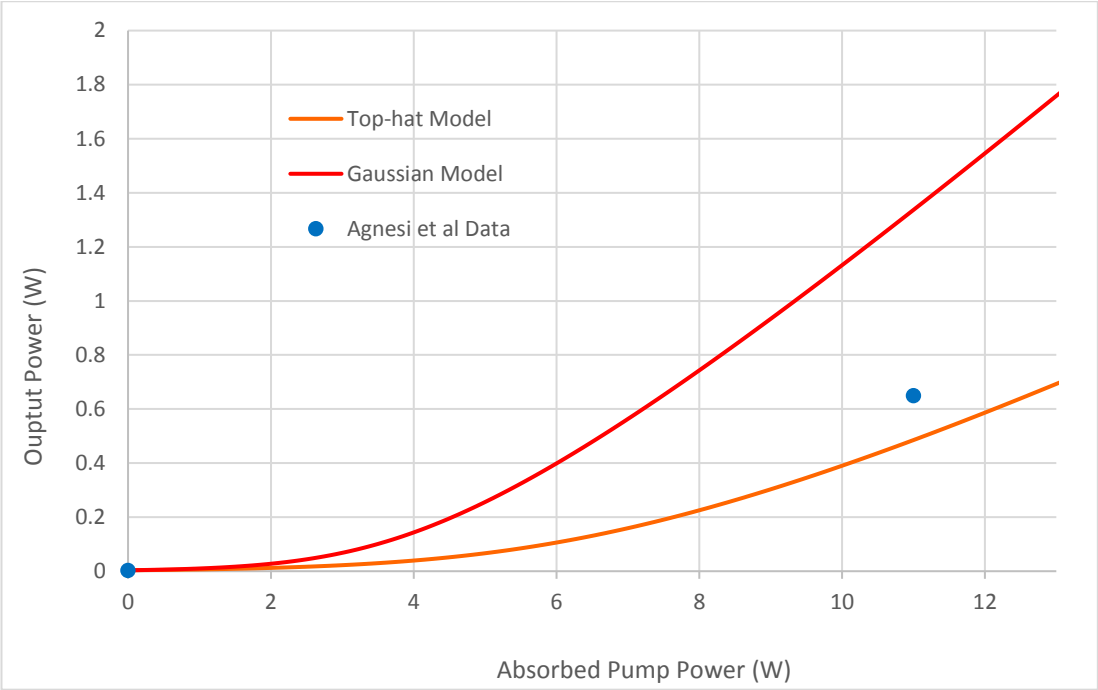

Figure 4.11 – A power transfer with data taken from Agnesi et al [3] *for the first stage in a microchip laser amplifier chain. The data taken from* [3] *is shown in blue. Also shown is modelled data of the Agnesi power transfer. The red line is the modelled data with a Gaussian shaped pump beam and the orange line is the modelled data with a top-hat shaped pump beam.*

4.4.2 Second and third amplifier stages

The second and third amplifier stages both shared the same pump laser which was unpolarised. The unpolarised pump beam was split into two using a polarising beam splitter, with the incident pump power to each amplifier being separately controlled using subsequent polarising beam splitting cubes and half wave-plates. This meant that the pump light incident on the gain medium for the second and third amplifier stages was polarised. As Nd:YVO_4 is anisotropic, it has different absorption coefficients for its different axes. When the pump light is unpolarised, the effective absorption coefficient is an average of the two separate absorption coefficients but with polarised pump light, the absorption in the gain media could be controlled with the pump polarisation aligned either to the weaker or stronger absorbing axis.

Aligning the pump polarisation parallel to the weaker absorbing axis has a deleterious effect on pump absorption efficiency but it spreads the energy more evenly through the gain medium leading to more effective cooling and ameliorating the negative effects of energy-transfer up-conversion, as described in Section 2.2.4 in Chapter 2.

4.4.2.1 Experimental setup

Figure 4.12 shows the experimental setup for both the second and third amplifier stages. Both stages share a diode pump laser that was delivered by a fibre with a 100 µm core diameter and was collimated with a 50 mm focal length lens. The pump beam was then split into two using a polarising beam splitting cube. The diode laser was unpolarised so the cube split the pump power in half and polarised the pump beam, which meant the absorption profile within the gain medium could be changed by aligning different crystal axes parallel to the pump beam polarisation. As both pump beams were now polarised, each pump beam was then passed through a half wave-plate and another polarising beam splitting cube to control the incident power on the amplifier stages. After the last polarising beam cube, each pump beam was focussed onto the amplifier gain medium, with a 50 mm focal length lens, giving a pump beam radius of approximately 160 µm and 170 µm for the second and third amplifier stages, respectively.

The gain medium for both amplifier stages was a-cut, 0.5 atm % Nd:YVO_4 with dimensions 3 x 3 x 5 mm, with the long axis in the direction of propagation of the pump and seed beams. The orientation of the Nd:YVO_4 gain medium could be changed by rotating the crystal within the mount so that the polarisation of the pump beam was parallel to either the a-axis or c-axis. For the second amplifier stage, the pump beam polarisation was always aligned to the a-axis, which is the more weakly absorbing axis, for the reasons described previously. The third amplifier stage was tested with the pump beam polarisation aligned to one axis and then the other, as discussed in Section 4.4.2.3. The seed beam's polarisation could

also be controlled using half wave-plates to ensure the seed beam polarisation was parallel with the c-axis which has a higher stimulated-emission cross-section.

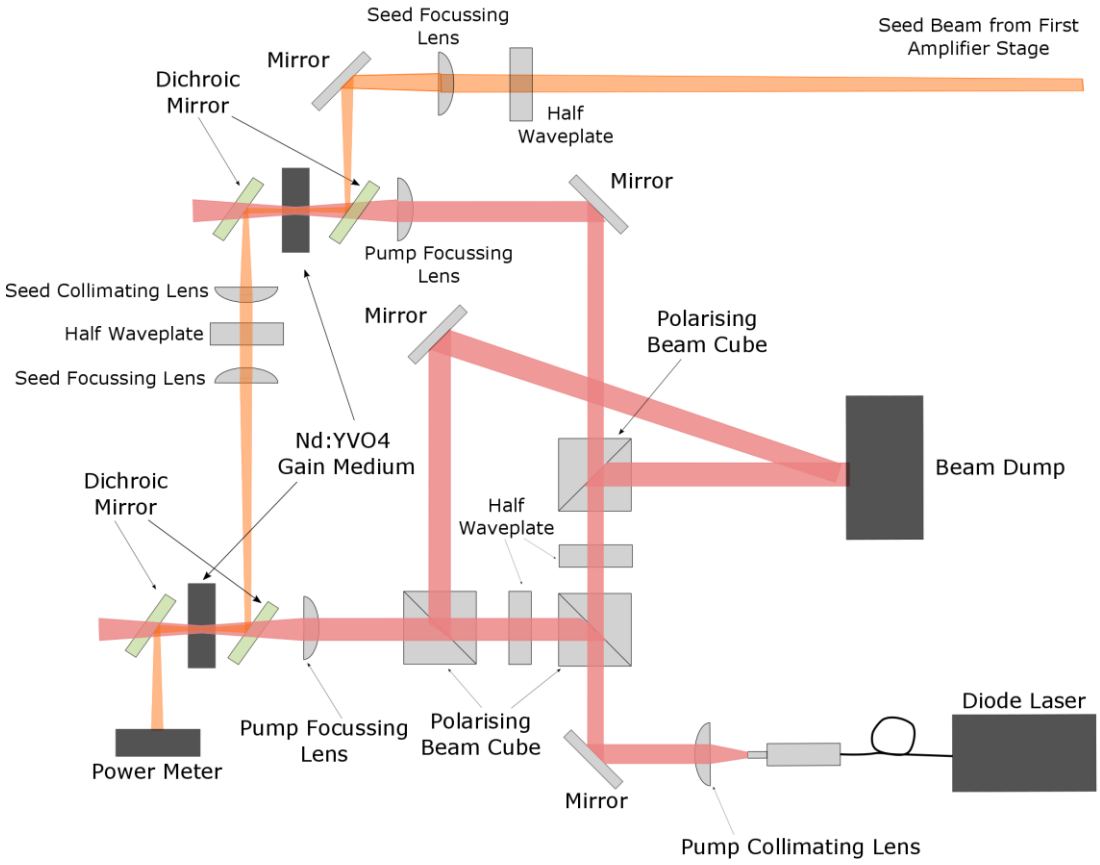

Figure 4.12 – A schematic of the second and third amplifier stages.

The output seed beam of the first amplifier stage acted as the input seed beam for the second stage, passing through a half wave-plate to ensure the polarisation was aligned to the c-axis of the Nd:YVO_4 to maximise the gain in the amplifier again. The seed beam was then focussed by a 300 mm focal length lens and directed onto the second amplifier gain material using a dichroic mirror. The seed beam radius was focussed to 120 µm at the centre of the gain medium along the beam axis. Another dichroic mirror at the other side of the gain material was used to separate the pump

and seed beams and the seed beam was collimated using another lens, with a focal length of 125 mm.

The output of the second stage then passed through an almost identical setup as before, making up the third amplifier stage, starting with a half wave-plate. The seed beam was focussed with a 500 mm focal length lens before being directed onto the gain material using a dichroic mirror giving a seed beam radius of 120 µm. Another dichroic mirror at the other side of the gain material separated the pump and seed beams again.

4.4.2.2 Second amplifier stage output

To measure the output of the second amplifier stage, a power meter was inserted into the beam path of the seed beam before it entered the third amplifier stage. The unabsorbed pump power was measured by placing a thermal power meter behind the dichroic mirror positioned after the gain medium. The dichroic mirror reflected the seed beam but allowed the unabsorbed pump power to pass through. The absorbed pump power was then inferred by subtracting the transmitted pump power from the incident pump power. Figure 4.13 shows the power transfer for the second amplifier stage.

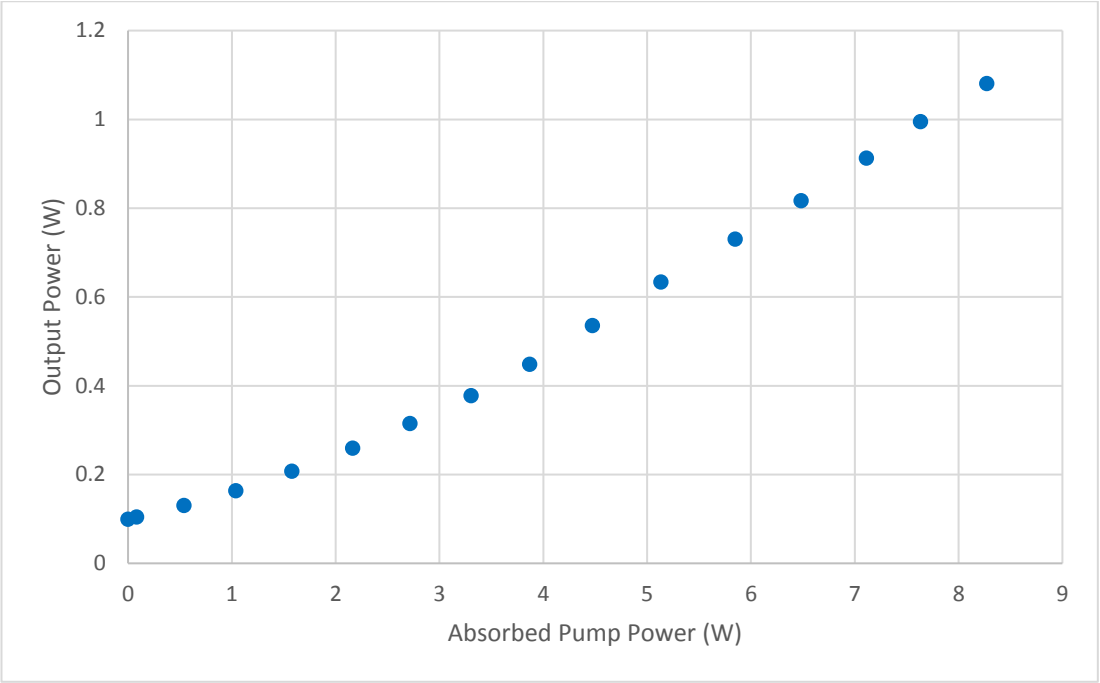

Figure 4.13 – Power transfer for the second amplifier stage.

An output power of approximately 1.1 W was achieved for an absorbed pump power of just over 8 W, which was expected based on modelling of the second amplifier stage. With an input power of 0.1 W, this was a gain of 11. The gain is high for the second amplifier stage as the input seed beam intensity is low enough to be well away from the saturation intensity of the amplifier. Even though the intensity of the input seed beam was 2.21 x 10^6 W/m^2 for the second amplifier, compared to an input seed intensity of 0.66 x 10^6 W/m^2 for the first amplifier stage, the gain was higher for the second stage. The gain was lower for the first stage due to the deleterious effects of ETU and temperature which was a consequence of the higher doping concentration used.

Figure 4.14 shows the same empirical data as in Figure 4.13 but with the addition of three sets of modelled data: the red modelled data is for a Gaussian pump beam shape without the effects of temperature or ETU included; the green modelled data is for a top-hat pump beam shape, also without the effects of temperature or ETU included; and the blue modelled data is for a top-hat pump beam shape but with

the effects of temperature and ETU included. The pump beam radius was modelled as 255 µm as the pump beam diverged within the gain medium and this value represents the average pump beam radius throughout the length of the crystal.

It can be seen from Figure 4.14 that the Gaussian model, with no temperature or ETU effects, provided the best fit to the data. This is in contrast to the first amplifier stage, as shown in Figure 4.9, where the Gaussian and top-hat models, with no temperature or ETU effects were a poor fit for the empirical data. For the first amplifier stage, the top-hat model, incorporating the effects of temperature and ETU, was the best fit to the empirical data, as shown in Figure 4.10. This can be explained by the differing doping concentration used for the different amplifiers. The first amplifier stage used 1 atm % Nd:YVO_4 as a gain medium and the second stage used 0.5 atm % Nd:YVO_4. The lower doping concentration leads to a lower temperature within the gain medium and the lower doping concentration also decreases the effects of ETU. In Figure 4.14, the two sets of modelled data with a top-hat pump beam shape, with and without the effects of temperature and ETU, are quite similar, showing that the effects of temperature and ETU are not as significant for this doping concentration.

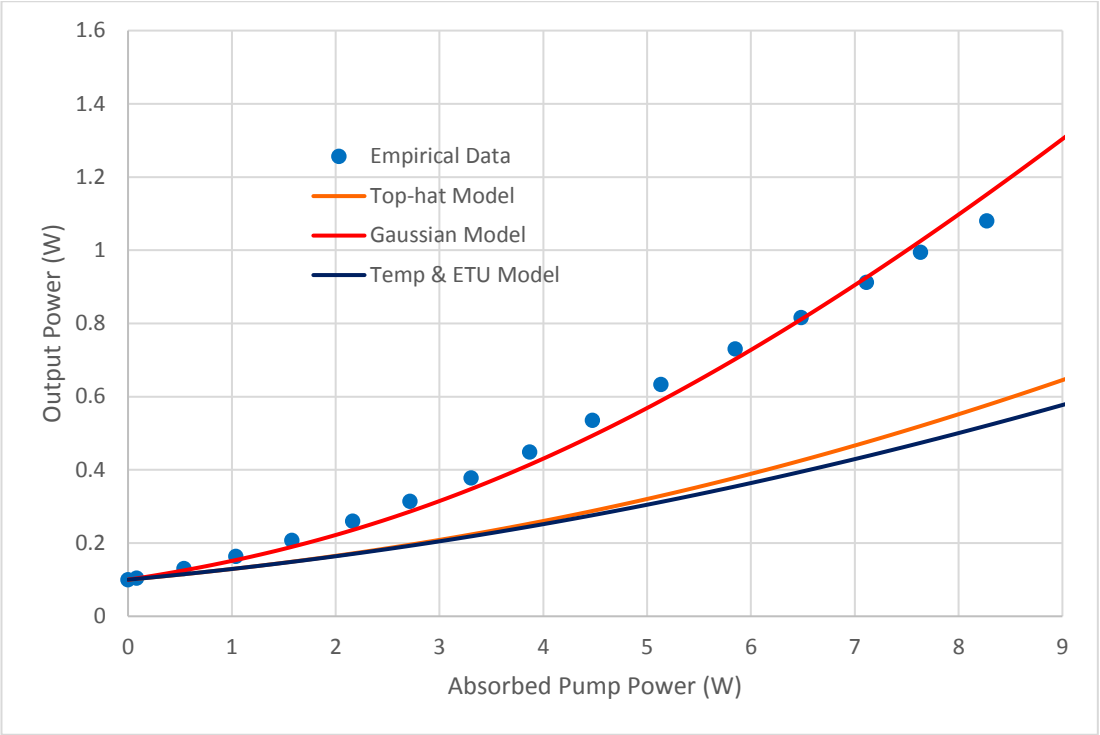

Figure 4.14 - Empirical data for the power transfer for the second amplifier stage is represented by blue dots, shown alongside three sets of modelled data of the same power transfer. The red and orange modelled data are for a Gaussian and top-hat pump beam shape, respectively, without the effects of temperature and ETU. The blue line represents the model with a top-hat pump beam shape with the effects of temperature and ETU present.

The second amplifier stage used by Agnesi et al [3] was, again, somewhat similar to the second amplifier stage used here. The second amplifier stage used by Agnesi also had a single pass of the seed beam but used a 10 mm long, 0.2 atm % Nd:YVO_4 crystal as the gain medium. In the second stage Agnesi amplifier, the pump beam was focussed to a radius of 140 µm with a maximum incident pump power of 25 W. The output seed beam of the first Agnesi amplifier stage, with a power of 650 mW, was used as the input seed beam to the second amplifier stage. With an incident pump power of 25 W, an absorbed pump power of 19 W was achieved with an output seed power of 6 W. The second Agnesi amplifier stage was modelled and the results of the modelling are shown in Figure 4.15, alongside the data taken from Agnesi et al [3].

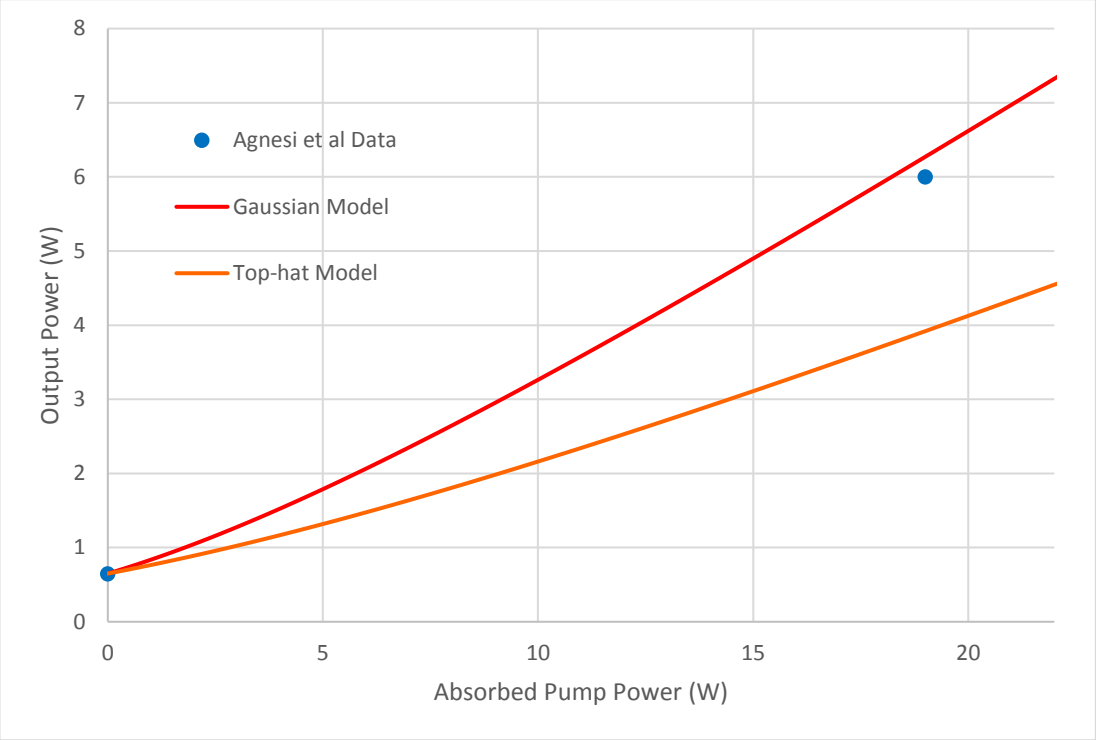

Figure 4.15 - A power transfer with data taken from Agnesi et al [3] *for the second stage of a microchip laser amplifier chain. The data taken from* [3] *is shown in blue. Also shown is modelled data of the Agnesi power transfer. The red line is the modelled data with a Gaussian shaped pump beam and the orange line is the modelled data with a top-hat shaped pump beam.*

The Agnesi second amplifier stage was modelled with similar assumptions made as when the first Agnesi amplifier stage was modelled. Again, the seed beam radius was not provided so it was assumed that it was the same size as the pump beam radius given, 140 µm in this case. The pump beam was also assumed to be divergent within the gain medium and so an average pump beam radius of 270 µm was used as this was similar to the average pump beam radius used to generate the modelled data in Figure 4.14. The fluorescence lifetime was increased to 117×10^{-6} s as the gain medium was 0.2 atm % Nd:YVO_4. This number was extrapolated from Figure 2.7 in Chapter 2 which shows the fluorescence lifetime of Nd:YVO_4 as a function of doping concentration. A Gaussian and top-hat pump beam shape were

both modelled and the Gaussian model was closest to the seed output power achieved by Agnesi et al.

Due to the variations between the Agnesi et al amplifier, which generated the data presented in Figure 4.15, and the second amplifier stage, which generated the data presented in Figure 4.13 and Figure 4.14, it is difficult to compare the performance of the two amplifiers. The agreement between the Gaussian model and the data from Agnesi et al in Figure 4.15 shows that the model can be used to estimate amplifier performance. Therefore, to better compare the difference in amplifier performance when using differing doping concentrations, two amplifier power transfers were modelled, one with a 0.2 atm % Nd:YVO_4 gain medium and one with a 0.5 atm % Nd:YVO_4 gain medium. Many parameters were kept the same for both modelled amplifiers: the length of the gain medium was 10 mm; the seed beam radius was 140 µm; the pump beam radius was 270 µm; and the input seed power was 650 mW. The fluorescence lifetime and the pump absorption coefficient were different and based on the relevant doping concentration. The results of the two modelled amplifiers are presented in Figure 4.16.

At an absorbed pump power of 20 W, the model with the 0.2 atm % gain medium predicted an output power of 6.6 W, compared to an output power of 5.4 W for the 0.5 atm % gain medium. This is a difference of 1.2 W in output power which is significant and it is therefore reasonable to assume that rod-type Nd:YVO_4 amplifiers benefit from lower doping concentrations.

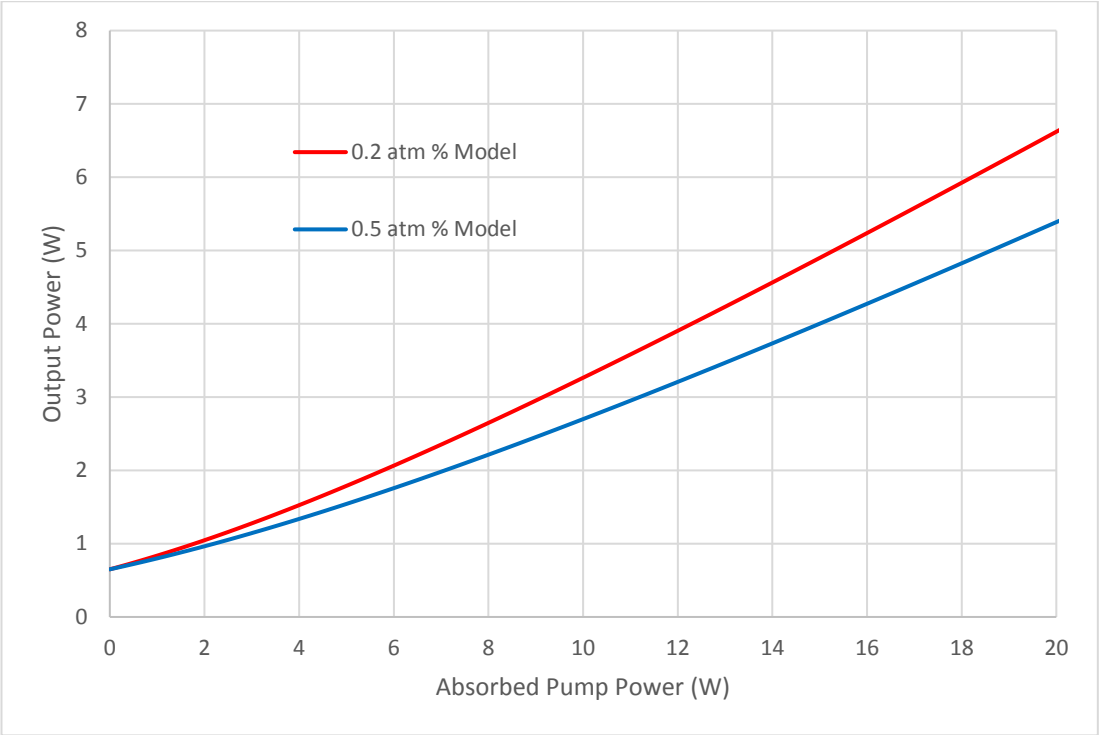

Figure 4.16 – Two amplifier power transfers modelled with Gaussian pump beam profiles. The red line represents a 0.2 atm % Nd:YVO_4 gain medium and the blue represents a 0.5 atm % Nd:YVO_4 gain medium.

The next section continues onto the third amplifier stage where the output seed beam of the second amplifier stage, as displayed in Figure 4.13 and Figure 4.14, was used as the input seed beam for the third amplifier stage. In the upcoming section, the effects of re-orientating the amplifier, to provide a greater pump absorption along the more strongly absorbing axis of the gain medium, are explored and the deleterious effects of temperature are evident again.

4.4.2.3 Third amplifier stage output

The third amplifier stage had an input seed beam power just slightly greater than 1 W. In this amplifier stage, the first power transfer of the amplifier was taken with the amplifier gain medium orientated with the a-axis of the crystal was parallel to the pump beam polarisation and then, secondly, so that the c-axis of the crystal was

parallel to the pump beam polarisation. The seed beam polarisation was rotated using a half wave-plate so that the seed beam polarisation was always parallel to the c-axis of the amplifier gain medium as that axis had the highest stimulated-emission cross-section and, therefore, the highest gain. Figure 4.17 shows the pump absorption for the amplifier gain medium in both orientations.

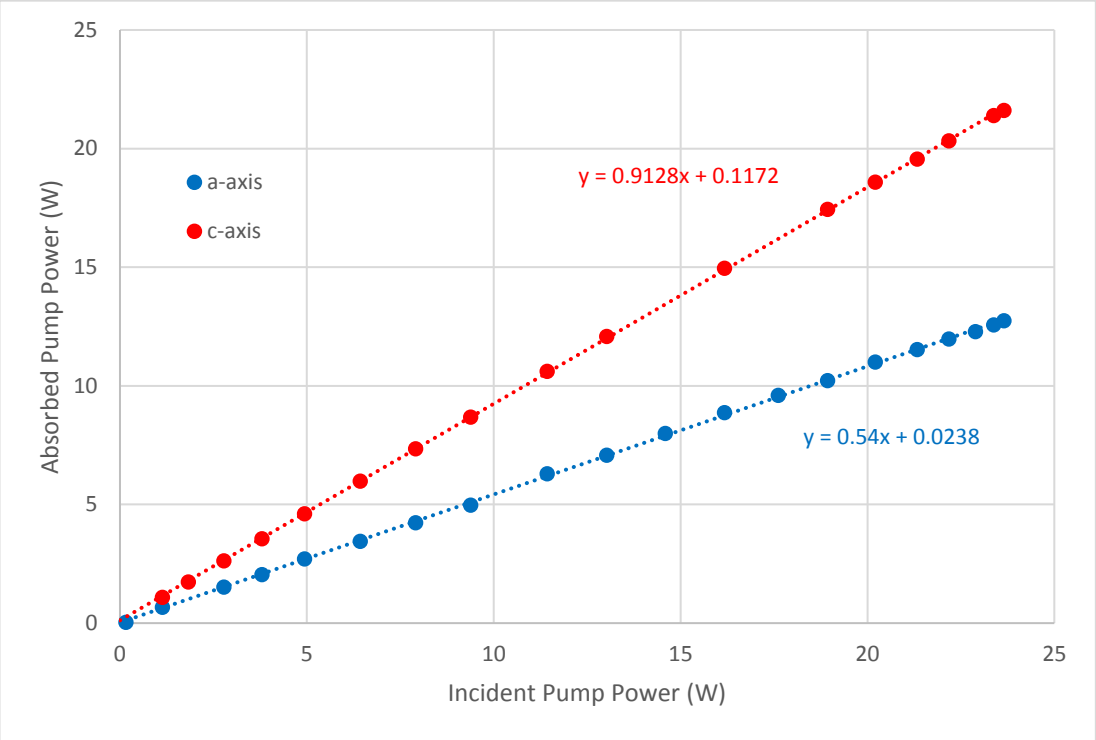

Figure 4.17 – the pump absorption of the amplifier with the amplifier gain medium orientated so that either the a-axis or the c-axis of the crystal was parallel to the pump beam polarisation.

From Figure 4.17, it can be seen that the pump absorption for the c-axis is stronger as it has a larger absorption coefficient. With the a-axis parallel to the pump beam polarisation, an absorption efficiency of 54 % was achieved but with the c-axis aligned parallel to the pump polarisation, the absorption efficiency was 91 %. While higher absorption is advantageous in terms of efficiency, it can be detrimental when using Nd:YVO_4 as a gain material due to the ill effects that are experienced at high

temperatures. The stronger absorption leads to higher peak temperatures and temperature gradients and poorer amplifier performance as seen in the power transfers for the third amplifier stage in Figure 4.18.

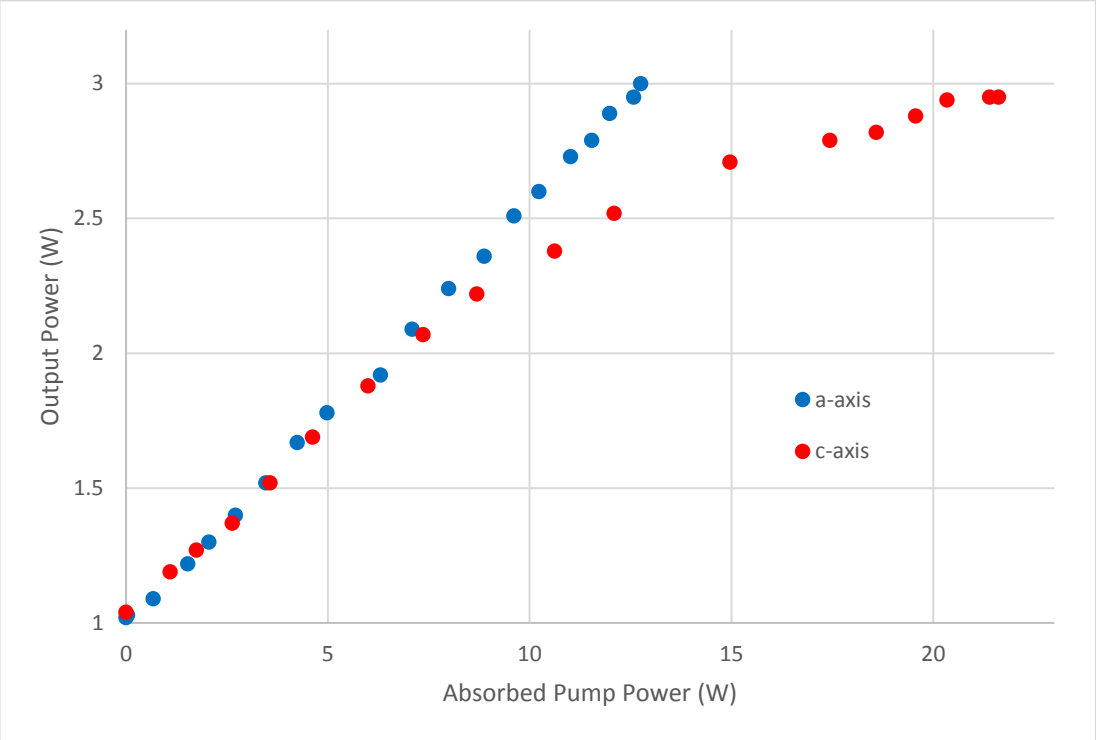

Figure 4.18 – Power transfer for the third amplifier stage showing the polarized pump absorption aligned to both the a-axis and c-axis of the Nd:YVO_4 crystal.

Both power transfers in Figure 4.18 had the same input seed beam and same pump beam profile. For absorbed pump powers up to 6 W, both power transfers behave similarly but at higher absorbed pump powers, they begin to diverge. The power transfer for the c-axis parallel to the pump beam polarisation starts to roll over, which is an indication that the temperature rise in the amplifier gain medium is beginning to cause deleterious effects as discussed in previous chapters. With the amplifier in the c-axis orientation, an output power of 2.95 W was achieved at an absorbed pump power of approximately 21.5 W, giving a gain of 2.8. A similar output power of 3 W was achieved for the a-axis orientation, but at a much lower

absorbed pump power of 12.75 W. The gain for this orientation was only slightly higher at 2.9. These results were in line with expectations according to the amplifier modelling, which will be discussed shortly. The power transfer for the a-axis orientation was stopped at an absorbed pump power of 12.75 W because this was the absorbed pump power when the maximum incident power of 23.7 W was reached. The power transfer for the c-axis orientation was also stopped at the same incident power.

The gain for this third stage was lower than the second stage as both amplifier stages had roughly the same pump beam diameter and the same seed beam diameter. As the input seed beam power for the second stage was significantly lower than for the third stage, the seed intensity was also much lower and the amplifier was far from the saturating regime. The third stage had a lower gain as it was closer to the saturating regime but also extracted the energy in the gain medium more efficiently.

These performs levels were in line with expectation gained through modelling of the third amplifier stage. Figure 4.19 shows the data from Figure 4.18 where the a-axis of the gain medium is aligned parallel to the polarisation of the pump beam, alongside modelled data of the amplifier with a Gaussian pump beam shape and a top-hat pump beam shape, both without the effects of temperature and ETU. The empirical data is slightly closer to the top-hat model but lies between the two models. Figure 4.20 shows the data from Figure 4.18 where the c-axis of the gain medium is aligned parallel to the polarisation of the pump beam, alongside modelled data of the amplifier with a top-hat shaped pump beam and also included the effects of temperature on the stimulated-emission cross-section and the effects of ETU. The model closely matches the empirical data in Figure 4.20.

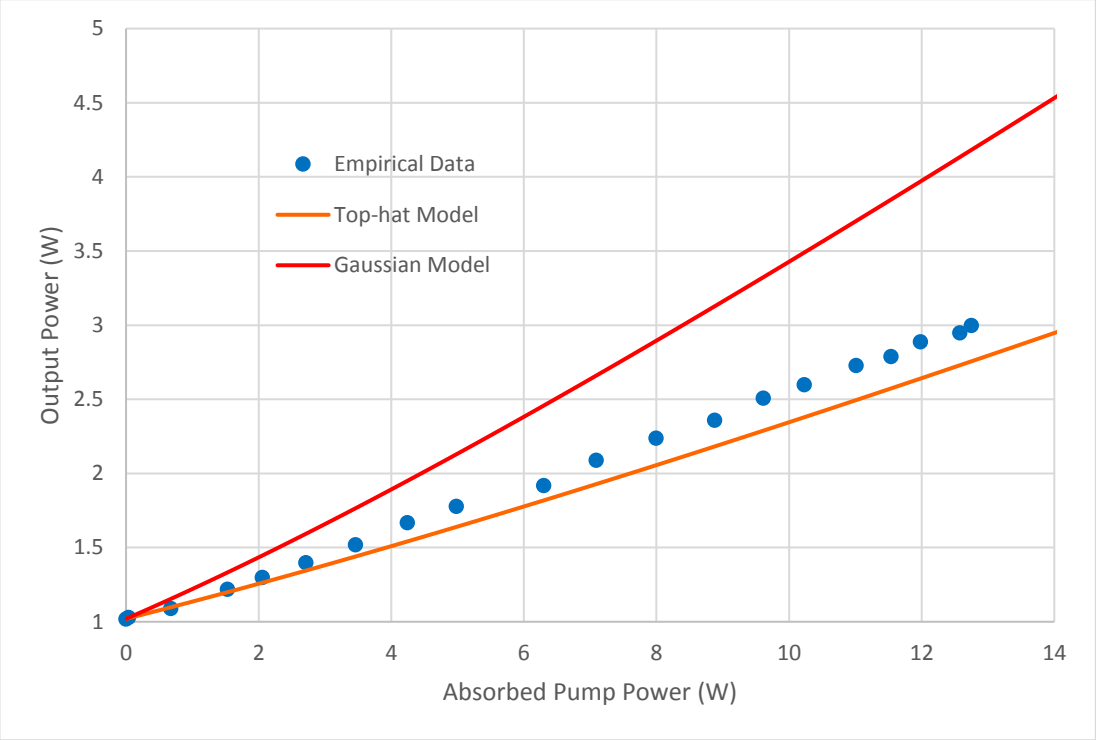

Figure 4.19 - Empirical data for the power transfer for the third amplifier stage, with the a-axis of the gain medium parallel to the pump beam polarisation, alongside modelled data of the same power transfer. The red line is the modelled data with a Gaussian shaped pump beam and the orange line is the modelled data with a top-hat shaped pump beam.

The increased absorption coefficient, that is a consequence of aligning the polarisation of the pump beam to the c-axis of the Nd:YVO_4 gain medium, leads to higher peak temperatures within the gain medium and the effects of temperature on the stimulated-emission cross-section become significant. As a result, the amplifier performance suffers as a consequence. It is advantageous to sacrifice pump absorption in order to ensure that the peak temperatures within the gain medium are minimised.

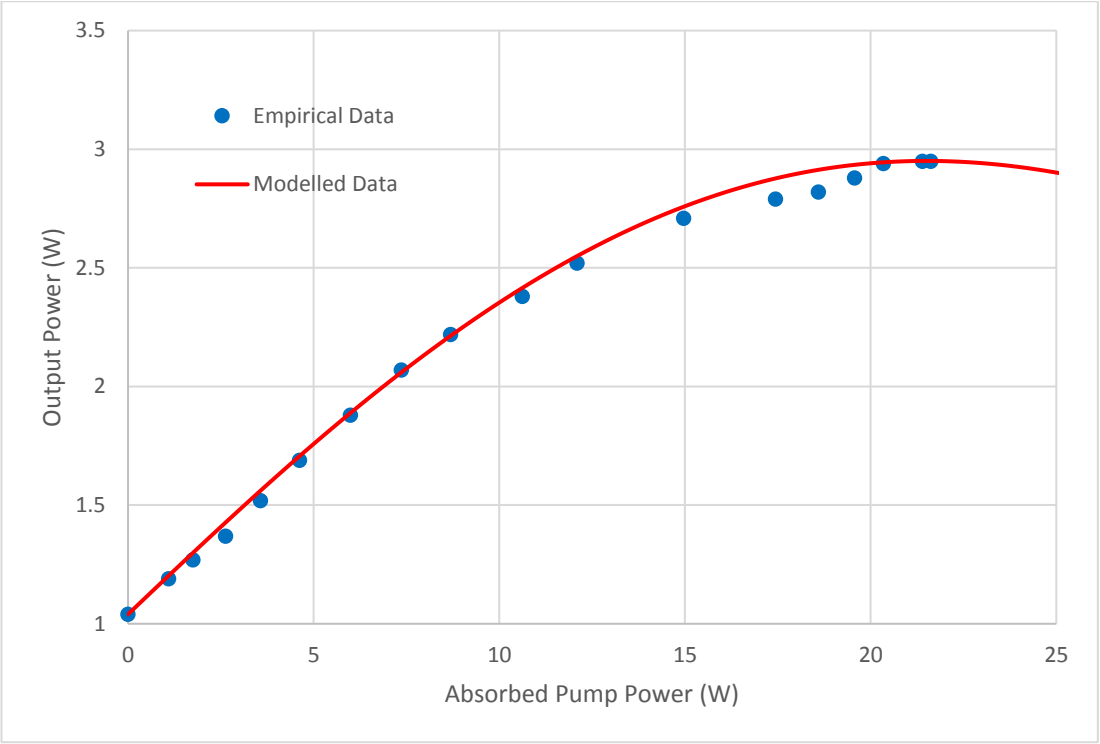

Figure 4.20 - Empirical data for the power transfer for the third amplifier stage, with the c-axis of the gain medium parallel to the pump beam polarisation, alongside modelled data of the same power transfer. The modelled data, in red, is with a top-hat shaped pump beam and includes the effects of temperature on the stimulated-emission cross-section and the effects of ETU.

The 43 mW output of an Nd:YVO_4, Q-switched, microchip was amplified to 3 W using three amplifier stages. The final output power achieved is less than that achieved in two amplifier stages by Agnesi et al [3] but the modelling suggests that this is due to the choice of various parameters, such as doping concentration, crystal length and pump and seed spot sizes, and that a similar performance could be achieved by altering such variables. In Figure 4.16, two amplifiers were modelled with identical parameters other than doping concentrations, one model utilising a doping concentration of 0.2 atm % and the other 0.5 atm %. At an absorbed pump power of 20 W, the 0.2 atm % model produced an output power of 6.6 W and the 0.5 atm % model, 5.4 W. The difference in output power, at an absorbed pump

power of 20 W, was 1.2 W. This suggests that sacrificing output power to accommodate a higher doping concentration may be beneficial in such circumstances where higher pump absorption is required, for example, if a compact amplifier design was necessary or when dealing with lower spatial brightness pumps.

The work in this chapter shows that careful consideration in the choice of doping concentration will be vital in achieving the desired balance of performance and practicality in such amplifiers. Further, it demonstrates that the models from Chapters 2 and 3 are useful tools in understanding the key role of the temperature dependent stimulated-emission cross-section and of ETU in determining the performance of these amplifiers.

4.5 Conclusions

This chapter explored the amplification of Q-switched microchip lasers as an alternative to expensive and complex mode-locked lasers for machining applications. Q-switched lasers are often simpler and cheaper to build compared to mode-locked lasers but typical pulse durations for Q-switched lasers are in the nanosecond regime. However, by using Q-switched microchip lasers, with shorter pathlengths, pulse durations can be achieved that are 10s to 100s of picoseconds, whilst still maintaining the simplicity and lower cost of Q-switched lasers. Nd:YVO_4 is also a promising gain medium for Q-switched microchip lasers and their amplification, with its high gain and high pump absorption, but care must be taken to avoid the deleterious effects of temperature that have been discussed in this thesis.

Firstly, a Q-switched microchip laser was purchased from Batop Optoelectronics (MCT-1064_90ps). The maximum output power reached was 43 mW, with an incident pump power of 399 mW and a repetition frequency of 302 kHz. This laser output served as the input seed beam to the first amplifier stage. The first stage incorporated a double-pass of the seed beam, through a 5 mm long, 1 atm %

Nd:YVO_4 gain medium and achieved an output power of 130 mW, providing a gain of 3.7. This result compared well with modelled data that considered the effects of temperature and ETU. The model was checked against a similar amplifier reported by Agnesi et al [3] and matched the data from that amplifier reasonably well.

The 130 mW output of the first amplifier stage was then used to seed the second amplifier stage, this time utilising a 5 mm long, 0.5 atm % Nd:YVO_4 gain medium. The seed beam was only passed through the gain medium once in this amplifier stage. The pump beam was polarised for this amplifier and aligned parallel to the a-axis of the gain medium. An output power of approximately 1.1 W was achieved, which was a gain of 11 for this amplifier stage. This result was predicted reasonably well by the model.

Agnesi et al [3] also reported on a second amplifier stage, using a 0.2 atm % Nd:YVO_4 gain medium, and this was, again, modelled with the modelled results matching the performance of the Agnesi amplifier. The model was then used to compare the theoretical performance of a 0.2 atm % Nd:YVO_4 amplifier and a 0.5 atm % Nd:YVO_4 amplifier. With an input seed power of 650 mW and an absorbed pump power of 20 W, for both amplifiers, the 0.2 atm % amplifier had a theoretical output power of 6.6 W compared to an output power of 5.4 W for the 0.5 atm % amplifier. Whilst the 0.2 atm % amplifier had a greater output power by a value of 1.2 W, the increased pump absorption of the 0.5 atm % amplifier could be advantageous in some circumstances where the increased pump absorption may be worth the sacrifice in output power. It may be possible to achieve higher output powers with a lower incident pump power using higher doping concentrations.

The output beam from the second amplifier stage was then used as the input seed beam to the third, and final, amplifier stage. This stage used another 5 mm long, 0.5 atm % Nd:YVO_4 crystal as the gain medium, with the polarisation of the pump beam aligned to the a-axis of the gain medium. This stage achieved an output power of 3 W at an absorbed pump power of 12.8 W, providing a gain of 2.9. The gain medium was rotated so that the polarised pump beam was parallel to the

c-axis of the gain medium and this provided a greater pump absorption but, with higher peak temperatures within the gain medium, the deleterious effects of temperature and ETU, which have been discussed in previous chapters, became evident again. With the third amplifier stage in this orientation, a peak output power of 2.95 W was achieved at an absorbed pump power of 21.6 W, providing a gain of 2.8.

Both orientations of the third amplifier stage were modelled. The amplifier with the pump polarisation aligned parallel to the a-axis of the gain medium was most closely matched to the model with a top-hat pump beam shape, without any of the effects of temperature or ETU included. The amplifier with the pump polarisation aligned parallel to the c-axis of the gain medium, however, closely matched the model that had a top-hat pump beam shape and included the effects of temperature and ETU.

This chapter shows that Nd:YVO_4 is a useful choice of gain medium for picosecond, Q-switched, microchip lasers and their amplification, where the power regime means the deleterious effects of temperature on the stimulated-emission cross-section can be avoided by some careful design considerations. The 43 mW output power of an Nd:YVO_4, Q-switched, microchip laser was amplified to a power of 3 W in three amplifier stages and, by comparison to the work of Agnesi et al [3], greater output powers should be able to be achieved by careful consideration of doping concentration and pump and seed beam sizes.

In combination with the laser analyses in earlier chapters, the amplifier experiments and modelling in this chapter highlight the importance of the temperature dependent stimulated-emission cross-section and of ETU in determining the performance limits of compact Nd:YVO_4 devices.

4.6 References

[1] G. J. Spühler *et al.*, "Experimentally confirmed design guidelines for passively Q-switched microchip lasers using semiconductor saturable absorbers: errata," *J. Opt. Soc. Am. B*, vol. 18, no. 6, p. 886, 2001.

[2] A. C. Butler, D. J. Spence, and D. W. Coutts, "Scaling Q-switched microchip lasers for shortest pulses," *Appl. Phys. B Lasers Opt.*, vol. 109, no. 1, pp. 81–88, 2012.

[3] A. Agnesi, L. Carrà, F. Pirzio, and G. Reali, "Low-power 100-ps microchip laser amplified by a two-stage Nd:YVO_4 amplifier module," *Appl. Phys. B Lasers Opt.*, vol. 109, no. 4, pp. 659–662, 2012.

[4] J. Nikkinen, A. Härkönen, I. Leino, and M. Guina, "Generation of Sub-100 ps Pulses at 532, 355, and 266 nm using a SESAM Q-Switched Microchip Laser," *IEEE Photonics Technol. Lett.*, vol. 29, no. 21, pp. 1816–1819, Nov. 2017.

[5] O. Svelto, *Principles of Lasers*, Fifth. Springer, 2009.

[6] R. Paschotta, *Field Guide to Laser Pulse Generation*. 2009.

[7] J. J. Zayhowski and C. Dill, "Coupled-cavity electro-optically Q-switched Nd:YVO_4 microchip lasers," *Opt. Lett.*, vol. 20, no. 7, p. 716, 1995.

Chapter Five

Conclusions

5.1 Ultrashort pulsed lasers for machining applications

Ultrashort pulsed lasers are a key industrial tool for precision machining [1]–[4] and there is a requirement to reach higher average powers of 100 W and beyond. This need led to a project that sought to assess the possibility of amplifying a commercially available, ultrafast laser using a simplified thin-disk amplifier with Nd:YVO_4 as the gain material. This project was undertaken with an industrial partner which meant that manufacturability and cost were important factors in the amplifier design, as well as technical feasibility.

A thin-disk architecture was chosen as this design is proven to be effective in regards to thermal management [5], which is a key focus when operating at high average powers. Thin-disks can, however, be quite complex in their design as they require many passes of both pump and seed beams. To create a less complex, and therefore more easily manufactured design, a thicker disk was considered in order to increase the interaction length of the pump and seed beam with the gain medium, reducing the number of passes of both beams. The choice of Nd:YVO_4 as the gain medium was largely necessitated by the emission wavelength of the commercially available laser that was to be amplified, which was 1064 nm. A neodymium doped gain material was required and Nd:YVO_4 was chosen due to its high stimulated-emission cross-section [6] and commercial availability.

5.2 Modelling Nd:YVO_4 laser amplifiers

Initially, a simplified model of an Nd:YVO_4 rod amplifier was constructed, with single passes of both the pump and seed beams. The model provided insight into the

important parameters to consider when designing an Nd:YVO_4 laser amplifier. The modelled results were corroborated with empirical data, from the small-signal to the highly saturated regime, but only for relatively low absorbed pump powers of up to 10 W, at a wavelength of 808 nm. This simplified model was also extended to include the effects of energy transfer upconversion (ETU), which can be significant in Nd:YVO_4 [7]. The empirical data was taken from experiments that amplified a commercially available, mode-locked, picosecond laser emitting a wavelength of 1064 nm. The pulse duration was less than 15 ps with a repetition rate of 1 MHz and the maximum average output power was 34 W. The amplifiers used Nd:YVO_4 rods as a gain medium with doping concentrations of 0.5 atm % and 1 atm % and explored various different pump and seed beam radii.

The model was then adapted for a thin-disk design, incorporating double-passes of the pump and seed beams. This adapted model was tested against empirical data taken from an amplifier experiment. The seed laser used for these experiments was another commercially available, mode-locked, picosecond laser with a wavelength of 1064 nm. This laser had a pulse duration of approximately 10 ps with a repetition rate of 200 kHz. The maximum average output power of this laser was 16 W. A larger pump laser was used for the amplifier, and this provided a maximum absorbed pump power of 35 W. The gain medium for these experiments was in a disk architecture with dimensions of 6 mm x 5 mm x 0.25 mm. Both 1 atm % and 2 atm % Nd:YVO_4 were used.

When various amplifier designs were tested, each power transfer exhibited a rollover that severely limited the performance of each amplifier, with a maximum output power of 20.1 W from an input seed power of 13 W. This rollover could not be explained using the available model. The deleterious effects of temperature of the stimulated-emission cross-section of Nd:YVO_4 [8] had to be incorporated in order to accurately model this rollover behaviour. To assist with the modelling of temperature related effects, the temperature rise within the gain material was measured as a function of absorbed pump power by measuring the shift in the peak emission of fluorescence when the gain medium was pumped, as this varies with temperature.

However, the amplifier was not seeded under these conditions and this led to a measured temperature rise that was overestimated when compared to a seeded amplifier. The temperature rise under unseeded conditions was then inferred by fitting the modelled data to the empirical data by varying the temperature rise as a function of pump power. This provided accurate models of amplifier performance.

5.3 Multi-pass amplifier

Additional passes of the seed beam were added to the laser amplifier to provide four passes in total. With the additional passes, a greater output power of 28.4 W, with an incident seed power of 16.1 W, was achieved, with pump and seed beam radii of 430 µm. This greater output power was due to the greater interaction length of the seed beam with the gain medium, but also because the greater extraction of energy from the gain medium ameliorated the negative effects of temperature on the stimulated-emission cross-section. A rollover in output power for this amplifier design was not observed with the pump power available.

The amplifier model was, again, adapted to include as many passes of the seed beam as required. This allowed various numbers of passes of the seed beam to be modelled at different pump and seed beam radii to determine a possible route to an output power of 100 W. Through this modelling, it was determined that adding more passes of the seed beam provides diminishing returns for each additional pass but, that adding more passes of the seed beam is more beneficial as the pump and seed beam radii are made larger. It was determined from the model that with a pump and seed radii of 800 µm and input seed power of 16 W, 99 passes of the seed beam would be required to reach an output power of 100 W. The number of passes of the seed beam required to reach an output power of 100 W could be reduced by increasing the pump and seed beam radii but the overall trend was towards a more traditional thin-disk approach with the added manufacturing complexity and cost that it brings. The deleterious effects of temperature on the stimulated-emission cross-section of Nd:YVO_4 made the idea of a thick-disk unfeasible.

In an attempt to explore a route to 100 W of output power in fewer passes, a different, more powerful, seed laser was used. The new seed laser was a commercially available, mode-locked, picosecond laser with an emission wavelength of 1064 nm. The pulse duration was less than 15 ps with a pulse repetition rate of 1 MHz and the maximum available power was 34 W. Amplifier experiments were conducted with this new seed laser at a variety of different pump and seed beam radii with a 250 µm thick, 1 atm % Nd:YVO_4 gain medium. With a double-pass of the seed beam, a maximum output power of 46.3 W was achieved with pump and seed beam radii of 540 µm and an initial seed power of 33.7 W.

With this new input seed power, the number of passes required to reach an output power of 100 W was modelled again. It was estimated that, with a pump and seed beam radii of 1300 µm, an output power of 100 W could be achieved with twenty passes of the seed beam. These results indicate that it would be advantageous to explore a multi-stage amplifier, considering the importance of the input seed power. This is likely to be a less complex and more easily manufactured design than trying to incorporate twenty passes of the seed beam in a single stage.

5.4 High Brightness

Output power is not the only consideration when amplifying a seed beam for precision machining. High brightness is also required in order to focus the beam to the appropriate sizes required. However, during the experiments that form the majority of this thesis, there was not a particular focus on improving beam quality but it was measured in the last set of experiments discussed in Section 5.2.

The commercially available seed laser that provided an input seed power of 34 W had excellent beam quality, with an M^2 value of 1.3. Beam quality measurements were taken with the amplifier un-pumped, in the middle of the power transfer and when the amplifier exhibited rollover behaviour and for four different pump and seed beam radii: 540 µm, 760 µm, 1000 µm and 1300 µm. For the two larger beam radii, the beam quality was slightly worse after passing through the un-pumped amplifier. For

the 1000 µm radii, the M^2 value was 1.63 and the M2 value for the 1300 µm radii was 2.17. At the rollover of the power transfer, the beam quality was at its worst for all spot sizes, although the larger beam radii cases fared better than the smaller. The M^2 values for the 540 µm, 760 µm, 1000 µm and 1300 µm beam radii at rollover were 6.84, 5.10, 2.84 and 2.11, respectively.

The effect of the ratio of the pump and seed beam radii on beam quality was also explored and it proved to be significant as the beam quality degraded as the seed to pump beam ratio was increased. With an absorbed pump power of 22 W, the ratio of the seed beam radius to pump beam radius was varied from 0.47 to 1.29. At a ratio of 0.47, the M^2 value measured was 1.12 with an output seed power of 41.0 W. With a seed to pump beam ratio of 1.29, the M^2 value was measured as 1.44 with an output seed power of 40.1 W. These results indicated that the high beam quality required could be realised without reducing the output power of the amplifier significantly. Ensuring good beam quality while reaching the high output powers required is an area that must be explored in any future work.

5.5 Q-switched microchip laser amplification

Work was also undertaken to explore the amplification of a Q-switched microchip laser for potential machining applications as an alternative to mode-locked lasers which can be expensive and complex. Q-switched lasers usually operate with pulse durations in nanoseconds but, as the pulse duration is a function of path length in Q-switched lasers, shorter path lengths can yield pulses that are 10s of picoseconds in duration [9], [10].

A commercially available Q-switched laser was purchased that achieved an average output power of 43 mW, a repetition frequency of 302 kHz and a pulse duration of 80 ps. This Q-switched laser served as the input seed beam to three subsequent amplifier stages, which amplified the laser to an average power of 3 W, a total gain of 70. The first amplifier stage utilised a 5 mm long, 1 atm % Nd:YVO_4 rod and, at an absorbed pump power of 7.8 W, amplified the seed beam to 130 mW with two passes

of the seed beam. The second stage had only one pass of the seed beam and the gain medium was 5 mm long, 0.5 atm % Nd:YVO_4. The seed beam was then amplified to a power of 1.1 W for an absorbed pump power of 8.3 W. The final amplifier stage, which amplified the seed beam to a power of 3 W at an absorbed pump power of 12.8 W, also utilised 5 mm long, 0.5 atm % Nd:YVO_4 as the gain medium.

Each amplifier stage was modelled with different versions of the model developed in earlier chapters, providing the best fit to the data for different amplifier stages. For the first stage, with a gain medium of 1 atm % Nd:YVO_4, the deleterious effects of temperature had to be taken into consideration in order for the model to agree with the empirical data. For the two latter stages, with 0.5 atm % Nd:YVO_4 as the gain medium, the empirical data agreed with the model that did not take into account the effects of temperature. This highlighted that, even at low absorbed pump powers, the doping concentration is an important parameter to consider when designing Nd:YVO_4 laser amplifiers due to the effects of temperature of the stimulated-emission cross-section.

5.6 Overall conclusions

The work in this thesis demonstrates the importance of understanding the detail of the operation of a particular gain material, particularly when pushing towards simpler and more manufacturable design approaches. In particular, the effect of temperature on the emission cross-section of Nd:YVO_4 is shown to significantly effect what can be achieved with compact amplifier designs, particularly those based on thin-disk approaches. Modular amplifiers to boost the power of existing picosecond lasers at 1064 nm would be very beneficial for upgrading existing materials processing capabilities, but requires both performance and practicality. The work presented here indicates that a multi-stage amplifier approach will be required to reach 100 W average powers without undue complexity. Similarly, for the amplification of picosecond microchip lasers, the use of longer, lightly doped amplifiers is shown to be necessary due to the performance degradation that results from temperature induced reduction in the emission cross-section.

5.7 References

[1] A. K. Dubey and V. Yadava, “Laser beam machining - A review,” *Int. J. Mach. Tools Manuf.*, vol. 48, no. 6, pp. 609–628, 2008.

[2] W. M. Steen and J. Mazumder, *Laser Material Processing*. 2010.

[3] J. Dutta Majumdar and I. Manna, “Laser processing of materials,” *Sadhana*, vol. 28, no. 3–4, pp. 495–562, 2003.

[4] H. Schulz and T. Moriwaki, “High-speed Machining,” *CIRP Ann. - Manuf. Technol.*, vol. 41, no. 2, pp. 637–643, 1992.

[5] A. Giesen and J. Speiser, “Fifteen years of work on thin-disk lasers: Results and scaling laws,” *IEEE J. Sel. Top. Quantum Electron.*, vol. 13, no. 3, pp. 598–609, 2007.

[6] Y. Sato and T. Taira, “Spectroscopic properties of neodymium-doped yttrium orthovanadate single crystals with high-resolution measurement,” *Japanese J. Appl. Physics, Part 1 Regul. Pap. Short Notes Rev. Pap.*, vol. 41, no. 10, pp. 5999–6002, Oct. 2002.

[7] S. Cante, S. J. Beecher, and J. I. Mackenzie, “Characterising energy transfer upconversion in Nd:YVO_4 at elevated temperatures,” *Opt. InfoBase Conf. Pap.*, vol. Part F75-A, no. 6, pp. 11935–11943, 2017.

[8] X. Délen, F. Balembois, and P. Georges, “Temperature dependence of the emission cross section of Nd:YVO_4 around 1064 nm and consequences on laser operation,” *J. Opt. Soc. Am. B*, vol. 28, no. 5, p. 972, Apr. 2011.

[9] G. J. Spühler *et al.*, “Experimentally confirmed design guidelines for passively Q-switched microchip lasers using semiconductor saturable absorbers: errata,” *J. Opt. Soc. Am. B*, vol. 18, no. 6, p. 886, 2001.

[10] A. C. Butler, D. J. Spence, and D. W. Coutts, “Scaling Q-switched microchip lasers for shortest pulses,” *Appl. Phys. B Lasers Opt.*, vol. 109, no. 1, pp. 81–88, 2012.